

**NMR spectroscopy studies  
to elucidate the role of SPX domains  
in phosphate homeostasis**

**Inauguraldissertation**

zur  
Erlangung der Würde eines Doktors der Philosophie

vorgelegt der

Philosophisch-Naturwissenschaftlichen Fakultät

der Universität Basel

von

**Joka Piperčević**

aus Slowenien

und

Deutschland

Basel, 2021

Genehmigt von der Philosophisch-Naturwissenschaftlichen Fakultät  
auf Antrag von  
Prof. Sebastian Hiller und Prof. Marek Basler

Basel, den 15. Dezember 2020

Prof. Dr. Marcel Mayor  
Dekan

*“Science is not only  
a disciple of reason,  
but, also,  
one of romance and passion.”*

- Stephen Hawking

## Acknowledgements

Firstly, I would like to express my gratitude to my head advisor Prof. Sebastian Hiller for allocating me interesting projects, his constant support, his openness to develop and work on my own ideas while using different techniques and working with different research groups.

Secondly, special thanks go to my current supervisor Dr. Bastian Kohl. His knowledge and experience at uncounted coffee breaks helped me to navigate through my various projects and make the best of it.

As well, I would like to thank my PhD advisory and exam committee: Prof. Marek Basler and Prof. Henning Stahlberg. I cannot understate the value of their personal and scientific guidance throughout the years for which I am incredibly grateful.

I will not forget the help of the following collaborators: Prof. Andreas Mayer and Dr. Sisley Austin at University of Lausanne; Prof. Michael Hothorn, Dr. Rebekka Wild and Dr. Martina Ried from University of Geneva; Prof. Dorothea Fiedler, Dr. Robert Harmel and Katy Franke from Leibniz Institute in Berlin for their help in the SPX project; Dr. Estefania Mulvihill and Dr. Stefania Mari from Prof. Daniel Müller Lab at D-BSSE for their help with my pore-building protein projects and Dr. Aris Roukounakis and Dr. Arnim Weber from Prof. Georg Häcker at University of Freiburg for their work on the apoptotic factor BIM; in-house collaborators on projects based on electron-microscopy were Prof. Henning Stahlberg, Dr. Kenneth Goldie, Dr. Ricardo Righetto, Dr. Mohamed Chami and Carola Alampi – on x-ray crystallography by Prof. Timm Maier, Dr. Roman Jakob and Dr. Dominik Herbst as well as on proteomics, Dr. Thomas Bock and Suzanne Moes and lastly to legendary Dr. Timothy Sharpe on biophysics aspects of my projects. Many thanks to you all!

I would also like to thank my student Christopher Kolloff who worked with me on my plant SPX project and all of my current and previous colleagues for their overall input: Dr. Lorenzo Sbongi, Dr. Hugo Correia, Prof. Björn and Dr. Irena Burmann, Dr. Lichun He, Dr. Leonor Morgado, Dr. Morgane Callon, Dr. Fabian Gruss, Dr. Raphael Böhm, Dr. Michael Zahn, Dr. Jean-Baptiste Hartmann, Dr. Stefan Bibow, Dr. Guillaume Mas, Dr.

Parthasarathi Rath, Dr. Hundeeep Major, Dr. Thomas Müntener, Dario Dörig, Elia Agustoni, Dr. Dritan Liko, Dr. Jakub Macošek, Majed Modaresi and especially on-side-PhD-buddy Johanna Ude. Without you, the fruitful lab meetings, lunch and coffee breaks would not have been as fun and enjoyable.

I would like to thank Fellowship for Excellence for believing in me, investing in my work with three years of sponsorship, and providing me with a hugely inspirational socializing platform which gave me access to PhD students and professors from other research fields at various events ranging from Fellowships for Excellence Symposium 2016 to Fellowships for Excellence excursions to Berlin and Munich organized greatly by Angie Klarer and Susanna Notz. I would like to also thank Antelope Career Program of University of Basel for giving me the chance to be a part of this great socializing and training unit that's helping us women to reach for stars.

Here I also express that it was an honour to be Chair of the PhD club at Biozentrum for two years. I am so thankful for the tremendous effort by numerous PhD representatives and external helpers which allowed us to offer many socializing, career and teaching events providing a socializing platform and guidance to others. Without the support of current Biozentrum director Prof. Alex Schier and previous Biozentrum director Prof. Erich Nigg as well as administration head Marcel Scheiwiller and various sponsors for our diverse events, this would have been impossible. Thanks again!

Mentioned as last but not least important was the unimaginable support I got from my husband, my son, my mum, my dad, my sister, my grandma, my in-laws and all my friends. You were my strength, my wisdom, my heart, my passion, and my joy in every challenge and every dream! Becoming a mummy during my PhD and ongoing corona crisis presented significant and daunting challenges. My dedicated husband, who took parental leave soon after the birth of our beautiful son, Josh, the tireless and selfless support of my mum, and a great daycare, previously, by daycare mum Nicole and currently by St. Elisabeth Kindergarten, made it possible to overcome seemingly impossible challenges during this most extraordinary journey of my life called PhD.

*“Science is not only  
a disciple of reason,  
but, also,  
one of romance and passion.”*

- Stephen Hawking

## Acknowledgements

Firstly, I would like to express my gratitude to my head advisor Prof. Sebastian Hiller for allocating me interesting projects, his constant support, his openness to develop and work on my own ideas while using different techniques and working with different research groups.

Secondly, special thanks go to my current supervisor Dr. Bastian Kohl. His knowledge and experience at uncounted coffee breaks helped me to navigate through my various projects and make the best of it.

As well, I would like to thank my PhD advisory and exam committee: Prof. Marek Basler and Prof. Henning Stahlberg. I cannot understate the value of their personal and scientific guidance throughout the years for which I am incredibly grateful.

I will not forget the help of the following collaborators: Prof. Andreas Mayer and Dr. Sisley Austin at University of Lausanne; Prof. Michael Hothorn, Dr. Rebekka Wild and Dr. Martina Ried from University of Geneva; Prof. Dorothea Fiedler, Dr. Robert Harmel and Katy Franke from Leibniz Institute in Berlin for their help in the SPX project; Dr. Estefania Mulvihill and Dr. Stefania Mari from Prof. Daniel Müller Lab at D-BSSE for their help with my pore-building protein projects and Dr. Aris Roukounakis and Dr. Arnim Weber from Prof. Georg Häcker at University of Freiburg for their work on the apoptotic factor BIM; in-house collaborators on projects based on electron-microscopy were Prof. Henning Stahlberg, Dr. Kenneth Goldie, Dr. Ricardo Righetto, Dr. Mohamed Chami and Carola Alampi – on x-ray crystallography by Prof. Timm Maier, Dr. Roman Jakob and Dr. Dominik Herbst as well as on proteomics, Dr. Thomas Bock and Suzanne Moes and lastly to legendary Dr. Timothy Sharpe on biophysics aspects of my projects. Many thanks to you all!

I would also like to thank my student Christopher Kolloff who worked with me on my plant SPX project and all of my current and previous colleagues for their overall input: Dr. Lorenzo Sbongi, Dr. Hugo Correia, Prof. Björn and Dr. Irena Burmann, Dr. Lichun He, Dr. Leonor Morgado, Dr. Morgane Callon, Dr. Fabian Gruss, Dr. Raphael Böhm, Dr. Michael Zahn, Dr. Jean-Baptiste Hartmann, Dr. Stefan Bibow, Dr. Guillaume Mas, Dr.

Parthasarathi Rath, Dr. Hundeeep Major, Dr. Thomas Müntener, Dario Dörig, Elia Agustoni, Dr. Dritan Liko, Dr. Jakub Macošek, Majed Modaresi and especially on-side-PhD-buddy Johanna Ude. Without you, the fruitful lab meetings, lunch and coffee breaks would not have been as fun and enjoyable.

I would like to thank Fellowship for Excellence for believing in me, investing in my work with three years of sponsorship, and providing me with a hugely inspirational socializing platform which gave me access to PhD students and professors from other research fields at various events ranging from Fellowships for Excellence Symposium 2016 to Fellowships for Excellence excursions to Berlin and Munich organized greatly by Angie Klarer and Susanna Notz. I would like to also thank Antelope Career Program of University of Basel for giving me the chance to be a part of this great socializing and training unit that's helping us women to reach for stars.

Here I also express that it was an honour to be Chair of the PhD club at Biozentrum for two years. I am so thankful for the tremendous effort by numerous PhD representatives and external helpers which allowed us to offer many socializing, career and teaching events providing a socializing platform and guidance to others. Without the support of current Biozentrum director Prof. Alex Schier and previous Biozentrum director Prof. Erich Nigg as well as administration head Marcel Scheiwiller and various sponsors for our diverse events, this would have been impossible. Thanks again!

Mentioned as last but not least important was the unimaginable support I got from my husband, my son, my mum, my dad, my sister, my grandma, my in-laws and all my friends. You were my strength, my wisdom, my heart, my passion, and my joy in every challenge and every dream! Becoming a mummy during my PhD and ongoing corona crisis presented significant and daunting challenges. My dedicated husband, who took parental leave soon after the birth of our beautiful son, Josh, the tireless and selfless support of my mum, and a great daycare, previously, by daycare mum Nicole and currently by St. Elisabeth Kindergarten, made it possible to overcome seemingly impossible challenges during this most extraordinary journey of my life called PhD.

## Table of Contents

Abstract.....	2
Introduction.....	4
Phosphate homeostasis .....	4
P <sub>i</sub> homeostasis during P <sub>i</sub> starvation.....	6
Pho4 - master switch of PHO pathway.....	6
Pho81 – main regulator of PHO pathway.....	7
P <sub>i</sub> transporters in the PHO pathway.....	8
Spl2 – regulator of P <sub>i</sub> -transport.....	9
P <sub>i</sub> storage by the VTC complex.....	9
P <sub>i</sub> scavenging by Pho4-linked phosphatases .....	12
Organic P <sub>i</sub> transport.....	13
P <sub>i</sub> homeostasis at high P <sub>i</sub> conditions.....	13
Kinase activity complex Pho80-Pho85.....	14
Low-affinity P <sub>i</sub> transporter Pho87 and Pho90.....	14
Vacuolar phosphate transporter Pho91 .....	15
Regulation of P <sub>i</sub> homeostasis.....	16
Inositol pyrophosphates.....	16
Bimodality of P <sub>i</sub> transporters .....	21
Biphasic transcriptional response .....	22
Other signaling pathways linked to P <sub>i</sub> homeostasis .....	23
Structural aspects of P <sub>i</sub> homeostasis.....	24
SPX domain.....	24
Ankyrin repeat domain .....	28
Aim.....	29
References .....	31
Background to NMR .....	42
General principles behind NMR .....	42
Chemical shift.....	45
Scalar coupling.....	46
Chemical exchange.....	46
Two-dimensional (2D) NMR spectroscopy .....	47

Backbone experiments.....	49
Secondary chemical shifts.....	51
Chemical shift differences.....	52
H/D – exchange spectroscopy.....	53
Residual dipolar coupling (RDC) .....	54
Protein dynamics.....	56
References .....	57
Regulation of an SPX – SPX domain interaction by inositol pyrophosphates.....	59
Abstract.....	61
One-sentence summary .....	61
Introduction.....	62
Results & Discussion .....	64
References: .....	69
Figures.....	72
Supplementary Materials.....	76
Material and Methods.....	77
Supplementary Table.....	82
Supplementary Figures .....	83
Supplementary references .....	93
In-depth discussion & outlook.....	95
Undiscovered structural element of the SPX domain .....	95
SPX as inhibitory unit of SPX proteins.....	96
Abolishment of SPX inhibition by inositol (pyro-) phosphates.....	96
Potential molecular mechanism of SPX .....	98
References .....	102
Abbreviations .....	104
Attachments.....	108

## Abstract

This PhD thesis focuses on two main areas of research. The first area deals with structural and functional studies of SPX domains in yeast and plants that are key to the understanding of the basis of eukaryotic phosphate ( $P_i$ ) homeostasis. A better understanding potentially offers a door-opener for future treatment of human primary familial brain calcification disease. Furthermore, engineered highly improved crops with better phosphate efficiencies could help to fight the imminent crisis due to overuse of soil biodiversity destructive  $P_i$  fertilizers and the limited world supply in  $P_i$  rock.

The second part deals with the pore-forming proteins bacterial *Escherichia coli* Colicin Ia and human Gasdermin D. Working with pore-forming toxin Colicin Ia can pave the way for novel drug-like antibiotics targeting *E. coli* related strains. The structure and function of Gasdermin D can help to develop therapeutics targeting aberrant inflammatory response causing neurodegenerative diseases like Alzheimer's, autoimmune disorders e.g. multiple sclerosis and macular degeneration as well as cardiometabolic disease type 2 diabetes.

This work focuses on SPX domains from yeast *Saccharomyces cerevisiae*. SPX domains are present in many functionally different proteins linked to  $P_i$  homeostasis. For the first time we were able to structurally and dynamically characterize a SPX domain in solution state by NMR discovering a previously unknown  $\alpha$ -helix7 expanding the known SPX domain boundaries. This  $\alpha$ -helix7 most likely plays a key role to diversify protein function of SPX-containing proteins. The molecular mechanism of the SPX-containing VTC complex in dependence of inositol pyrophosphates that are known to modulate  $P_i$  homeostasis was elucidated. We show for the first time that SPX domains form of a non-active inhibitory state comprised of a SPX-SPX heterodimer. Upon addition of inositol pyrophosphates or inositol phosphate this interaction is disrupted forming single monomers. The ligand binding induces a conformational change of the conserved  $\alpha$ -helix1 reorienting. The  $\alpha$ -helix1 is not only involved in the ligand binding, known from earlier studies, but also in protein-protein interactions.  $\alpha$ -helix1 contributes to the binding to other SPX domains as well as to the central TTM domain of Vtc2 suggesting a competitive binding mode. We propose a molecular mechanism for the function of SPX to consist of two main events – the inhibition of the function of SPX domain in the absence of inositol pyrophosphates and a second event activating the function of SPX

protein by inositol pyrophosphates, an event that is most likely protein specific. For SPX system in VTC complex, we speculate that the  $\alpha$ -helix7 could get exposed upon inositol (pyro-) phosphate binding and subsequently phosphorylated by cellular kinases and pyrophosphorylated by inositol pyrophosphates enabling the activation of ATPase activity for the required synthesis of polyphosphate chains. The findings of this study offer a new dimension for understanding cellular  $P_i$  homeostasis regulation.

My work on the role of SPX domains in plants resulted in a co-authored paper that can be found in the attachments. Here we show that the coiled-coil (CC) domain of a PSR transcription factor - known to interact with a stand-alone SPX protein in the presence of inositol pyrophosphates - is able to bind inositol pyrophosphate by itself. This is suggesting inositol pyrophosphate to act as molecular glue between stand-alone SPX proteins and the PSR transcription factor. This complex is important for inactivation of  $P_i$ -starvation genes under conditions with excess  $P_i$ .

Furthermore, I performed electron microscopy and x-ray crystallography studies on membrane-bound Colicin Ia demonstrating that the only known structure of colicin - the membrane-inserted pore of Colicin Ia at a low-resolution by negative-stain electron microscopy - is actually a contamination. We identified the contamination to be the oligomeric protein Dps from *E. coli* induced under mitomycin C reagent. The manuscript is in the submission phase and attached to this thesis. It will help the scientific community to rethink potential pore-forming mechanisms based on this wrong interpretation of the data.

Finally, the cryo-electron microscopy I conducted on caspase-cleaved Gasdermin D shed light on its previously unclear function. Gasdermin D was known to be a crucial substrate for inflammatory caspases causing pyroptosis via IL-1 $\beta$  and IL-18, however, the mechanism of Gasdermin D was still unknown. I observed gigantic membrane pores in the liposomes that were not reported before identifying the Gasdermin D as a pore-forming protein.

## Introduction

### Phosphate homeostasis

Phosphorus is one of the most widely and versatilely used chemical elements in cells. Its derivative orthophosphate,  $\text{PO}_4^{3-}$  or  $\text{P}_i$ , is a part of many biologically crucial molecules like deoxyribonucleic acid (DNA), ribonucleic acid (RNA), carbohydrates, fats, phospholipids and phosphorylated amino acids. But most importantly, phosphate is part of the energy currency as a building block of adenosine triphosphate (ATP). The ATP can get hydrolysed to ADP hereby releasing around  $-30\text{kJ/mol}$ . The actual energy status of the cell is determined by the cellular concentration of ATP and adenosine diphosphate (ADP). Hereby, ADP is generated from ATP by release of its gamma-phosphate. The ATP/ADP ratio serves as a driving force for a plethora of enzymatic reactions and as maintenance of proton motor force on plasma membranes.

With phosphate being so crucial for the cell, it is important that the cellular  $\text{P}_i$  homeostasis is tightly controlled. It includes the interplay of different proteins involved in  $\text{P}_i$  transport along with proteins linked to  $\text{P}_i$  scavenging and  $\text{P}_i$  storage as well as regulative proteins mediating  $\text{P}_i$  status to other phosphate-response signaling pathways of the cell [1]. Fluctuations in the external  $\text{P}_i$  phosphate availability bring along constant adjustments in the cell and thus a deficient  $\text{P}_i$  homeostasis can be fatal. While  $\text{P}_i$  deficiency can cause a cell arrest in yeast [2] and renal filtering dysfunction [3] in mice leading to kidney and bone impairment, an unregulated accumulation of phosphate can be lethal to yeast [4] and lead to growth deficiencies in plants [5], [6] as well as to phosphate deposits in the human brain causing neurodegeneration [7]. *Saccharomyces cerevisiae*, Baker's yeast, is a good model to study eukaryotic  $\text{P}_i$  homeostasis as it has been widely characterized under various  $\text{P}_i$  conditions and has potential relevance to understanding  $\text{P}_i$  homeostasis in higher eukaryotes like humans. In yeast, the  $\text{P}_i$  homeostasis can be divided in two pathways according to the external  $\text{P}_i$  availability like indicated in Fig. 1.

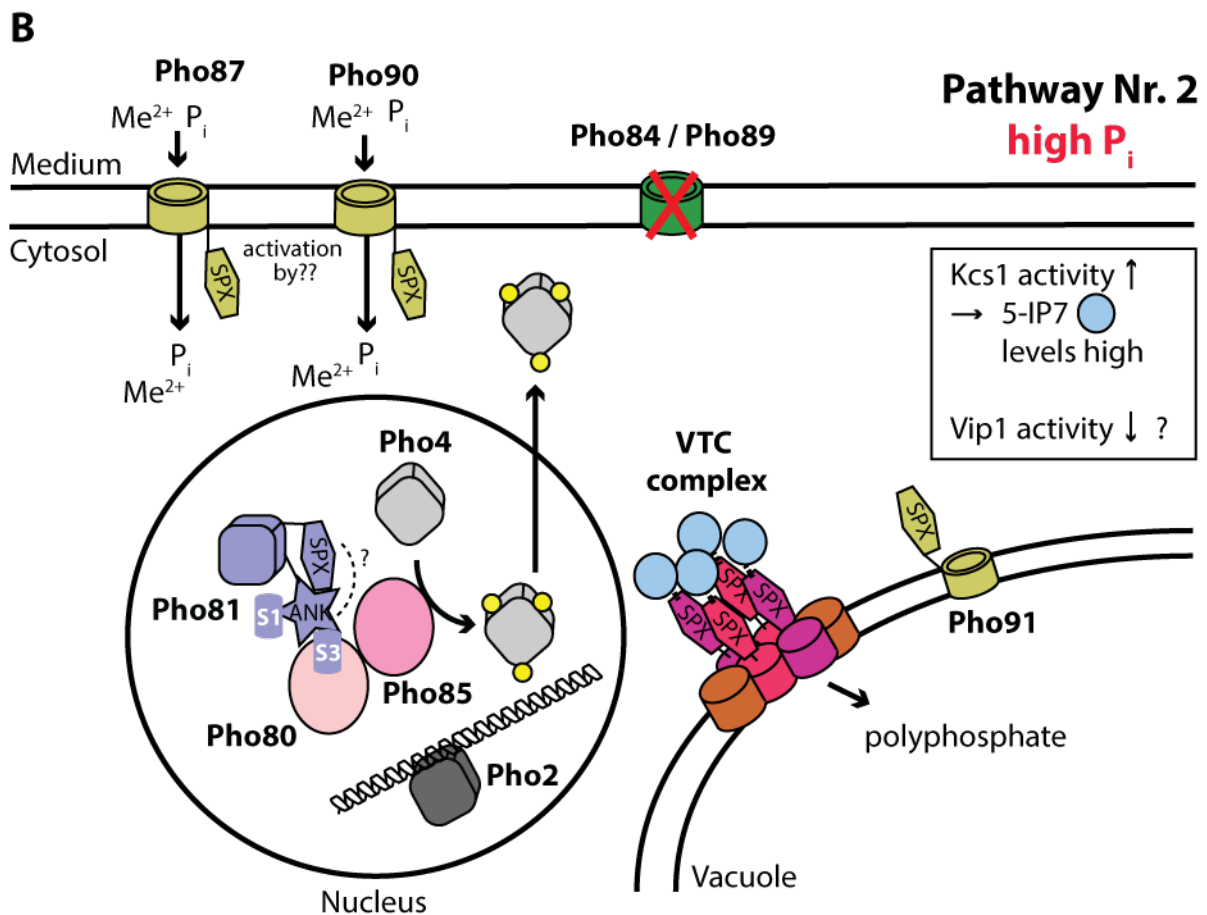
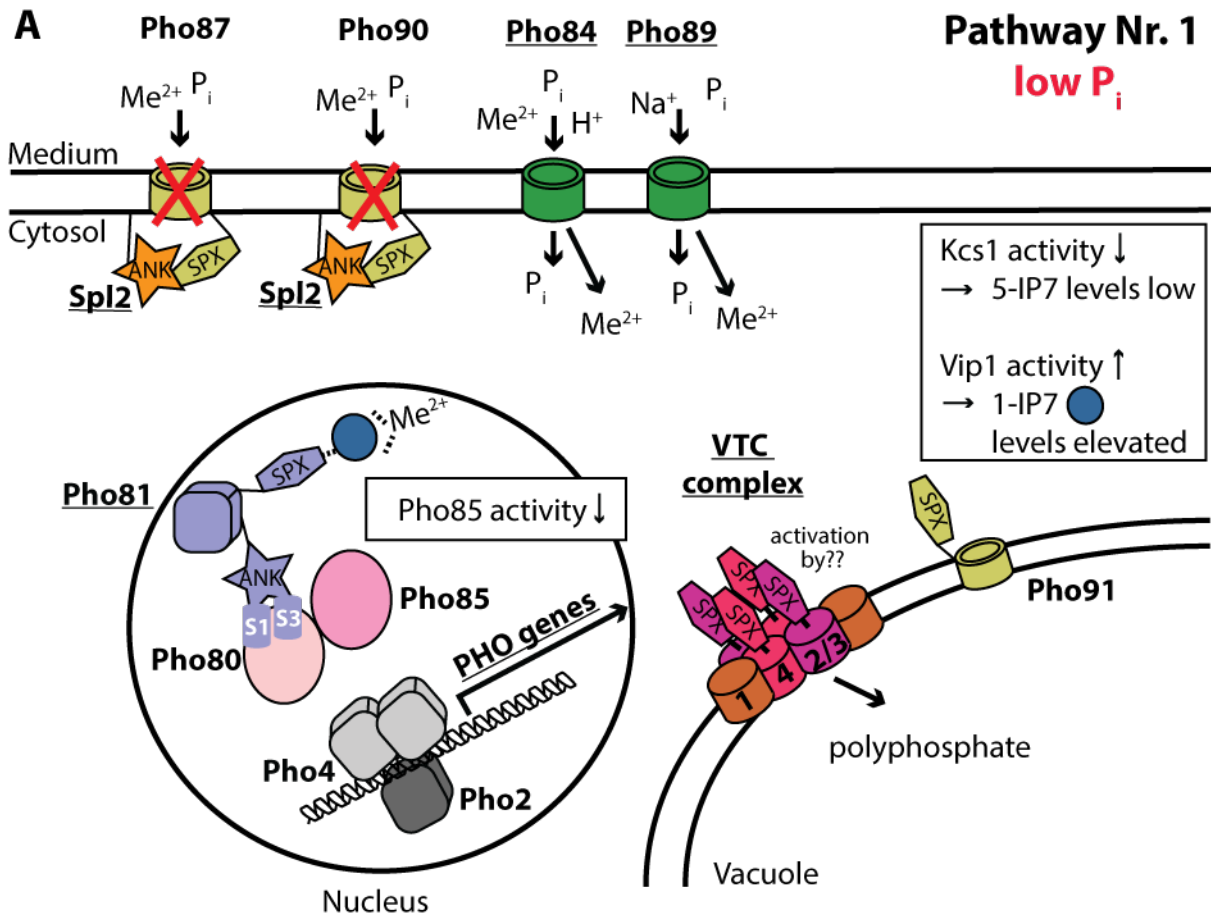


**Fig. 1: P<sub>i</sub> homeostasis in yeast divided according to external P<sub>i</sub> conditions.** (A) At very low P<sub>i</sub> concentrations; high-affinity P<sub>i</sub> transporters Pho84 and Pho89 are active while low-affinity P<sub>i</sub> transporters Pho87 and Pho90 are down regulated. Vip1 generated 1-IP7 activates Pho81. Hereby segment 3 (S3) binds to Pho80 and inhibits the kinase activity of Pho80-Pho85. Pho4 is less phosphorylated associating to Pho2 and leading to expression of PHO genes. The translated proteins are underlined. Upregulated VTC complex components generate polyphosphate chains. (B) At very high P<sub>i</sub> concentrations; low-affinity P<sub>i</sub> transporters Pho87 and Pho90 are active. Pho80-Pho85 is hyper-phosphorylating Pho4 (yellow circles) leading to Pho4 export to cytosol. 5-IP7 stimulates VTC complex generating polyphosphate chains. Proteins containing SPX or ANK domains have the domains annotated. S1 and S3 are parts of ANK domain from Pho81. The different components of VTC complex are labeled with the number 1 (=Vtc1), 2 (=Vtc2), 3 (=Vtc3) and 4 (=Vtc4). Different Inositol pyrophosphates, 1-IP7 (dark blue) or 5-IP7 (light blue), respectively, are colored in shown as circles. The figure was adapted from [1] and updated according to recent findings. Me<sup>2+</sup> is a divalent metal ion.

At high P<sub>i</sub> conditions, P<sub>i</sub>-linked proteins involved in P<sub>i</sub> homeostasis are responsible to prevent P<sub>i</sub>-based cell intoxication [4]. The low-affinity P<sub>i</sub> transporters Pho90 and Pho87 import P<sub>i</sub> moderately into the cell and leak internal P<sub>i</sub> [4], while potential cellular P<sub>i</sub>-surplus is handled by vacuolar proteins of the VTC complex [8], [9] and the vacuolar P<sub>i</sub>-transporter Pho91 [10], [11]. At P<sub>i</sub>-limiting conditions, a second group of proteins regulating P<sub>i</sub> homeostasis takes over. Activation of the PHO pathway enables transcription of phosphate-responsive genes like high-affinity P<sub>i</sub> transporters Pho84 and Pho89 and regulator Spl2 [8] that downregulates low-affinity P<sub>i</sub> transporters [4]. Their role is to ensure that the cells takes up as much external P<sub>i</sub> as possible and inactivate other transporters by inhibition or vacuolar degradation that could leak any P<sub>i</sub> [4]. They allow the cellular machinery to keep running to maintain intracellular P<sub>i</sub> levels - reflected in the ATP/ADP ratio - required for a plethora of reactions.

## **P<sub>i</sub> homeostasis during P<sub>i</sub> starvation**

Yeast regulates P<sub>i</sub> homeostasis during P<sub>i</sub> starvation through the PHO pathway [12]. Pho4 is the master switch of PHO regulon. It upregulates proteins linked to P<sub>i</sub> transport, P<sub>i</sub> scavenging, P<sub>i</sub> storage and others [8]. Many of the upregulated proteins contain a SPX domain or an ankyrin repeats domain [1], [13].

### **Pho4 - master switch of PHO pathway**

Pho4 is a basic helix-loop-helix transcription factor [14] upregulating transcription of phosphate-responsive genes in the P<sub>i</sub>-limiting conditions [8]. It is constitutively

expressed in low amounts independently of  $P_i$  availability [15] and its activity is controlled by its phosphorylation state [16], [17]. At high  $P_i$  conditions Pho4 can get phosphorylated on several serine-proline (SP) dipeptide phosphorylation sites (SP). This is enabled by the Pho80-Pho85 kinase complex [17] in a semi-processive way [18]. The phosphorylation has an effect on the subcellular localization of Pho4 [4] and on binding to a co-transcriptor of Pho4-responsive genes [19]. Hereby, a phosphorylation on SP2 and SP3 [19] are responsible for nuclear export of Pho4 to the cytosol by importin- $\beta$ -family member Msn5 bound to Gsp1-GTP [20]. Vice-versa, nuclear import of Pho4 is inhibited by Pse1/Kap121 [21] when Pho4 is phosphorylated on SP4 [19]. Furthermore, phosphorylated SP6 was shown to inhibit a binding to co-transcriptor Pho2 [19] while de-phosphorylated SP6 leads to a Pho4-Pho2 association that builds a fully functional transcription factor upregulating phosphate-responsive genes [22], [23]. Interestingly, Pho4 in its fully de-phosphorylated state can transcribe all phosphate-responsive genes while in a hypo-phosphorylated state it can only act upon a subset of them and transcribe them [24].

### **Pho81 – main regulator of PHO pathway**

Pho81 has a pivotal role in  $P_i$  homeostasis. It is as an activator of the PHO pathway. An enhanced expression of the Pho81 gene as well as low external  $P_i$ -concentrations are therefore required [25]. A yeast with deleted Pho81 was not able to act upon environmental  $P_i$  fluctuations [10]. This is due to the missing inhibitory effect of Pho81 upon cyclin-dependent kinase Pho80-Pho85 that takes place according to the exogenous phosphate status [26]. Pho80-Pho85 is known to control Pho4 which is the master switch of the PHO pathway [16], [17]. Pho81 binds a specific inositol pyrophosphate 1-IP7 (1-inositol pyrophosphates diphosphoinositol pentakisphosphate, 1-PP-InsP5) [27], which is present under  $P_i$  deprivation and thereupon inhibits kinase activity [17], [25], [26], [28]. Therefore, the N-terminal segment of Pho81 harbouring a SPX domain [1] was shown to be of enormous importance. This domain is negatively influencing Pho81 activity at high  $P_i$  conditions. A lack of the complete SPX domain [29], several point mutations in the inositol pyrophosphate pocket [30] or a certain single point mutations outside the binding pocket [29] of this domain leads to a constitutive activation of the PHO pathway at high  $P_i$  concentrations – at  $P_i$  levels where the PHO pathway would normally be repressed [25]. Pho81 is constitutively bound to Pho80 which is associated

with Pho85 and is restricted to nucleus [17]. Biophysical studies have shown that Pho81 is binding to Pho80 via its segment S3 ranging from amino acid 665 to 701 regardless of  $P_i$  status. Hereby, the position 693-695 is essential for the binding between Pho81 and Pho80. Any mutations in this region were shown to completely abolish Pho81 function [28]. In the case of  $P_i$  deprivation where Pho81 is acting as inhibitor of the kinase activity, another segment S1 of Pho81 - ranging from amino acid 702 to 723 - additionally binds to Pho80 and contributes to higher binding affinity between Pho81 and Pho80 [28]. This binding event takes place only in the presence of 1-IP7 that is generated by inositol hexakisphosphate kinase Vip1 and in presence of a divalent cation like  $Mg^{2+}$ ,  $Mn^{2+}$  or  $Zn^{2+}$  [27]. Subsequently, the kinase substrate Pho4 is phosphorylated less and can thus activate the PHO pathway by upregulating numerous phosphate-linked proteins. [8], [16]. It was shown the Pho81 segments, which are binding to Pho80, are not belonging to the SPX domain and that the SPX domain is essential for  $P_i$ -linked activity of Pho81. Taken together, it raises the hypothesis that the SPX domain is inhibiting S3 segment in 1-IP7-dependent fashion.

### **$P_i$ transporters in the PHO pathway**

The PHO pathway regulates  $P_i$  uptake by the high-affinity  $P_i$  transporters Pho84 and Pho89. The activity of these transporters is depending on external  $P_i$  status. Yeast with sufficient  $P_i$  represses the high-affinity  $P_i$  transporters Pho84 and Pho89 while yeast devoid of external  $P_i$  phosphate sources, derepresses [19] and transcriptionally up-regulates these transporters in the PHO pathway [8]. Pho89 is a type III transporter that is  $Na^+/P_i$ -coupled working at alkaline pH with a  $K_m$  of 0.5  $\mu M$  [31], [32]. Pho84 is the predominant high-affinity  $P_i$  transporter belonging to the major facilitator superfamily (MFS). It is  $H^+/P_i$ -coupled operating at acidic conditions [33]–[35] and having a Michaelis-Menten-constant ( $K_m$ ) of around 7  $\mu M$  [31], [36], [37].

It was shown that Pho84 is targeted to the plasma membrane with the help of Pho86 [38] which is upregulated during  $P_i$ -limiting conditions by the PHO pathway [8]. Pho86 is residing in the endoplasmic reticulum (ER) and is responsible for packaging of Pho84 into COPII vesicles, which are targeting ER-derived proteins to plasma membrane via golgi apparatus [38]. A surplus of  $P_i$  leads to a phosphorylation and an ubiquitination of Pho84 [39]. Thereupon, Pho84 is internalized by endocytosis and transported to the vacuole for degradation [38], [39].

### **Spl2 – regulator of P<sub>i</sub>-transport**

Spl2 is another component of the PHO pathway [40] that is upregulated upon P<sub>i</sub>-starvation conditions [8], [37]. It is found to be largely cytosolic and to a small extent associated with membranes, possibly by interacting with them via its hydrophobic N-terminus and predicted myristoylation site [40]. Spl2 is a negative regulator of the low-affinity P<sub>i</sub> transporters Pho87 and Pho90 [4], [37] and suggested to down-regulate and eventually inactivate low-affinity P<sub>i</sub> transporters during PHO pathway [37] allowing the high-affinity P<sub>i</sub> phosphate transporters to take over the P<sub>i</sub> import into the cell. Yeast cells that are overexpressing Spl2 at high P<sub>i</sub> conditions, indeed, show lower P<sub>i</sub> uptake. It is similar to the case where both low-affinity transporters and vacuole P<sub>i</sub> transporter Pho91 are lacking, while Pho84 is de-repressed indicating active PHO pathway [37] under high P<sub>i</sub> conditions.

Studies from Huerliman *et al.* show that Spl2 physically interacts with Pho87 and Pho90 and negatively regulates P<sub>i</sub>-influx and -efflux through these transporters via its SPX domain [4].

Spl2, was also observed to contribute to vacuolar targeting of P<sub>i</sub> transporter Pho87 that is conveyed by the SPX-domain [41]. On the opposite, Pho90 vacuolar targeting was shown to be dependent on the SPX domain of the P<sub>i</sub> transporter but independent of Spl2 [41].

### **P<sub>i</sub> storage by the VTC complex**

Eukaryotic cells can store P<sub>i</sub> in the form of polyphosphate [42]. In yeast, polyphosphate was shown to be responsible for the buffering of the intracellular P<sub>i</sub> concentration [10], [43], [44], the cell cycle [44], [45], the genomic stability [45], the oxidative stress response [9] and even the symbiosis of mycorrhizal yeast and plant [46]. Main storage of polyphosphate in yeast is the vacuole [47], [48] but there is evidence that also organelles like nucleus [49] and mitochondria [48] harbour polyphosphate pools. Proteins from all cellular compartments were found to be involved in polyphosphate maintenance [50]. Polyphosphate can be generated and imported into the vacuole [9] by the Vacuolar transport chaperone (Vtc) complex [51] whose components are

transcribed constitutively and upregulated by the PHO pathway [8]. Vtc protein family is only found in protists [52], [53], fungi [54] and diatoms [55], [56] but no obvious homologue in plants or animals was found yet. In *saccharomyces cerevisiae*, two subtypes of VTC complexes are known so far; a VTC complex residing within the vacuolar plasma membrane composed of the following membrane proteins – Vtc3/Phm2, Vtc4/Phm3 as well as membrane protein Vtc1/Phm4 [9]. And in the periphery - likely in the ER and nuclear envelope [9], [57] - a second VTC complex, which contains Vtc2/Phm1 instead of Vtc3 [9]. Under  $P_i$ -limiting conditions, the second subtype of the complex mostly gets translocated to the vacuolar membrane [9]. Recently, Vtc5 was identified as another component contributing to generation of polyphosphate. It enhanced the function of Vtc-based polyphosphate synthesis but it was shown not to be present in every complex [58].

Vtc2, Vtc3 and Vtc4 all share a N-terminal SPX domain, a homologous central triphosphate tunnel metalloenzyme (TTM) domain and a homologous C-terminal transmembrane domain. SPX and TTM domains are soluble cytosolic domains [59]. Vtc2 and Vtc3 are to 58 % identical in amino-acid sequence [8] while Vtc2 and Vtc3 both share a 28 % amino-acid identity to Vtc4 [60]. Vtc1 has no cytosolic part and is a three-helices membrane protein that is homologous to the C-terminal domain of Vtc2-4 [60]. Vtc5 topologically resembles Vtc2-4 and it has a N-terminal SPX domain as well as a transmembrane region containing three helices [58].

The polyphosphate synthesis is facilitated by a TTM domain of Vtc4 that bears a highly positive charged tunnel-shaped  $\beta$ -barrel with 8 antiparallel  $\beta$ -strands and accessory helices on sides and a half opening [9]. In the barrel, polyphosphate is generated and pyrophosphate,  $PP_i$ , as well as  $P_i$  might serve as a primer for a new polyphosphate chain [9]. A nascent polyphosphate chains is handed over to a C-terminal membrane-integrated domain possibly containing a channel for dropping polyphosphate into the vacuole [9], [60]. This event is based on a proton gradient across a vacuolar membrane, which is maintained by the V-ATPase [60]. Vtc1 and Vtc4 are necessary for the function of VTC complex [8], [9]. Adversely, Vtc2 and Vtc3 are suggested to have a regulatory role. Firstly, the deletion of Vtc2 or Vtc3, respectively, does reduce total polyphosphate content but does not abolish polyphosphate accumulation [8], [50]. Secondly, TTM

domains of Vtc2 and Vtc3, which have a substitution of an isoleucine in the Vtc2-TTM or of a leucine in the Vtc3-TTM, lead to abolished or reduced polyphosphate function in comparison to a catalytically enrolled Vtc4-TTM-residue lysine 458 [9]. This would explain *in-vitro* experiments with the TTM domain of Vtc2 or Vtc3 where binding of ATP was either less efficient with around 50  $\mu\text{M}$  – for Vtc2 – or not observed – for Vtc3 – in comparison to a 0.3-2  $\mu\text{M}$  binding constant of Vtc4 [9]. Also, ATP is required for the synthesis of polyphosphate [9]. Thirdly, there are numerous experimentally determined phosphorylated serine and threonine sites in the cytosolic regions of Vtc2 and Vtc3 whereas Vtc4 only has two of these sites (*BioGrid 3.5*).

The polyphosphate synthesis is operating in the presence of an ATP, a divalent cation – bound by the TTM domain [9] – and an inositol phosphate-based ligand bound by the SPX domain [6], [61]. Also,  $\text{P}_i$  or sulphate were shown to serve as a ligand [6]. The mentioned ligands have different potencies on polyphosphate synthesis. Interestingly, inositol phosphates IP6 and 5-IP7 bind to Vtc2-SPX with a similar nanomolar affinity [6] but in terms of Vtc activity, 5-IP7 is a much more potent ligand [6], [61]. This is underlined by *in-vivo* experiments that show that the deletion of a kinase generating 5-IP7 abolishes polyphosphate pools [62], [63]. Furthermore, 1,5-IP8 ligand leads to an activation of polyphosphate *in-vitro* but not *in-vivo* [61] suggesting that, although all inositol pyrophosphates can induce Vtc activity specifically 5-IP7 is relevant for biological activity of the VTC complex [61].

It was observed, in addition, that particular mutual mutations in the SPX domain of Vtc3 and Vtc4 can ligand-independently facilitate polyphosphate synthesis or lead to a disrupted polyphosphate synthesis [6]. The polyphosphate synthesis can also be influenced by Vtc5. The latter can modulate polyphosphate synthesis, firstly, in the presence of a ligand in an enhanced way and in the absence of a ligand to small extend as well as, secondly, by influencing Vtc4 translocation to the vacuole and hence the amount of Vtc4 present on the vacuole [58]. Structurally, it is yet not clear how all these factors influence polyphosphate synthesis.

In addition to polyphosphate generation and its importance in the  $\text{P}_i$  homeostasis, VTC complex was discovered to be contributing to the stability of the vacuolar V-

ATPase [51], membrane trafficking [59], [64] as well as to microautophagy [57] and homotypic vacuolar fusion [64]. It is however, not yet clear whether this contribution is due to a direct involvement of Vtc or due to polyphosphate [65].

### **P<sub>i</sub> scavenging by Pho4-linked phosphatases**

If essential P<sub>i</sub> is externally limiting, the PHO pathway upregulates several phosphatases to mobilize P<sub>i</sub> from diverse extracellular and intracellular resources [8]. During P<sub>i</sub>-starvation, the yeast repressible acid phosphatases Pho5 [66], [67], Pho11 [68] and Pho12 [68] are de-repressed by PHO pathway. Thereupon, they get secreted to degrade a broad spectrum of extracellular phosphate ester substrates like β-glycerophosphate and α-naphthyl phosphate [66], [68] to generate P<sub>i</sub>. Subsequently, P<sub>i</sub> transporters are able to import P<sub>i</sub> into the cells.

Several internal phosphatases utilize cellular phosphate ester substrates to scavenge P<sub>i</sub>. For example, nuclear and Mg<sup>2+</sup>-dependent Phm8 hydrolyses lysophosphatidic acid [69] and nucleotide monophosphates [70] leading to generation of triacylglycerol [69] and nucleotides [70]. Vacuolar repressible alkaline phosphatase Pho8 dephosphorylates phosphotyrosine peptides [71] while vacuolar phosphatases Ppn1 [72], [73] and Ppn2 [74] are mobilizing P<sub>i</sub> from the large polyphosphate pool located in the vacuole. The vacuolar polyphosphate pool is depleted during P<sub>i</sub>-starvation [43], [62]. Ppn1 is responsible for non-processive degradation of longer polyphosphate chains to P<sub>i</sub> and P<sub>3</sub> entities [72] as cytosolic P<sub>i</sub> concentration drops otherwise [75]. Ppn1 has to be first proteolytically cleaved on N-terminus to be converted to a functional polyphosphatase [76]. ADP positively influences its activity while ATP acts as its inhibitor. The activity mode is depending on the presence of metals; it acts as an endopolyphosphatase in the presence of Co<sup>2+</sup> while as an exopolyphosphatase when Mg<sup>2+</sup> is present [77]. Ppn2 is another polyphosphatase in the vacuole. It has an endopolyphosphatase activity that is Zn<sup>2+</sup> dependent [74]. P<sub>i</sub> that is liberated from polyphosphate is transported to the cytosol by constitutively expressed vacuolar P<sub>i</sub> transporter Pho91 [11].

Ppx1 and Ddp1 are two further polyphosphatases that are suggested to degrade existing polyphosphate outside the vacuole [60], [65]. Ppx1 was found in the cytosol and the nucleus [78] as well as on the plasma membrane and mitochondria [79], [80]. It is a

Mg<sup>2+</sup>- or Mn<sup>2+</sup>-dependent [81] exopolyphosphatase belonging to the DHH phosphoesterase superfamily, which is responsible for cleaving P<sub>i</sub> and pyrophosphate from polyphosphate chains [82], [83]. On the opposite, Ddp1 displays endopolyphosphatase activity *in-vitro* [62]. It belongs to the Nudix hydrolase family that is found in the cytosol and nucleus [78].

### **Organic P<sub>i</sub> transport**

The yeast P<sub>i</sub> homeostasis is maintained not only by low- and high-affinity P<sub>i</sub> transporters but also by help of the organic P<sub>i</sub> transporter Git1 [84]–[86]. Git1 imports external glycerophosphoinositol [84] and phosphatidylcholine [86]. Interestingly, depletion of all known low- and high-affinity P<sub>i</sub> transporters is lethal in yeast. However, overexpressing Git1 can rescue this phenotype in the presence of a high P<sub>i</sub> content despite the absence of any phosphates [85]. Hence Git1 can also function as an alternative P<sub>i</sub> transporter [85].

The yeast cells were also shown to be able to grow with glycerophosphoinositol [84] or phosphatidylcholine [86] as a sole supplement due to Git1.

Gde1 is the only characterized glycerophosphodiester phosphodiesterase in yeast so far and hydrolyses imported glycerophosphoinositol as well as phosphatidylcholine to its derivatives glycerol-3-phosphate and P<sub>i</sub> or choline, respectively [86]. Like many other P<sub>i</sub>-responsive proteins it has a SPX domain [1].

Both, Git1 and Gde1, get upregulated under P<sub>i</sub>-limiting conditions in a Pho4-dependent manner [8], [86]. It seems that Git1 transcription completely depends on Pho4 as a transcription factor as the deletion of Pho4, leads to an abolishment of Git1 [87].

### **P<sub>i</sub> homeostasis at high P<sub>i</sub> conditions**

P<sub>i</sub> homeostasis is regulated in a Pho4-independent fashion and thus is PHO pathway-independent at high P<sub>i</sub> conditions. Many proteins linked to P<sub>i</sub> homeostasis at high P<sub>i</sub>

conditions are either constitutively active or being negatively regulated upon  $P_i$  limitation, either by an inactivation mechanism or a vacuolar degradation.

### **Kinase activity complex Pho80-Pho85**

The nuclear cyclin-dependent kinase Pho85 kinase interacts with different cyclins modulating various cellular mechanisms ranging from cell cycle, carbohydrates and amino acid metabolism as well as calcium signaling pathway [88]–[90]. In association with cyclin Pho80 [90], [91] it regulates  $G_0$ -entry in the cell proliferation by modulating protein kinase Rim15 [92] and  $P_i$  homeostasis [91] by modulating its master switch Pho4 [16], [17]. Pho4 gets hyperphosphorylated by Pho85-Pho80 kinase at high  $P_i$  conditions [16], [17], which leads to delocalization [19], [20] and thus repression of the PHO pathway activation.

### **Low-affinity $P_i$ transporter Pho87 and Pho90**

Low-affinity  $P_i$  transporter Pho87 and Pho90 [85] are constitutively expressed in yeast independently of the external phosphate availability [93]. They transport extracellular  $P_i$  into the cytosol as  $Na^+/P_i$  symporters and are suggested to belong to SLC13/DASS family [94]. Their  $K_m$  values range between 150  $\mu$ M and 1 mM [10], [37], [85], [95]. Interestingly, these low-affinity  $P_i$  transporters not only seem to facilitate  $P_i$  import but are also able to export  $P_i$  [4]. Both transporters contain a N-terminal SPX domain that is responsible for regulating  $P_i$  import and  $P_i$  export while influencing  $P_i$  transport velocity. In a medium with a very high  $P_i$  condition of  $\sim 50$  mM, the lack of the SPX domain leads to lethality of yeast cells [4]. It was shown that polyphosphate accumulation is significantly higher in mutants lacking SPX domain [4]. Hence, a possible cause of intoxication in SPX mutants could be resulting from maximally reached capacities of polyphosphate pools that are not able to further convert accumulating toxic amounts of intracellular  $P_i$  to polyphosphate. Another explanation would be that the VTC complex is not able to convert  $P_i$  into polyphosphate fast enough leading to intoxicating elevated intracellular  $P_i$  levels in the cells. Therefore, basic constitutive-restrictive amounts of transporters, their  $P_i$  export ability as well the presence of a regulative SPX domain

might serve as surviving mechanisms to prevent the cell from  $P_i$  toxicity occurring in a  $P_i$  abundant state.

Pho87 and Pho90 can be influenced by their negative regulator Spl2 [4], [37]. Spl2 is known to be upregulated by the PHO pathway when  $P_i$  replenishes [8]. Overexpressing Spl2 in the presence of an overexpressed Pho90 or Pho87, significantly reduces the polyphosphate storage [4]. However, this was only observed for a full-length transporter and not for a transporter lacking its SPX domain. This is indicating that the negative impact of Spl2 is facilitated through the SPX domain of the low-affinity  $P_i$  transporter. This was further confirmed by a split-ubiquitin assay and co-immunoprecipitation experiments revealing a direct interaction of Spl2 and low-affinity transporters [4]. Under  $P_i$ -starvation, Spl2 was also shown to be responsible for SPX-dependent vacuolar targeting of Pho87 but not Pho90 [41], whereby they are subjected to proteasomal degraded [41].

Overall, up-regulation of the negative regulator Spl2 of Pho87 and Pho90 as well as their eventual vacuolar degradation by the PHO pathway clearly display that the function of Pho87 and Pho90 as  $P_i$  transporters is strongly reduced during  $P_i$ -starvation.

### **Vacuolar phosphate transporter Pho91**

Vacuolar Pho91 is a SPX-containing low-affinity transporter [85] that belongs to the DASS family. It is constitutively expressed and is not upregulated by PHO regulon [93]. It has been suggested that Pho91 is exporting phosphate from the vacuole to the cytosol [11]. It re-mobilizes polyphosphate stored in vacuoles as indicated by experiments conducted on yeast lacking Pho91. Pho91-deficient yeast is accumulating large polyphosphate pools [11]. This yeast mutant also has a de-repressed PHO pathway at high- $P_i$  conditions [11] suggesting that either Pho91 itself or Pho91-related  $P_i$  derived from vacuolar polyphosphates is buffering intracellular  $P_i$  levels and keeping the PHO pathway inhibited during high  $P_i$  conditions. Indeed, measured intracellular  $P_i$  concentration is elevated in yeast lacking Pho91 [10] and hence controlled less well. Interestingly, the overexpression of Pho91 does not lead to significant changes on polyphosphate pools [11] indicating that Pho91 alone is not controlling intracellular  $P_i$  concentration but rather that its function is regulated tightly in any given situation. This regulation could be mediated by inositol pyrophosphates. Isolated yeast vacuoles that

were extracted after hypo-osmotic shock and contain Pho91, were conducting  $\text{Na}^+/\text{P}_i$  ion currents upon addition of 5-IP7. This event was abolished in the yeast vacuoles having Pho91 with lacking SPX-domain or a point mutation in the SPX localized in the binding pocket of inositol pyrophosphates [96].

## **Regulation of $\text{P}_i$ homeostasis**

There are several layers of regulations interleaved in the  $\text{P}_i$  homeostasis. Every layer contains one or several feedback loops that are activating, synergizing or disabling other layer(s). This allows the cells to adjust rapidly to any fluctuations in the external or internal  $\text{P}_i$  availability. The first layer of control are inositol pyrophosphates. They serve as the sensors of the cellular  $\text{P}_i$  levels [6]. They link the components of the  $\text{P}_i$  machinery so that they act jointly to any given  $\text{P}_i$  situation. This is carried out by the SPX domain that is present in many proteins participating in the  $\text{P}_i$  homeostasis[1]. The SPX domain binds inositol pyrophosphates [6] and modifies the protein function accordingly. The second regulation layer is the presence of a  $\text{P}_i$  transport system based on the bimodality. A  $\text{P}_i$  transport system contains a set of low-affinity and a set of high-affinity  $\text{P}_i$  transporters. This allows the cells to adjust the  $\text{P}_i$  import and -export according to a given  $\text{P}_i$  condition [37]. In this way the cells can acquire essential  $\text{P}_i$  when  $\text{P}_i$  is scarce as well as act appropriately upon  $\text{P}_i$  abundance [10]. The latter is ensured by exporting  $\text{P}_i$  [4] or storing  $\text{P}_i$  in a form of polyphosphate to prevent the cells from a toxic  $\text{P}_i$  accumulation [60]. It was also shown that a dual transport system gives the cell sufficient time to prepare for the up-coming starvation or facilitate recovery [97]. The third layer of control is a biphasic transcriptional response upon  $\text{P}_i$  replenishment. It guarantees that not all PHO genes/ $\text{P}_i$ -response genes get transcribed at once but in two waves according to the needs of the cell [98].

## **Inositol pyrophosphates**

$\text{P}_i$  homeostasis is regulated by inositol pyrophosphates. In the literature they are also referred to as diphospho-inositol phosphates or pyrophospho-inositol phosphates [99]. They contain a completely or partially phosphorylated *myo*-inositol and have one or two pyrophosphates attached to the sugar backbone [99]. Pyrophosphate has a

phosphoanhydride bond with a high free energy of 28 kJ/mol [100]. *In-vivo*, especially 1-IP7 (1-diphospho-inositol tetrakisphosphate) [101], [102], 5-IP7 (5-diphospho-inositol tetrakisphosphate) [103]–[105] and 1,5-IP8 (1,5-bis-diphospho-inositol tetrakisphosphate) [102] influence  $P_i$  homeostasis in yeast and mammals [63], [106]–[109]. Studies from different organisms indicate that at high  $P_i$  conditions, 5-IP7 amounts range between 0.5 and 5  $\mu\text{M}$  [100], [101], [110] and 1,5-IP8 is present half as much [111], [112]. This makes up 1-5% of 5-IP7 and 0.05-0.25% of 1,5-IP8 in comparison to constant total IP6 level [99]. Hereby, the levels of 1-IP7 are around 2% of total IP7 pool [113].

There are two inositol pyrophosphate kinases in yeast. 5-IP7 is generated from inositol phosphate, IP6. This is conducted by the inositol hexakisphosphate kinase Kcs1 [103], whereas diphosphoinositol pentakisphosphate kinase Vip1 [114], [115] produces 1-IP7 from inositol phosphate [101], [116] and 1,5-IP8 from 5-IP7 [114], [116], [117]. Both kinase activities are displayed in Fig. 2. Vip1 is a bimodal enzyme carrying both kinase and phosphatase activity. As phosphatase it is hydrolysing 5-IP7 and 1-IP7 [117] and 1,5-IP8 [118], [119].

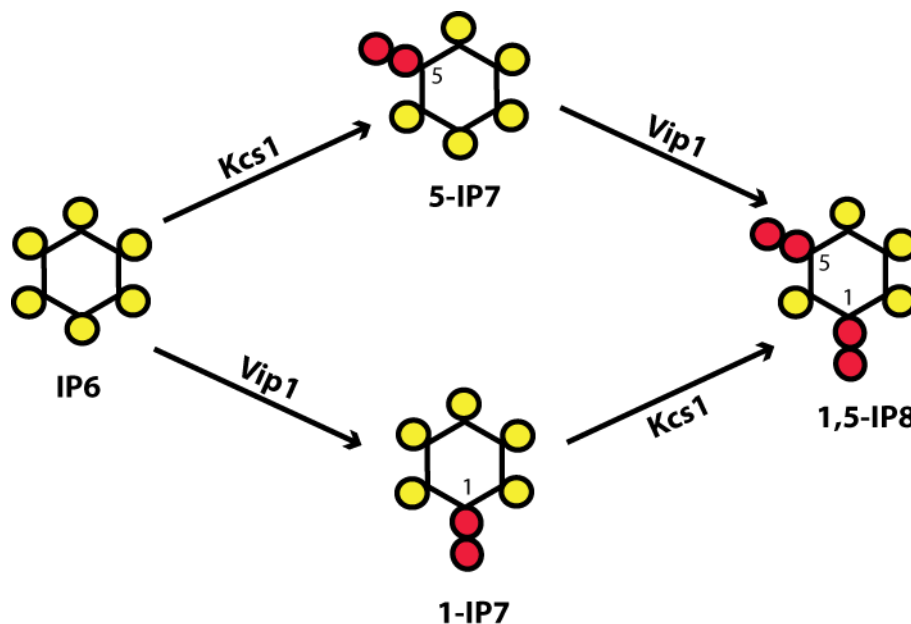


Fig. 2: Overview of Kcs1 and Vip1 kinase and their products. Adapted from [61].

It has been suggested that the cellular ATP level is linked to the external  $P_i$  availability. An ATP decrease was observed when external  $P_i$  was reduced [120], [121]. There is a hypothesis stating that this link is derived from a ratio between products of different inositol pyrophosphates kinases. Namely, a ratio between Kcs1 product 5-IP7 and Vip product 1-IP7 or even 1,5-IP8 explaining their roles in the  $P_i$  homeostasis [121]. In mammalian cells, studies displayed that treatment with particular kinase inhibitors and oligomycin reduces not only ATP concentration but concomitantly also significantly reduces IP7 levels [122]. Vice versa, an addition of ATP leads to a simultaneous increase of 5-IP7 [123]. Both cytosolic kinases Kcs1 and Vip1 generating different inositol pyrophosphates are ATP-dependent but appear to have different binding affinities to it based on mammalian homologues. Kcs1 has a  $K_M$  to ATP of around 1.1-1.5 mM while  $K_M$  of Vip1 is around 130  $\mu$ M [99]. A yeast growing at high  $P_i$  conditions has an ATP level of around 1-2 mM [124] that is near  $K_M$  of Kcs1 suggesting Kcs1 to be partially active at these conditions and generating 5-IP7. This is underlined by studies of Kcs1 mutants [62], [104] and mutants of enzymes required for the purine *de novo* synthesis acting upstream of ATP generation [121] that abolish the majority of the IP7 pool at high  $P_i$  conditions. Additionally, it has been shown that elevated  $P_i$  levels contribute to enhanced kinase activity of Kcs1 in yeast [117].

Altogether this would indicate that the product of Kcs1, 5-IP7, linked to high cellular ATP levels is responsible for  $P_i$  homeostasis at high external  $P_i$  conditions. Indeed, 5-IP7 was shown to be required for processes observed during  $P_i$  high external  $P_i$  conditions. These are external  $P_i$  uptake at high  $P_i$  conditions [107], [125], [126] linked to low-affinity transporters,  $P_i$  release from vacuole to cytosol [96] and maintenance of the vacuolar polyphosphate pool generated from VTC complex [61] independent of cellular  $P_i$  state and most importantly a repression of the PHO pathway [63], [106].

What about Vip1 and its potential role in the  $P_i$  homeostasis? The potential role of Vip1 in  $P_i$  homeostasis has been investigated in several studies. They indicate that Vip1 could regulate cellular ATP levels through its bifunctional mode to act as a pyrophosphate kinase and as a pyrophosphatase [117]. In ATP deficient mutants PHO pathway is constitutively active while an additional deletion in Vip1 reverses this phenotype indicating that Vip1 is responsible for PHO activation and not ATP level *per se*.  $\Delta Vip1$

cells display a large delay of PHO pathway activation upon  $P_i$  replenishment [98], [121]. Usually,  $P_i$  replenishment would lead to an immediate expression of PHO genes [98]. This de-repression of the PHO pathway is controlled by Vip1 generated inositol pyrophosphate(s) [101], [108]. Pho80-Pho85 kinase activity that represses Pho4 activation - and thus the PHO pathway - is inhibited by a lysate containing low molecular weight fraction extracted from  $P_i$ -starved cells [108]. This showed that the inhibition is Pho81-dependent [27], [108], takes place in a presence of divalent metals like  $Mn^{2+}$ ,  $Mg^{2+}$  and  $Zn^{2+}$  [27] and has an allosteric and reversible nature [27]. In correlation, in cases where Vip1 product(s) were lacking, Pho4 was inactive [27], [108] and PHO pathway repressed. Hitherto, it is not clear which inositol pyrophosphate of Vip1 exactly - 1-IP7 or 1,5-IP8- influences  $P_i$  homeostasis during  $P_i$  starvation. *In-vitro*, supplementation of  $P_i$  and high ATP levels lead to an increase of 1,5-IP8 amounts in yeast [117]. This was also observed in mammals where Shears' Group in addition showed that cellular  $P_i$  and ATP content as well as amount of 5-IP7 and IP6 did not change [123].  $P_i$  was inhibiting phosphatase activity of PPIP5K2, a Vip1 homologue in humans, indicating its predominant kinase activity generating 1,5-IP8 and less probable conversion of 1,5-IP8 back to IP7 isomer [123]. Taken together, this suggests that Vip1 product 1,5-IP8 is generated *in-vivo* under high  $P_i$  conditions when the PHO pathway is repressed and hence has another function than activating the PHO pathway. This would be in accordance with studies conducted in plants. 1,5-IP8 was suggested to enable the interaction between stand-alone SPX proteins and  $P_i$ -responsive transcription factor PHR [127] that only takes place at high  $P_i$  conditions [5], [128]. Furthermore, in mammals it was shown that 1,5-IP8 influenced  $P_i$  export by Xpr1 whose activity is dependent on external  $P_i$  conditions. The higher the external  $P_i$  concentrations, the higher the  $P_i$ -efflux [129] suggesting 1,5-IP8 to be acting during high  $P_i$  conditions. Therefore, most likely 1-IP7 acts as a switch for activation of the PHO pathway upon  $P_i$  replenishment. This would also explain a  $P_i$ -starving phenotype of  $P_i$ -hyperaccumulation in plants that do not synthesize 1,5-IP8 [117]. In humans, a mutation in the phosphatase domain of the Vip1 homologue PPIP5K leads to an autosomal recessive nonsyndromic hearing loss indicating that balancing the ratio of different inositol pyrophosphates in the cell is important and a disbalance can lead to diseases [130].

Another switch for activating the PHO pathway could be the reduced pool of 5-IP7 *per se*. This was observed upon  $P_i$  replenishment [117]. As mentioned above, a replenishment of  $P_i$  led to a lower cellular ATP level. The Kcs1 kinase ability is reduced at lower ATP levels, hence less 5-IP7 can be produced. In line, mutations in the enzymes required for the purine *de novo* synthesis and subsequent ATP generation, displayed an active PHO pathway at high  $P_i$  [121].

Additionally, the yeast cells display reduced gene expression of Kcs1 after  $P_i$  replenishment [98]. The master switch of PHO pathway, Pho4, can contribute to this. Pho4 enables transcription of antisense and intragenic RNAs from the KCS1 locus that down-regulate Kcs1 [131]. Furthermore, the reduced 5-IP7 pool could originate from an increase in the Vip1 phosphatase activity upon 5-IP7 as shown at lower ATP conditions [117] and phosphatases like cytosolic phosphatase Ddp1 [62] and phosphatase Siw14 [132]. They can further decrease 5-IP7 pools and contribute to  $P_i$  homeostasis as well. In turn, the reduced activity of Kcs1 and reduced pool of 5-IP7 could have a positive effect on the Vip1 kinase activity. There is less competition to Kcs1 over the mutual precursor IP6 utilized for inositol pyrophosphate generation and hence an increase in 1-IP7 amounts would be possible. This hypothesis would also explain the Kcs1 mutant phenotype. Some Kcs1 mutants have a nuclear Pho4 representing an active PHO pathway that is normally not observed at high  $P_i$  conditions [108]. Also Choi *et al.* showed that the PHO pathway is enhanced much more in the Kcs1 mutant as in comparison to  $P_i$ -starved state [121].

A decade ago, there was a controversy in this field for a long time in regards to whether 5-IP7 levels get elevated or reduced during starving  $P_i$  conditions. Lee *et al.* showed with the traditional [ $^3$ H]-inositol labelling method that IP7 pool levels increased during  $P_i$  starvation [108] while other groups showed the opposite [62]. Only, in 2019 it was shown that - at least in mammals - the cells utilize not only exogenous inositol but also generate their own endogenous inositol used subsequently for generation of inositol pyrophosphates [133]. This likely suggests that [ $^3$ H]-inositol labelling in yeast does not display a complete picture. Yeast contains two enzymes for *de novo* synthesis of inositols - *myo*-inositol-3-phosphate synthase (MIPS) [134], [135] and inositol

monophosphatase [136], [137]. It has to be further investigated if exogenous and endogenous inositols have different impacts on inositol pyrophosphates and linked  $P_i$  homeostasis.

### **Bimodality of $P_i$ transporters**

Yeast contains a bimodal/dual  $P_i$  transport system based on the transporters responding to  $P_i$  with different affinities. There are two high-affinity transporters (Pho84 and Pho89) and four low-affinity transporters of which three are canonical – two integrated into a plasma membrane (Pho87 and Pho90) and one acting on the vacuolar plasma membrane (Pho91) – and the non-canonical Gde1 that actually prefers to transport glycerophosphoinositol [84] and phosphatidylcholine [86]. It was shown to be able to transport  $P_i$  only after all other  $P_i$  transporters are lacking and only at high  $P_i$  conditions [85].

A bimodal transport system gives the cell sufficient time to prepare for the up-coming starvation or facilitate recovery [97]. The yeast cells adjust adequately to the fluctuations of external  $P_i$  availability. Wykoff *et al.* showed that at intermediate phosphate concentrations between approximately 100 and 200  $\mu\text{M}$ , two subpopulations of yeast cells co-exist displaying similar velocity of  $P_i$  uptake. The one subpopulation, which operates with apparent  $K_m$  of  $P_i$  uptake of around 150  $\mu\text{M}$ , is suggesting low-affinity  $P_i$  transporters to be involved in the  $P_i$  transport while the other cell subpopulation most likely engages Pho84 with an apparent  $K_m$  of  $P_i$  uptake of 7  $\mu\text{M}$ . A change in the external  $P_i$  concentration leads to a shift of these two subpopulations. In a medium with no  $P_i$ , the cells display only one subpopulation with high expression of Pho84 and Spl2. At  $P_i$  concentrations over 300  $\mu\text{M}$ , on the opposite, the subpopulation with low-affinity  $P_i$  transporters is active [37]. It is suggested that the rise of these two subpopulations originates from the presence of an upregulated Spl2. Spl2 gets upregulated in the PHO pathway [8] and it is known to be a negative regulator of the low-affinity  $P_i$  transporters [4]. It was shown that a lack of the predominant  $P_i$  transporter Pho84 at  $P_i$ -limiting conditions – conditions at which the transporter is usually employed – leads to constitutive induction of PHO genes [93] but surprisingly no  $P_i$  transport was observed [36], [37]. The  $P_i$  transport takes place only if this yeast

mutant is supplemented with  $P_i$  rich medium [75] or after a mutual lack of  $P_i$  transporter Pho84 and Pho4 [36], [37] under the same  $P_i$ -limiting conditions [37]. This indicates that PHO pathway upregulates a protein that negatively regulates other  $P_i$  transporters employed only at rich  $P_i$  conditions and in a PHO-independent manner. A mutant with a mutual deletion in  $P_i$  transporter Pho84 and Spl2 was able to indeed restore  $P_i$  transport at low phosphate conditions [37], indicating that Spl2 regulates the bimodality of  $P_i$  transport in the yeast.

### **Biphasic transcriptional response**

Biphasic transcriptional response is another characteristic of  $P_i$  homeostasis observed upon  $P_i$  replenishment. It ensures that only the required  $P_i$ -response genes get transcribed according to the needs of the cell [98].

Barkai Group investigated transcriptional expression of different PHO components by high-throughput RNA sequencing in the time dependence [98]. First, they have grown yeast in rich- $P_i$  conditions and subsequently transferred it into a medium with no  $P_i$ . They observed a  $P_i$ -response gene expression in two phases. The first group of PHO components expressed within the first hour after  $P_i$  replenishment is composed of the *SPL2* – a negative regulator of low-affinity  $P_i$  transporters – that is expressed at earliest stage, followed by a high-affinity  $P_i$  transporter *PHO84* and its auxiliary factor *PHO86*, negative regulator of cyclin-cyclin dependent kinase *PHO81*, components of the polyphosphate generating VTC complex as well as of secreted phosphatases *PHO11* and *PHO12*. Approximately two hours after cells are devoid of  $P_i$ , the second group of  $P_i$ -associated genes get upregulated. They are secreted acid phosphatase *PHO5*, nuclear phosphatase *PHM8*, nuclear and cytosolic polyphosphate phosphatase DDP1 as well as second high-affinity  $P_i$  transporter *PHO89*. *PHM6* is also a prominent gene upregulated at this time point but hitherto its function is still unknown.

The biphasic transcriptional response was first observed for *PHO84* and *PHO5* [43]. The gene expression of *PHO84* was shown to be more sensitive to external  $P_i$  concentrations than the expression of *PHO5* [43]. This sensitivity arises most likely from partial phosphorylation of transactivator Pho4 [24]. Most favourable initial phosphorylation of Pho80-Pho85 upon Pho4 [18] is on its phosphorylation site SP6. In this phosphorylated

state Pho4 efficiently binds the promoter of *PHO85* and much less strongly to the promoter of *PHO5* [24].

It was postulated that the biphasic transcriptional response allows regulation of the PHO pathway with the first transcription wave expressing the  $P_i$  responsive genes *PHO81*, *PHO84* and *SPL2* that stabilize the positive feedback loop of the PHO pathway. On the opposite, the second wave contains mostly  $P_i$  scavenging proteins that can increase intracellular  $P_i$  by downregulating Pho4 activity as a negative feedback loop [98].

The time delay between the gene expression phases seem to be facilitated by the presence of polyphosphate pools operating as  $P_i$  buffer. In yeast fully disrupted in polyphosphate synthesis by lacking *Vtc1* or *Vtc4*, the biphasic transcriptional response was not observed any more [43], [98]. In accordance, larger polyphosphate pools are able to further extend the delay between phases [43].

## **Other signaling pathways linked to $P_i$ homeostasis**

$P_i$  homeostasis is linked to many other cellular processes by its different components. In yeast, the high-affinity  $P_i$  transporter Pho84 was found essential for growth recovery from  $P_i$  limiting conditions by a rapid activation of the PKA pathway in the presence of glucose [41], [138], [139]. The PKA pathway is important in metabolism, nutrient dependent control of growth and stress response [140], [141]. Pho84 also plays a role in the metal homeostasis of *S. cerevisiae*. It imports  $Mn^{2+}$ ,  $Cu^{2+}$ ,  $Co^{2+}$ , and  $Zn^{2+}$  [142] as well as selenite [143]. In pathogenic yeast *Candida albicans*, a deletion of Pho4 increased sensitivity to metals and non-metal cations such as spermidine and concurrently reduced intracellular  $P_i$  [144], [145]. In another yeast model, pathogenic *Cryptococcus neoformans*, the sensitivity to a metal like  $Ca^{2+}$  could be rescued by supplementation of the media with phosphate [146] indicating  $P_i$  homeostasis to balance metal homeostasis.

$P_i$  homeostasis based on the PHO pathway normally takes place under  $P_i$  deprivation. The latter can be influenced by adenine nucleotide metabolism. In this condition, the PHO pathway was found derepressed at high  $P_i$  conditions if genes encoding for

adenosine nucleotides enzymes - adenosine kinase (*ADO1*), adenylate kinase (*ADK1*) [147] and adenine deaminase (*AAH1*) [121] were lacking. Hereby, Adk1 was associated to Pho85 and Pho81 [148] suggesting regulation of kinase activity of Pho4 while Ado1 and Aah1 were found to negatively regulate the PHO pathway in a Vip1-dependent manner.

PHO pathway regulator Pho81 influences activity of Rim15 in trehalose metabolism [149] as well as in the cell cycle. For the latter, the activity of Pho85-Pho80-Pho81 allows inhibition of the Rim15 kinase negatively influencing  $G_0$  initiators under  $P_i$  limiting conditions allowing the cell to enter into the quiescent  $G_0$  phase [92]. In addition, Pho85-Pho80-Pho81 modifies cyclin Cln3 preventing the exit from  $G_0$  [150].

Polyphosphate is an integral part of  $P_i$  homeostasis in yeast. In *S. cerevisiae* it is generated by VTC complex via SPX-related binding to inositol pyrophosphate [6], [61] serving as a cellular  $P_i$  buffering system [43], [98]. It has been shown that polyphosphate is essential not only for yeast but also other organisms. In different bacteria such as *Vibrio cholerae*, *Salmonella spp.*, *Shigella flexneri*, *Neisseria meningitidis*, *Mycobacterium tuberculosis* and *Pseudomonas aeruginosa*, it is responsible for virulence [151]. Moreover, lacking polyphosphate in unicellular parasites - *Trypanosoma brucei*, *Toxoplasma gondii*, or *Leishmania major* - reduced their pathogenicity (reviewed in [152]). Lastly, in mammals polyphosphate was shown to be involved in a plethora of cellular processes. It has a regulative role in the proliferative signaling pathway of mTOR [153], blood related pathways like blood coagulation [154]–[156] and apoptosis of plasma cells [157] as well as in the biomineralization of bone [158] and teeth [159].

## **Structural aspects of $P_i$ homeostasis**

### **SPX domain**

A tight regulation of intracellular  $P_i$  concentration is essential for every cell. Many  $P_i$  responsive proteins contain a N-terminal SPX domain composed of around 140-380 amino acids [13]. SPX is named after three proteins that contain this domain - the Suppressor of Yeast Gpa1 (*Syg1*), yeast kinase inhibitor Pho81 and human Xenotropic

and Polytopic Retrovirus receptor1 (Xpr1) [160]. The importance of the SPX domain was initially shown back in 1995. A lack of the SPX domain – at that time a still uncharacterized domain - in Pho81 led to a de-repression of the PHO pathway at high  $P_i$  conditions [25]. Normally, the PHO pathway would be de-repressed only at  $P_i$ -limiting conditions [12]. It took around a decade to annotate the SPX domain [160] and associate it to  $P_i$  homeostasis [1], [13] and another decade to structurally characterize it [6]. SPX domains have been found so far in many eukaryotes ranging from fungi, protozoans, plants, slime molds to mammals [160]. Hitherto, SPX domain was shown to have a regulative role in  $P_i$ -responsive proteins with different functionalities. As inhibitory unit in yeast, Pho81-SPX was shown to be an internal inhibitor of the PHO pathway activation [25] and the SPX domain of the putative  $P_i$  exporter Syg1 indicated a negative effect upon the transduction of mating pheromone signaling [161]. Similarly, SPX domains of the low-affinity  $P_i$  transporters were shown to negatively regulate  $P_i$  uptake-velocity and thus prevent  $P_i$  caused intoxication [4]. In plants, so called stand-alone SPX proteins prevent  $P_i$  starvation response (PSR) transcription factor from DNA binding in rice [128], [162] and in *Arabidopsis thaliana* [5]. In some other cases, SPX domain was associated with a positive regulation. It enables polyphosphate generation by the SPX-containing vacuolar VTC complex [6], [61] and  $P_i$  efflux by Pho91 in yeast and *Trypanosoma brucei* [96] as well as by human Xpr1 [129]. All these regulative roles of the SPX domain are linked to various inositol pyrophosphates and  $P_i$  homeostasis in different ways. The activity of Pho91 was stimulated by inositol pyrophosphate 5-IP7 [96] whereas  $P_i$  efflux of Xpr1 [129] was 1,5-IP8-dependent [127]. The inhibition of plant stand-alone SPX proteins to PHR proteins [6], [127] as well the yeast VTC complex activity can be stimulated *in-vitro* by all biologically relevant pyrophosphates– 1-IP7, 5-IP7 and 1,5-IP8 as facilitate - whereas only 1-IP7 specifically abrogates inhibition of yeast Pho81 [27], [108]. The latter is accomplished in a way that a stretch of amino acids unrelated to the SPX domain can bind a kinase [27] and allosterically inhibit its activity [90]. Possibly this stretch of amino acids is not solvently accessible in the absence of 1-IP7 and it gets released when SPX is bound to 1-IP7 in presence of  $Mg^{2+}$ . The regulation of SPX-containing low-affinity transporters known to be active at high  $P_i$  conditions was not explored yet. Possibly it is linked to 5-IP7 or 1,5-IP8 derived from 5-IP7 as the activity of human kinase generating 5-IP7 was shown to be required for external  $P_i$  uptake at high  $P_i$  conditions [107], [125], [126]. Interestingly, grouping  $P_i$ -

responsive SPX proteins according to their inositol pyrophosphate stimulation corresponding to external  $P_i$  status could explain  $P_i$  homeostasis to some extent. The presence of 5-IP7 and 1,5-IP8 at rich  $P_i$  conditions would explain the  $P_i$ -efflux activity of human Xpr1 and the activities in the yeast comprised of polyphosphate generating VTC complex, vacuolar  $P_i$  exporter Pho91 and possibly low-affinity  $P_i$  transporters. 1-IP7 which was shown to be present at  $P_i$ -limiting conditions [27], [108] would explain the function of yeast Pho81 as activator of the PHO pathway and ongoing activity of VTC complex whose components are upregulated upon PHO pathway activation [8]. The hypothesis based on certain inositol pyrophosphate being present to different extent in dependence of  $P_i$  conditions, would imply that constitutively expressed vacuolar  $P_i$  exporter Pho91, which is required at all  $P_i$  conditions [10], [11], should respond upon all different inositol pyrophosphates and putative  $P_i$ -exporter Syg1 upon of 5-IP7 or 1,5-IP8 assumed to be largely present during rich  $P_i$  conditions. This is something that was not explored so far.

X-ray structures of different SPX domains from human, *S. cerevisiae* and fungal *Chaetomium thermophilum* show that the SPX domain is a three-helix bundle consisting of six  $\alpha$ -helices [6]. There are two long core helices -  $\alpha$ -helix3 and  $\alpha$ -helix4 - of approximately 80 Å each. C-terminal  $\alpha$ -helix5 and  $\alpha$ -helix6 are in parallel to the core helices and are forming another long  $\alpha$ -helix together, which is separated by a short loop. At the N-terminus,  $\alpha$ -helix1 and  $\alpha$ -helix2 form a helical hairpin that is part of the binding pocket. In the crystal structures of SPX, the hairpin was found to bind to an axial phosphate of IP6 at position 2 (C2) or to a sulphate. The binding pocket is comprised of residues from a helical hairpin - Y22 and K26 in Vtc2 - which together with one lysine from  $\alpha$ 4 (K131) represent a conserved basic phosphate binding cluster (PBC) and of a vicinal lysine surface cluster (KSC) containing K127, K130 and K134 located on helix4. Any mutations of the residues from these two clusters or a reductive methylation of surface lysines lead to an impaired binding of  $P_i$ .  $P_i$  and sulphate bind to the SPX domain of Vtc2 in a low millimolar range but are not potent inducers of VTC complex activity. On the opposite, IP6 and 5-IP7 bind to the SPX domain of Vtc2 in a middle nanomolar range with a 1: 1 stoichiometry and are strong agonists of VTC complex activity. Many inositol pyrophosphates with one or two pyrophosphates effectively simulate polyphosphate synthesis in the VTC complex on isolated vacuoles [61]. However, 5-IP7 was found to be the most relevant inositol pyrophosphate for the VTC complex [61].

Despite having X-ray structures solved in apo- and holo-forms, the structure-function mechanism of the SPX domain as a regulator is still largely elusive. There are many ambiguities. Firstly, it was noticed that  $\alpha$ -helix6 was found in various orientations. These might be due to artifacts arising from crystal contact packing or this actually displays a functional difference between helix6 variants in SPX domains. Secondly, conserved  $\alpha$ -helix1 revealed no visible electron density in some of the apo X-ray structures suggesting that the helix is disordered. This is not the case in crystal structures where  $\alpha$ -helix1 was bound to a ligand like IP6 or sulphate. As ligands like  $P_i$  and IP6 induced large chemical shift perturbations in NMR spectra of the SPX domain of Vtc2 this raises the hypothesis that  $\alpha$ -helix1 has an important role in the ligand-induced conformation of SPX and its mechanism. The importance of a conserved binding pocket is underlined by functional studies of other SPX proteins. Single mutual mutations in PBC or KSC of Vtc3 and Vtc4 impair the polyphosphate generation capability of the VTC complex [6]. An alanine mutation in KSC –Vtc3-K126/Vtc4-K129 –even leads to pseudo-activity in VTC complex *in-vitro* [6] and *in-vivo* [61]. Several mutations either in PBC or KSC or a lack of the  $\alpha$ -helix1 region in the plant  $P_i$  exporter AtPho1 show dwarfism due to impaired  $P_i$  homeostasis while hyperaccumulating  $P_i$  [6]. Similarly, mutations either in PBC or KSC of the plant AtSPX1, a stand-alone SPX protein, lead to abolished interaction with the  $P_i$  starvation response transcription factor AtPHR1 [127] and constitutive  $P_i$  starvation response. A mutation in PBC – in the residue Y22F – of yeast Pho91 or Pho91 of *Trypanosoma brucei* cannot restore  $Na^+/P_i$  current as wild-type would [96]. KSC mutations in K221, K224 and K228 of Pho81 from pathogenic yeast *Cryptococcus neoformans* [30] and single mutations in G4 ( $\alpha$ -helix1), E79 ( $\alpha$ -helix3) or G147R ( $\alpha$ -helix4) - all residues near binding pocket - of *S. cerevisiae* [29] lead to a de-repressed PHO pathway. Mutations of KSC residues in Xpr1 of mammalian cells abolish  $P_i$  efflux [163].

In addition, mutations outside the binding pocket might have an impact on the function of SPX proteins. Mutations in the Xpr1 gene located near the binding pocket (K53) and outside the binding pocket of SPX [7], [164], [165] can lead to primary familial brain calcification (PFBC) manifested in movement disorders and neuropsychiatric abnormalities [166]. These mutation are localized opposite to the binding region in  $\alpha$ -helix3 (L87P) [167] or  $\alpha$ -helix4 (S136N, L140P, L145P) of SPX as well as in the linker

region between SPX and adjacent domain (L218S) [7] and outside SPX domain [7], [164]. In mammalian cells, Xpr1 mutation L145P [168] and L87P [167] were tested that are known as cause of PFBC and they have shown reduced  $P_i$ -efflux.

SPX domains are conserved in the  $\alpha$ -helix1,  $\alpha$ -helix2,  $\alpha$ -helix3 and partly in  $\alpha$ -helix4. These are  $\alpha$ -helices involved in the inositol phosphate and pyrophosphate binding. On the opposite, another part of the  $\alpha$ -helix4 as well as  $\alpha$ -helix5,  $\alpha$ -helix6 and loops are variable [1], [6], [13]. It is still unclear what causes the different functions in SPX-containing proteins. Are those the variable parts of SPX domains or possibly the relationship of SPX to adjacent domains that can differ in SPX-containing proteins? Only one SPX-containing protein so far – the cytosolic part of Vtc4 - was crystalized with SPX and an adjacent domain in two isomeric forms. One structure reveals that the SPX domain interacts with central TTM domain on the bottom part of the SPX domain that is opposite to binding pocket. In the second structure, both domains are detached. In both crystal structures, the linker connecting the SPX domain with the adjacent domain did not reveal any electrical density.

Disentangling the SPX structure-mechanism would help to understand not only  $P_i$  homeostasis but also SPX-related membrane fusion. It was shown that low-affinity  $P_i$  transporters were targeted to vacuolar degradation by their SPX domains [41]. So far, no inositol pyrophosphates dependence is known.

### **Ankyrin repeat domain**

Diverse proteins containing ankyrin (ANK) repeat domains are associated with  $P_i$  homeostasis. ANK domains are known to facilitate protein-protein interactions [169]. They are composed of two helices separated by a loop in a canonical helix-turn-helix conformation similar to hairpin-like  $\beta$ -sheets (reviewed in [169]). Negative regulator of low-affinity  $P_i$  transporters, Spl2, has an ANK domain [40] as well as PHO pathway regulator Pho81 [40] and glycerophosphodiester phosphodiesterase Gde1 [86]. The latter are the only two yeast proteins which contain both, SPX and ANK domains. In case of Pho81, amino acids residing in the fifth and the sixth repeat of ANK (aa 584-724) [25] were shown to carry the ability to inhibit kinase activity of Pho85-Pho80 and repress PHO pathway active at  $P_i$  limiting conditions. O'Shea Group discovered that Pho81 is

binding to kinase cyclin Pho80 physically in the sixth repeat of ANK. Namely, to amino acid stretch 665 to 701 in a constitutive and to 702 to 723 in a 1-IP7-dependent manner [27]. Still untested is if 1-IP7 is bound by SPX domain of Pho81. So far, 1-IP7 binding to SPX domain was seen for VTC complex *in-vitro* but was not tested for any further SPX proteins [61].

The SPX domain of low-affinity  $P_i$  transporters Pho87 and Pho90 was shown to interact with Spl2 by co-immunoprecipitation and split-ubiquitin assay [4]. Spl2 was shown to negatively regulate low-affinity  $P_i$  transporters Pho87 and Pho90 by their SPX domains influencing their  $P_i$ -uptake capability [4]. Also, vacuolar targeting of Pho87 is facilitated by its SPX domain of Pho87 and Spl2 [41].

Hitherto, no direct relation between SPX, ANK and inositol pyrophosphates was investigated yet.

## **Aim**

As the SPX domain is a part of many  $P_i$  responsive proteins of eukaryotic  $P_i$  homeostasis regulated by inositol pyrophosphates the aim was to investigate the SPX structure-function in relation to inositol (pyro-) phosphates. The elucidation of many X-ray structures of SPX in the apo- and holo-states alone was not sufficient to understand SPX function at the molecular level. Although one SPX-containing system in plants was shown to require inositol pyrophosphates for its protein-protein interaction, its structural mechanism is poorly understood.

In this work, NMR spectroscopy and other biophysical methods were used to study a SPX domain of yeast VTC complex that is known to regulate polyphosphates synthesis. I studied the isolated SPX domain of Vtc2 (SPX2) that was suggested to have a regulative role in the VTC complex. Vtc2 and homologous Vtc3 have almost no ATPase activity required for synthesis of polyphosphates. To understand the structural and functional role of SPX2, its apo- and different holo-states were compared alone and in the presence of Vtc4 that represents the functional unit of the VTC complex. Here we could show that

SPX domains of Vtc2 and Vtc4 interact electrostatically with substantial contribution of conserved  $\alpha$ -helix1 and non-conserved as well as previously unknown  $\alpha$ -helix7 of SPX2. The inositol (pyro-) phosphates and particular mutations causing pseudo-activity abrogate this interaction. This is suggesting that the domains of Vtc complex inhibit VTC activity and that the role of the inositol (pyro-) phosphates is to disrupt the molecular-assembly.

## References

- [1] D. Secco, C. Wang, H. Shou, and J. Whelan, "Phosphate homeostasis in the yeast *Saccharomyces cerevisiae*, the key role of the SPX domain-containing proteins," *FEBS Lett.*, vol. 586, no. 4, pp. 289–295, 2012.
- [2] A. J. Saldanha, M. J. Brauer, and D. Botstein, "Nutritional Homeostasis in Batch and Steady-State Culture of Yeast," *Mol. Biol. Cell*, vol. 15, no. 9, pp. 4089–4104, 2004.
- [3] C. Ansermet, M. B. Moor, G. Centeno, M. Auberson, D. Z. Hu, R. Baron, S. Nikolaeva, B. Haenzi, N. Katanaeva, I. Gautschi, V. Katanaev, S. Rotman, R. Koesters, L. Schild, S. Pradervand, O. Bonny, and D. Firsov, "Renal Fanconi Syndrome and Hypophosphatemic Rickets in the Absence of Xenotropic and Polytopic Retroviral Receptor in the Nephron," *J Am Soc Nephrol*, vol. 28, no. 4, p. J Am Soc Nephrol, 2016.
- [4] H. C. Huerlimann, B. Pinson, M. Stadler-Waibel, S. C. Zeeman, and F. M. Freimoser, "The SPX domain of the yeast low-affinity phosphate transporter Pho90 regulates transport activity," *EMBO*, vol. 10, no. 9, pp. 1003–1008, 2009.
- [5] M. I. Puga, I. Mateos, R. Charukesi, Z. Wang, J. M. Franco-Zorrilla, L. De Lorenzo, M. L. Irigoyen, S. Masiero, R. Bustos, J. Rodríguez, A. Leyva, V. Rubio, H. Sommer, and J. Paz-Ares, "SPX1 is a phosphate-dependent inhibitor of PHOSPHATE STARVATION RESPONSE 1 in Arabidopsis," *PNAS*, vol. 111, no. 41, pp. 14947–52, 2014.
- [6] R. Wild, R. Gerasimaite, J.-Y. Jung, V. Truffault, I. Pavlovic, A. Schmidt, A. Saiardi, H. J. Jessen, Y. Poirier, M. Hothorn, and A. Mayer, "Control of eukaryotic phosphate homeostasis by inositol polyphosphate sensor domains," *Science*, vol. 352, no. 6288, pp. 986–990, 2016.
- [7] A. Legati, D. Giovannini, G. Nicolas, U. López-sánchez, B. Quintáns, J. Oliveira, R. L. Sears, E. M. Ramos, E. Spiteri, M.-J. Sobrido, Á. Carracedo, C. Castro-Fernández, S. Cubizolle, B. L. Fogel, C. Goizet, J. C. Jen, S. Kirdlarp, A. E. Lang, Z. Miedzybrodzka, W. Mitarnun, M. Paucar, H. Paulson, J. Pariente, A.-C. Richard, N. S. Salins, S. A. Simpson, P. Striano, P. Svenningsson, F. Tison, V. K. Unni, O. Vanakker, M. W. Wessels, S. Wetchaphanphesat, M. Yang, F. Boller, D. Champion, D. Hannequin, M. Sitbon, D. H. Geschwind, J.-L. Battini, and G. Coppola, "Mutations in XPR1 cause primary familial brain calcification associated with altered phosphate export," *Nat Genet.*, vol. 47, no. 6, pp. 579–581, 2015.
- [8] N. Ogawa, J. Derisi, and P. O. Brown, "New Components of a System for Phosphate Accumulation and Polyphosphate Metabolism in *Saccharomyces cerevisiae* Revealed by Genomic Expression Analysis," *Mol. Biol. Cell*, vol. 11, no. December, pp. 4309–4321, 2000.
- [9] M. Hothorn, H. Neumann, E. D. Lenherr, M. Wehner, V. Rybin, P. O. Hassa, A. Uttenweiler, M. Reinhardt, A. Schmidt, J. Seiler, A. G. Ladurner, C. Herrmann, K. Scheffzek, and A. Mayer, "Catalytic Core of a Membrane-Associated Eukaryotic Polyphosphate Polymerase," *Science*, vol. 324, no. 5926, pp. 513–516, 2009.
- [10] B. Pinson, M. Merle, and J. Franconi, "Low-Affinity Orthophosphate Carriers Regulate PHO genes Expression Independently of Internal Orthophosphate Concentration in *Saccharomyces cerevisiae*," *J. Biol. Chem.*, vol. 279, no. 34, pp. 35273–35280, 2004.
- [11] H. C. Huerlimann, M. Stadler-Waibel, T. P. Werner, and F. M. Freimoser, "Pho91 Is a Vacuolar Phosphate Transporter That Regulates Phosphate and Polyphosphate Metabolism in *Saccharomyces cerevisiae*," *Mol. Biol. Cell*, vol. 18, pp. 4438–4445, 2007.
- [12] Y. Oshima, "The phosphatase system in *Saccharomyces cerevisiae*," *Genes Genet. Syst.*, vol. 72, no. 6, pp. 323–334, 1997.
- [13] D. Secco, C. Wang, B. A. Arpat, Z. Wang, Y. Poirier, S. D. Tyerman, P. Wu, H. Shou, and J. Whelan, "The emerging importance of the SPX domain-containing proteins in phosphate homeostasis," *New Phytol.*, vol. 193, pp. 842–851, 2012.

- [14] F. Fisher, P. Jayaraman, and C. Goding, "C-myc and the yeast transcription factor PHO4 share a common CACGTG-binding motif," *Oncogene*, vol. 6, no. 7, pp. 1099–1104, 1991.
- [15] K. Yoshida, Z. Kuromitsu, N. Ogawa, and Y. Oshima, "Mode of expression of the positive regulatory genes PHO2 and PHO4 of the phosphatase regulon in *Saccharomyces cerevisiae*," *Mol Gen Genet*, vol. 217, no. 1, pp. 31–39, 1989.
- [16] A. Kaffman, I. Herskowitz, R. Tjian, and E. K. O. Shea, "Phosphorylation of the Transcription Factor PHO4 by a Cyclin-CDK Complex, PH080-PH085," *Science*, vol. 263, no. February, pp. 1153–1157, 1994.
- [17] E. M. O. Neill, A. Kaffman, E. R. Jolly, and E. K. O. Shea, "Regulation of PHO4 Nuclear Localization by the PH080-PH085 Cyclin-CDK Complex," *Science*, vol. 271, no. 5246, pp. 209–212, 1996.
- [18] D. A. Jeffery, M. Springer, D. S. King, E. K. O. Shea, and S. Francisco, "Multi-site Phosphorylation of Pho4 By the Cyclin-CDK Pho80-Pho85 is Semi-processive with Site Preference," *J. Mol. Biol.*, vol. 306, pp. 997–1010, 2001.
- [19] A. Komeili and E. K. O. Shea, "Roles of Phosphorylation Sites in Regulating Activity of the Transcription Factor Pho4," *Science*, vol. 284, no. 5416, pp. 977–981, 1999.
- [20] A. Kaffman, N. M. Rank, E. M. O. Neill, L. S. Huang, and E. K. O. Shea, "The receptor Msn5 exports the phosphorylated transcription factor Pho4 out of the nucleus," *Nature*, vol. 396, no. 6710, pp. 482–486, 1998.
- [21] A. Kaffman, N. M. Rank, and E. K. O. Shea, "Phosphorylation regulates association of the transcription factor Pho4 with its import receptor Pse1/Kap121," *Genes Dev.*, vol. 12, pp. 2673–2683, 1998.
- [22] D. Shao, L. W. Bergman, and C. L. Creasy, "Interaction of *Saccharomyces cerevisiae* Pho2 with Pho4 increases the accessibility of the activation domain of Pho4," *Mol Gen Genet*, vol. 251, pp. 358–364, 1996.
- [23] S. Barbaric and M. Mu, "Cooperative Pho2-Pho4 Interactions at the PHO5 Promoter Are Critical for Binding of Pho4 to UASp1 and for Efficient Transactivation by Pho4 at UASp2," *Mol. Cell. Biol.*, vol. 18, no. 5, pp. 2629–2639, 1998.
- [24] M. Springer, D. D. Wykoff, N. Miller, and E. K. O. Shea, "Partially Phosphorylated Pho4 Activates Transcription of a Subset of Phosphate-Responsive Genes," *PLoS Biol.*, vol. 1, no. 2, pp. 261–270, 2003.
- [25] N. Ogawa, K. Noguchi, H. Sawai, and Y. Yamashita, "Functional Domains of Pho81p, an Inhibitor of Pho85p Protein Kinase, in the Transduction Pathway of Pi Signals in *Saccharomyces cerevisiae*," *Mol. Cell. Biol.*, vol. 15, no. 2, pp. 997–1004, 1995.
- [26] K. R. Schneider, R. L. Smith, and E. K. O. Shea, "Phosphate-Regulated Inactivation of the Kinase PHO80-PHO85 by the CDK Inhibitor PHO81," *Science*, vol. 266, no. October, pp. 122–126, 1994.
- [27] Y. Lee, K. Huang, F. A. Quioco, and E. K. O. Shea, "Molecular basis of cyclin-CDK-CKI regulation by reversible binding of an inositol pyrophosphate," *Nat. Chem. Biol.*, vol. 4, no. 1, pp. 25–32, 2008.
- [28] S. Huang, D. A. Jeffery, M. D. Anthony, and E. K. O. Shea, "Functional Analysis of the Cyclin-Dependent Kinase Inhibitor Pho81 Identifies a Novel Inhibitory Domain," *Mol. Cell. Biol.*, vol. 21, no. 19, pp. 6695–6705, 2001.
- [29] C. L. Creasy, S. L. Madden, and L. W. Bergman, "Molecular analysis of the PHO81 *cerevisiae* of *Saccharomyces*," *Nucleic Acids Res.*, vol. 21, no. 8, pp. 1975–1982, 1993.
- [30] D. Desmarini, S. Lev, D. Furkert, B. Crossett, A. Saiardi, K. Kaufman-Francis, C. Li, T. C. Sorrell, L. Wilkinson-White, J. Matthews, D. Fiedler, and J. T. Djordjevic, "IP7-SPX Domain Interaction Controls Fungal Virulence by Stabilizing Phosphate Signaling Machinery," *MBio*, vol. 11, no. 5, pp. e01920–20, Oct. 2020.
- [31] P. Persson and B. L. Martinez, "Identification, cloning and characterization of a derepressible Na<sup>+</sup>-coupled phosphate transporter in *Saccharomyces cerevisiae*," *Mol Gen Genet*, vol. 258, pp. 628–638, 1998.
- [32] R. A. Zvyagil'skaya, F. Lundh, D. Samyn, J. Pattison-granberg, Y. Popova, J. M. Thevelein, and B. L. Persson, "Characterization of the Pho89 phosphate transporter by functional hyperexpression in *Saccharomyces cerevisiae*," *FEMS Yeast Res.*, vol. 8, pp. 685–696, 2008.

- [33] A. Berhe, U. Fristedt, and B. L. Persson, "Expression and purification of the high-affinity phosphate transporter of *Saccharomyces cerevisiae*," *Eur. J. Biochem.*, vol. 227, pp. 566–572, 1995.
- [34] U. Fristedt, A. Berhe, K. Ensler, B. Norling, and B. L. Persson, "Isolation and Characterization of Membrane Vesicles of *Saccharomyces cerevisiae* Harboring the High-Affinity Phosphate Transporter," vol. 330, no. 1, pp. 133–141, 1996.
- [35] J. Pattison-Granberg and B. L. Persson, "Regulation of Cation-Coupled High-Affinity Phosphate Uptake in the Yeast *Saccharomyces cerevisiae*," *J. Bacteriol.*, vol. 182, no. 17, pp. 5017–5019, 2000.
- [36] M. Bun-ya, M. Nishimura, S. Harashima, and Y. Oshima, "The PH084 Gene of *Saccharomyces cerevisiae* Encodes an Inorganic Phosphate Transporter," *Mol. Cell. Biol.*, vol. 11, no. 6, pp. 3229–3238, 1991.
- [37] D. D. Wykoff, A. H. Rizvi, J. M. Raser, B. Margolin, and E. K. O'Shea, "Positive feedback regulates switching of phosphate transporters in *S. cerevisiae*," *Mol. Cell.*, vol. 27, no. 6, pp. 1005–1013, 2007.
- [38] W. W. Lau, R. W. Howson, P. Malkus, R. Schekman, and E. K. O. Shea, "Pho86p, an endoplasmic reticulum (ER) resident protein in *Saccharomyces cerevisiae*, is required for ER exit of the high-affinity phosphate transporter Pho84p," *PNAS*, vol. 97, no. 3, pp. 1107–1112, 2000.
- [39] F. Lundh, J. Mouillon, D. Samyn, K. Stadler, Y. Popova, J. O. Lagerstedt, J. M. Thevelein, and B. L. Persson, "Molecular Mechanisms Controlling Phosphate-Induced Downregulation of the Yeast Pho84 Phosphate Transporter," *Biochemistry*, vol. 48, pp. 4497–4505, 2009.
- [40] J. S. Flick and J. Thorner, "An Essential Function of a Phosphoinositide-Specific Phospholipase C is Relieved by Inhibition of a Cyclin-Dependent Protein Kinase in the Yeast," *Genetics*, vol. 148, pp. 33–47, 1998.
- [41] R. Ghillebert, E. Swinnen, P. D. E. Snijder, B. Smets, and J. Winderickx, "Differential roles for the low-affinity phosphate transporters Pho87 and Pho90 in *Saccharomyces cerevisiae*," *Biochem. J.*, vol. 434, pp. 243–251, 2011.
- [42] N. N. Rao, M. R. Gomez-Garcia, and A. Kornberg, "Inorganic Polyphosphate: Essential for Growth and Survival," *Annu. Rev. Biochem.*, vol. 78, pp. 605–647, 2009.
- [43] M. R. Thomas and E. K. O. Shea, "An intracellular phosphate buffer filters transient fluctuations in extracellular phosphate levels," *PNAS*, vol. 102, no. 27, pp. 9565–9570, 2005.
- [44] D. W. Neef and M. P. Kladde, "Polyphosphate Loss Promotes SNF / SWI- and Gcn5-Dependent Mitotic Induction of PHO5," *Mol. Cell. Biol.*, vol. 23, no. 11, pp. 3788–3797, 2003.
- [45] S. Bru, J. M. Mart, D. Canadell, and J. Ari, "Polyphosphate is involved in cell cycle progression and genomic stability in *Saccharomyces cerevisiae*," *Mol. Microbiol.*, vol. 101, no. 3, pp. 367–380, 2016.
- [46] R. Ohtomo and M. Saito, "Polyphosphate dynamics in mycorrhizal roots during colonization of an arbuscular mycorrhizal fungus," *New Phytol.*, vol. 167, no. 2, pp. 571–578, 2005.
- [47] K. J. Indge, "Polyphosphates of the Yeast Cell Vacuole," *J. Gen. Microbiol.*, vol. 51, no. 3, pp. 447–455, 1968.
- [48] K. Urech, M. Durr, A. Wiemken, and J. Schwencke, "Localization of Polyphosphate in Vacuoles of *Saccharomyces cerevisiae*," *Arch. Microbiol.*, vol. 116, no. 3, pp. 275–278, 1978.
- [49] K. Saito, R. Ohtomo, Y. Kuga-Uetake, T. Aono, and M. Saito, "Direct Labeling of Polyphosphate at the Ultrastructural Level in *Saccharomyces cerevisiae* by Using the Affinity of the Polyphosphate Binding Domain of *Escherichia coli* Exopolyphosphatase," *Appl. Environ. Microbiol.*, vol. 71, no. 10, pp. 5692–5701, 2005.
- [50] F. M. Freimoser, H. C. Hürlimann, C. A. Jakob, T. P. Werner, and N. Amrhein, "Systematic screening of polyphosphate (poly P) levels in yeast mutant cells reveals strong interdependence with primary metabolism," *Genome Biol.*, vol. 7, no. 11, p. R109, 2006.

- [51] A. Cohen, N. Perzov, H. Nelson, N. Nelson, and T. Aviv, "A Novel Family of Yeast Chaperons Involved in the Distribution of V-ATPase and Other Membrane Proteins \*," *J. Biol. Chem.*, vol. 274, no. 38, pp. 26885–26893, 1999.
- [52] J. Fang, F. A. Ruiz, M. Docampo, S. Luo, J. C. F. Rodrigues, L. S. Motta, P. Rohloff, and R. Docampo, "Overexpression of a Zn<sup>2+</sup>-sensitive Soluble Exopolyphosphatase from *Trypanosoma cruzi* Depletes Polyphosphate and Affects Osmoregulation," *J. Biol. Chem.*, vol. 282, no. 44, pp. 32501–32510, 2007.
- [53] P. J. Rooney, L. Ayong, C. M. Tobin, S. N. J. Moreno, and L. J. Knoll, "Molecular & Biochemical Parasitology TgVTC2 is involved in polyphosphate accumulation in *Toxoplasma gondii*," *Mol. Biochem. Parasitol.*, vol. 176, no. 2, pp. 121–126, 2010.
- [54] A. L. Gomes-vieira, J. G. Wideman, L. Paes-vieira, S. L. Gomes, T. A. Richards, and J. R. Meyer-fernandes, "Evolutionary conservation of a core fungal phosphate homeostasis pathway coupled to development in *Blastocladiella emersonii*," *Fungal Genet. Biol.*, vol. 115, pp. 20–32, 2018.
- [55] H. M. C. de Carvalho, H. Sun, C. Bowler, and N. Chua, "Noncoding and coding transcriptome responses of a marine diatom to phosphate fluctuations," *New Phytol.*, vol. 210, no. 2, pp. 497–510, 2016.
- [56] S. T. Dyhrman, B. D. Jenkins, T. A. Ryneerson, M. A. Saito, M. L. Mercier, H. Alexander, L. P. Whitney, A. Drzewianowski, V. V. Bulygin, E. M. Bertrand, Z. Wu, C. Benitez-nelson, and A. Heithoff, "The Transcriptome and Proteome of the Diatom *Thalassiosira pseudonana* Reveal a Diverse Phosphorus Stress Response," *PLoS One*, vol. 7, no. 3, p. e33768, 2012.
- [57] A. Uttenweiler, H. Schwarz, H. Neumann, and A. Mayer, "The Vacuolar Transporter Chaperone (VTC) Complex Is Required for Microautophagy," *Mol. Biol. Cell*, vol. 18, no. 1, pp. 166–175, 2007.
- [58] Y. Desfougères, R. Gerasimaité, H. J. Jessen, and A. Mayer, "Vtc5, a Novel Subunit of the Vacuolar Transporter Chaperone Complex, Regulates Polyphosphate Synthesis and Phosphate Homeostasis in Yeast," *J. Biol. Chem.*, vol. 291, no. 42, pp. 22262–22275, 2016.
- [59] O. Mueller, H. Neumann, M. J. Bayer, and A. Mayer, "Role of the Vtc proteins in V-ATPase stability and membrane trafficking," *J. Cell Sci.*, vol. 116, no. 6, pp. 1107–1115, 2003.
- [60] R. Gerasimaite, S. Sharma, and Y. Desfouge, "Coupled synthesis and translocation restrains polyphosphate to acidocalcisome-like vacuoles and prevents its toxicity," *J. Cell Sci.*, vol. 127, pp. 5093–5104, 2014.
- [61] R. Gerasimaite, I. Pavlovic, S. Capolicchio, A. Hofer, A. Schmidt, H. J. Jessen, and A. Mayer, "Inositol Pyrophosphate Specificity of the SPX-Dependent Polyphosphate Polymerase VTC," *ASC Chem. Biol.*, no. 12, p. 648–653, 2017.
- [62] A. Lonetti, Z. Sziogyarto, D. Bosch, O. Loss, C. Azevedo, and A. Saiardi, "Identification of an Evolutionarily Conserved Family of Inorganic Polyphosphate Endopolyphosphatases," *J. Biol. Chem.*, vol. 286, no. 37, pp. 31966–31974, 2011.
- [63] C. Auesukaree, H. Tochio, and S. Harashima, "Plc1p, Arg82p, and Kcs1p, Enzymes Involved in Inositol Pyrophosphate Synthesis, Are Essential for Phosphate Regulation and Polyphosphate Accumulation in *Saccharomyces cerevisiae* \*," *J. Biol. Chem.*, vol. 280, no. 26, pp. 25127–25133, 2005.
- [64] O. Mueller, M. J. Bayer, C. Peters, J. S. Andersen, M. Mann, and A. Mayer, "The Vtc proteins in vacuole fusion: coupling NSF activity to V0 trans-complex formation," *EMBO J.*, vol. 21, no. 3, pp. 259–269, 2002.
- [65] R. Gerasimaité and A. Mayer, "Enzymes of yeast polyphosphate metabolism: structure, enzymology and biological roles," *Biochem. Soc. Trans.*, vol. 44, no. 1, pp. 234–239, 2016.
- [66] H. J. M. Van Rijn, P. Boer, and E. P. Steyn-Parve, "Biosynthesis of acid phosphatase of baker's yeast. Factors influencing its production by protoplasts and characterization of the secreted enzyme," *Biochim. Biophys. Acta*, vol. 268, no. 2, pp. 431–441, 1972.
- [67] M. E. Lenburg and E. K. O. Shea, "Signaling phosphate starvation," *Trends Biochem. Sci.*, vol. 21, no. 10, pp. 383–387, 1996.

- [68] M. G. Shnyreval, E. V. Petrova, S. N. Egorov, and A. Hinnen, "Biochemical properties and excretion behavior of repressible acid phosphatases with altered subunit composition," *Microbiol. Res.*, vol. 151, no. 3, pp. 291–300, 1996.
- [69] V. S. Reddy, A. K. Singh, and R. Rajasekharan, "The *Saccharomyces cerevisiae* PHM8 Gene Encodes a Soluble Magnesium-dependent Lysophosphatidic Acid Phosphatase," *J. Biol. Chem.*, vol. 283, no. 14, pp. 8846–8854, 2008.
- [70] Y. Xu, F. Letisse, F. Absalan, W. Lu, E. Kuznetsova, G. Brown, A. A. Caudy, A. F. Yakunin, J. R. Broach, and J. D. Rabinowitz, "Nucleotide degradation and ribose salvage in yeast," *Mol. Syst. Biol.*, vol. 9, no. 665, pp. 1–12, 2013.
- [71] A. Donella-Deana, S. Ostoji, L. A. Pinna, and S. Barbari, "Specific dephosphorylation of phosphopeptides by the yeast alkaline phosphatase encoded by PHO8 gene," *Biochim. Biophys. Acta*, vol. 1177, no. 2, pp. 221–228, 1993.
- [72] K. D. Kumble and A. Kornberg, "Endopolyphosphatases for Long Chain Inorganic Polyphosphate in Yeast and Mammals," *J. Biol. Chem.*, vol. 271, no. 43, pp. 27146–27151, 1996.
- [73] A. Sethuraman, N. N. Rao, and A. Kornberg, "The endopolyphosphatase gene: Essential in *Saccharomyces cerevisiae*," *PNAS*, vol. 98, no. 15, pp. 8542–8547, 2001.
- [74] R. Gerasimaite and A. Mayer, "Ppn2 , a novel Zn<sup>2+</sup>-dependent polyphosphatase in the acidocalcisome-like yeast vacuole," *J. Cell Sci.*, vol. 130, pp. 1625–1636, 2017.
- [75] C. Auesukaree, T. Homma, H. Tochio, M. Shirakawa, Y. Kaneko, and S. Harashima, "Intracellular Phosphate Serves as a Signal for the Regulation of the PHO Pathway in *Saccharomyces cerevisiae*," *J. Biol. Chem.*, vol. 279, no. 17, pp. 17289–17294, 2004.
- [76] X. Shi and A. Kornberg, "Endopolyphosphatase in *Saccharomyces cerevisiae* undergoes post-translational activations to produce short-chain polyphosphates," *FEBS*, vol. 579, no. 9, pp. 2014–2018, 2005.
- [77] N. Andreeva, L. Trilisenko, M. Eldarov, and T. Kulakovskaya, "Polyphosphatase PPN1 of *Saccharomyces cerevisiae* : Switching of Exopolyphosphatase and Endopolyphosphatase Activities," *PLoS One*, vol. 10, no. 3, pp. 1–11, 2015.
- [78] W. Huh, J. V. Falvo, L. C. Gerke, A. S. Carroll, R. W. Howson, J. S. Weissman, and E. K. O. Shea, "Global analysis of protein localization in budding yeast," *Nature*, vol. 425, no. 6959, pp. 686–691, 2003.
- [79] L. P. Lichko, N. A. Andreeva, T. V. Kulakovskaya, and I. S. Kulaev, "Exopolyphosphatases of the yeast *Saccharomyces cerevisiae*," *FEMS Yeast Res.*, vol. 3, no. 3, pp. 233–238, 2003.
- [80] L. Lichko, T. V. Kulakovskaya, N. Pestov, and I. Kulaev, "Inorganic Polyphosphates and Exopolyphosphatases in Cell Compartments of the Yeast *Saccharomyces cerevisiae* Under Inactivation of PPX1 and PPN1 Genes," *Biosci. Rep.*, vol. 26, no. 1, pp. 45–54, 2006.
- [81] M. Tammenkoski, V. M. Moiseev, M. Lahti, E. Ugochukwu, T. H. C. Brondijk, S. A. White, R. Lahti, and A. A. Baykov, "Kinetic and Mutational Analyses of the Major Cytosolic Exopolyphosphatase from *Saccharomyces cerevisiae* \*," *J. Biol. Chem.*, vol. 282, no. 13, pp. 9302–9311, 2007.
- [82] H. Wurst and A. Kornberg, "A Soluble Exopolyphosphatase of *Saccharomyces cerevisiae*. Purification and characterization," *J. Biol. Chem.*, vol. 269, no. 15, pp. 10996–11001, 1994.
- [83] H. Wurst, T. Shiba, and A. Kornberg, "The Gene for a Major Exopolyphosphatase of *Saccharomyces cerevisiae*," *J. Bacteriol.*, vol. 177, no. 4, pp. 898–906, 1995.
- [84] J. L. Patton-Vogt and S. A. Henry, "GIT1, a Gene Encoding a Novel Transporter for Glycerophosphoinositol," *Genetics*, vol. 149, no. 4, pp. 1707–1715, 1998.
- [85] D. D. Wykoff and E. K. O. Shea, "Phosphate Transport and Sensing in *Saccharomyces cerevisiae*," *Genetics*, vol. 159, no. 4, pp. 1491–1499, 2001.

- [86] E. Fisher, C. Almaguer, R. Holic, P. Griac, and J. Patton-vogt, "Glycerophosphocholine-dependent Growth Requires Gde1p (YPL110c) and Git1p in *Saccharomyces cerevisiae*," *J. Biol. Chem.*, vol. 280, no. 43, pp. 36110–36117, 2005.
- [87] C. Almaguer, D. Mantella, and E. Perez, "Inositol and Phosphate Regulate GIT1 Transcription and Glycerophosphoinositol Incorporation in *Saccharomyces cerevisiae*," *Eukaryot. Cell*, vol. 2, no. 4, pp. 729–736, 2003.
- [88] A. Toh-e, K. Tanaka, Y. Uesono, and R. B. Wickner, "PH085, a negative regulator of the PHO system, is a homolog of the protein kinase gene, CDC28, of *Saccharomyces cerevisiae*," *Mol Gen Genet*, vol. 214, no. 1, pp. 162–164, 1988.
- [89] A. Toh-e and M. Nishizawa, "Structure and function of cyclin-dependent Pho85 kinase of *Saccharomyces cerevisiae*," *J. Gen. Appl. Microbiol.*, vol. 117, no. 3, pp. 107–117, 2001.
- [90] K. Huang, I. F. Connell, W. Zhang, G. A. Leonard, E. K. O. Shea, and F. A. Quioco, "Structure of the Pho85-Pho80 CDK-cyclin Complex of the Phosphate-responsive Signal Transduction Pathway," *Mol Cell*, vol. 28, no. 4, pp. 614–623, 2007.
- [91] Y. Uesono, M. Tokai, K. Tanaka, and A. Toh-e, "Negative regulators of the PHO system of *Saccharomyces cerevisiae*: characterization of PH080 and PH085," *Mol Gen Genet*, vol. 231, no. 3, pp. 426–432, 1992.
- [92] V. Wanke, I. Pedruzzi, and C. De Virgilio, "Regulation of G0 entry by the Pho80–Pho85 cyclin–CDK complex," *EMBO J.*, vol. 24, no. 24, pp. 4271–4278, 2005.
- [93] C. Auesukaree, T. Homma, Y. Kaneko, and S. Harashima, "Transcriptional regulation of phosphate-responsive genes in low-affinity phosphate-transporter-defective mutants in *Saccharomyces cerevisiae*," *Biochem. Biophys. Res. Commun.*, vol. 306, no. 4, pp. 843–850, 2003.
- [94] H. Takahashi, P. Buchner, N. Yoshimoto, M. J. Hawkesford, S. Shiu, and J. M. Jez, "Evolutionary relationships and functional diversity of plant sulfate transporters," *Front. Plant Sci.*, vol. 2, no. 119, pp. 1–9, 2012.
- [95] Y. Tamai, A. Toh-e, and Y. Oshima, "Regulation of Inorganic Phosphate Transport Systems in *Saccharomyces cerevisiae*," *J. Bacteriol.*, vol. 164, no. 2, pp. 964–968, 1985.
- [96] E. Potapenko, C. D. Cordeiro, G. Huang, M. Storey, C. Wittwer, A. K. Dutta, H. J. Jessen, V. J. Starai, and R. Docampo, "5-Diphosphoinositol Pentakisphosphate (5-IP7) Regulates Phosphate Release from Acidocalcisomes and Yeast Vacuoles," *J. Biol. Chem.*, vol. 293, no. 49, pp. 19101–19112, 2018.
- [97] S. Levy, M. Kafri, M. Carmi, and N. Barkai, "The Competitive Advantage of a Dual-Transporter System," *Science*, vol. 334, no. 6061, pp. 1408–1412, 2011.
- [98] N. Vardi, S. Levy, I. Amit, N. Vardi, S. Levy, Y. Gurvich, T. Polacheck, M. Carmi, D. Jaitin, I. Amit, and N. Barkai, "Sequential Feedback Induction Stabilizes the Phosphate Starvation Response in Budding Yeast Sequential Feedback Induction Stabilizes the Phosphate Starvation Response in Budding Yeast," *Cell*, vol. 9, pp. 1122–1134, 2014.
- [99] T. Wundenberg and G. W. Mayr, "Synthesis and biological actions of diphosphoinositol phosphates (inositol pyrophosphates), regulators of cell homeostasis," *Biol. Chem.*, vol. 393, no. 9, pp. 979–998, 2012.
- [100] L. Stephens, T. Radenbergtl, U. Thielii, G. Vogeli, K. Khoo, A. Dell, T. R. Jackson, P. T. Hawkins, and G. W. Mayr, "The Detection, Purification, Structural Characterization, and Metabolism of Diphosphoinositol Pentakisphosphate(s) and Bisdiphosphoinositol Tetrakisphosphate(s)," *J. Biol. Chem.*, vol. 268, no. 6, pp. 4009–4015, 1993.
- [101] H. Lin, P. C. Fridy, A. A. Ribeiro, J. H. Choi, D. K. Barma, J. R. Falck, S. B. Shears, J. D. York, and G. W. Mayr, "Structural Analysis and Detection of Biological Inositol Pyrophosphates Reveal That the Family of VIP/Diphosphoinositol Pentakisphosphate Kinases," *J. Biol. Chem.*, vol. 284, no. 3, pp. 1863–1872, 2009.
- [102] H. Wang, J. R. Falck, T. M. T. Hall, and S. B. Shears, "Structural basis for an inositol pyrophosphate kinase surmounting phosphate crowding," *Nat. Chem. Biol.*, vol. 8, no. 1, pp. 111–116, 2011.

- [103] A. Saiardi, H. Erdjument-bromage, A. M. Snowman, P. Tempst, and S. H. Snyder, "Synthesis of diphosphoinositol pentakisphosphate by a newly identified family of higher inositol polyphosphate kinases," *Curr. Biol.*, vol. 9, no. 22, pp. 1323–1326, 1999.
- [104] A. Saiardi, J. J. Caffrey, S. H. Snyder, S. B. Shears, and S. H. Curr, "The Inositol Hexakisphosphate Kinase Family. Catalytic Flexibility and Function in Yeast Vacuole Biogenesis," *J. Biol. Chem.*, vol. 275, no. 32, pp. 24686–24692, 2000.
- [105] P. Draskovic, A. Saiardi, R. Bhandari, A. Burton, G. Ilc, M. Kovacevic, S. H. Snyder, and M. Podobnik, "Article Inositol Hexakisphosphate Kinase Products Contain Diphosphate and Triphosphate Groups," *Chem. Biol.*, vol. 15, no. 3, pp. 274–286, 2008.
- [106] M. El Alami, F. Messenguy, B. Scherens, and E. Dubois, "Arg82p is a bifunctional protein whose inositol polyphosphate kinase activity is essential for nitrogen and PHO gene expression but not for Mcm1p chaperoning in yeast," *Mol. Mi*, vol. 49, no. 2, pp. 457–468, 2003.
- [107] A. Saiardi, R. Bhandari, and A. C. Resnick, "Phosphorylation of Proteins by Inositol Pyrophosphates," *Science*, vol. 306, no. 5704, pp. 2101–2106, 2004.
- [108] Y. Lee, S. Mulugu, J. D. York, and E. K. O. Shea, "Regulation of a Cyclin-CDK-CDK Inhibitor Complex by Inositol Pyrophosphates," *Science*, vol. 316, no. 5821, pp. 109–112, 2007.
- [109] C. Gu, H. Nguyen, A. Hofer, H. J. Jessen, X. Dai, H. Wang, and S. B. Shears, "The Significance of the Bifunctional Kinase/Phosphatase Activities of Diphosphoinositol Pentakisphosphate Kinases (PPIP5Ks) for Coupling Inositol Pyrophosphate Cell Signaling to Cellular Phosphate Homeostasis," *J. Biol. Chem.*, vol. 292, no. 11, pp. 4544–4555, 2017.
- [110] C. J. Barker, J. Wright, P. J. Hughes, C. J. Kirk, and R. H. Michell, "Complex changes in cellular inositol phosphate complement accompany transit through the cell cycle," *Biochem. J.*, vol. 473, no. Pt 2, pp. 465–473, 2004.
- [111] M. C. Glennon and S. B. Shears, "Turnover of inositol pentakisphosphates , inositol hexakisphosphate and diphosphoinositol polyphosphates in primary cultured hepatocytes," *Biochem. J.*, vol. 293, no. Pt 2, pp. 583–590, 1993.
- [112] C. Albert, S. T. Safrany, M. E. Bembenek, K. M. Reddy, K. K. Reddy, J. R. Falck, M. Broecker, S. B. Shears, and G. W. Mayr, "Biological variability in the structures of diphosphoinositol polyphosphates in Dictyostelium discoideum and mammalian cells," *Biochem. J.*, vol. 327, no. Pt 2, pp. 553–560, 1997.
- [113] C. Gu, M. S. C. Wilson, H. J. Jessen, A. Saiardi, and B. Shears, "Inositol Pyrophosphate Profiling of Two HCT116 Cell Lines Uncovers Variation in InsP8 Levels," *PLoS One*, vol. 11, no. 10, p. e0165286, 2016.
- [114] S. Mulugu, W. Bai, P. C. Fridy, R. J. Bastidas, J. C. Otto, D. E. Dollins, T. A. Haystead, A. A. Ribeiro, and J. D. York, "A Conserved Family of Enzymes That Phosphorylate Inositol Hexakisphosphate," *Science*, vol. 316, no. 5821, pp. 106–110, 2007.
- [115] P. C. Fridy, J. C. Otto, D. E. Dollins, and J. D. York, "Cloning and Characterization of Two Human VIP1-like Inositol Hexakisphosphate and Diphosphoinositol Pentakisphosphate Kinases," *J. Biol. Chem.*, vol. 282, no. 42, pp. 30754–30762, 2007.
- [116] O. Losito, Z. Szigyarto, A. C. Resnick, and A. Saiardi, "Inositol Pyrophosphates and Their Unique Metabolic Complexity: Analysis by Gel Electrophoresis," *PLoS One*, vol. 4, no. 5, p. e5580, 2009.
- [117] J. Zhu, K. Lau, R. Puschmann, R. K. Harmel, Y. Zhang, V. Pries, P. Gaugler, L. Broger, A. K. Dutta, H. J. Jessen, G. Schaaf, A. R. Fernie, L. A. Hothorn, D. Fiedler, and M. Hothorn, "Two bifunctional inositol pyrophosphate kinases / phosphatases control plant phosphate homeostasis," *Elife*, vol. 8, p. e43582, 2019.
- [118] H. Wang, V. S. Nair, A. A. Holland, S. Capolicchio, J. Henning, M. K. Johnson, S. B. Shears, U. States, and U. States, "Asp1 from Schizosaccharomyces pombe binds a [2Fe-2S](2+) cluster which inhibits inositol pyrophosphate 1-phosphatase activity," *Biochemistry*, vol. 54, no. 42, pp. 6462–6474, 2016.

- [119] D. E. Dollins, W. Bai, P. C. Fridy, J. C. Otto, J. L. Neubauer, S. G. Gattis, K. P. M. Mehta, and J. D. York, "Vip1 is a kinase and pyrophosphatase switch that regulates inositol diphosphate signaling," *PNAS*, vol. 117, no. 14, pp. 9356–9364, 2020.
- [120] V. M. Boer, C. A. Crutchfield, P. H. Bradley, D. Botstein, and J. D. Rabinowitz, "Growth-limiting Intracellular Metabolites in Yeast Growing under Diverse Nutrient Limitations," *Mol. Biol. Cell*, vol. 21, no. 1, pp. 198–211, 2010.
- [121] J. Choi, A. Rajagopal, Y. Xu, J. D. Rabinowitz, and E. K. O'Shea, "A systematic genetic screen for genes involved in sensing inorganic phosphate availability in *Saccharomyces cerevisiae*," *PLoS One*, vol. 12, no. 5, p. e0176085, 2017.
- [122] K. Choi, E. Mollapour, J. H. Choi, and S. B. Shears, "Cellular Energetic Status Supervises the Synthesis of Bis-Diphosphoinositol Tetrakisphosphate Independently of AMP-Activated Protein Kinase," *Mol. Pharmacol.*, vol. 74, no. 2, pp. 527–536, 2008.
- [123] C. Gu, H. Nguyen, D. Ganini, Z. Chen, H. J. Jessen, Z. Gu, H. Wang, and S. B. Shears, "KO of 5-InsP7 kinase activity transforms the HCT116 colon cancer cell line into a hypermetabolic, growth-inhibited phenotype," *PNAS*, vol. 114, no. 45, pp. 11968–11973, 2017.
- [124] J. M. Gancedo and C. Gancedo, "Concentrations of intermediary metabolites in yeast .," *Biochimie*, vol. 55, no. 2, pp. 205–211, 1973.
- [125] F. Norbis, M. Boll, G. Stange, D. Markovich, F. Verrey, J. Biber, and H. Murer, "Identification of a cDNA/Protein Leading to an Increased Pi-uptake in *Xenopus laevis* Oocytes," *J. Membr. Biol.*, vol. 156, no. 1, pp. 19–24, 1997.
- [126] M. J. Schell, A. J. Letcher, C. A. Brearley, H. Murer, and R. F. I. Y, "PiUS (Pi uptake stimulator) is an inositol hexakisphosphate kinase," *FEBS Lett.*, vol. 461, no. 3, pp. 169–172, 1999.
- [127] M. K. Ried, R. Wild, J. Zhu, L. Broger, R. K. Harmel, L. A. Hothorn, D. Fiedler, and M. Hothorn, "Inositol pyrophosphates promote the interaction of SPX domains with the coiled-coil motif of PHR transcription factors to regulate plant phosphate homeostasis," *BioRxiv*, vol. 12, 2019.
- [128] Z. Wang, W. Ruan, J. Shi, L. Zhang, D. Xiang, C. Yang, C. Li, Z. Wu, and Y. Liu, "Rice SPX1 and SPX2 inhibit phosphate starvation responses through interacting with PHR2 in a phosphate-dependent manner," *PNAS*, vol. 111, no. 41, pp. 14953–14958, 2014.
- [129] X. Li, C. Gu, S. Hostachy, S. Sahu, C. Wittwer, H. J. Jessen, D. Fiedler, H. Wang, and S. B. Shears, "Control of XPR1-dependent cellular phosphate efflux by InsP8 is an exemplar for functionally-exclusive inositol pyrophosphate signaling," *PNAS*, vol. 117, no. 7, pp. 3568–3574, 2020.
- [130] R. Yousaf, C. Gu, Z. M. Ahmed, S. N. Khan, B. Friedman, S. Riazuddin, S. B. Shears, and S. Riazuddin, "Mutations in Diphosphoinositol- Pentakisphosphate Kinase PPIP5K2 are associated with hearing loss in human and mouse," *PLoS Genet.*, vol. 14, no. 3, p. e1007297, 2018.
- [131] M. Nishizawa, T. Komai, Y. Katou, K. Shirahige, T. Ito, and A. Toh-e, "Nutrient-Regulated Antisense and Intragenic RNAs Modulate a Signal Transduction Pathway in Yeast," *PLoS Biol.*, vol. 6, no. 12, p. e326, 2008.
- [132] E. A. Steidle, L. S. Chong, M. Wu, E. Crooke, D. Fiedler, A. C. Resnick, and R. J. Rolfes, "A Novel Inositol Pyrophosphate Phosphatase in *Saccharomyces cerevisiae*," *J. Biol. Chem.*, vol. 291, no. 13, pp. 6772–6783, 2016.
- [133] Y. Desfougères, M. S. C. Wilson, D. Laha, G. J. Miller, and A. Saiardi, "ITPK1 mediates the lipid-independent synthesis of inositol phosphates controlled by metabolism," *PNAS*, vol. 116, no. 49, pp. 24551–24561, 2019.
- [134] J. P. Hirsch and S. A. Henry, "Expression of the *Saccharomyces cerevisiae* Inositol-1-Phosphate Synthase (INO1) Gene Is Regulated by Factors That Affect Phospholipid Synthesis," *Mol. Cell. Biol.*, vol. 6, no. 10, pp. 3320–3328, 1986.

- [135] J. M. Lopes, J. P. Hirschl, P. A. Chorgo, K. L. Schulze, and S. A. Henry, "Analysis of sequences in the INO1 promoter that are involved in its regulation by phospholipid precursors," *Nucleic Acids Res.*, vol. 19, no. 7, pp. 1687–1693, 1991.
- [136] M. Murray and M. L. Greenberg, "Regulation of inositol monophosphatase in *Saccharomyces cerevisiae*," *Mol. Microbiol.*, vol. 25, no. 3, pp. 541–546, 1997.
- [137] F. Lopez, M. Leube, R. Gil-mascarell, J. P. Navarro-Avino, and R. Serrano, "The yeast inositol monophosphatase is a lithium- and sodium-sensitive enzyme encoded by a non-essential gene pair," *Mol. Microbiol.*, vol. 31, no. 4, pp. 1255–1264, 1999.
- [138] F. Giots, M. C. V Donaton, and J. M. Thevelein, "Inorganic phosphate is sensed by specific phosphate carriers and acts in concert with glucose as a nutrient signal for activation of the protein kinase A pathway in the yeast *Saccharomyces cerevisiae*," *Mol. Microbiol.*, vol. 47, no. 4, pp. 1163–1181, 2003.
- [139] J. M. Thevelein, R. Geladé, I. Holsbeeks, O. Lagatie, Y. Popova, F. Rolland, F. Stolz, S. Van de Velde, P. Van Dijck, P. Vandormael, A. Van Nuland, K. Van Roey, G. Van Zeebroeck, and B. Yan, "Nutrient sensing systems for rapid activation of the protein kinase A pathway in yeast," *Biochem. Soc. Trans.*, vol. 33, no. 1, pp. 253–256, Feb. 2005.
- [140] B. Smets, R. Ghillebert, P. De Snijder, M. Binda, E. Swinnen, C. De Virgilio, and J. Winderickx, "Life in the midst of scarcity: adaptations to nutrient availability in *Saccharomyces cerevisiae*," *Curr. Genet.*, vol. 56, no. 1, p. 1–32, Feb. 2010.
- [141] M. Rubio-Teixeira, G. Van Zeebroeck, K. Voordeckers, and J. M. Thevelein, "*Saccharomyces cerevisiae* plasma membrane nutrient sensors and their role in PKA signaling," *FEMS Yeast Res.*, vol. 10, no. 2, pp. 134–149, Mar. 2010.
- [142] L. T. Jensen, M. Ajuja-Alemanji, and V. C. Culotta, "The *Saccharomyces cerevisiae* High Affinity Phosphate Transporter Encoded by PHO84 Also Functions in Manganese Homeostasis," *J. Biol. Chem.*, vol. 278, no. 43, pp. 42036–42040, 2003.
- [143] J. B. C. Papers and M. Doi, "Uptake of Selenite by *Saccharomyces cerevisiae* Involves the High and Low Affinity Orthophosphate Transporters," *J. Biol. Chem.*, vol. 285, no. 42, pp. 32029–32037, 2010.
- [144] M. A. C. Ikeh, S. L. Kastora, A. M. Day, C. M. Herrero-de-Dios, E. Tarrant, K. J. Waldron, A. P. Banks, J. M. Bain, D. Lydall, E. A. Veal, D. M. MacCallum, L. P. Erwig, A. J. P. Brown, and J. Quinn, "Pho4 mediates phosphate acquisition in *Candida albicans* and is vital for stress resistance and metal homeostasis," *Mol. Biol. Cell*, vol. 27, no. 17, pp. 2784–2801, Sep. 2016.
- [145] V. Urrialde, D. Prieto, J. Pla, and R. Alonso-Monge, "The *Candida albicans* Pho4 Transcription Factor Mediates Susceptibility to Stress and Influences Fitness in a Mouse Commensalism Model," *Front. Microbiol.*, vol. 7, p. 1062, 2016.
- [146] S. Lev, K. Kaufman-Francis, D. Desmarini, P. G. Juillard, C. Li, S. A. Stifter, C. G. Feng, T. C. Sorrell, G. E. R. Grau, Y.-S. Bahn, and J. T. Djordjevic, "Pho4 Is Essential for Dissemination of *Cryptococcus neoformans* to the Host Brain by Promoting Phosphate Uptake and Growth at Alkaline pH," *mSphere*, vol. 2, no. 1, pp. e00381–16, Feb. 2017.
- [147] S. Huang and E. K. O'Shea, "A Systematic High-Throughput Screen of a Yeast Deletion Collection for Mutants Defective in PHO5 Regulation," *Genetics*, vol. 1871, no. 4, pp. 1859–1871, 2005.
- [148] Y. Ho, A. Gruhler, A. Heilbut, G. D. Bader, L. Moore, S.-L. Adams, A. Millar, P. Taylor, K. Bennett, K. Boutilier, L. Yang, C. Wolting, I. Donaldson, S. Schandorff, J. Shewnarane, M. Vo, J. Taggart, M. Goudreau, B. Muskat, C. Alfarano, D. Dewar, Z. Lin, K. Michalickova, A. R. Willems, H. Sassi, P. A. Nielsen, K. J. Rasmussen, J. R. Andersen, L. E. Johansen, L. H. Hansen, H. Jespersen, A. Podtelejnikov, E. Nielsen, J. Crawford, V. Poulsen, B. D. Sørensen, J. Matthiesen, R. C. Hendrickson, F. Gleeson, T. Pawson, M. F. Moran, D. Durocher, M. Mann, C. W. V Hogue, D. Figeys, and M. Tyers, "Systematic identification of protein complexes in *Saccharomyces cerevisiae* by mass spectrometry," *Nature*, vol. 415, no. 6868, pp. 180–183, 2002.

- [149] E. Swinnen, J. Rosseels, and J. Winderickx, "The minimum domain of Pho81 is not sufficient to control the Pho85 – Rim15 effector branch involved in phosphate starvation-induced stress responses," *Curr. Genet.*, vol. 48, no. 1, pp. 18–33, 2005.
- [150] S. Menoyo, N. Ricco, S. Bru, M. Aldea, and J. Clotet, "Phosphate-Activated Cyclin-Dependent Kinase Stabilizes G1 Cyclin To Trigger Cell Cycle Entry," *Mol Cell Biol*, vol. 33, no. 7, pp. 1273–1284, 2013.
- [151] A. Kornberg, "Abundant Microbial Inorganic Polyphosphate, Poly P Kinase Are Underappreciated," *Microbe Mag.*, vol. 3, pp. 119–123, Mar. 2008.
- [152] R. Docampo and S. N. J. Moreno, "Acidocalcisomes," *Cell Calcium*, vol. 50, no. 2, pp. 113–119, 2011.
- [153] L. Wang, C. D. Fraley, J. Faridi, A. Kornberg, and R. A. Roth, "Inorganic polyphosphate stimulates mammalian TOR , a kinase involved in the proliferation of mammary cancer cells," *PNAS*, vol. 100, no. 20, pp. 11249–11254, 2003.
- [154] S. A. Smith, N. J. Mutch, D. Baskar, P. Rohloff, R. Docampo, and J. H. Morrissey, "Polyphosphate modulates blood coagulation and fibrinolysis," *Proc. Natl. Acad. Sci. U. S. A.*, vol. 103, no. 4, p. 903 LP – 908, Jan. 2006.
- [155] F. Müller, N. J. Mutch, W. A. Schenk, S. A. Smith, L. Esterl, H. M. Spronk, S. Schmidbauer, W. A. Gahl, J. H. Morrissey, and T. Renné, "Platelet polyphosphates are proinflammatory and procoagulant mediators in vivo," *Cell*, vol. 139, no. 6, pp. 1143–1156, Dec. 2009.
- [156] S. H. Choi, S. A. Smith, and J. H. Morrissey, "Polyphosphate is a cofactor for the activation of factor XI by thrombin," *Blood*, vol. 118, no. 26, pp. 6963–6970, Dec. 2011.
- [157] L. Hernandez-Ruiz, C. Castro, F. A. Ruiz, and U. Puerta, "Inorganic polyphosphate and specific induction of apoptosis in human plasma cells," *Haematologica*, vol. 91, no. 9, pp. 1180–1186, 2006.
- [158] B. Hoac, T. Kiffer-Moreira, J. L. Millán, and M. D. McKee, "Polyphosphates inhibit extracellular matrix mineralization in MC3T3-E1 osteoblast cultures," *Bone*, vol. 53, no. 2, pp. 478–486, 2013.
- [159] S. Omelon and M. Grynpas, "Polyphosphates Affect Biological Apatite Nucleation," *Cells Tissues Organs*, vol. 194, no. 2–4, pp. 171–175, 2011.
- [160] D. Hamburger, E. Rezzonico, J. M. Petétot, C. Somerville, and Y. Poirier, "Identification and Characterization of the Arabidopsis PHO1 Gene Involved in Phosphate Loading to the Xylem," *Plant Cell*, vol. 14, no. April, pp. 889–902, 2002.
- [161] B. H. Spain, D. Koo, M. Ramakrishnan, B. Dzudzor, and J. Colicelli, "Truncated Forms of a Novel Yeast Protein Suppress the Lethality of a G Protein  $\alpha$  Subunit Deficiency by Interacting with the  $\beta$  Subunit," *J. Biol. Chem.*, vol. 270, no. 43, pp. 25435–25444, 1995.
- [162] F. Liu, Z. Wang, H. Ren, C. Shen, Y. Li, H. Ling, C. Wu, and X. Lian, "OsSPX1 suppresses the function of OsPHR2 in the regulation of expression of OsPT2 and phosphate homeostasis in shoots of rice," *Plant J.*, vol. 62, no. 3, pp. 508–517, 2010.
- [163] U. López-Sánchez, S. Tury, G. Nicolas, M. S. Wilson, S. Jurici, X. Ayrignac, V. Courgnaud, A. Saiardi, M. Sitbon, and J.-L. Battini, "Interplay between PFBC-associated SLC20A2 and XPR1 phosphate transporters requires inositol polyphosphates for control of cellular phosphate homeostasis," *J. Biol. Chem.*, vol. 295, no. 28, pp. 9366–9378, 2020.
- [164] U. López-Sánchez, G. Nicolas, 1, A.-C. Richard, 2, D. Maltête, M. Charif, X. Ayrignac, C. Goizet, J. Touhami, G. Labesse, J.-L. Battini, and S. Marc, "Characterization of XPR1 / SLC53A1 variants located outside of the SPX domain in patients with primary familial brain calcification," *Sci. Rep.*, vol. 9, p. 6776, 2019.
- [165] B. Xu, I. Ionita-laza, J. L. Roos, B. Boone, S. Woodrick, S. Levy, J. A. Gogos, and M. Karayiorgou, "De novo gene mutations highlight patterns of genetic and neural complexity in schizophrenia Bin," *Nat Genet.*, vol. 44, no. 12, pp. 1365–1369, 2013.

- [166] G. Nicolas, C. Pottier, C. Charbonnier, L. Guyant-mare, P. Labauge, X. Ayrignac, L. Defebvre, I. Le Ber, O. Martinaud, R. Lefaucheur, O. Guillin, D. Wallon, B. Chaumette, P. Rondepierre, N. Derache, T. Lebouvier, O. Rouaud, S. Jurici, M. Sauve, A. Rovelet-lecrux, T. Frebourg, C. Thauvin-robinet, and D. Campion, "Phenotypic spectrum of probable and genetically-confirmed idiopathic basal ganglia calcification," *Brain*, vol. 136, no. Pt 11, pp. 3395–3407, 2013.
- [167] M. Anheim, U. López-sánchez, D. Giovannini, J. Touhami, N. Ludovic, G. Rudolf, T. Frébourg, D. Hannequin, M. Anheim, U. López-sánchez, D. Giovannini, A. Richard, J. Touhami, A. Richard, and G. Rudolf, "XPR1 mutations are a rare cause of primary familial brain calcification," *J Neurol*, vol. 263, no. 8, pp. 1559–1564, 2019.
- [168] X. Yao, M. Zhao, C. Wang, X. Guo, H. Su, E. Dong, H. Chen, J. Lai, Y. Liu, N. Wang, and W. Chen, "Analysis of gene expression and functional characterization of XPR1: a pathogenic gene for primary familial brain calcification," *Cell Tissue Res*, vol. 370, no. 2, pp. 267–273, 2017.
- [169] S. Al-Khodor, C. T. Price, A. Kalia, and Y. Abu Kwaik, "Functional diversity of ankyrin repeats in microbial proteins," *Trends Microbiol.*, vol. 18, no. 3, p. 132–139, Mar. 2010.

## Background to NMR

NMR is a versatile technique for the characterization of protein structures at atomic resolution. It is reporting on proteins' residue-specific local conformations and dynamics covering wide time-scales. While x-ray crystallography and cryo-EM study largely rigid proteins and protein complexes, NMR can characterize dynamic protein or protein-protein conformation(s) under various conditions allowing a better understanding of their biological function. Nowadays, improved NMR spectroscopy hardware – cryogenic NMR probes and magnets reaching up to 1.2 GHz proton Larmor frequency-, optimized isotope-labeled protein samples, fast acquisition of NMR spectra by improved NMR pulse sequences [1], [2] suppressing unwanted water signals [3] or using optimized shape elements [4], [5] as well as sampling data non-uniformly [6], [7] enables studies of protein complexes up to a megadalton [8], [9].

## General principles behind NMR

Many atoms have a nuclear spin that acts like a magnet and can orient parallel to an external magnetic field ( $B_0$ ). Protein NMR makes use of spin  $\frac{1}{2}$  isotopes e.g.,  $^1\text{H}$ ,  $^{13}\text{C}$  and  $^{15}\text{N}$ . While  $^1\text{H}$  is the predominant isotope (99.98%),  $^{13}\text{C}$  and  $^{15}\text{N}$  isotopes have a natural abundance of around 1.11% or 0.36%, respectively. The application of a static  $B_0$  magnetic field causes the spins to align and rotate with a precession frequency called the Larmor frequency around the  $B_0$  field (see Fig. 1). The induced bulk magnetization ( $M_z$ ) is proportional to the population difference of  $\alpha$ -spins - a spin  $+1/2$  - and  $\beta$ -spins that represent spin  $-1/2$ . The two states are populated according to the Boltzmann distribution (1) :

$$\frac{N(\alpha)}{N(\beta)} = e^{2\mu B_0/k_B T} \approx \frac{1.00001}{1} \quad (1)$$

with number of states ( $N$ ), magnetic moment ( $\mu$ ), Boltzmann constant ( $k_B$ ) and temperature ( $T$ ). The population difference is 1 in 100'000 resulting in a

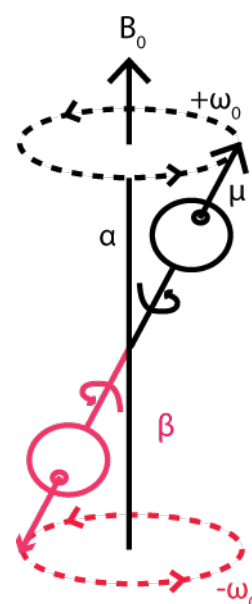


Fig. 1: The precession movement of two nuclear spins in the  $\alpha$  and  $\beta$  state.

generally low sensitivity for NMR methods. High protein concentrations ( $\mu\text{M}$  to  $\text{mM}$ ), summation of multiple scans and high magnetic field strengths are beneficial for obtaining a sufficiently large signal-to-noise ratio.

In a static magnetic  $B_0$  field the application of a spin-dependent Larmor frequency ( $\omega_0$ ), corresponding to an energy difference  $\Delta E$  causes spins to transition between the  $\alpha$ - and  $\beta$ -state (Fig. 2) resulting in a non-equilibrium state.

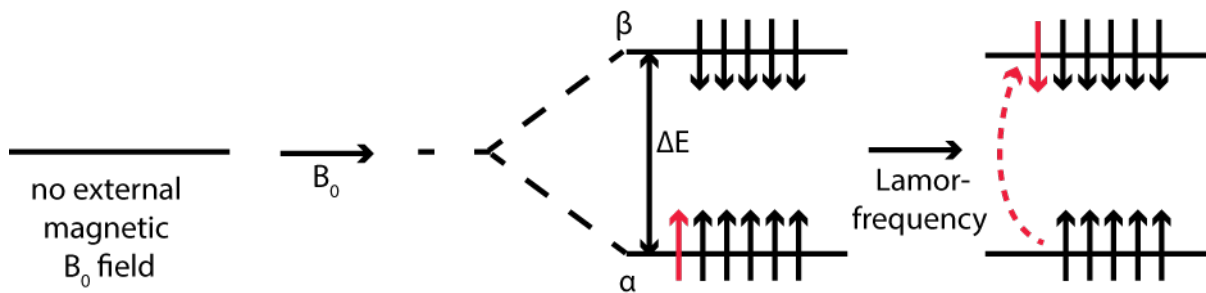


Fig. 2: The reorientation of  $\alpha$ - and  $\beta$ -spins after applying a spin-dependent Larmor frequency.

The energy difference  $\Delta E$  can be calculated using equation 2,

$$\Delta E = \hbar \cdot \omega_0 = \hbar \cdot \gamma \cdot B_0 \quad (2)$$

where  $\hbar$  is Plancks constant,  $\gamma$  is the gyromagnetic ratio of the specific nuclei and  $B_0$  is the magnetic field induction in tesla (T).

In practice, NMR spectroscopy experiments are performed in such a way that radiofrequency pulses with the nuclear spin specific Larmor frequency are applied transversally to the external magnetic field. A  $90^\circ$  pulse along the x axis causes the bulk magnetization initially aligned along the z -axis to completely rotate to the -y axis. At point,  $M_{xy}(0)$ , the phases of all spins are coherently aligned in the transverse plane. The spin-spin and spin-lattice interferences affect the coherent  $M_{xy}$  magnetization causing it to dephase over time. This is described by a time-dependent exponential dephasing named transverse relaxation  $T_2$  (eq. 3).

$$M_{xy}(t) = M_{xy}(0)e^{-t/T_2} \quad (3)$$

The  $T_2$  driven decay of the free-induction decay (FID) represents itself in the width of NMR peaks after being transformed to a frequency domain by Fourier transformation (see Fig. 3).

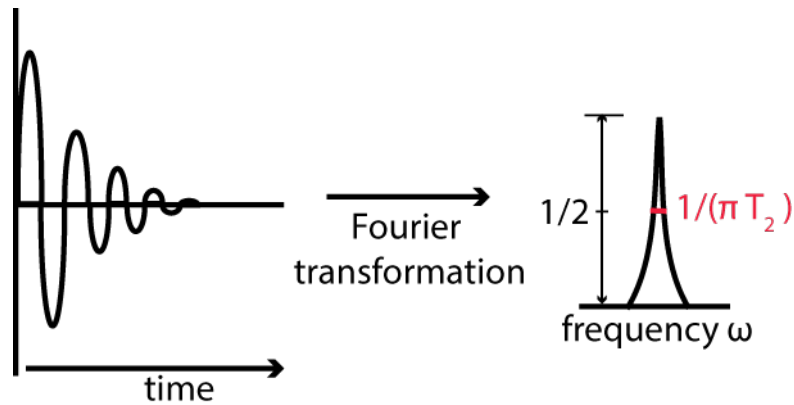


Fig. 3: Transformation of a time- to a frequency domain.

The width  $\Delta\omega$  of a NMR signal at half of the height is inversely proportional to  $T_2$  (eq. 4).

$$\Delta\omega = \frac{1}{\pi T_2} \quad (4)$$

The  $T_2$  relaxation of a particular spin arises due to other surrounding spins and their direct dipole-dipole interactions. The higher the density of these spins in the local environment, the higher the probability of the spin to “relax” faster. In addition, a low molecular reorientation rate increases  $T_2$  relaxation. This is the case for large proteins or molecules in highly viscous liquids. A fast  $T_2$  relaxation is reflected in a broad peak width leading to a decrease in resolution and signal-to-noise ratio. The use of fully deuterated (perdeuterated) protein helps to dilute the density of proton nuclear spins and hence causing a slower  $T_2$  relaxation.

The environment also interferes with spins leading to a longitudinal  $T_1$  relaxation. It is characterized by an energy exchange with the lattice (the environment) triggered by fluctuating magnetic fields around the spins caused by dipolar coupling and molecular tumbling. If this exchange energy is matching the Larmor frequency, the reoriented

spins can return back to their thermal equilibrium following the equation described in (5). The  $T_1$  relaxation time defines the rate at which repeated scans in an NMR experiment can be performed.

$$M_z(t) = M_z(0)[1 - e^{-t/T_1}] \quad (5)$$

### Chemical shift

The effective magnetic field a nuclear spin experiences is influenced by its surrounding and proximity to other nuclei and electrons. This leads to a perturbation in the Larmor frequency of the nuclear spin creating a chemical shift. Hence, a chemical shift is a mirror of the local chemical environment.

The nuclear spin of the proton can be influenced by -inductive (“-I”) effect and -mesomeric (“-M”) effect leading to deshielding of the nuclear spin. On the other hand, +I and +M-effects shield the respective proton. The I-effect is characterized by an unequal distribution of an electron that is shared in the bond of two atoms leading to a permanent dipole. Halogens are withdrawing electron density having a -I effect whereas alkyl groups are electron donors termed by +I-effect. Also functional groups containing  $\pi$ -electrons can in similar fashion influence the electron density and are referred to as having a - or + mesomeric (M) effect. A shielding of a proton is displayed in the Larmor frequency of the respective nuclear spin being shifted upfield, whereas a deshielded proton has the Larmor frequency shifted downfield (Fig. 4).

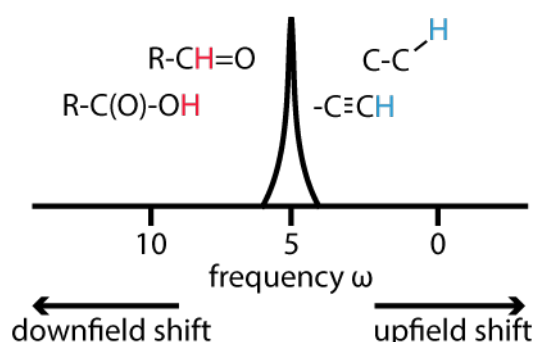


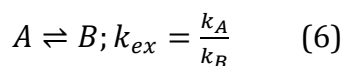
Fig. 4: Frequency shift caused by I- and M- effects. Blue protons are shielded while red protons are deshielded.

## Scalar coupling

Scalar coupling is also referred to as a  $J$ -coupling, it defines a distance and orientation-dependent interaction between two nuclear spins that is mediated through one or more bonds. The number of coupling neighbors is reflected in the multiplicity of the splitted peaks separated by their respective  $J$ -couplings. Depending on the geometry and the nuclei involved  $J$ -couplings can reach from a few tenths of Hertz up to several hundred Hertz for  $^1J$  couplings. The scalar couplings are used in NMR spectroscopy to correlate different nuclear spins in two or more-dimensional NMR experiments.

## Chemical exchange

One nuclear spin can experience two or more exchanging chemical local environments arising due to a conformational change e.g., a bond rotation or a kinetic change e.g., chemical reaction. This is reflected in a change of e.g., chemical shift, scalar coupling or  $T_2$  relaxation rate. This chemical exchange rate ( $k_{ex}$ ) between two states, A and B, is described by equation 6, where  $k_A$  is the forwards reaction rate and  $k_B$  the back-reaction rate.



In the NMR spectrum, these two states can be observed as two different populations having different chemical shift,  $\delta_A$  and  $\delta_B$  if their resonance frequency difference ( $\Delta\omega$ ) is significantly larger than the chemical exchange rate. In this case the molecule is in slow exchange compared to the NMR timescale and two signals are observed (Fig. 5). An intermediate exchange is characterized by  $\Delta\omega$  and  $k_{ex}$  being of similar magnitude resulting in an extremely broadened signal, that most often is broadened beyond detection. A fast exchange occurs when  $k_{ex}$  is much larger than  $\Delta\omega$ . The result is a single sharp peak located in the middle of both  $\delta_A$  and  $\delta_B$  if states A and B are equally populated. The chemical exchange rate can be shifted by a change in temperature causing a spin to transition from the unfavorable intermediate exchange regime to the either slow or fast exchange regime where it can be more easily detected. For a given temperature increasing the magnetic field strength increases the chemical shift separation  $\Delta\omega$  in Hertz thus changing the temperature at which extreme broadening is

observed. Both strategies are highly valuable to obtain residue-specific information of a population being in the intermediate exchange.

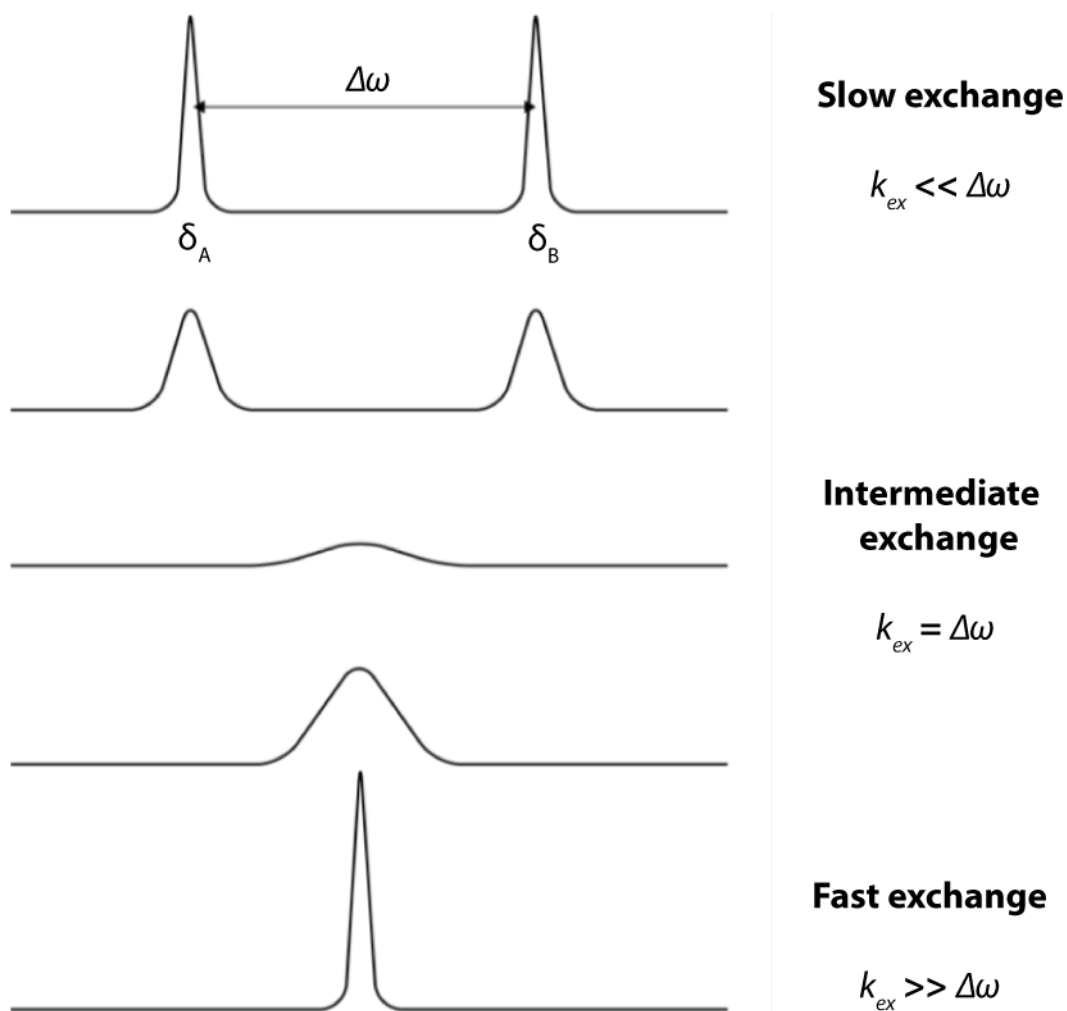


Fig. 5: Chemical exchange regimes of a nuclear spin at different temperatures or magnetic field strengths.

## Two-dimensional (2D) NMR spectroscopy

A 2D fingerprint spectrum serves as a basis for most NMR studies of protein structures or protein dynamics. It is mostly correlating chemical shifts of two different nuclei (heteronuclear) via their scalar coupling. A [<sup>15</sup>N, <sup>1</sup>H]-HSCQ (heteronuclear single quantum correlation) spectrum displays the amides of the protein [10]. It is

correlating proton  $H^N$  to nitrogen N from the backbone as well as the amides present in the side chain of arginine, lysine and tryptophane. Proline is the only amino acid with no amide proton and hence has no signals in such a 2D spectrum.

The NMR pulse sequence is composed of several blocks like shown in Fig. 6. A preparation block that ensures the re-establishment of spins' thermal equilibrium. An INEPT block that transfers magnetization from a proton to a nitrogen spin via their  $^1J$  coupling for correlating the two spins. The following evolution period  $t_1$  frequency labels the chemical shift of the coupling nitrogen. During this period the connected protons are decoupled. A second INEPT (back-INEPT) transfers the magnetization back from nitrogen to the connected proton. Finally the chemical shifts of the protons are detected directly by  $t_2$  evolution while nitrogen atoms are decoupled. A decoupled HSQC for a large protein (see NMR section in Fig. 7, middle).

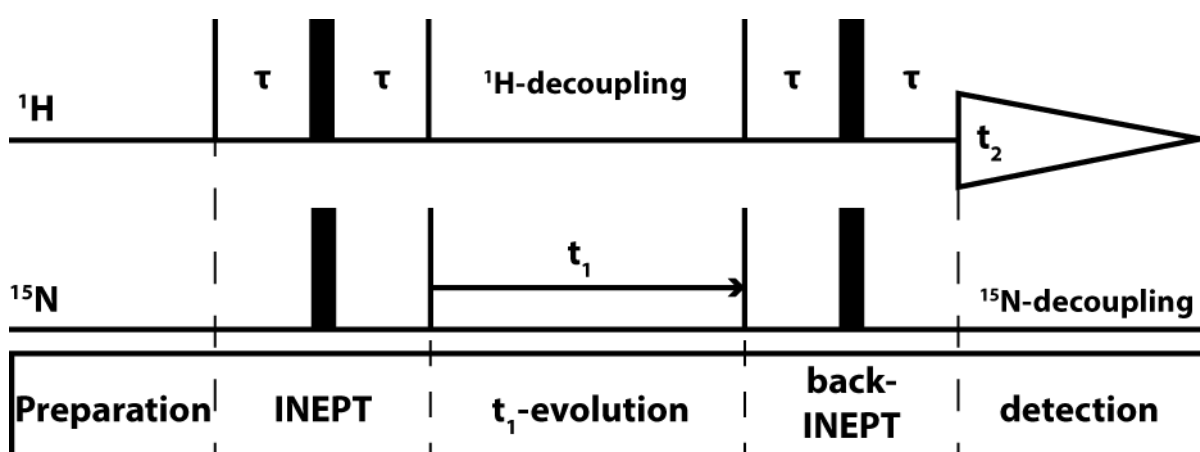


**Fig. 6: Simplified pulse sequence for 2D- $^{15}\text{N}$ , $^1\text{H}$ -HSQC.** 90° elements are shown as vertical lines and 180° elements as thick black boxes. Time delay  $\tau$  is  $1/(4J_{\text{HN}})$ . Adapted from [11].

The HSQC experiment is most useful for molecules below 20 kDa whereas above this size the quality of the HSQC spectrum deteriorates. A HSQC recorded with no decoupling elements gives a rise to four peaks separated by  $J_{\text{HN}}$  due to the  $J$ -evolution (see Fig 7, left). Two of them are homonuclear diagonal peaks and two of them are [ $^{15}\text{N}$ ,  $^1\text{H}$ ]-correlated crosspeaks.

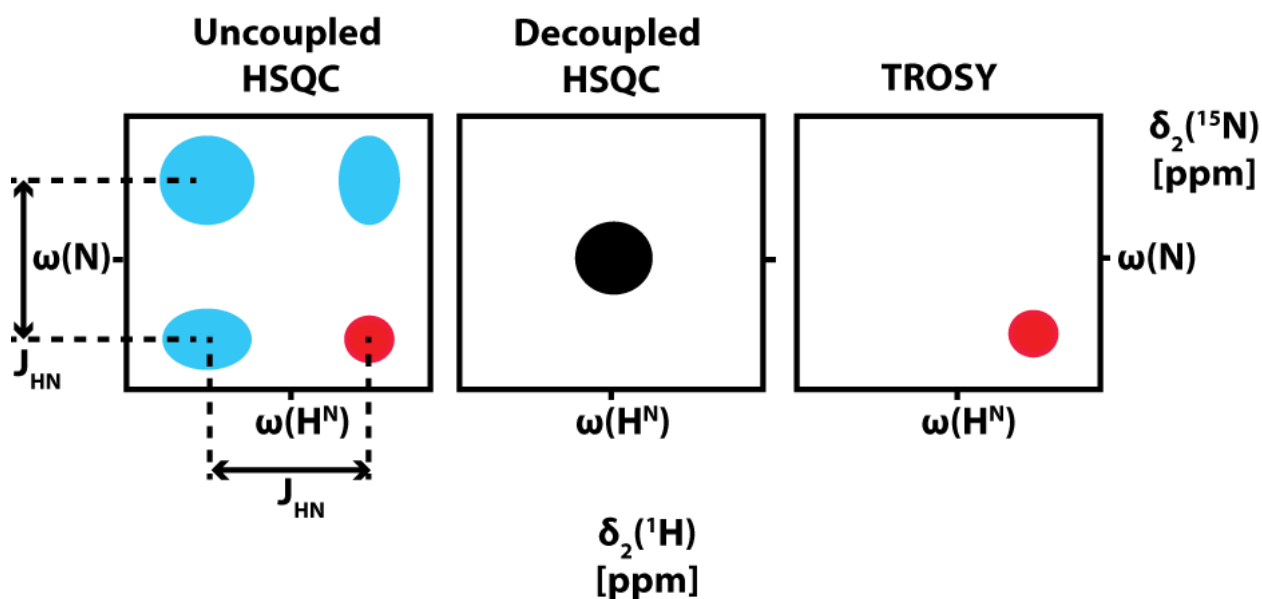


**Fig. 7:**  $^{15}\text{N}$ - $^1\text{H}$  peaks from different type of  $^{15}\text{N}$ - $^1\text{H}$ -correlation spectra. The scalar coupling,  $J_{\text{HN}}$ , of uncoupled spectrum is indicated in one of the NMR section. Adapted from [11].

For larger molecules, these peaks have different relaxation rates mirrored in the peak line widths. These arise due to the constructive or destructive interferences between dipole-dipole (DD) interaction and chemical shift anisotropy (CSA) effect. CSA is the chemical shift difference between an isotropic and an anisotropic field contributing to spin relaxation. The most narrow  $^{15}\text{N}$ ,  $^1\text{H}$ -correlated crosspeak contains a destructive interference of field-independent DD and field dependent CSA ( $\sim B_0^2$ ) that is comparable to CSA at high magnetic fields. The consequence is that it has a slower relaxation. Transverse-relaxation optimized spectroscopy (TROSY) is designed to exploit this destructive interference by only selecting the most narrow component [1] (see Fig. 7, right).

## Backbone experiments

Different standard triple-resonance NMR experiments can be used to determine residue-specific intra- and intermolecular connections. By using a set of multidimensional NMR spectra of uniformly labeled protein constructs,  $[\text{U-}^{15}\text{N}, ^{13}\text{C}]$  or  $[\text{U-}^2\text{H}, ^{15}\text{N}, ^{13}\text{C}]$ , the assignment of the  $^{15}\text{N}$ ,  $^1\text{H}$ -amide moieties in the given 2D fingerprint spectrum can be established [2], [12]. The strategies used behind the assignments of HNCACB, HNCOC and HN(CA)CO are depicted in the Fig. 8.

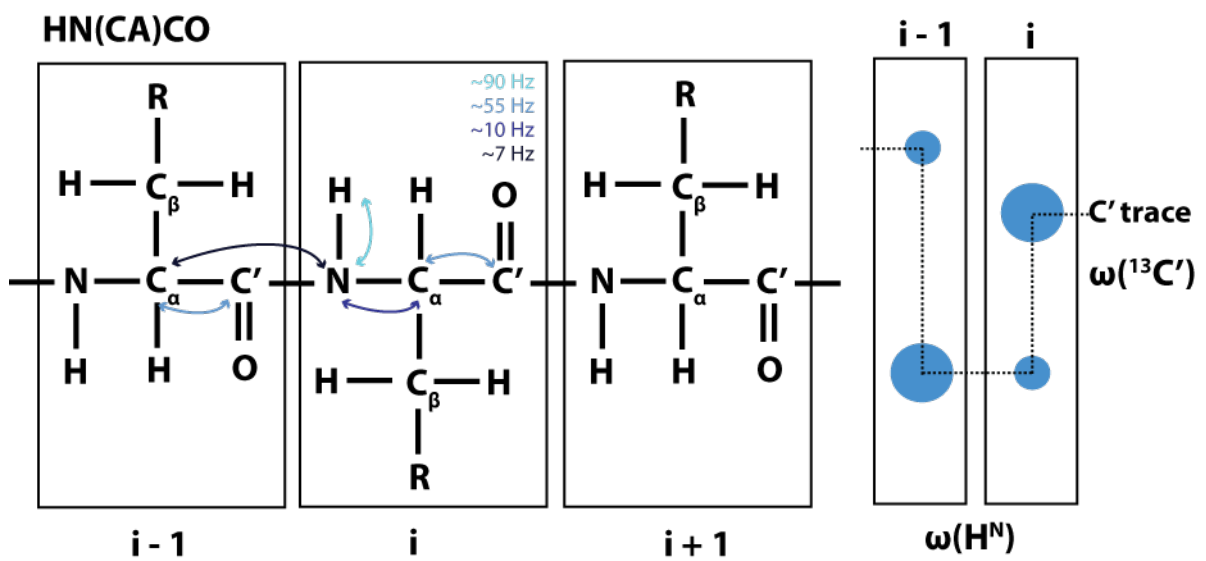
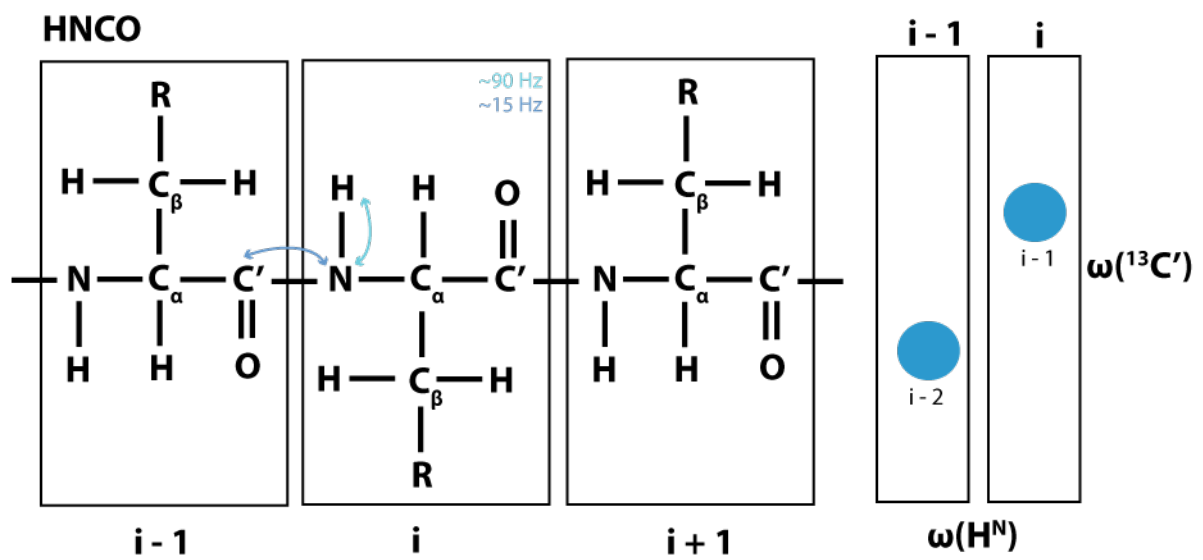
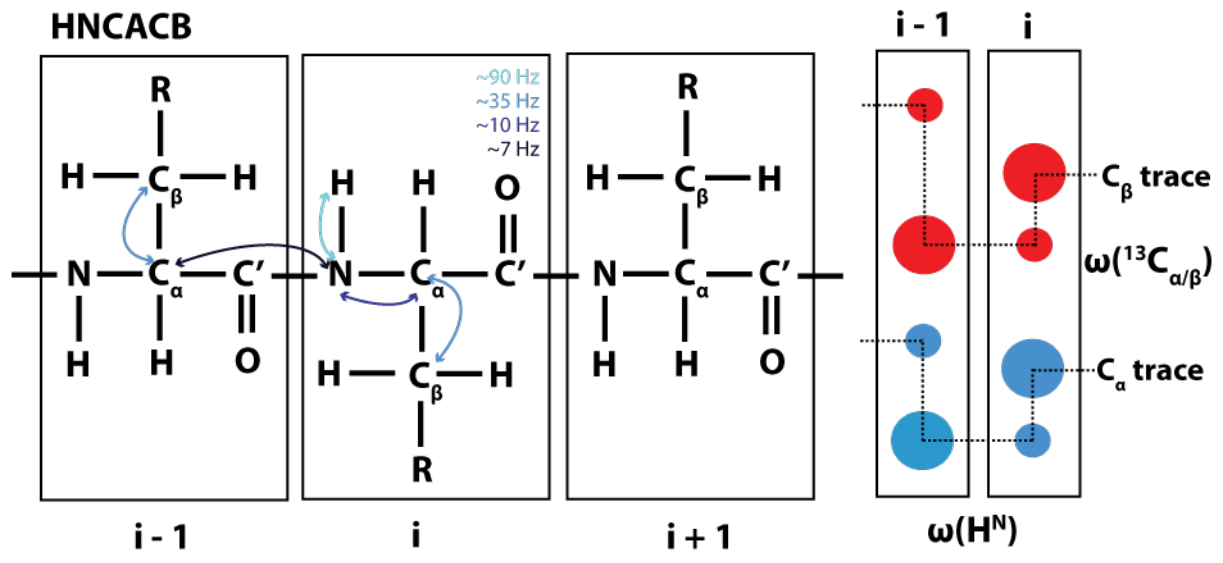


**Fig. 8: Magnetization transfer via different scalar couplings between nuclei and the assignment strategy.** The scalar coupling used are indicated in the magnetization scheme. For the assignment strategy the different carbon traces,  $C_\alpha$ ,  $C_\beta$  and  $C'$ , related to neighboring information were used. The color is indicating positive (blue) and negative (red) peaks. The dashed black lines correlate the neighboring peaks.

## Secondary chemical shifts

The analysis of secondary chemical shifts helps to identify secondary structure elements in proteins. The experimentally determined  $^{13}C_\alpha$  and  $^{13}C_\beta$  of every backbone residue are compared to so-called random coil (rc) chemical shifts [13] forming secondary chemical shift values (SS) according to equation 7.

$$SS = \Delta\Delta\delta = \Delta\delta_{^{13}C_\alpha} (\delta_{^{13}C_\alpha exp} - \delta_{^{13}C_\alpha rc}) - \Delta\delta_{^{13}C_\beta} (\delta_{^{13}C_\beta exp} - \delta_{^{13}C_\beta rc}) \quad (7)$$

Random coil chemical shifts are typical  $^{13}C_\alpha$  and  $^{13}C_\beta$  shifts found in the disordered regions of proteins. Protein residue specific  $^{13}C_\alpha$  and  $^{13}C_\beta$  shifts close to random coil chemical shifts are thus indicative of loop regions. In  $\alpha$ -helical structures the  $^{13}C_\alpha$  chemical shifts are shifted downfield, whereas  $^{13}C_\alpha$  shifts of  $\beta$ -sheet structures are shifted upfield [14]. Therefore, a stretches of positive or negative (SS) values allows an identification of a secondary structure element in the protein sequence. A positive stretch of SS values represents a helical region whereas a negative stretch depicts a  $\beta$ -sheet element. The examination of the example depicted in Fig. 9 shows two secondary structure elements, one  $\alpha$ -helix and one  $\beta$ -sheet.

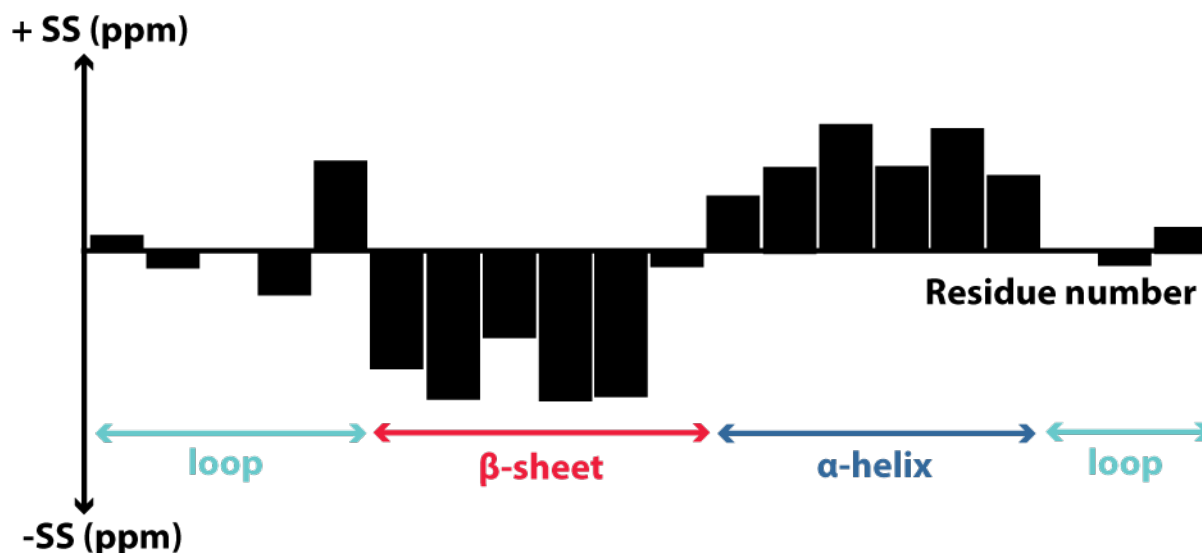


**Fig. 9: Secondary chemical shift plot of an imaginary protein.** The stretches of positive or negative SS values display secondary structure elements annotated by an arrow.

## Chemical shift differences

A ligand binding event causes chemical shifts perturbations (CSP) on the amide moieties that get influenced by the binding. For the peaks that are undergoing fast chemical exchange upon ligand binding shown in Fig. 10, the ligand can be titrated to the labeled protein till it reaches its saturation state. This is displayed by a static amide peak that is not experiencing any further CSP upon ongoing ligand titration.

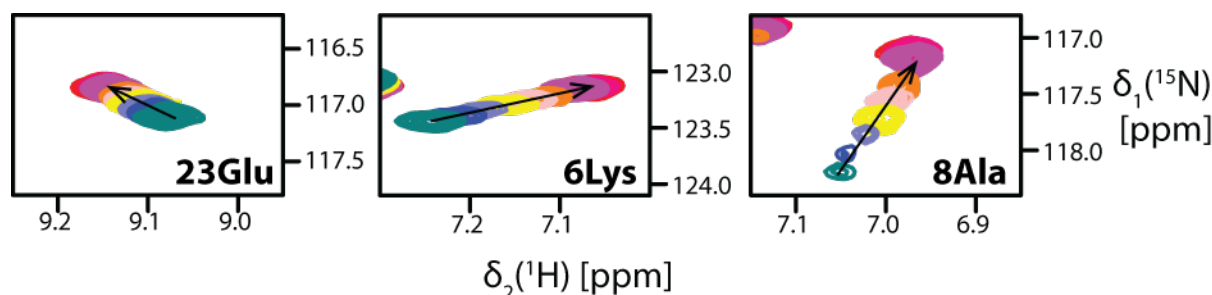


**Fig. 10:  $^{15}\text{N}$ - $^1\text{H}$  amide moieties of a particular SPX2 construct experiencing the fast chemical exchange.** Different molar ratios of protein to ligand are indicated by different colors and the arrow displays the chemical shift perturbation direction upon ligand titration.

The last chemical shift represents the saturated holo-state of the protein which can be compared to the initial reference state to evaluate the CSP (eq. 8). A plot of the residue specific CSP on a structural model maps the binding pocket of the protein.

$$CSP = \sqrt{(\Delta\delta_2)^2 + (\Delta\delta_1/5)^2} \quad (8)$$

Two differently long protein constructs can be compared in the same way as a ligand binding event. Areas displaying large CSP, due to the lacking protein regions, indicate the localization of these deleted areas to be mapped there. However, cross-validation with other methods is needed to exclude allosteric effects.

### H/D – exchange spectroscopy

H/D – exchange spectroscopy is an easy method to elucidate protein cores. These are well protected from the solvent while the protein surface is solvent accessible (see Fig. 11A)

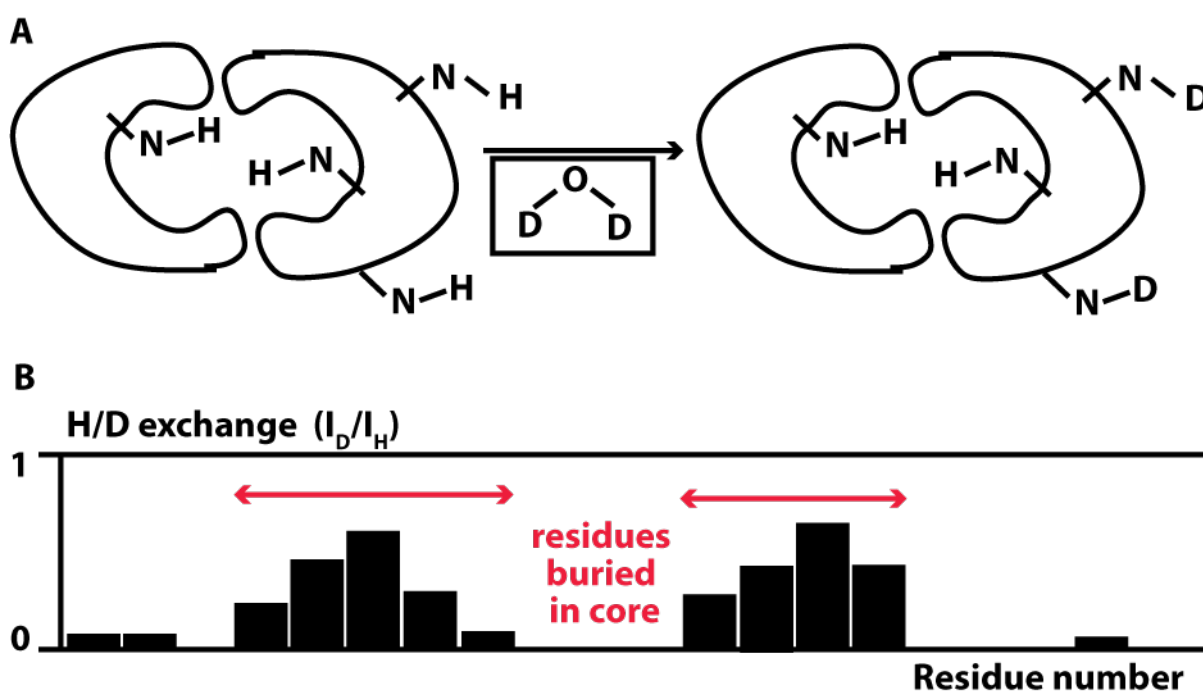


**Fig. 11: H/D-exchange spectroscopy.** (A) Cartoon of a deuterium incorporation depending on solvent accessibility. (B) A H/D exchange plot of an imaginary protein indicating regions buried in the core.

The solvent exchange is monitored by the rate of deuterium incorporation. It can be measured in different ways; mass spectrometry, neutron crystallography and NMR spectroscopy reviewed in [15]. In NMR spectroscopy, the intensities of the peaks in a 2D fingerprint spectrum measured in H<sub>2</sub>O ( $I_H$ ) and D<sub>2</sub>O ( $I_D$ ) are compared. An example is shown in Fig. 11B. The exchange of proton to deuterium reduces the intensity of the amide peaks as the residue specific <sup>1</sup>H spins get diluted.

## Residual dipolar coupling (RDC)

Dipolar couplings  $D$  are a through space interaction of two spins  $i$  and  $j$ . The magnitude depends on their spatial distance and relative orientation (eq. 9).

$$D_{ij} = -\frac{\gamma_i \gamma_j \mu_0 \hbar}{8\pi^3 r_{ij}^3} \langle 3 \frac{\cos^2 \theta - 1}{2} \rangle \quad (9)$$

Where,  $r_{ij}$  is the effective distance,  $\theta$  an effective angle and  $\mu_0$  is the permittivity of space. In an isotropic solution, dipolar couplings are averaged to zero due to Brownian motion. However, if not all orientations of a molecule are equally likely dipolar couplings are not averaged to zero and are observable as orientation dependent residual dipolar couplings (RDCs). Additives like filamentous phages [16], [17], bicelles [18], [19] or polyacrylamide gels [20], [21] are creating an anisotropy causing a protein to have a preferential orientation. This results in a macroscopic observation of residue specific RDC values. The maximum RDC value will be reached for an orientation of the internuclear vector along the z-axis of the alignment tensor. The alignment tensor ( $A_{xx}$ ,  $A_{yy}$ ,  $A_{zz}$ ) describes the magnitude and direction of the alignment for three orthogonal orientations of the protein (see Fig. 12A).

Recording a TROSY and a semi-TROSY spectrum of the protein in a isotropic („Ref“) and an anisotropic phage („pf1“) medium allows the determination of residue-specific RDCs. The scalar coupling ( $J$ ) measured between the TROSY and semi-TROSY peak in an anisotropic medium is subtracted from the scalar coupling measured in an isotropic medium (see Fig. 12B). The RDC values of a single alignment data set allow the

identification of the relative orientation of secondary structure elements in relation to the alignment medium. An example of a RDC plot is shown in Fig. 11C.

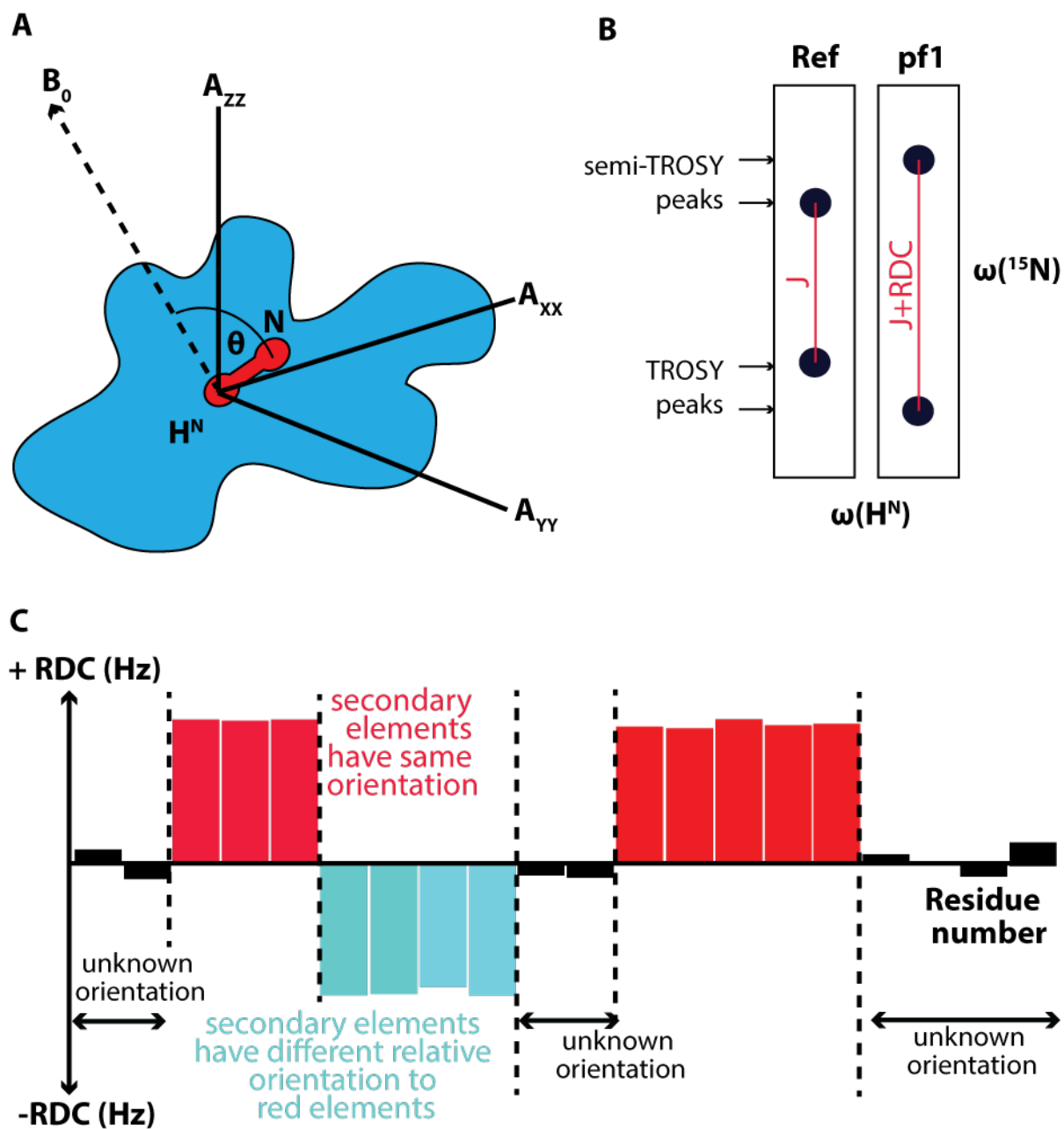


**Fig. 12: The principle behind RDC.** (A) Schematic representation of amide vector in  $\theta$ -dependence aligned along  $B_0$  and alignment tensors  $A_{xx}$ ,  $A_{yy}$  and  $A_{zz}$ . Adapted from [22]. (B) Stripes from an amide moiety aligned in phage, pf1, and in an isotropic medium, Ref, with both TROSY and semi-TROSY peaks. (C) RDC plot indicating in red the secondary elements with same orientation and in blue with a different orientation. The unknown orientations are indicated by arrows.

## Protein dynamics

The backbone amides of the protein can be used to evaluate the dynamics of the protein on the pico- to nanoseconds timescale by the help of the internuclear vector of amide residues,  $^1\text{H}^{\text{N}}\text{-}^{15}\text{N}$ . Although its dipolar interaction averages to zero in an isotropic solution because of the molecular tumbling, the time-dependent relaxation of each amide can vary. The amide vectors experience fluctuations of the local magnetic fields that are sensitive to the internal motions. Hence from  $T_1$ ,  $T_2$  and hetNOE data residue-specific dynamic properties can be derived.  $T_1$  relaxation times can be determined by a series of inversion recovery experiments whereas  $T_2$  relaxation times are obtained from a series of spin echo experiments. The initial bulk magnetization  $M_z$  flipped to a non-equilibrium or the decay of transversal  $M_{xy}$  magnetization can be monitored over time by variable increasing relaxation delays. Exponential fitting of the residual signal intensity vs the relaxation delay provides access to the respective relaxation time (see Fig. 13).

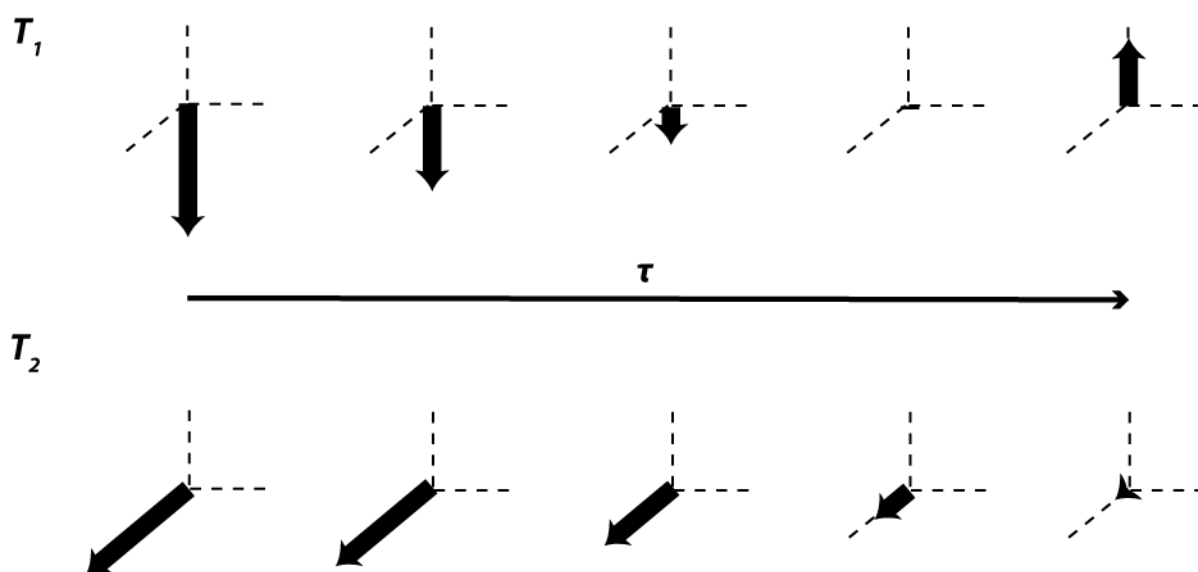


**Fig. 13: Schematic representation of the backbone amide relaxation experiments.** The relaxation delay  $\tau$  varies in the NMR experiment series. Adapted from [23].

The backbone  $^1\text{H}^{\text{N}}\text{-}^{15}\text{N}$  heteronuclear NOE experiment estimates the motion of individual amides. A decreased NOE value compared to the average indicates a local motion faster than the overall tumbling of the molecule corresponding to increased dynamics.

## References

- [1] K. Pervushin, R. Riek, G. Wider, and K. Wüthrich, "Attenuated T2 relaxation by mutual cancellation of dipole-dipole coupling and chemical shift anisotropy indicates an avenue to NMR structures of very large biological macromolecules in solution," *PNAS*, vol. 94, no. 11, pp. 12366–12371, 1997.
- [2] M. Salzmann, G. Wider, K. Pervushin, H. Senn, and K. Wüthrich, "TROSY-type Triple-Resonance Experiments for Sequential NMR Assignments of Large Proteins," *JACS*, vol. 121, no. 4, pp. 844–848, 1999.
- [3] S. Grzesiek and A. Bax, "The importance of not saturating water in protein NMR. Application to sensitivity enhancement and NOE measurements," *J. Am. Chem. Soc.*, vol. 115, no. 26, pp. 12593–12594, Dec. 1993.
- [4] P. Schanda, E. Kupce, and B. Brutscher, "SOFAST-HMQC experiments for recording two-dimensional heteronuclear correlation spectra of proteins within a few seconds," *J. Biomol. NMR*, vol. 33, no. 4, p. 199–211, Dec. 2005.
- [5] N. Khaneja, T. Reiss, C. Kehlet, T. Schulte-Herbrüggen, and S. J. Glaser, "Optimal control of coupled spin dynamics: design of NMR pulse sequences by gradient ascent algorithms," *J. Magn. Reson.*, vol. 172, no. 2, pp. 296–305, 2005.
- [6] F. Delaglio, G. S. Walker, K. A. Farley, R. Sharma, J. C. Hoch, L. W. Arbogast, R. G. Brinson, and J. P. Marino, "Non-Uniform Sampling for All: More NMR Spectral Quality, Less Measurement Time," *Am. Pharm. Rev.*, vol. 20, no. 4, p. 339681, 2017.
- [7] S. G. Hyberts, S. A. Robson, and G. Wagner, "Exploring signal-to-noise ratio and sensitivity in non-uniformly sampled multi-dimensional NMR spectra," *J. Biomol. NMR*, vol. 55, no. 2, pp. 167–178, 2013.
- [8] J. Fiaux, E. B. Bertelsen, A. L. Horwich, and K. Wüthrich, "NMR analysis of a 900K GroEL GroES complex," *Nature*, vol. 418, no. 6894, p. 207–211, Jul. 2002.
- [9] R. Sprangers and L. E. Kay, "Quantitative dynamics and binding studies of the 20S proteasome by NMR," *Nature*, vol. 445, no. 7128, pp. 618–622, 2007.
- [10] T. J. Norwood, J. Boyd, J. E. Heritage, N. Soffe, and I. D. Campbell, "Comparison of techniques for 1H-detected heteronuclear 1H-15N Spectroscopy," *J. Magn. Reson.*, vol. 87, no. 3, pp. 488–501, 1990.
- [11] G. Wider and K. Wüthrich, "NMR spectroscopy of large molecules and multimolecular assemblies in solution," *Curr. Opin. Struct. Biol.*, vol. 9, no. 5, pp. 594–601, 1999.
- [12] M. Sattler, J. Schleucher, and C. Griesinger, "Heteronuclear multidimensional NMR experiments for the structure determination of proteins in solution employing pulsed field gradients," *Prog. Nucl. Magn. Reson. Spectrosc.*, vol. 34, no. 2, pp. 93–158, 1999.
- [13] D. S. Wishart, C. G. Bigam, A. Holm, R. S. Hodges, and B. D. Sykes, "1H, 13C and 15N random coil NMR chemical shifts of the common amino acids. I. Investigations of nearest-neighbor effects," *J. Biomol. NMR*, vol. 5, no. 1, pp. 67–81, 1995.
- [14] D. S. Wishart and B. D. B. T.-M. in E. Sykes, "[12] Chemical shifts as a tool for structure determination," in *Nuclear Magnetic Resonance, Part C*, vol. 239, Academic Press, 1994, pp. 363–392.
- [15] J. Claesen and T. Burzykowski, "Computational methods and challenges in hydrogen/deuterium exchange mass spectrometry," *Mass Spectrom. Rev.*, vol. 36, no. 5, pp. 649–667, Sep. 2017.
- [16] G. M. Clore, M. R. Starich, and A. M. Gronenborn, "Measurement of Residual Dipolar Couplings of Macromolecules Aligned in the Nematic Phase of a Colloidal Suspension of Rod-Shaped Viruses," *J. Am. Chem. Soc.*, vol. 120, no. 40, pp. 10571–10572, Oct. 1998.
- [17] M. R. Hansen, L. Mueller, and A. Pardi, "Tunable alignment of macromolecules by filamentous phage yields dipolar coupling interactions," *Nat. Struct. Biol.*, vol. 5, no. 12, pp. 1065–1074, 1998.

- [18] J. A. Losonczi and J. H. Prestegard, "Nuclear Magnetic Resonance Characterization of the Myristoylated, N-Terminal Fragment of ADP-Ribosylation Factor 1 in a Magnetically Oriented Membrane Array," *Biochemistry*, vol. 37, no. 2, pp. 706–716, Jan. 1998.
- [19] N. Tjandra and A. Bax, "Direct Measurement of Distances and Angles in Biomolecules by NMR in a Dilute Liquid Crystalline Medium," *Science*, vol. 278, no. 5340, p. 1111 LP – 1114, Nov. 1997.
- [20] H.-J. Sass, G. Musco, S. J. Stahl, P. T. Wingfield, and S. Grzesiek, "Solution NMR of proteins within polyacrylamide gels: Diffusional properties and residual alignment by mechanical stress or embedding of oriented purple membranes," *J. Biomol. NMR*, vol. 18, no. 4, pp. 303–309, 2000.
- [21] R. Tycko, F. J. Blanco, and Y. Ishii, "Alignment of Biopolymers in Strained Gels: A New Way To Create Detectable Dipole–Dipole Couplings in High-Resolution Biomolecular NMR," *J. Am. Chem. Soc.*, vol. 122, no. 38, pp. 9340–9341, Sep. 2000.
- [22] T. K. Karamanos, A. P. Kalverda, G. S. Thompson, and S. E. Radford, "Progress in Nuclear Magnetic Resonance Spectroscopy Mechanisms of amyloid formation revealed by solution NMR," *Prog. Nucl. Magn. Reson. Spectrosc.*, vol. 88–89, no. 8, pp. 86–104, 2015.
- [23] A. Mittermaier and L. E. Kay, "New Tools Provide New Insights in NMR Studies of Protein Dynamics," *Science*, vol. 312, no. 5771, pp. 224–229, 2006.

## **Regulation of an SPX – SPX domain interaction by inositol pyrophosphates**

Joka Pipercevic<sup>1</sup>, Bastian Kohl<sup>1\*</sup>, Thomas Müntener<sup>1</sup>, Elia Agustoni<sup>1</sup>, Véronique Comte-Miserez<sup>3</sup>, Dorothea Fiedler<sup>2</sup>, Andreas Mayer<sup>3</sup>, Sebastian Hiller<sup>1\*</sup>

<sup>1</sup>Biozentrum, University of Basel, 4056 Basel, Switzerland.

<sup>2</sup>Department of Chemical Biology, Leibniz-Forschungsinstitut für Molekulare Pharmakologie, 13125 Berlin, Germany

<sup>3</sup>Department of Biochemistry, University of Lausanne, Chemin des Boveresses 155, CP51 1066 Epalinges, Switzerland

\*Correspondence to: [bastian.kohl@unibas.ch](mailto:bastian.kohl@unibas.ch), [sebastian.hiller@unibas.ch](mailto:sebastian.hiller@unibas.ch)

**Keywords:** SPX, molecular mechanism of SPX, inositol pyrophosphate, polyphosphate, VTC complex, inhibitory effect, phosphate homeostasis

**Acknowledgments:** We thank Prof. Michael Hothorn for a SPX2 plasmid lacking  $\alpha$ -helix7. We thank also the technical support given by Timothy Sharpe from Biophysics Facility at University of Basel.

**Funding:** This project was supported by Swiss National Foundation Sinergia Grant (CRSII5\_170925) given to S.H, D. F and A.M. Fellowship for Excellence granted by Biozentrum belonging to University of Basel supported J.P.

**Author contributions:** J.P., B.K. and S.H conceptuated the framework. J.P designed plasmids, expressed and purified proteins, performed protein stability, NMR, cross-linking and MST experiments as well as analyzed them thereupon. B.K. and T.M. helped with few NMR set-ups. E. A. did bioinformatical analysis. V. C.-M. conducted *in-vitro* VTC activity assay. Inositol phosphate and pyrophosphates were obtained by D. F. The manuscript was written by J. P. All authors gave manuscript comments.

## **Abstract**

SPX domains of phosphate-responsive proteins regulate eukaryotic phosphate homeostasis by binding to inositol pyrophosphates. How SPX domains of diverse proteins function on a molecular level is elusive. Here we report that the SPX domain of vacuolar transporter chaperone 2 interacts with the SPX domain of vacuolar transporter chaperone 4 by an SPX-SPX interaction. The interaction involves the conserved  $\alpha$ -helix1 and a previously undescribed  $\alpha$ -helix7. Inositol pyrophosphates, inositol phosphate or specific amino-acid substitutions causing pseudo-activity in VTC complex, respectively, abrogated this interaction. The SPX domains of Vtc thus act as internal inhibitors of VTC polyphosphate generation and inositol pyrophosphates as molecular-assembly disruptors.

## **One-sentence summary**

Inositol pyrophosphates modulate  $P_i$  homeostasis in the VTC complex by liberation of an inhibitory SPX-SPX interaction.

## Introduction

The SPX (Syg1/Pho81/Xpr1) domain is present in phosphate ( $P_i$ ) importers,  $P_i$  exporters and in proteins involved in the storing and the depletion of  $P_i$  [1], [2]. So far, SPX domains have been found to regulate diverse  $P_i$ -related functions. SPX has been shown to negatively regulate the  $P_i$ -uptake rate of low-affinity  $P_i$  transporters in yeast [3], to have an inhibitory effect on Pho81, thus preventing  $P_i$ -responsive signaling (PHO) pathway activation [4], [5] and to inhibit  $P_i$ -starvation response (PSR) transcription factor [6]–[10]. Inositol pyrophosphates were found to bind directly to SPX and influence the function of  $P_i$ -responsive proteins [11]. The function of yeast Pho81 as inhibitor of kinase activity repressing PHO pathway is regulated by 1-diphospho-inositol tetrakisphosphate, 1-IP7 [12], [13], whereas  $P_i$ -efflux [14] of human SPX-containing Xpr1 is stimulated by 1,5-bis-diphospho-inositol tetrakisphosphate, 1,5-IP8 [15]. *In vitro*, the vacuolar  $P_i$ -transport by Pho91 of yeast and *Trypanosoma brucei* is facilitated by 5-diphospho-inositol tetrakisphosphate, 5-IP7 [16], while all inositol pyrophosphates were evoking the function of yeast VTC complex generating polyphosphate *in vitro* [11] VTC complex is comprised of Vtc1, Vtc4 and Vtc3. Vtc2 is homologous to Vtc3 and found in VTC complex on the cell periphery [17]. Hereby Vtc4 harbors ATPase activity required for polyphosphate generation while Vtc2 and Vtc3 suggested to be regulative units due to its negligible ATPase activity. VTC complex activity is limited to the activation of SPX domain [18], [19]. IP8 stimulates polyphosphate generation by VTC complex the most efficiently with an  $EC_{50}$  around 20 times lower as of IP7 that is 350-500 nM [19]. Lastly IP6 stimulates the activity above 100  $\mu$ M [11], [19]. Latter is at the upper limit or above the physiological levels of IP6 found in the cell that depends on the organism being constant between 10-100 $\mu$ M [20]–[24]. 5-IP7 and 1,5-IP8 were suggested to be relevant *in vivo* for VTC activity [19]. Additives like  $PP_i$  and  $PPP_i$  have shown to concentration-dependent elevate the ATPase activity linked to polyphosphate synthesis even up to 90 times [17].

An altered conserved binding pocket for inositol pyrophosphates led to impairment of the respective function of  $P_i$  responsive SPX-containing proteins [4], [11], [16], [19], [25], [26]. Not only this binding pocket of SPX appears to be important for protein function; there are also mutations in SPX domain outside this binding pocket [27]–[29] and in the region between currently annotated SPX and adjacent domain [27] causing

malfunction like primary familial brain calcification (PFBC) manifested in neuropsychiatric abnormalities and movement disorders [30]. In plants, there is a mutation outside the binding pocket leading to unusual hyperaccumulation of  $P_i$  [11]. So far, the only regulative molecular mechanism described between inositol pyrophosphate and SPX is the one taking place in plants. Here, inositol pyrophosphate act as a facilitator of an interaction between stand-alone SPX and positively charged surface patch of coiled-coil domain in PHR [11], [31]–[34]. *In-vitro*, they bind to each other in a low micromolar ( $\mu\text{M}$ ) range in the presence of 1,5-IP8 and 5-IP7 [10], [11] and ten times less efficient by inositol phosphate, IP6 [11]. It has been suggested that inositol pyrophosphate has a regulative role as a kind of molecular glue as the mutations in the SPX binding pocket for inositol pyrophosphates abolished the interaction between SPX and CC-domain and 1,5-IP8 was shown to bind to PHR in a low millimolar range unregard of impaired charged surface patch involved in the interaction. To study the molecular mechanism of inositol pyrophosphates upon SPX in other SPX-containing system, we investigated the structure and the function of SPX domain of Vtc2 (SPX2) within Vtc complex by NMR spectroscopy and other biophysical methods.

## Results & Discussion

We base our characterization of SPX2 in aqueous solution in solution NMR spectroscopy. Sequence-specific resonance assignments of SPX2 were obtained by standard triple-resonance NMR experiments (Fig. S1). Secondary chemical shifts (SS) derived from  $^{13}\text{C}_\alpha$  and  $^{13}\text{C}_\beta$  nuclei display the presence of secondary structure elements in the protein. In aqueous solution, SPX2 comprises a total of 8  $\alpha$ -helices (Fig. 1A). Out of these, helices  $\alpha$ 1-  $\alpha$ 6, including the helix  $\alpha$ 3' were previously known from crystallographic structures of other SPX domains [11]. In addition, SPX2 contains helix  $\alpha$ 7 at C-terminus, comprising residues 186-189. This segment has a helical population of around 50% as evidenced from the SS values, suggesting that it rapidly interconverts between helical and random-coil conformations. This interpretation is underlined by NMR relaxation measurements of the protein backbone dynamics, which show that  $\alpha$ -helix7 features increased dynamics on the ps-ns timescale in comparison to other helical regions (Figs. S2A, B, C). The presence of  $\alpha$ -helix7 significantly stabilizes the SPX domain as evidenced by thermal melting and hence this region is an integral structural part of the SPX2 domain (Fig. 1B). By analyzing the chemical shift perturbations caused by truncation of helix  $\alpha$ 7, we localize it between  $\alpha$ -helix4 and  $\alpha$ -helix6 as these are experiencing the largest chemical shift differences (Fig. 1C, E). Similarly, the linker region C-terminal to  $\alpha$ -helix7 and leading to the adjacent TTM domain interacts with helices  $\alpha$ 1,  $\alpha$ 4 and  $\alpha$ 5 (Fig. 1D, F). This is at the known binding pocket of inositol phosphates [11]. This interpretation is in agreement with H/D exchange NMR data that show two regions in SPX2 to be exchange-protected – a patch near known binding pocket and a region between  $\alpha$ -helix4 and  $\alpha$ -helix6 at the opposite side to the known binding pocket (Figs. S2D, E). Helix  $\alpha$ 7 is likely of key functional role. On the one hand, its motif is conserved but only found in few SPX proteins. It is a part of Vtc2 and Vtc3 proteins from different organisms as well as in few proteins containing SPX adjacent to ANK, MFS, EXS or ZnF domain (Figs. 1G, H). On the other hand, many reported phosphorylation sites of Vtc2 and Vtc3 and other  $\text{P}_i$  responsive SPX proteins map to this region. In addition, the mutations of PFBC patients map to this region (Table S1).

In a next step, we wanted to study the interaction between Vtc2 and Vtc4 that are part of the VTC complex. To this end, we used constructs that lack the transmembrane domains, here annotated as Vtc2\* and Vtc4\*. MST measurements showed that these two proteins

interact in the low  $\mu\text{M}$  range (Fig. 2A). SPX2 alone binds to Vtc4\* with similar affinity (Fig. 2A) showing that the TTM2 of Vtc2\* does not significantly contribute to binding. Because we were not able to prepare stable samples of purified SPX4, we titrated SPX2 to TTM4, and found only a very weak interaction in the mM range (Fig. 2A). Taken together, these data show that SPX2 mainly interacts with SPX4. This SPX2–SPX4 interaction comprises substantial electrostatic contributions, as evidenced by measurements of the affinity in the presence of high concentrations of sodium chloride (Fig. 2B). Addressing salt influence at the structural level of SPX2 displayed that salt-sensitive residues were largely within helices  $\alpha 1$  and  $\alpha 7$ .  $\alpha$ -helix1 residues reveal a change in its kinetics observed by NMR peak intensities whereas residues of  $\alpha 7$  experience large chemical shift perturbations (Fig. S3A). Indeed, truncation of either helix  $\alpha 7$  or  $\alpha 1$  reduced SPX2 binding affinity to Vtc4\* dramatically (Figs. 2C) but had no reduced binding to TTM4 (Figs. S3B). Single point mutations of either serine 187 or 189 to alanine in helix  $\alpha 7$  decrease the binding affinity between SPX2 and Vtc4\* (Fig. S3C), suggesting these residues to be part of the interaction interface. Altogether, these show that SPX2 binds with high affinity to Vtc4\*. In the biological context, this interaction might likely play a role as an inhibitor of the VTC complex activity.

Indeed, each of the inositol phosphates and pyrophosphates IP6, 5-IP7 and IP8, led to a disruption of SPX2 binding to Vtc4\* (Fig. 2D). This finding was further corroborated by solution NMR spectroscopy and cross-linking experiment (Figs. S4A, B). IP6 is known to bind SPX domains at  $\alpha$ -helix1,  $\alpha$ -helix2 and C-terminal part of  $\alpha$ -helix4 [11]. Similarly, we observe here that binding of either IP6, IP7 or IP8 – jointly termed here IPx – causes large chemical shift perturbations in  $\alpha$ -helix1,  $\alpha$ -helix2, the C-terminal part of  $\alpha$ -helix4, the N-terminal part of  $\alpha$ -helix3 with its adjacent loop and the loop region adjacent to  $\alpha$ -helix7 (Figs. S4C, D, E). This is confirming the known binding pocket of inositol phosphate and predicted binding pocket of inositol pyrophosphates. The effects of the IPx differ in their impact on the SPX2 dynamics in the loop between  $\alpha$ -helix2 and  $\alpha$ -helix3, the loop between  $\alpha$ -helix5 and  $\alpha$ -helix6 as well as in the  $\alpha$ -helix7 region. Notably, their interaction is in intermediate exchange – most pronounced for IP8 (Fig. S4C). As all holo-states were recorded at the same spectrometer frequencies, this difference in the chemical exchange regime for the respective regions could be due to increased level of hydrogen bonding towards water and less to other structural elements. This would

be reflected in the protein stability measurements. Indeed, IP6 stabilized the SPX2 the most by 13 °C followed by 10 °C through IP7 and lastly 4 °C by IP8 (Fig. S4F).

The holo-state differences seen in the local dynamics and stability of SPX2 as its binding capacities to Vtc4\* could explain *in-vitro* activity of VTC complex to some degree. The potency as an agonist is highest for IP8, followed by IP7 and lastly IP6 [11], [19]. Latter tendencies order is also seen in our experiments. Possibly, the elements revealing the differences in the kinetics explain only the direct effect of IPx caused on SPX domain and SPX-SPX interaction but have to be studied in context to other subsequent events. As speculation, phosphorylation on serines of  $\alpha$ -helix7 detected in earlier studies (Table S1) could serve as basis to non-enzymatically transfer the  $\beta$ -phosphoryl group of IP7 or IP8 non-enzymatically [35], [36]. A dynamically detaching pyrophosphorylated  $\alpha$ -helix7 could be a key event to activate VTC complex at the catalytic site in an analogous way as it was shown for pyrophosphate  $PP_i$  [17]. This could explain *in-vivo* data; six mutation of five serines and one threonine at  $\alpha$ -helix7 region of Vtc3 completely abolished polyphosphate pools (unpublished data, personal communication to Andreas Mayer).

Structurally, the binding of IP6 to SPX2 does not lead to significant changes of the secondary structure elements for most parts of the protein (Fig. S5A). Residual dipolar couplings (RDC) show that the helices  $\alpha$ -helix2 to  $\alpha$ -helix6 in the apo-state have the same relative orientation, in agreement with the crystal structure (Fig. S5B). The relative orientation of helices  $\alpha$ -helix1 with adjacent loop and  $\alpha$ -helix3' changed upon addition of IP6 (Fig S5B). Considering that the  $\alpha$ -helix1 is involved in the complex formation, this ligand-induced reorientation of the conserved  $\alpha$ -helix1 and its loop as does the binding of the highly negatively charged ligand could both most likely contribute to the disruption of the complex. Comparing apo- to holo-state of SPX2 alone in terms of dynamics, the region  $\alpha$ 1,  $\alpha$ 2 and its adjacent loop displayed reduced dynamics while a C-terminal part of  $\alpha$ 4 and loop next to  $\alpha$ 7 shows increased dynamics (Figs. S5E, F, H) confirming the changes of SPX dynamics upon ligand binding.

Most of the structural studies were conducted on isolated SPX2. As a control, structural ligand induced changes were tested in Vtc2 that contained SPX2 and the adjacent central domain. Overall, the holo-state of isolated SPX2 in SPX in Vtc2\* reveal the overlapping

resonance peaks (Figs. S6B, D) indicating being both structurally similar. On the opposite, the apo-state of SPX2 in the Vtc2\* displayed chemical shift differences (Figs. S6A, C) in helices  $\alpha$ 1 (Fig. S6D) and  $\alpha$ 5 (Fig. S6E). This is suggesting that SPX2 and TTM2 are interacting in the apo-state. Hence, altogether, the overall data proposes a competitive mode of SPX4, TTM2 or IPx to “gain the upper hand” over the conserved  $\alpha$ -helix1.

The molecular mechanism linking SPX in correlation to a function was investigated while working with known as well as unreported mutations causing pseudo-activity of VTC complex *in-vitro* [11], [19] and *in-vivo* [19]. Here specific single mutations in SPX domain of both, Vtc3 and Vtc4 (Fig. 3A) residing in the VTC complex were introduced. These mutations activated polyphosphate activity in the absence of any ligand (Fig. 3B, C). To obtain biophysical and structural information of this event, the homologous mutation was inserted in the SPX domain of Vtc2 and the same set of experiments was performed as for IPx studies. Biophysically, these single mutations lead to a disrupted binding to Vtc4\* (Fig. 3D). Their dissociation constants were higher by six to 30 times in comparison to the wild-type SPX2. Structurally, a comparison of these SPX2 mutants to the wild-type SPX2 reveals changes in the helices  $\alpha$ 1,  $\alpha$ 2 and  $\alpha$ 4 belonging to the known binding pocket as well as in the  $\alpha$ -helix3 and in the loop between helices  $\alpha$ 5 and  $\alpha$ 6 (Figs. S7A, B, C). Most of these regions of SPX2 are also influenced upon IPx binding suggesting that IPx and the pseudo-active mutations activate VTC complex structurally in a similar way. Altogether, the pseudo-active mutations of SPX underline the importance of SPX domain as inhibitor for VTC complex.

This is structurally the most extensively characterized SPX system so far explaining the molecular mechanism behind SPX-SPX interaction of VTC complex in dependence of inositol pyrophosphates that are known to modulate  $P_i$  homeostasis. Our suggested emerging model is that a presence of IPx as well as a pseudo-active mutation directly effects a SPX-SPX interaction. We could show that they disrupt the interaction of SPX4 to SPX2 or SPX3, respectively, suggesting  $\alpha$ -helix1 involved in the complex formation to undergo a ligand-induced conformational change suggested in earlier studies [11]. A confirmed perturbed binding pocket of inositol phosphates and predicted binding pocket of pyrophosphates harboured among  $\alpha$ 1,  $\alpha$ 2 and  $\alpha$ 4 [11] and a subsequent

reorientation of helix1 and its adjacent loop upon ligand binding seem to be essential for the function. An impaired binding pocket abolished  $P_i$  responsive functions [4], [11], [16], [19], [25], [26]. This conformational change most likely exposes  $\alpha$ -helix7 whose serines are involved in the complex formation. This is displayed by estimated by the increase of dynamics of SPX2 in its holo-state.

We speculate that secondary events following could be key events for the activity itself. We could imagine that a disrupted complex displays an open gate of  $\beta$ -barrel in TTM4 shown to carry ATPase and polyphosphate activity of VTC complex [17] that is sterically hindered by SPX domains in its apo-state. This could allow  $PP_i$  to enter, bind to interior of  $\beta$ -barrel, enhance ATPase activity and hence contribute to polyphosphate synthesis. This would explain the pseudo-activity of SPX mutations. Secondly, an exposed  $\alpha$ -helix7 of SPX2/3 would allow phosphorylation by cellular kinases and subsequently inositol pyrophosphates could pyrophosphorylate exposed phosphorylated serines of  $\alpha$ -helix7. Due to increased dynamics of  $\alpha$ -helix7 its localization between  $\beta$ -barrel of TTM4 and SPX2/3 could be possible yielding an active VTC complex in analogous way as  $PP_i$ . Bioinformatical data display a preserved  $\alpha$ -helix7 motif seen in few SPX proteins and mapping this area to other SPX proteins reveals detected phosphorylation sites. Hence,  $\alpha$ -helix7-related area is protein specific and could be the main attribute to the diversification of SPX protein functions.

We suggest that SPX domains could have a dual role – as inhibitors in the absence of inositol (pyro-) phosphates as well as, mutually, molecular-assembly disruptors and activators in the presence of inositol pyrophosphates. This reveals a completely new dimension to understand eukaryotic  $P_i$  homeostasis.

## References:

- [1] D. Secco, C. Wang, B. A. Arpat, Z. Wang, Y. Poirier, S. D. Tyerman, P. Wu, H. Shou, and J. Whelan, "The emerging importance of the SPX domain-containing proteins in phosphate homeostasis," *New Phytol.*, vol. 193, pp. 842–851, 2012.
- [2] D. Secco, C. Wang, H. Shou, and J. Whelan, "Phosphate homeostasis in the yeast *Saccharomyces cerevisiae*, the key role of the SPX domain-containing proteins," *FEBS Lett.*, vol. 586, no. 4, pp. 289–295, 2012.
- [3] H. C. Huerlimann, B. Pinson, M. Stadler-Waibel, S. C. Zeeman, and F. M. Freimoser, "The SPX domain of the yeast low-affinity phosphate transporter Pho90 regulates transport activity," *EMBO*, vol. 10, no. 9, pp. 1003–1008, 2009.
- [4] C. L. Creasy, S. L. Madden, and L. W. Bergman, "Molecular analysis of the PHO81 *cerevisiae* of *Saccharomyces*," *Nucleic Acids Res.*, vol. 21, no. 8, pp. 1975–1982, 1993.
- [5] N. Ogawa, K. Noguchi, H. Sawai, and Y. Yamashita, "Functional Domains of Pho81p, an Inhibitor of Pho85p Protein Kinase, in the Transduction Pathway of P<sub>i</sub> Signals in *Saccharomyces cerevisiae*," *Mol. Cell. Biol.*, vol. 15, no. 2, pp. 997–1004, 1995.
- [6] M. I. Puga, I. Mateos, R. Charukesi, Z. Wang, J. M. Franco-Zorrilla, L. De Lorenzo, M. L. Irigoyen, S. Masiero, R. Bustos, J. Rodríguez, A. Leyva, V. Rubioa, H. Sommer, and J. Paz-Ares, "SPX1 is a phosphate-dependent inhibitor of PHOSPHATE STARVATION RESPONSE 1 in *Arabidopsis*," *PNAS*, vol. 111, no. 41, pp. 14947–52, 2014.
- [7] F. Liu, Z. Wang, H. Ren, C. Shen, Y. Li, H. Ling, C. Wu, and X. Lian, "OsSPX1 suppresses the function of OsPHR2 in the regulation of expression of OsPT2 and phosphate homeostasis in shoots of rice," *Plant J.*, vol. 62, no. 3, pp. 508–517, 2010.
- [8] Z. Wang, W. Ruan, J. Shi, L. Zhang, D. Xiang, C. Yang, C. Li, Z. Wu, and Y. Liu, "Rice SPX1 and SPX2 inhibit phosphate starvation responses through interacting with PHR2 in a phosphate-dependent manner," *PNAS*, vol. 111, no. 41, pp. 14953–14958, 2014.
- [9] W. Qi, I. W. Manfield, S. P. Muench, and A. Baker, "AtSPX1 affects the AtPHR1 – DNA-binding equilibrium by binding monomeric AtPHR1 in solution," *Biochem. J.*, vol. 474, no. 21, pp. 3675–3687, 2017.
- [10] M. K. Ried, R. Wild, J. Zhu, L. Broger, R. K. Harmel, L. A. Hothorn, D. Fiedler, and M. Hothorn, "Inositol pyrophosphates promote the interaction of SPX domains with the coiled-coil motif of PHR transcription factors to regulate plant phosphate homeostasis," *BioRxiv*, vol. 12, 2019.
- [11] R. Wild, R. Gerasimaite, J.-Y. Jung, V. Truffault, I. Pavlovic, A. Schmidt, A. Saiardi, H. J. Jessen, Y. Poirier, M. Hothorn, and A. Mayer, "Control of eukaryotic phosphate homeostasis by inositol polyphosphate sensor domains," *Science*, vol. 352, no. 6288, pp. 986–990, 2016.
- [12] Y. Lee, S. Mulugu, J. D. York, and E. K. O. Shea, "Regulation of a Cyclin-CDK-CKI Inhibitor Complex by Inositol Pyrophosphates," *Science*, vol. 316, no. 5821, pp. 109–112, 2007.
- [13] Y. Lee, K. Huang, F. A. Quioco, and E. K. O. Shea, "Molecular basis of cyclin-CDK-CKI regulation by reversible binding of an inositol pyrophosphate," *Nat. Chem. Biol.*, vol. 4, no. 1, pp. 25–32, 2008.
- [14] D. Giovannini, J. Touhami, P. Charnet, M. Sitbon, and J. Battini, "Inorganic Phosphate Export by the Retrovirus Receptor XPR1 in Metazoans," *Cell Rep.*, vol. 3, no. 6, pp. 1866–1873, 2013.
- [15] J. Battini, J. E. J. Rasko, and A. D. Miller, "A human cell-surface receptor for xenotropic and polytropic murine leukemia viruses: Possible role in G protein-coupled signal transduction," *PNAS*, vol. 96, no. February, pp. 1385–1390, 1999.
- [16] E. Potapenko, C. D. Cordeiro, G. Huang, M. Storey, C. Wittwer, A. K. Dutta, H. J. Jessen, V. J. Starai, and R. Docampo, "5-Diphosphoinositol Pentakisphosphate (5-IP7) Regulates Phosphate Release from Acidocalcisomes and Yeast Vacuoles," *J. Biol. Chem.*, vol. 293, no. 49, pp. 19101–19112, 2018.

- [17] M. Hothorn, H. Neumann, E. D. Lenherr, M. Wehner, V. Rybin, P. O. Hassa, A. Uttenweiler, M. Reinhardt, A. Schmidt, J. Seiler, A. G. Ladurner, C. Herrmann, K. Scheffzek, and A. Mayer, "Catalytic Core of a Membrane-Associated Eukaryotic Polyphosphate Polymerase," *Science*, vol. 324, no. 5926, pp. 513–516, 2009.
- [18] A. Lonetti, Z. Sziogyarto, D. Bosch, O. Loss, C. Azevedo, and A. Saiardi, "Identification of an Evolutionarily Conserved Family of Inorganic Polyphosphate Endopolyphosphatases," *J. Biol. Chem.*, vol. 286, no. 37, pp. 31966–31974, 2011.
- [19] R. Gerasimaite, I. Pavlovic, S. Capolicchio, A. Hofer, A. Schmidt, H. J. Jessen, and A. Mayer, "Inositol Pyrophosphate Specificity of the SPX-Dependent Polyphosphate Polymerase VTC," *ASC Chem. Biol.*, no. 12, p. 648–653, 2017.
- [20] C. Albert, S. T. Safrany, M. E. Bembenek, K. M. Reddy, K. K. Reddy, J. R. Falck, M. Broecker, S. B. Shears, and G. W. Mayr, "Biological variability in the structures of diphosphoinositol polyphosphates in *Dictyostelium discoideum* and mammalian cells," *Biochem. J.*, vol. 327, no. Pt 2, pp. 553–560, 1997.
- [21] C. J. Barker, J. Wright, P. J. Hughes, C. J. Kirk, and R. H. Michell, "Complex changes in cellular inositol phosphate complement accompany transit through the cell cycle," *Biochem. J.*, vol. 473, no. Pt 2, pp. 465–473, 2004.
- [22] C. Illies, J. Gromada, R. Fiume, B. Leibiger, J. Yu, K. Juhl, S.-N. Yang, D. K. Barma, J. R. Falck, A. Saiardi, C. J. Barker, and P.-O. Berggren, "Requirement of Inositol Pyrophosphates for Full Exocytotic Capacity in Pancreatic b Cells," *Science*, vol. 318, no. 5854, pp. 1299–1303, 2007.
- [23] H. Lin, P. C. Fridy, A. A. Ribeiro, J. H. Choi, D. K. Barma, J. R. Falck, S. B. Shears, J. D. York, and G. W. Mayr, "Structural Analysis and Detection of Biological Inositol Pyrophosphates Reveal That the Family of VIP/Diphosphoinositol Pentakisphosphate Kinases," *J. Biol. Chem.*, vol. 284, no. 3, pp. 1863–1872, 2009.
- [24] T. Wundenberg and G. W. Mayr, "Synthesis and biological actions of diphosphoinositol phosphates (inositol pyrophosphates), regulators of cell homeostasis," *Biol. Chem.*, vol. 393, no. 9, pp. 979–998, 2012.
- [25] D. Desmarini, S. Lev, D. Furkert, B. Crossett, A. Saiardi, K. Kaufman-Francis, C. Li, T. C. Sorrell, L. Wilkinson-White, J. Matthews, D. Fiedler, and J. T. Djordjevic, "IP7-SPX Domain Interaction Controls Fungal Virulence by Stabilizing Phosphate Signaling Machinery," *MBio*, vol. 11, no. 5, pp. e01920–20, Oct. 2020.
- [26] U. López-Sánchez, S. Tury, G. Nicolas, M. S. Wilson, S. Jurici, X. Ayrignac, V. Courgnaud, A. Saiardi, M. Sitbon, and J.-L. Battini, "Interplay between PFBC-associated SLC20A2 and XPR1 phosphate transporters requires inositol polyphosphates for control of cellular phosphate homeostasis," *J. Biol. Chem.*, vol. 295, no. 28, pp. 9366–9378, 2020.
- [27] A. Legati, D. Giovannini, G. Nicolas, U. López-sánchez, B. Quintáns, J. Oliveira, R. L. Sears, E. M. Ramos, E. Spiteri, M.-J. Sobrido, Á. Carracedo, C. Castro-Fernández, S. Cubizolle, B. L. Fogel, C. Goizet, J. C. Jen, S. Kirdlarp, A. E. Lang, Z. Miedzybrodzka, W. Mitarnun, M. Paucar, H. Paulson, J. Pariente, A.-C. Richard, N. S. Salins, S. A. Simpson, P. Striano, P. Svenningsson, F. Tison, V. K. Unni, O. Vanakker, M. W. Wessels, S. Wetchaphanphesat, M. Yang, F. Boller, D. Champion, D. Hannequin, M. Sitbon, D. H. Geschwind, J.-L. Battini, and G. Coppola, "Mutations in XPR1 cause primary familial brain calcification associated with altered phosphate export," *Nat Genet.*, vol. 47, no. 6, pp. 579–581, 2015.
- [28] U. López-Sánchez, G. Nicolas, 1, A.-C. Richard, 2, D. Maltête, M. Charif, X. Ayrignac, C. Goizet, J. Touhami, G. Labesse, J.-L. Battini, and S. Marc, "Characterization of XPR1 / SLC53A1 variants located outside of the SPX domain in patients with primary familial brain calcification," *Sci. Rep.*, vol. 9, p. 6776, 2019.
- [29] B. Xu, I. Ionita-laza, J. L. Roos, B. Boone, S. Woodrick, S. Levy, J. A. Gogos, and M. Karayiorgou, "De novo gene mutations highlight patterns of genetic and neural complexity in schizophrenia Bin," *Nat Genet.*, vol. 44, no. 12, pp. 1365–1369, 2013.
- [30] G. Nicolas, C. Pottier, C. Charbonnier, L. Guyant-mare, P. Labauge, X. Ayrignac, L. Defebvre, I. Le Ber, O. Martinaud, R. Lefaucheur, O. Guillin, D. Wallon, B. Chaumette, P. Rondepierre, N. Derahe, T. Lebouvier, O. Rouaud, S. Jurici, M. Sauve, A. Rovelet-lecru, T. Frebourg, C. Thauvin-robinet, and D. Champion, "Phenotypic spectrum of probable and genetically-confirmed idiopathic basal ganglia calcification," *Brain*, vol. 136, no. Pt 11, pp. 3395–3407, 2013.

- [31] J. Dong, G. Ma, L. Sui, M. Wei, V. Satheesh, R. Zhang, S. Ge, J. Li, T. Zhang, C. Wittwer, H. J. Jessen, H. Zhang, G. An, D. Chao, D. Liu, and M. Lei, "Inositol Pyrophosphate InsP<sub>8</sub> Acts as an Intracellular Phosphate Signal in Arabidopsis," *Mol. Plant*, vol. 12, no. 11, pp. 1463–1473, 2019.
- [32] J. Zhu, K. Lau, R. Puschmann, R. K. Harmel, Y. Zhang, V. Pries, P. Gaugler, L. Broger, A. K. Dutta, H. J. Jessen, G. Schaaf, A. R. Fernie, L. A. Hothorn, D. Fiedler, and M. Hothorn, "Two bifunctional inositol pyrophosphate kinases / phosphatases control plant phosphate homeostasis," *Elife*, vol. 8, p. e43582, 2019.
- [33] Q. Lv, Y. Zhong, Y. Wang, Z. Wang, L. Zhang, J. Shi, Z. Wu, Y. Liu, C. Mao, K. Yi, and P. Wu, "SPX4 Negatively Regulates Phosphate Signaling and Homeostasis through Its Interaction with PHR2 in Rice," *Plant Cell*, vol. 26, no. 4, pp. 1586–1597, 2014.
- [34] Y. Zhong, Y. Wang, J. Guo, X. Zhu, J. Shi, Q. He, Y. Liu, Y. Wu, L. Zhang, Q. Lv, and C. Mao, "Rice SPX6 negatively regulates the phosphate starvation response through suppression of the transcription factor PHR2," *New Phytol.*, vol. 219, no. 1, pp. 135–148, 2018.
- [35] C. E. Hand and J. F. Honek, "Phosphate transfer from inositol pyrophosphates InsP<sub>5</sub>PP and InsP<sub>4</sub>(PP)<sub>2</sub>: A semi-empirical investigation," *Bioorg. Med. Chem. Lett.*, vol. 17, no. 1, pp. 183–188, 2007.
- [36] R. Bhandari, A. Saiardi, Y. Ahmadibeni, A. M. Snowman, A. C. Resnick, T. Z. Kristiansen, H. Molina, A. Pandey, J. K. Werner, K. R. Juluri, Y. Xu, G. D. Prestwich, K. Parang, and S. H. Snyder, "Protein pyrophosphorylation by inositol pyrophosphates is a posttranslational event," *Proc. Natl. Acad. Sci.*, vol. 104, no. 39, p. 15305 LP – 15310, Sep. 2007.
- [37] J. Kyte and R. F. Doolittle, "A simple method for displaying the hydropathic character of a protein," *J. Mol. Biol.*, vol. 157, no. 1, pp. 105–132, 1982.

## Figures

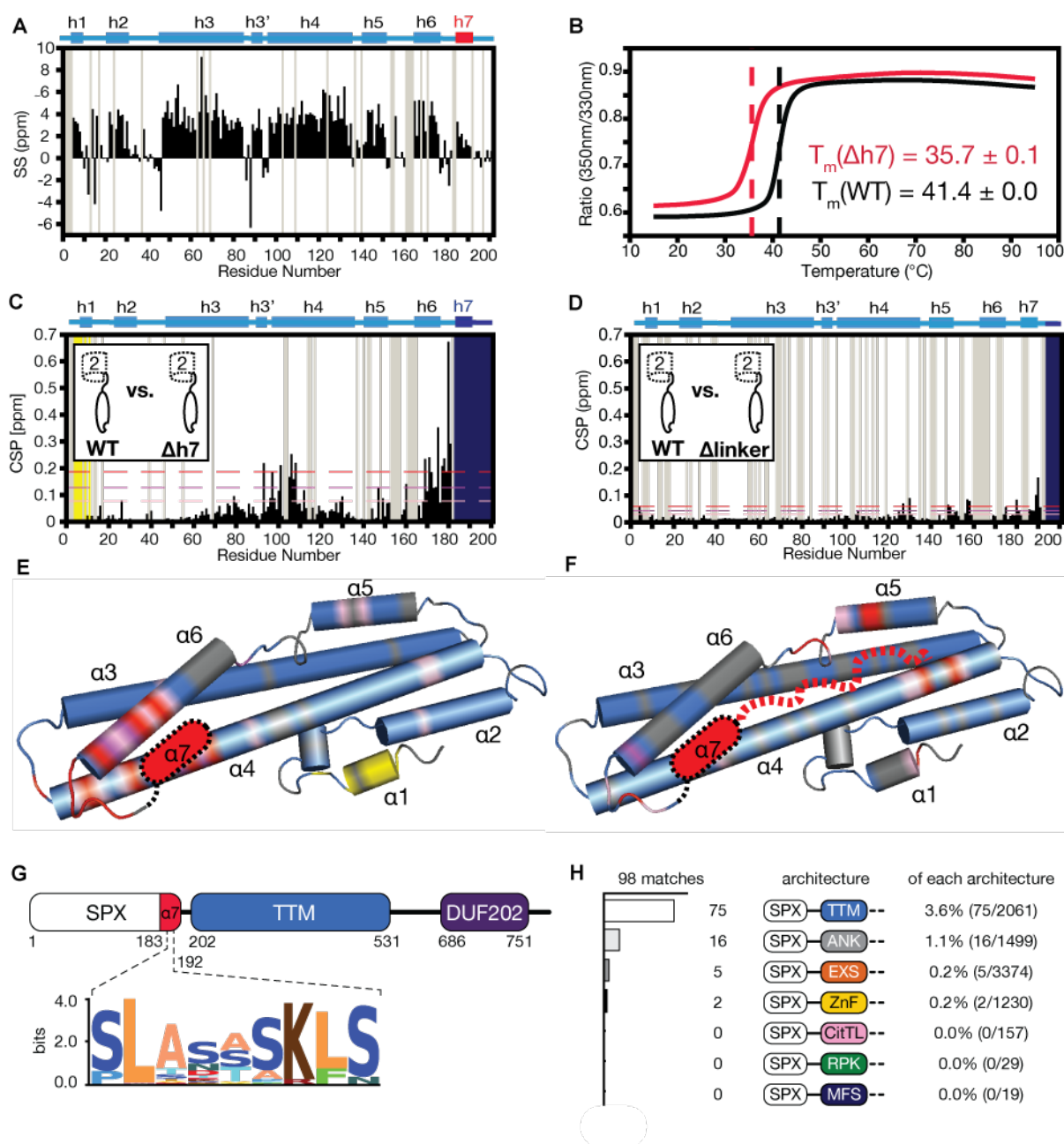


**Fig. 1: SPX2 contains a conserved  $\alpha$ -helix7.** (A) Identification of secondary elements of soluble SPX2 by secondary chemical shifts (SS) determined by standard triple-resonance NMR experiments. (B) Determination of protein stability of SPX2 and SPX2 $\Delta$ h7 by Prometheus (*Nanotemper Technologies*). (C, D) Chemical shift differences of SPX2 upon truncation of helix  $\alpha$ 7 or the linker region. Yellow – residues experiencing intermediate chemical exchange, gray – residues not assigned, dark blue – residues that were deleted. (E, F) plotting the differences on a structural model derived from x-ray structures by *Phyre2* server. Yellow – residues experiencing intermediate chemical

exchange, gray – residues not assigned, thresholds of chemical shift differences shown in rosa ( $\mu + 0.2 \sigma$ ), magenta ( $\mu + 0.8 \sigma$ ) and red ( $\mu + 1.5 \sigma$ ). (G, E) Protein sequence motif of  $\alpha$ -helix7 extracted from SPX-containing proteins that were found in SPX proteins of different domain architectures. Buffer used for all lab experiments was 25mM HEPES pH 7.0, 250mM NaCl, 0.5mM EDTA, 0.5mM TCEP.

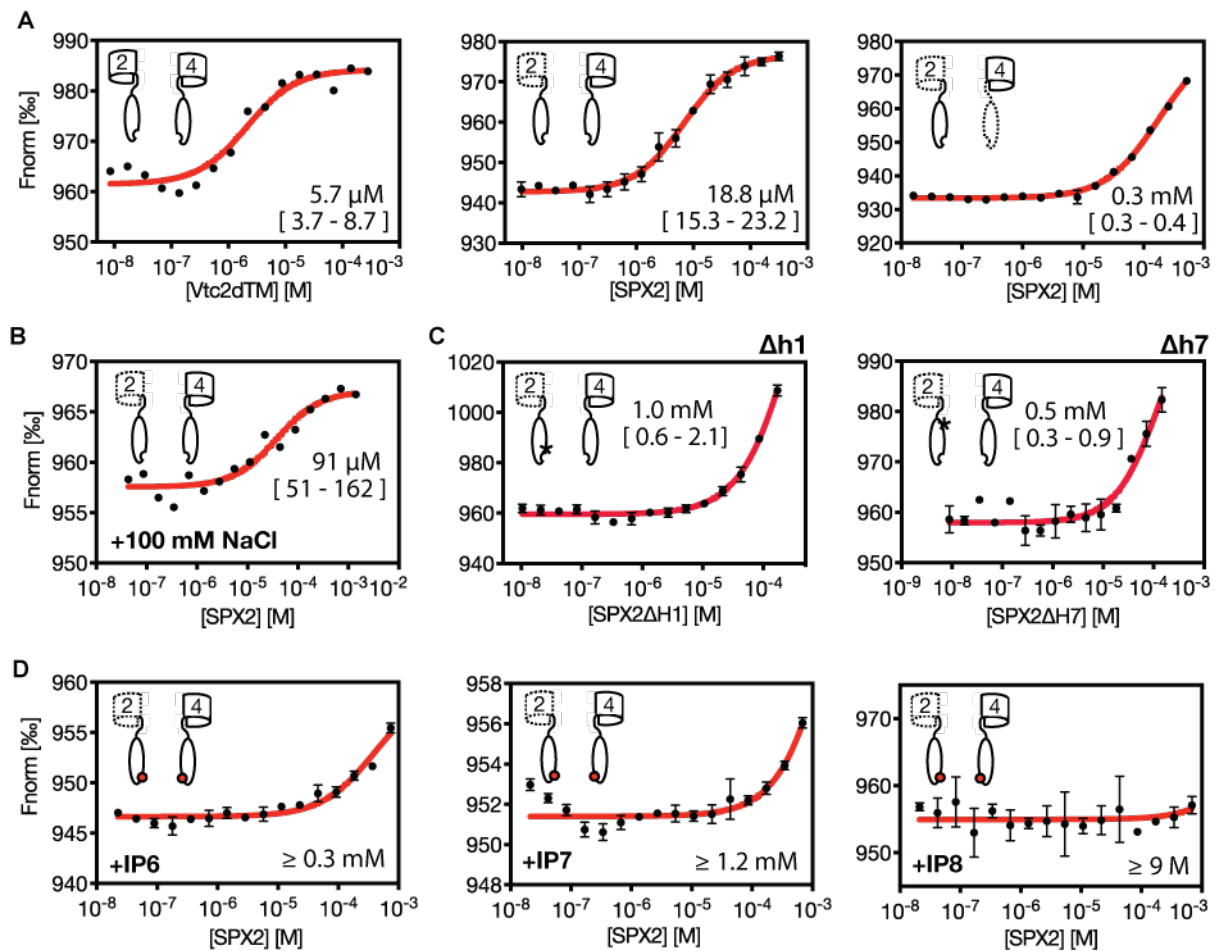


**Fig. 2: Vtc2 and Vtc4 interact via their SPX domains in an IPx-dependent manner.**

(A) Binding affinities of Vtc2\* to Vtc4\*, SPX2 to Vtc4\* and SPX2 to TTM4. They were measured by MST. (B) MST binding affinities of SPX2 to Vtc4\* at elevated NaCl conditions. (C) Binding affinities of SPX2 $\Delta$ h1 or SPX2 $\Delta$ h7, respectively, to Vtc4\* measured by MST. Asterisks display the protein lacking areas in the cartoon scheme. (D) Binding affinities of SPX2 to Vtc4\* in the presence of 2.5 mM IP6, IP7 or IP8 measured by MST. Red filled circles display the binding areas of IP6, IP7 or IP8 in the cartoon scheme. Dissociation constant estimated is mentioned near the fits.

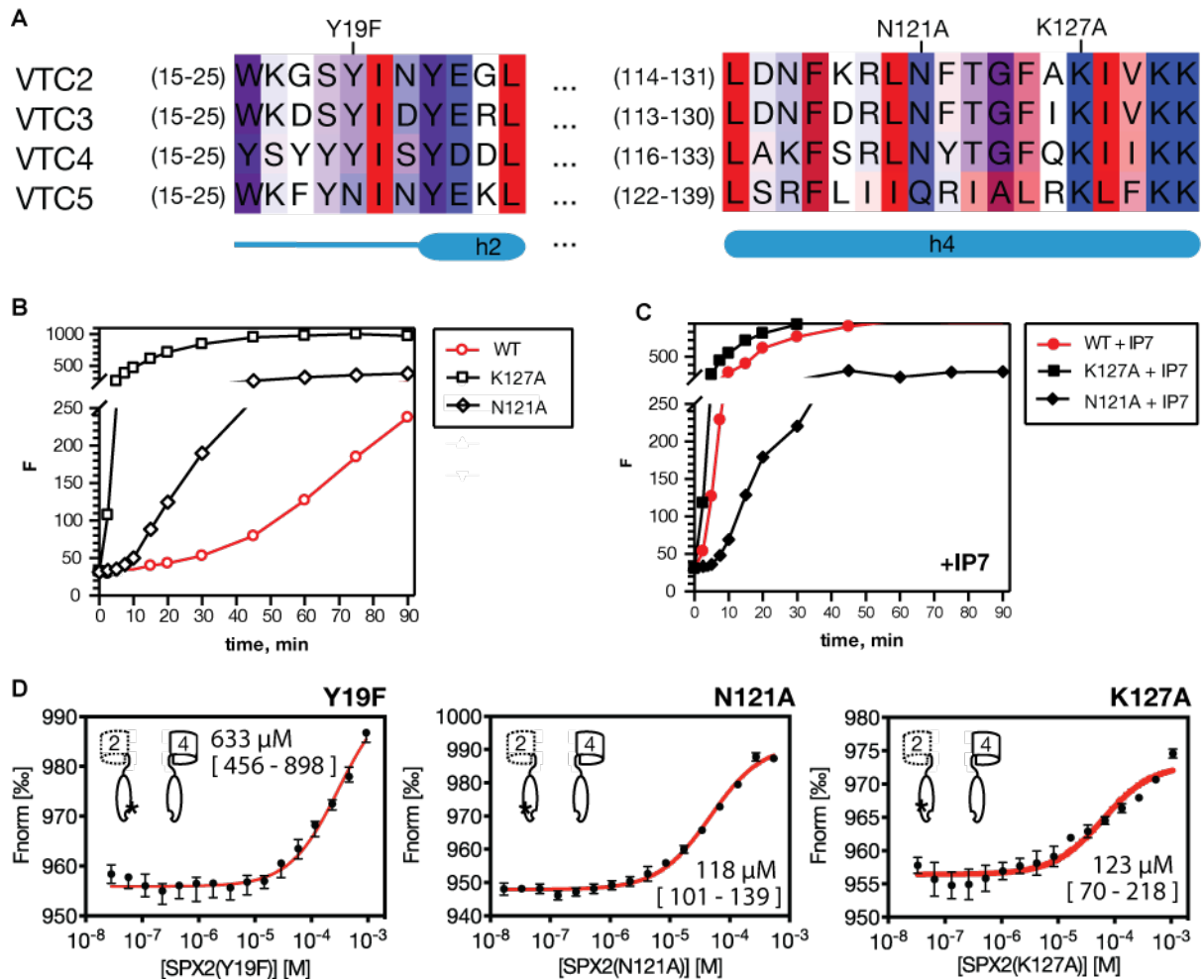


**Fig. 3: Specific mutations in SPX2 disrupt binding to Vtc4\* and cause pseudo-activity in Vtc complex.** (A) Multiple sequence alignment of SPX-containing Vtc proteins with displayed pseudo-active mutations. The alignment is colored according to hydrophobicity [37]. (B, C) Polyphosphate synthesis of Vtc complex comprised of Vtc1/3/4 measured in the isolated vacuoles in the absence and the presence of IP7. (C) MST binding affinities of pseudo-active mutations (Y19F, N121A, K127A) in SPX2 to Vtc4\*. Dissociation constant estimated is mentioned near the fits. Asterisks display the mutations in the cartoon scheme.

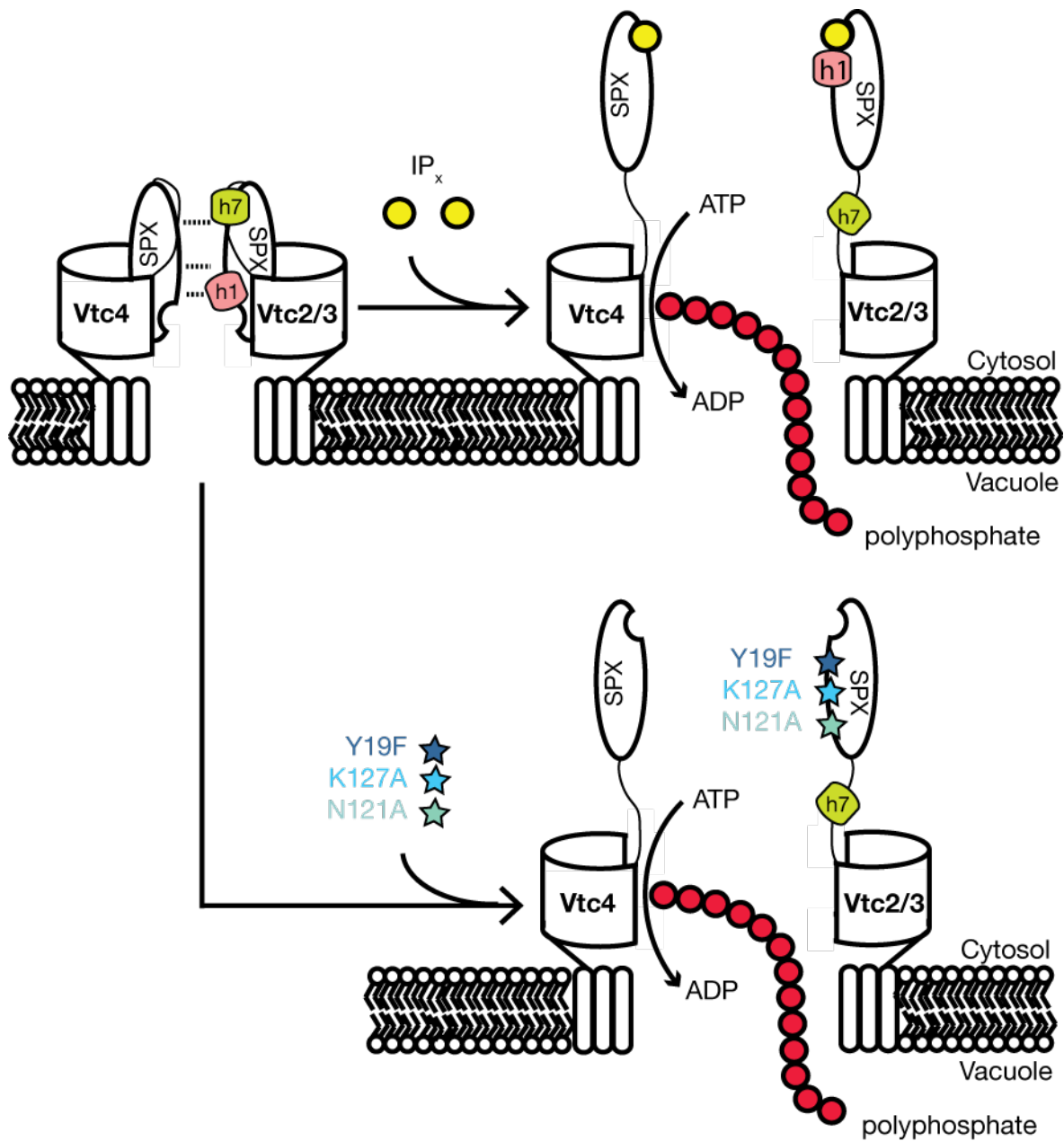


**Fig. 4: Emerging mechanism model of Vtc complex.** SPX-SPX interaction of Vtc4 and Vtc2 or Vtc3, respectively, is based on electrostatics of  $\alpha$ -helix1 and  $\alpha$ -helix7. InsPx or pseudo-active mutations lead to a ligand-induced  $\alpha$ -helix1 reorientation, liberated  $\alpha$ -helix7 and hence a disruption of Vtc4 and Vtc2/3. This initiates a indirect activation of VTC.

## Supplementary Materials

### Inositol pyrophosphates abrogate direct inhibition by SPX

Joka Pipercevic<sup>1</sup>, Bastian Kohl<sup>1\*</sup>, Thomas Müntener<sup>1</sup>, Elia Agustoni<sup>1</sup>, Véronique Comte-Miserez<sup>3</sup>, Dorothea Fiedler<sup>2</sup>, Andreas Mayer<sup>3</sup>, Sebastian Hiller<sup>1\*</sup>

\*Correspondence to: [bastian.kohl@unibas.ch](mailto:bastian.kohl@unibas.ch), [sebastian.hiller@unibas.ch](mailto:sebastian.hiller@unibas.ch)

## Material and Methods

### Protein Expression and purification

pET vector (pMH- HC) based Vtc2(1-182) with a C-terminal His<sub>5</sub>-tag was kindly gifted by Hothorn Lab [11]. A TEV cleavable site was engineered adjacent to the His<sub>5</sub>-Tag (SPX2Δh7). A stretch of residues was inserted by Q5 Kit (*NEB*) to generate longer Vtc2 constructs: Vtc2(1-193), SPX2Δlinker, and Vtc2(1-201), SPX2. The site-specific mutations were introduced into SPX2 by the QuikChange II mutagenesis protocol (*Stratagene*) by using Phusion DNA polymerase (*Thermo Scientific*) and were verified by gene sequencing.

SPX2 proteins were recombinantly expressed in *E. coli* Lemo21(DE3) BL21 cells (*NEB*). They were transformed with the respective plasmid and grown in either 1 L LB for expressing unlabeled proteins or 1 L M9 medium supplemented by <sup>15</sup>NH<sub>4</sub>Cl for [*U*-<sup>15</sup>N]-labeled constructs. For expressing [*U*-<sup>2</sup>H,<sup>15</sup>N] or [*U*-<sup>2</sup>H,<sup>15</sup>N,<sup>13</sup>C]-labeled constructs 1 L M9 medium supplemented by either [*U*-<sup>2</sup>H]- or [*U*-<sup>2</sup>H,<sup>13</sup>C]-glucose, respectively, as well as <sup>15</sup>NH<sub>4</sub>Cl and D<sub>2</sub>O was used. All cultures were supplemented by 30 mg kanamycin per 1 L medium. The cells were grown at 37 °C to an optical density (600 nm) of 0.4-0.6. At this point, the temperature of the shaker was reduced to 16 °C. After one hour, the cells were induced with 0.3 mM isopropyl-β-thiogalactopyranoside and harvested after 12 hours. Cells were resuspended in 50 mL of buffer A (20 mM Tris-HCl pH 8.0, 500 mM NaCl, 2 mM β-mercaptoethanol) with additional 20 mM imidazole, 0.5% Triton, 2 mM MgCl<sub>2</sub>, and 500 units of Turbo Nuclease (*BioVision*). The cells were disrupted with lysozyme and a microfluidizer and the cell lysis was centrifuged at 42'500xg for 40 minutes at 4 °C. Protein present in the supernatant was filtered via 0.22 μm membrane and isolated by using a Ni-NTA based HisTrap (*GE Health*) column equilibrated with buffer A. The protein was eluted with a linear gradient 0–60 % by twenty column volumes (CV) of buffer A supplemented with 0.5 M imidazole. The fractions containing the protein were collected and TEV protease was added. The sample was incubated at 4 °C overnight. After a buffer exchange against buffer A, the sample was applied on the HisTrap following the same procedures above. The protein contained in the flow through fractions was collected and diluted 10x in a buffer B (50mM Na-Ac pH 4.5, 20mM NaCl) and subsequent applied on equilibrated HiTrap SP HP (*GE Health*). The protein was eluted with buffer B supplemented by 1M NaCl. The pure protein sample was subjected to Superdex 75pg 16/600 (*GE Health*) for buffer exchange to 25mM HEPES pH 7.0,

250mM NaCl, 0.5mM EDTA and 0.5mM TCEP. The central fractions of the elution peak were collected and used for all subsequent experiments.

pET27b(+) based Vtc2(1-553), Vtc2\*, and Vtc4(1-487), Vtc\*, as well as TTM4 of Vtc4(192-487) with a C-terminal TEV cleaving site and a His<sub>10</sub>-tag were ordered by *GenScript*. They were expressed and purified like the SPX2 proteins with the following modifications. Affinity chromatography by HisTrap contained several wash steps in a length of 2CV. The protein was first washed with buffer A, a wash with buffer A supplemented with 200 mM potassium phosphate and a wash with buffer A containing 1M NaCl followed by a subsequent washing with buffer A. Finally, a linear gradient (0-100 %) of buffer A supplemented with 0.5mM imidazole (20CV) eluted the protein. A cation exchange chromatography by SP HP was not performed and the size-exclusion chromatography was conducted by Superdex 200pg 16/600 (*GE Health*) in the same buffer.

#### NMR spectroscopy

NMR experiments were recorded at 27 °C on cryogenic 600 and 900 MHz NMR spectrometers (*Bruker*) equipped with a triple resonances (TXI) probe. Unless stated otherwise, the NMR buffer contained 25mM HEPES pH 7.0, 250mM NaCl, 0.5mM EDTA, 0.5mM TCEP and 5% D<sub>2</sub>O.

*Backbone experiments.* The assignments on backbone amides were obtained on 500 μM [*U*-<sup>2</sup>H,<sup>15</sup>N,<sup>13</sup>C]-labeled SPX2. TROSY [38] and TROSY-based 3D HNCACB, HNCOC and HN(CA)CO triple resonance NMR spectra [39] were recorded at 600 MHz while 3D H(N)NH NOE TROSY spectrum [40] was recorded at 900 MHz with a mixing time of 100 ms. The NMR spectra were processed by PROSA [41] and were analyzed by CARA and XEASY [42]. CS plots were calculated by C<sub>α</sub> and C<sub>β</sub> values that considered random chemical shifts of every amino acid and were extracted by a CARA software.

*Relaxation experiments.* <sup>15</sup>N-T<sub>1</sub>, <sup>15</sup>N-T<sub>2</sub> and hetNOE [43] were recorded on 380 μM [*U*-<sup>15</sup>N]-labeled SPX2 at 600 MHz. The interscan delay used for <sup>15</sup>N-T<sub>1</sub> and <sup>15</sup>N-T<sub>2</sub> was 7.0 seconds and for hetNOE was 5.3 seconds, respectively. The relaxation spectra of varying t<sub>1</sub> and t<sub>2</sub> times were processed with Topspin and fitted by exponential decay equation and covariance error method estimation in CCPNMR [44].

*Chemical shift difference.* TROSY spectra of 500  $\mu\text{M}$  [ $U\text{-}^2\text{H},^{15}\text{N}$ ]-labeled SPX2, SPX2 $\Delta\text{h7}$  or SPX2 $\Delta\text{linker}$  were recorded at 600 MHz. They were analyzed with CCPNMR and chemical shift differences were calculated in MATLAB using the following equation.

$$\Delta\delta = \sqrt{(\delta_{1\text{Ref}}(^1\text{H}) - \delta_1(^1\text{H}))^2 + (\delta_{2\text{Ref}}(^{15}\text{N})/5 - \delta_2(^{15}\text{N})/5)^2}$$

*H/D exchange spectroscopy.* A protonated SPX2 sample was exchanged from  $\text{H}_2\text{O}$ - to  $\text{D}_2\text{O}$ -containing buffer by multiple centrifugation steps using Amicon Ultra centricon (Merck Millipore) and was incubated in  $\text{D}_2\text{O}$ -containing buffer for 12 hours before recording H/D exchange. H/D exchange was calculated by intensity comparison of backbone amides derived from TROSY spectra of 200  $\mu\text{M}$  [ $^2\text{H}, ^{15}\text{N}, ^{13}\text{C}$ ]-labeled SPX2 in protonated buffer and of 200  $\mu\text{M}$  [ $^2\text{H}, ^{15}\text{N}, ^{13}\text{C}$ ]-labeled SPX2 in the  $\text{D}_2\text{O}$  containing buffer. The NMR spectra were acquired at 900 MHz in a buffer containing 25mM HEPES pH 7.0, 50mM NaCl, 0.5mM EDTA and 0.5mM TCEP.

*Titration experiments.*  $^{15}\text{N}$  TROSY spectra were recorded on 200  $\mu\text{M}$  [ $U\text{-}^{15}\text{N}$ ]-labeled SPX2 under different buffer conditions at 600 MHz. The salt influence was compared between a NMR buffer containing 50mM NaCl vs. 350 mM NaCl while IPx titration was compared in a buffer with no IPx vs. a 10x molar excess of IPx. The peak lists were extracted by CCPNMR and chemical shift perturbations were calculated in MATLAB using the following equation:  $\Delta\delta = \sqrt{(\delta_{1\text{Ref}}(^1\text{H}) - \delta_1(^1\text{H}))^2 + (\delta_{2\text{Ref}}(^{15}\text{N})/5 - \delta_2(^{15}\text{N})/5)^2}$ .

*Binding experiments.* TROSY spectra of 85  $\mu\text{M}$  [ $U\text{-}^{15}\text{N}$ ]-labelled SPX2 were recorded in the presence and absence of 255  $\mu\text{M}$  unlabeled Vtc4\*. Another TROSY spectra were recorded after IP6 was added in a 40x molar excess.

*RDC experiments.* Bacteriophage pf1 (ASLA Biotech) was added to the SPX2 sample and buffer exchanged by few ultracentrifugation steps (95'000 xg for 45 minutes at 4°C in the TLA-100 Beckman rotor). TROSY and anti-TROSY spectra were acquired of 200  $\mu\text{M}$  of [ $^2\text{H}, ^{15}\text{N}$ ]-labeled SPX2 and [ $^2\text{H}, ^{15}\text{N}$ ]-labeled SPX2 that contained approximately 18 mg/mL bacteriophage causing quadrupolar deuterium splitting of 7 Hz. The NMR experiments were recorded at 900 MHz and analyzed using CCPNMR.

### Bioinformatic analysis

*Structural modeling.* SPX2 protein sequence was submitted to Phyre2 Protein Fold Recognition server [45] for SPX2 structure calculation based on known x-ray structures.

*Classification of SPX proteins by domain architecture.* A list of SPX-containing protein sequences was obtained from the UniRef100 database, release 2020\_05 [46], [47].

Architecture information for each sequence in the list was scraped from the InterPro database [48] using a custom Python script and used to build a local SPX protein database (SPXdb). The generated SPXdb was filtered based on: (i) SPX domain position = 1; (ii) number of adjacent domains  $\geq 1$ ; (iii) SPX domain length  $\geq 130$  aa (based on *Secco et al., 2012*) [1]; and (iv) interdomain linker length  $\leq 300$  aa. Sequences in the filtered SPXdb were then grouped depending on the domain C-terminally adjacent to SPX.

*Motif search.* A list of protein sequences similar to Vtc2 from *S. cerevisiae* was obtained from Vtc2's UniRef50 cluster (id: UniRef50\_P43585) and aligned with Clustal-Omega [49] with default parameters (Gonnet matrix, 6 bits gap opening penalty, 1 bit gap extension penalty). Sequences were removed from the list if 100% identical to other entries or if not aligning well with Vtc2 in the linker region. SPX's helix 7 gap-less stretch was extracted from the alignment and used to generate a position-specific scoring matrix (PSSM) and a sequence logo [50], [51] using a custom Python script. The linker sequence of each entry of SPXdb was scanned with the generated PSSM. Hits were considered as such if the log-likelihood score exceeded the threshold value.

#### Protein stability measurements

The stability of protein samples was measured by thermal denaturation (15-95 °C) monitored by detecting the intrinsic fluorescence at 330 and 350 nm (Prometheus NT.48, *Nanotemper Technologies*). 50  $\mu\text{M}$  of SPX2 and 50  $\mu\text{M}$  of SPX2 $\Delta$ h7 were loaded into standard capillaries and measured at 75% laser power. 200  $\mu\text{M}$  of SPX2 alone as well as in the presence of a different ligand in a 10 times molar excess were applied into standard capillaries and measured at 20% laser power. The measurements were conducted in triplicates. The buffer used was 25mM HEPES pH 7.0, 250mM NaCl, 0.5mM EDTA and 0.5mM TCEP.

#### MicroScale Thermophoresis binding affinities

Vtc2, SPX2, Vtc4 and TTM4 proteins were first buffer exchanged to MST buffer (15mM HEPES pH 7.0, 50mM NaCl and 2mM DTT). Some MST buffer contained an additional 100 mM of NaCl or 2.5 mM of IPx. 0.2  $\mu\text{M}$  of His-tagged protein was mixed with 0.1  $\mu\text{M}$  of RED-tris-NTA 2nd generation dye (*Nanotemper Technologies*), incubated for 30 minutes at room temperature and subsequently centrifuged for 10 minutes at 21'000xg at 4 °C. The fluorescent protein sample was mixed in a serial dilution with the protein titrant,

loaded into premium capillaries and measured on Monolith NT.115 (*Nanotemper Technologies*) using 100 % laser power. Experiments were conducted in triplicates. The thermophoresis of the first 1.5 seconds after laser irradiation was considered and evaluated by Prism8 software (*GraphPad*).

#### Crosslinking-experiment

30  $\mu$ L of reactions containing 80  $\mu$ M of SPX2 and 80  $\mu$ M Vtc4\* in the presence or the absence of 20 molar excess of IP6 as well as negative controls comprising either 80  $\mu$ M of SPX2 and 80  $\mu$ M or Vtc4dTM, respectively, were kept on ice. The samples were heated to room temperature within 5 minutes and 2 mM 1,1'-carbonyldiimidazole (CDI) dissolved in 100% dimethyl sulfoxide (DMSO) was added. The reaction was quenched by the addition of 500 mM Tris pH 8.0 solution after 30 seconds. The reaction buffer used was 25mM HEPES pH 7.0, 150mM NaCl, 0.5mM EDTA and 0.5mM TCEP.

#### Vtc activity assay

The measurements of polyphosphate activity by Vtc complex were conducted as described previously [11].

## Supplementary Table

**Table S1: Overview of detected phosphorylation sites and mutation sites localized between SPX-helix  $\alpha 6$  and adjacent domain of SPX proteins.** The phosphorylation sites of *S. cerevisiae* were extracted from yeast database *thebiogrid.org* repository 4.2 and of *A. thaliana* from Arabidopsis database *PhosPhAt 4.0* [52]–[54].

<b>Protein</b>	<b>Organism</b>	<b>Phosphorylation sites / Mutation site*</b>
Vtc2	<i>S. cerevisiae</i>	S182, S187, S192, S193, S196
Vtc3	<i>S. cerevisiae</i>	S187, S190, S192, S195, S198
Gde1	<i>S. cerevisiae</i>	S254, T255, S256
Pho81	<i>S. cerevisiae</i>	T215
Pho91	<i>S. cerevisiae</i>	S295, S311, S312, T297
Syg1	<i>S. cerevisiae</i>	S342
SPX2	<i>A. thaliana</i>	S195
PHO1;H3	<i>A. thaliana</i>	S188
Xpr1	Human	*L218S [27]



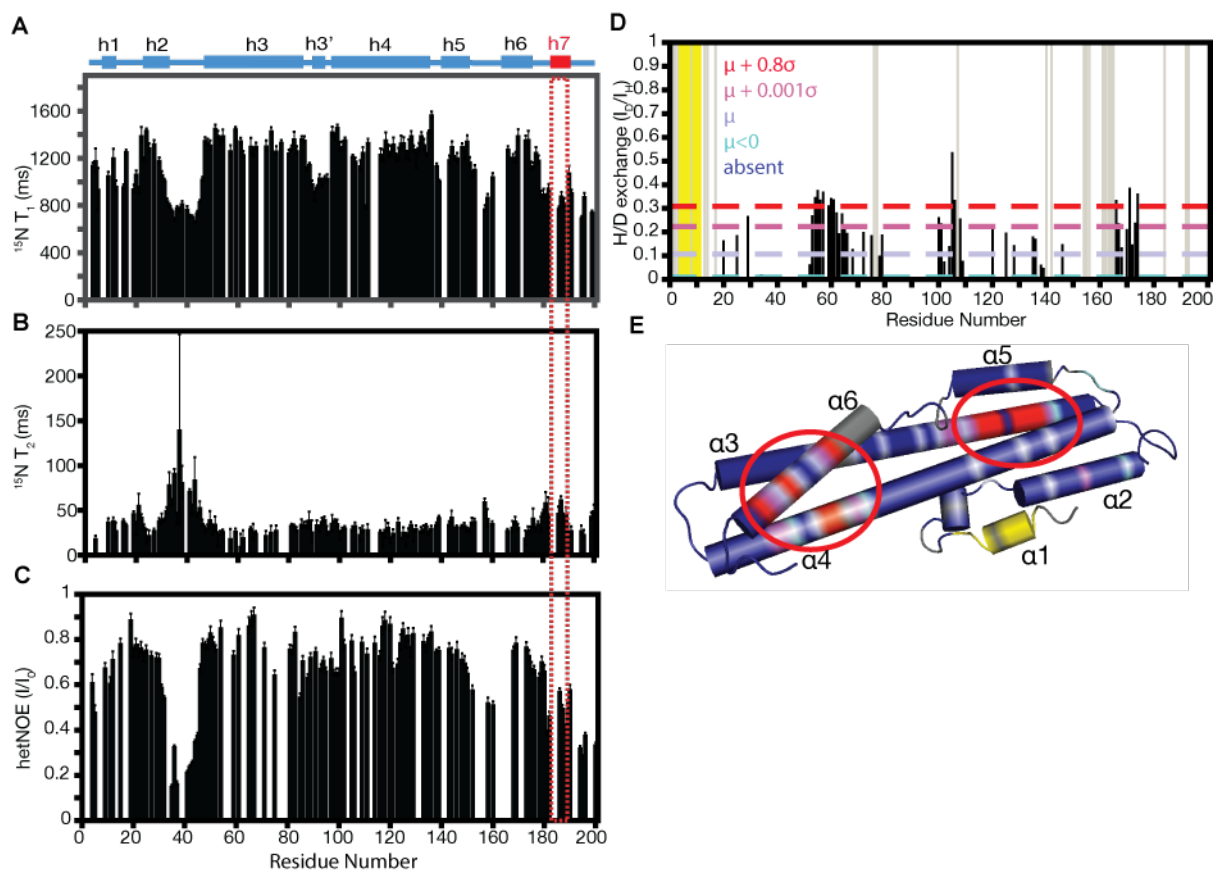


**Fig. S2: NMR characterization of SPX2.** (A, B, C) Relaxation of SPX2 evaluated by  $^{15}\text{N}$   $T_1$ ,  $^{15}\text{N}$   $T_2$  and hetNOE. Red dashed line represents the residues of  $\alpha$ -helix7. The buffer used was 25mM HEPES pH 7.0, 250mM NaCl, 0.5mM EDTA and 0.5mM TCEP. (D, E) H/D exchange plot of SPX2 residues and their indicated thresholds plotted on the structural model generated by *Phyre2*.  $I_D$  – intensities of resonances measured in  $\text{D}_2\text{O}$  buffer,  $I_H$  – intensities of resonances measured in  $\text{H}_2\text{O}$  buffer, yellow – residues experiencing intermediate chemical exchange, gray – residues not assigned. The buffer used was 25mM HEPES pH 7.0, 50mM NaCl, 0.5mM EDTA, 0.5mM TCEP.

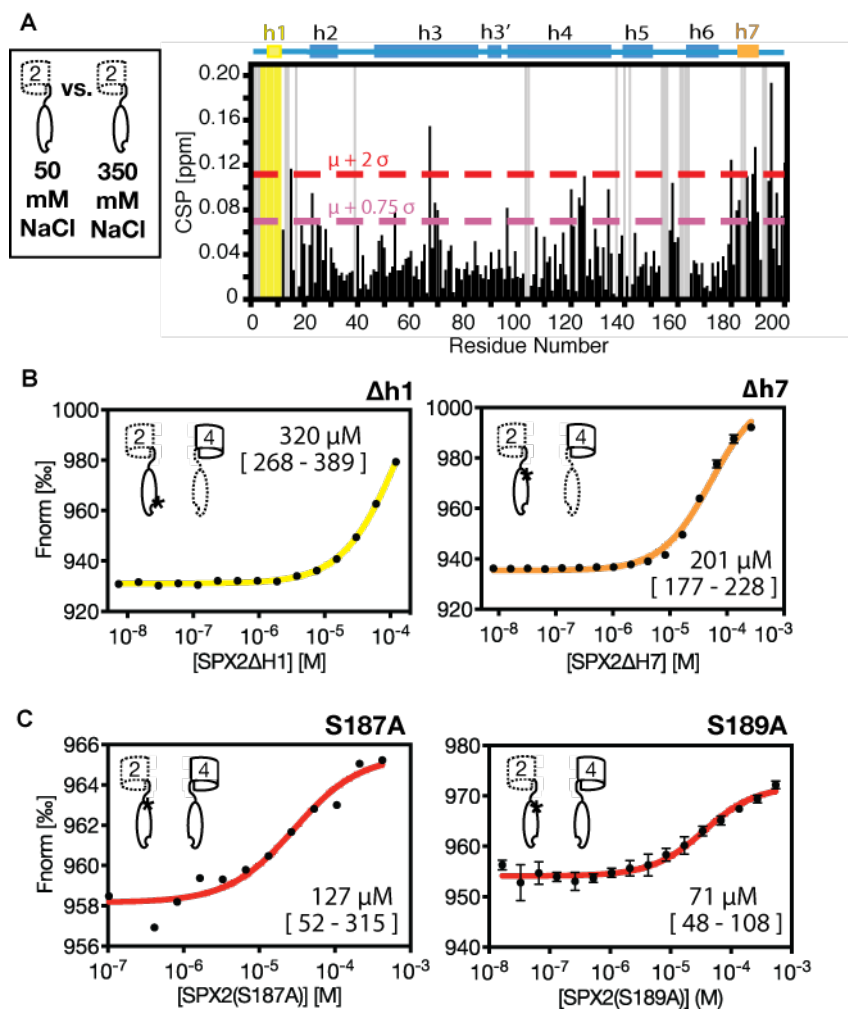


**Fig. S3: Characterization of the binding between SPX2 and Vtc4 constructs.** (A) Chemical shift perturbation plot of SPX2 induced by sodium chloride titration. Yellow - residues experiencing intermediate chemical exchange, gray - residues not assigned. (B) Binding affinities of SPX2 $\Delta$ h1 or SPX2 $\Delta$ h7, respectively, to TTM4 measured by MST. Asterisks display the lacking areas of protein in the cartoon scheme. (C) MST binding affinities of SPX2 with single mutations to Vtc4\*. Asterisks show the mutated positions in the cartoon scheme. The dissociation constants determined are displayed besides fits. The buffer used was 25mM HEPES pH 7.0, 50mM NaCl, 0.5mM EDTA, 0.5mM TCEP.

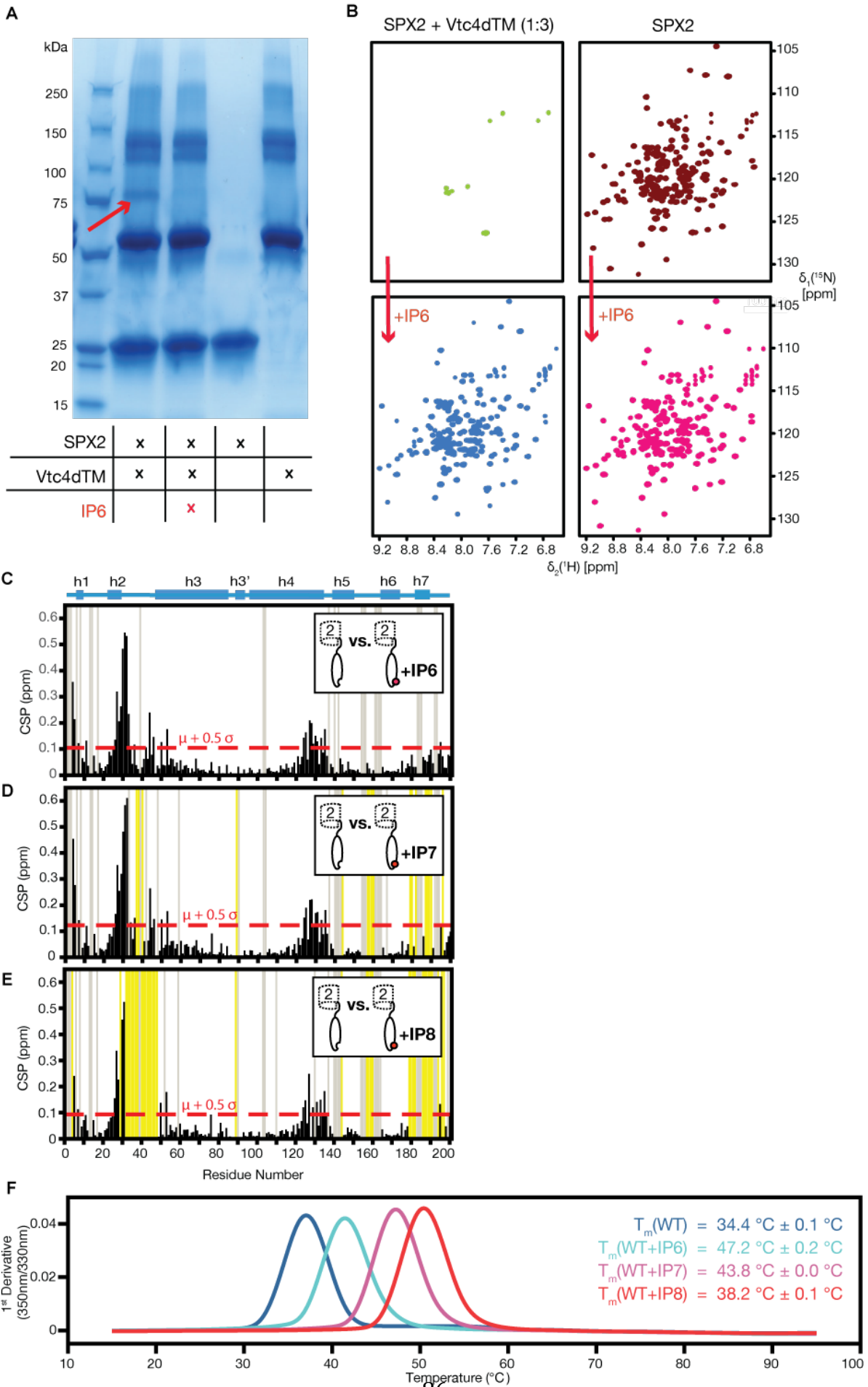


**Fig. S4: Characterization of SPX2 holo-states.** (A) Verification of SPX2 binding to Vtc4\* by a cross-linking experiment SPX and Vtc4dTM were cross-linked by CDI in either absence (1<sup>st</sup> lane) or presence of 20x molar excess of IP6 (2<sup>nd</sup> lane). Negative controls (3<sup>rd</sup> and 4<sup>th</sup> lane) are single components cross-linked in the absence of a IP6. The buffer used was 25mM HEPES pH 7.0, 150mM NaCl, 0.5mM EDTA, 0.5mM TCEP.

(B) Verification of SPX2 binding to Vtc4\* by NMR spectroscopy. [ $U$ - $^{15}N$ ]-SPX2 and unlabeled Vtc2dTM were recorded in a molar ratio 1:3 in the absence of IP6 and the presence of IP6 in a 40x molar excess. The buffer used was 25mM HEPES pH 7.0, 250mM NaCl, 0.5mM EDTA, 0.5mM TCEP. (C, D, E) Chemical shift perturbation plots of SPX2 apo- vs. holo-state while being bound to different ligands in a 10x molar excess. The buffer used was 25mM HEPES pH 7.0, 250mM NaCl, 0.5mM EDTA, 0.5mM TCEP. Yellow - residues experiencing intermediate chemical exchange, gray - residues not assigned. (F) Determination of protein stability of SPX2 in presence of different ligands by Prometheus (*Nanotemper Technologies*) in 25mM HEPES pH 7.0, 250mM NaCl, 0.5mM EDTA, 0.5mM TCEP.

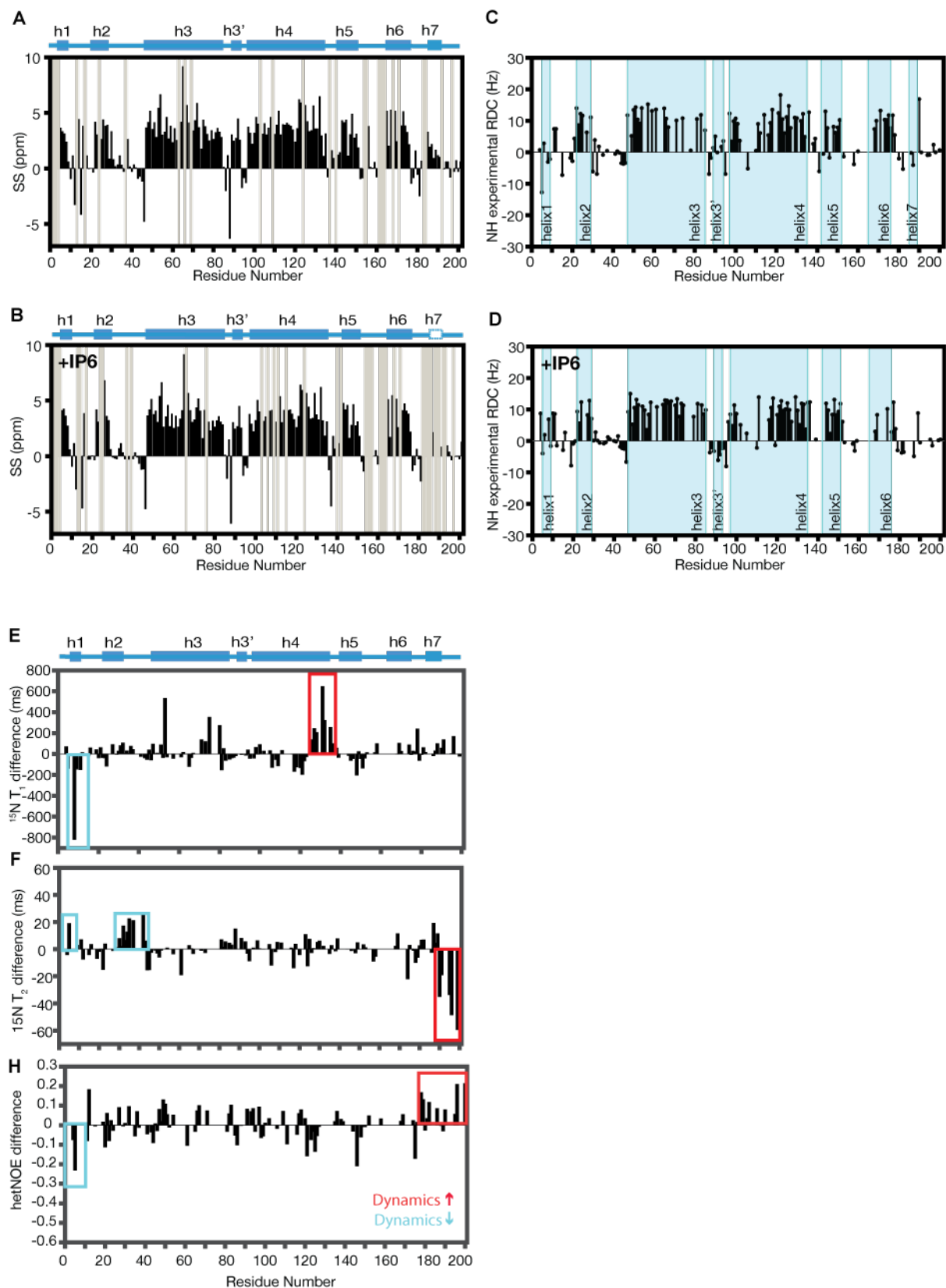


**Fig. S5: Structural and dynamics characterization of holo-state SPX2.** (A, B) Secondary elements determination by secondary chemical shift (SS) plots of SPX2 in the absence and the presence of 10x molar excess of IP6. (C, D). RDC plots of SPX  $\alpha$ -helices

in the absence and the presence of 10x molar excess of IP6. The buffer used was 25mM HEPES pH 7.0, 250mM NaCl, 0.5mM EDTA and 0.5mM TCEP. **(E, F, G)** Relaxation compared of apo- and holo-state of SPX2 while bound to IP6. Relaxation measurements recorded were  $^{15}\text{N}$   $T_1$ ,  $^{15}\text{N}$   $T_2$  and hetNOE and holo-state values were subtracted from apo-state values. The areas with reduced dynamics shown in cyan whereas increased dynamics are shown in red. For all experiments the buffer used was 25mM HEPES pH 7.0, 250mM NaCl, 0.5mM EDTA and 0.5mM TCEP.

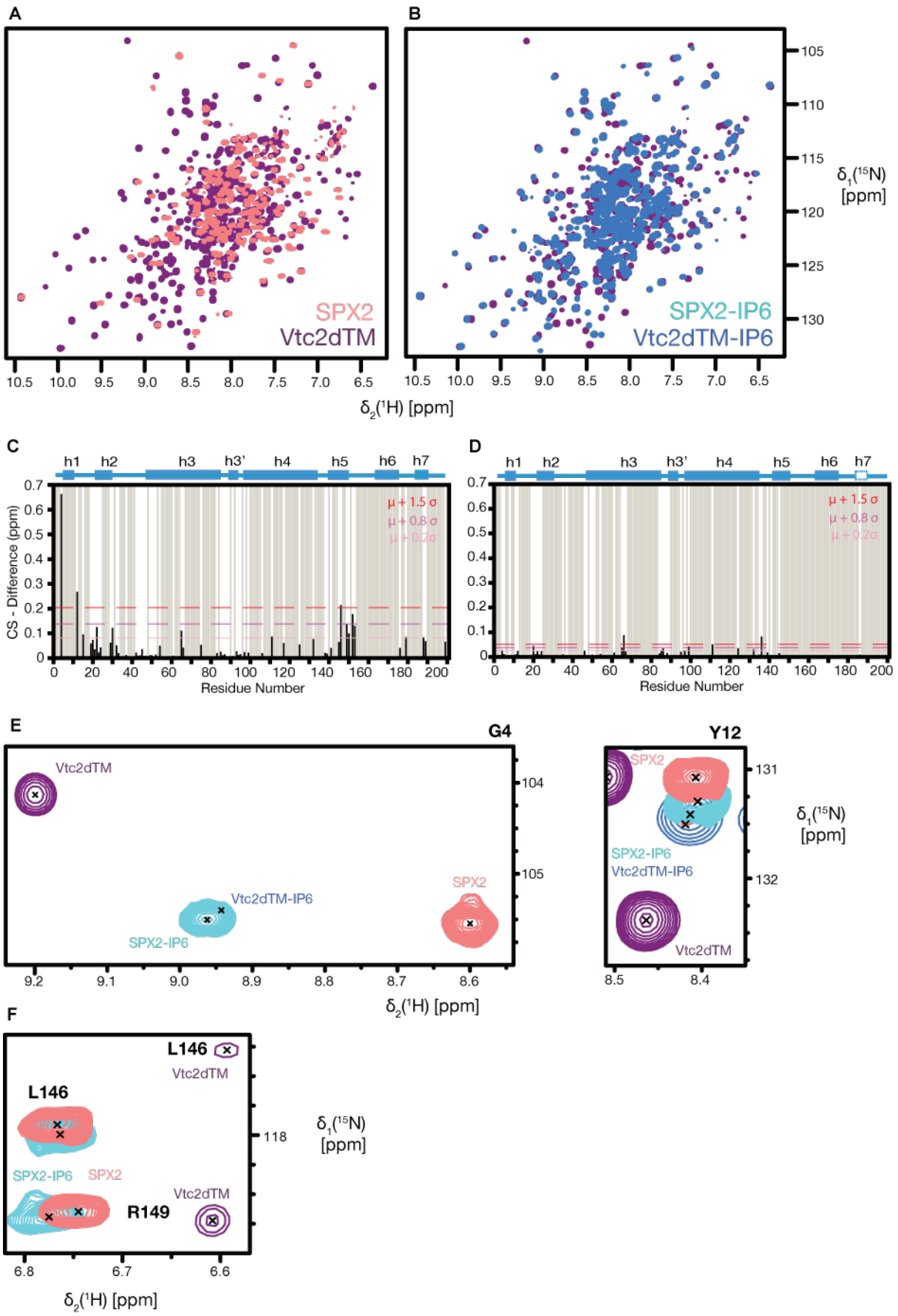
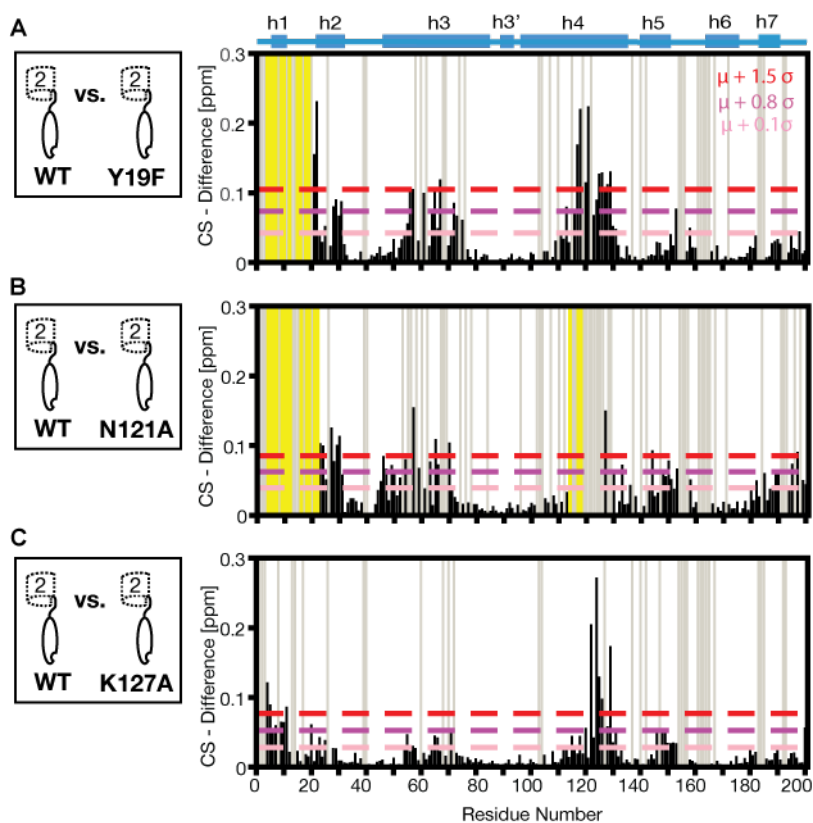


**Fig. S6: Structural characterization of SPX2 in Vtc2\* in the apo- and holo-state. (A, B) Overlay of NMR spectra between SPX2 and Vtc2dTM or SPX2-IP6 and Vtc2dTM-IP6, respectively. (C, D) Chemical shift differences between SPX2 and Vtc2dTM or SPX2-IP6 and Vtc2dTM-IP6, respectively. (E) NMR section of residues of apo and holo-states in  $\alpha$ -helix1 and in the loop region between  $\alpha$ -helix1 and  $\alpha$ -helix2. (F) NMR section of residues of apo and holo-states in  $\alpha$ -helix5. The buffer used was 25mM HEPES pH 7.0, 250mM NaCl, 0.5mM EDTA and 0.5mM TCEP.**



**S7: Structural characterization of pseudo-active mutants of SPX2.** (A, B, C) The plots are displaying chemical shift difference between the wild-type SPX2 and single-point mutations of SPX2 (Y19F, N121A, K127A). Yellow - residues experiencing intermediate chemical exchange, gray - residues not assigned.

## Supplementary references

- [38] K. Pervushin, R. Riek, G. Wider, and K. Wüthrich, "Attenuated T2 relaxation by mutual cancellation of dipole-dipole coupling and chemical shift anisotropy indicates an avenue to NMR structures of very large biological macromolecules in solution," *PNAS*, vol. 94, no. 11, pp. 12366–12371, 1997.
- [39] M. Salzmann, G. Wider, K. Pervushin, H. Senn, and K. Wüthrich, "TROSY-type Triple-Resonance Experiments for Sequential NMR Assignments of Large Proteins," *JACS*, vol. 121, no. 4, pp. 844–848, 1999.
- [40] Y. Xia, K. Sze, and G. Zhu, "Transverse relaxation optimized 3D and 4D 15N/15N separated NOESY experiments of 15N labeled proteins," *J. Biomol. NMR*, vol. 18, no. 3, pp. 261–268, 2000.
- [41] P. Güntert, V. Dötsch, G. Wider, and K. Wüthrich, "Processing of multi-dimensional NMR data with the new software PROSA," *J. Biomol. NMR*, vol. 2, no. 6, pp. 619–629, Nov. 1992.
- [42] C. Bartels, T. Xia, M. Billeter, P. Güntert, and K. Wüthrich, "The program XEASY for computer-supported NMR spectral analysis of biological macromolecules," *J. Biomol. NMR*, vol. 6, no. 1, pp. 1–10, 1995.
- [43] G. Zhu, Y. Xia, L. K. Nicholson, and K. H. Sze, "Protein Dynamics Measurements by TROSY-Based NMR Experiments," *J Magn Reson.*, vol. 143, no. 2, pp. 423–426, 2000.
- [44] W. F. Vranken, W. Boucher, T. J. Stevens, R. H. Fogh, A. Pajon, M. Llinas, E. L. Ulrich, J. L. Markley, J. Ionides, and E. D. Laue, "The CCPN data model for NMR spectroscopy: development of a software pipeline," *Proteins*, vol. 59, no. 4, pp. 687–96, Jun. 2005.
- [45] L. A. Kelley, S. Mezulis, C. M. Yates, M. N. Wass, and M. J. E. Sternberg, "The Phyre2 web portal for protein modeling, prediction and analysis," *Nat. Protoc.*, vol. 10, no. 6, pp. 845–858, 2015.
- [46] T. U. Consortium, "UniProt: a worldwide hub of protein knowledge," *Nucleic Acids Res.*, vol. 47, no. D1, pp. D506–D515, Jan. 2019.
- [47] B. E. Suzek, Y. Wang, H. Huang, P. B. McGarvey, C. H. Wu, and the U. Consortium, "UniRef clusters: a comprehensive and scalable alternative for improving sequence similarity searches," *Bioinformatics*, vol. 31, no. 6, pp. 926–932, Mar. 2015.
- [48] M. Blum, H.-Y. Chang, S. Chuguransky, T. Grego, S. Kandasamy, A. Mitchell, G. Nuka, T. Paysan-Lafosse, M. Qureshi, S. Raj, L. Richardson, G. A. Salazar, L. Williams, P. Bork, A. Bridge, J. Gough, D. H. Haft, I. Letunic, A. Marchler-Bauer, H. Mi, D. A. Natale, M. Necci, C. A. Orengo, A. P. Pandurangan, C. Rivoire, C. J. A. Sigrist, I. Sillitoe, N. Thanki, P. D. Thomas, S. C. E. Tosatto, C. H. Wu, A. Bateman, and R. D. Finn, "The InterPro protein families and domains database: 20 years on," *Nucleic Acids Res.*, Nov. 2020.
- [49] F. Madeira, Y. mi Park, J. Lee, N. Buso, T. Gur, N. Madhusoodanan, P. Basutkar, A. R. N. Tivey, S. C. Potter, R. D. Finn, and R. Lopez, "The EMBL-EBI search and sequence analysis tools APIs in 2019," *Nucleic Acids Res.*, vol. 47, no. W1, pp. W636–W641, Jul. 2019.
- [50] T. D. Schneider and R. M. Stephens, "Sequence logos: a new way to display consensus sequences," *Nucleic Acids Res.*, vol. 18, no. 20, pp. 6097–6100, Oct. 1990.
- [51] A. Tareen and J. B. Kinney, "Logomaker: beautiful sequence logos in Python," *Bioinformatics*, vol. 36, no. 7, pp. 2272–2274, Apr. 2020.
- [52] J. L. Heazlewood, P. Durek, J. Hummel, J. Selbig, W. Weckwerth, D. Walther, and W. X. Schulze, "PhosPhAt: a database of phosphorylation sites in *Arabidopsis thaliana* and a plant-specific phosphorylation site predictor," *Nucleic Acids Res.*, vol. 36, no. suppl\_1, pp. D1015–D1021, Jan. 2008.
- [53] P. Durek, R. Schmidt, J. L. Heazlewood, A. Jones, D. MacLean, A. Nagel, B. Kersten, and W. X. Schulze, "PhosPhAt: the *Arabidopsis thaliana* phosphorylation site database. An update," *Nucleic Acids Res.*, vol. 38, no. suppl\_1, pp. D828–D834, Jan. 2010.

- [54] M. Zulawski, R. Braginets, and W. X. Schulze, "PhosPhAt goes kinases—searchable protein kinase target information in the plant phosphorylation site database PhosPhAt," *Nucleic Acids Res.*, vol. 41, no. D1, pp. D1176–D1184, Jan. 2013.

## In-depth discussion & outlook

The eukaryotic, intracellular homeostasis relies on many proteins that contain a SPX domain. Previous studies indicated that SPX domains are stimulated by inositol phosphate and inositol pyrophosphates *in-vitro* [1] and specific inositol pyrophosphates *in-vivo* [2], [3]. The structure-function relation and its dependence upon inositol (pyro-) phosphate is largely elusive.

### Undiscovered structural element of the SPX domain

The SPX domain of Vtc2, SPX2, residing in the VTC complex is the first SPX domain assigned in solution. It is in good agreement with the known SPX structures in the crystalline state, which contain  $\alpha$ -helix1 to  $\alpha$ -helix6 including a  $\alpha$ -helix3' that was seen in one of the SPX structures [1]. The assessment of SPX structure in the solution revealed another unreported helical region at the C-terminus of SPX ( $\alpha$ -helix7) expanding the known SPX domain boundaries. The first reported data on the dynamics of the SPX domain suggests that  $\alpha$ -helix7 is a partial  $\alpha$ -helix. This would be in consensus with Vtc4. It is the only SPX protein crystalized so far that contains  $\alpha$ -helix7-related area. In the two crystalized isoforms the  $\alpha$ -helix7-region was disordered [1]. This dynamic nature of  $\alpha$ -helix7 could be responsible for not obtaining protein crystals of SPX2 and Vtc2 and having a low quality spectra of side-chain NMR assignment experiments and NOESY spectra of specifically ILV-labeled samples (not shown here) that are useful for precise structure calculation. The motif of  $\alpha$ -helix7 is preserved in few of the SPX proteins with a particular domain architecture suggesting that the  $\alpha$ -helix7 is protein specific and raises the question if it has a functional relevance. Here it was found that  $\alpha$ -helix7 has most likely a key functional role while involved in the interaction with the SPX domain of Vtc4. The functional relevance of this region in other SPX proteins could be addressed while using the read outs from known functional assays. If deletion of the region mapped to  $\alpha$ -helix7 would have a similar effect on the PP<sub>i</sub> homeostasis as deficiency or lack of the whole SPX domain, this is a good indicator of the functional relevance of  $\alpha$ -helix7 for the respective SPX protein. Deleting  $\alpha$ -helix7-region of SPX in yeast Pho81 would result in a constitutively active PHO pathway and a upregulation of P<sub>i</sub> responsive genes [4], [5]. For SPX-containing Pho1 or stand-alone SPX proteins in

plants, a deleted  $\alpha$ -helix7-region would lead to a hyper-accumulation of  $P_i$  that is causing dwarfism of plants [1], [3]. In mammalian cells, the deficiency of SPX by deletion of its  $\alpha$ -helix7-region in Xpr1 by would impair the  $P_i$  efflux [6].

### **SPX as inhibitory unit of SPX proteins**

The potential functional role of SPX2 within the VTC complex was investigated by the protein binding studies. Earlier pull-down experiments indicated that Vtc components, Vtc1-4, interact with each other but no further biophysical studies were conducted [7]. Here it was shown that the cytosolic components of Vtc2 and Vtc4 interact in a low  $\mu$ M range via their SPX domains. This is the first time a SPX-SPX interaction was reported. It hypothesized that the conserved  $\alpha$ -helix1 and protein specific  $\alpha$ -helix7 substantially contribute to this electrostatic interaction. Highly negatively charged inositol (pyro-) phosphates were shown to disrupt the SPX-SPX interaction interface. Also amino-acid substitutions, which cause pseudo-activity in the VTC complex *in-vitro* [1] and *in-vivo* [2], abrogated this interaction. Altogether, this suggests that the SPX domain of Vtc2 acts as an internal inhibitor of VTC polyphosphate activity. Indeed, this could explain observations to previous published studies. SPX was shown to have a negative effect on  $P_i$ -uptake rate of low-affinity  $P_i$  transporters in yeast [8] and on Pho81, which is keeping  $P_i$ -responsive signaling (PHO) pathway repressed [4], [5]. Furthermore, SPX was shown to act as an inhibitor of  $P_i$ -starvation response (PSR) transcription factor repressing  $P_i$ -starvation signaling in plants [3], [9]–[12].

### **Abolishment of SPX inhibition by inositol (pyro-) phosphates**

Earlier studies annotated the binding pocket of inositol phosphate in SPX domains supported by x-ray crystallography and mutational studies [1]. Selected mutations in the binding pocket not only affected IP6 binding but also the binding of inositol pyrophosphate [1]. The results shown here confirm this finding by displaying that inositol phosphate and pyrophosphate bind at same SPX site. Additionally, it was shown that ligand binding induces a change in the relative orientation of helix  $\alpha$ 1 and its adjacent loop as well as in helix  $\alpha$ 3'. This is in agreement with the study of Wild *et al.* suggesting that  $\alpha$ -helix1 allows a ligand-induced change of SPX conformation. Few of

their apo-SPX structures had a disordered  $\alpha$ -helix1 and a deletion of  $\alpha$ -helix1 and its adjacent loop affected dramatically ligand-binding affinity [1]. Considering that  $\alpha$ -helix1 is involved in the ligand binding but also contributes to the SPX-SPX interaction between Vtc2 and Vtc4 and to a binding between SPX2 and TTM2, a central domain of Vtc2, would allow the hypothesis that the ligand competes with SPX4 and TTM2 for  $\alpha$ -helix1-binding. This could be one of the key elements of the molecular mechanism of SPX. Indeed, inositol (pyro-) phosphate was shown to stimulate protein activity via its SPX domain in many cases [1]–[3], [13]–[17]. The functional importance of the SPX binding pocket is underlined by the fact that many SPX proteins are dysfunctional if the binding pocket of inositol (pyro-) phosphates is impaired [1], [2], [4], [17]–[19].

This work shows that inositol (pyro-) phosphates and pseudo-activating mutations in the SPX domain disrupt the SPX-SPX interaction. This is correlated to unleashing VTC activity. Thus, this suggests that inositol (pyro-) phosphates are molecular-assembly disruptors. Inositol (pyro-) phosphates and pseudo-activating mutations could facilitate liberation of protein-elements or proteins from the internal or external inhibitory SPX domains. This could possibly explain the mechanism behind the Pho81 function. Pho81 consists of a SPX domain and two other domains. Its inhibitor activity is unleashed after adding 1-IP7 [13], [14]. Under this condition, a part of the central ANK domain of Pho81 binds to Pho80-Pho85 kinase [14], [20]. Possibly, this part of the ANK domain was bound earlier by SPX and was hence not accessible to the kinase. Once the inhibitory effect of SPX is abolished by 1-IP7, part of ANK can get exposed, bind to the kinase and inhibit its activity.

Possibly, this could be similar for stand-alone SPX domains that facilitate a binding to a transcription factor upon the presence of inositol (pyro-) phosphates [1], [3]. These stand-alone SPX proteins have around 50-70 residues at C-terminus that are not annotated [21] and delocalize from the nucleus to the cytosol upon deletion of the SPX domain [11]. Possibly, SPX and the C-terminal part of stand-alone SPX proteins interact. 1,5-IP8, which is suggested to play a role *in-vivo* [3], could disrupt the binding between the SPX domain and the C-terminal part of the protein allowing the SPX domain of the stand-alone SPX proteins to interact with the PSR transcription factor. An impaired binding pocket abolishes the binding of the stand-alone SPX proteins and the PSR transcription factor [3]. An impaired binding pocket might also affect both, the binding

of SPX to the C-terminal part of the protein as well as the binding to PSR transcription factor. Subsequently, Together with collaborators we could show that CC domain of PSR transcription factor responsible for this protein interaction can bind 1,5-IP8 itself. This is suggesting that 1,5-IP8 acts as a molecular glue between stand-alone SPX proteins and the PSR transcription factor; see the publication in the attachments cited as [3].

SPX domain negatively influences the  $P_i$  uptake rate of low-affinity  $P_i$  transporters in a Spl2-dependent way [8]. This direct inhibitory effect caused by Spl2 was not yet tested in any dependence of inositol pyrophosphate. However, other studies indicate that 5-IP7 could play an important role during  $P_i$  homeostasis at rich  $P_i$  conditions [22] under which low-affinity  $P_i$  transporters import  $P_i$  [23]. It is possible that these  $P_i$  transporters are open in the presence of 5-IP7 abolishing any inhibitory effects.

## Potential molecular mechanism of SPX

The molecular mechanism of the VTC complex is composed of two main events. The first event, as mentioned above, comprises the abolishment of the inhibitory effect of SPX domains after inositol (pyro-) phosphate binding. This is reflected in ligand-induced conformation change of conserved  $\alpha$ -helix1. The second part of the mechanism is a key event for the activity itself. We speculate that binding of inositol (pyro-) phosphates to SPX exposes  $\beta$ -barrel of TTM4 and  $\alpha$ -helix7. Thereupon, the serines of  $\alpha$ -helix7 could get phosphorylated by cellular kinases and subsequently pyrophosphorylated by inositol pyrophosphates. The pyrophosphorylated  $\alpha$ -helix7 could activate the VTC complex. This could explain many observations from previous and our study.  $\alpha$ -helix7 is contributing to the formation of the inhibitory SPX interaction via its serines and has increased dynamics in the ps-ns time range when a ligand is bound to SPX allowing to fluctuate between different domains.  $\alpha$ -helix7 of Vtc2 and Vtc3 contains many detected phosphorylated serines - listed in *thebiogrid.org* - that could be used as a basis to transfer the  $\beta$ -phosphoryl group of inositol pyrophosphates non-enzymatically [24], [25]. Inositol pyrophosphates were shown to be potent agonists of VTC activity in sub- $\mu$ M range while inositol phosphate stimulates VTC activity only above 100  $\mu$ M [1], [2] although all of them bind tightly to the SPX domain (data not shown here).  $PP_i$  could serve as the actual activator of ATPase activity of TTM4, which is required for the synthesis of polyphosphate chains, while enhancing the reaction time by up to 90

times [7]. It is possible that dynamic pyrophosphorylated  $\alpha$ -helix7 reaching out to TTM4 could activate VTC complex in an analogous way. Most importantly,  $\alpha$ -helix7 whose several serines were mutated to alanines abolished polyphosphate pools *in-vivo* (personal communication to Andreas Mayer) and led to a disrupted binding between SPX2 and Vtc4 *in-vitro* (data not shown).

Theoretically, this second event should have been reflected in the determined dissociation constant values for SPX2 and Vtc4 as well. However, as Vtc4 was produced recombinantly in *E. coli*, it lacked any post-translational modifications like phosphorylations. These are essential for the above-described mechanism.

Bioinformatical data indicated that the motif of  $\alpha$ -helix7 is preserved in few SPX proteins. A mapping of  $\alpha$ -helix7 region to other SPX proteins reveals protein sequences that contain phosphorylation sites and a mutation causing a protein malfunction in humans [26]. Hence,  $\alpha$ -helix7 is a protein specific element of the SPX domain and could be responsible for diversification of SPX protein functions.

The comprehensive understanding of SPX system in the VTC complex by this work can help to develop new experimental concepts for other SPX systems. Knowing specific inositol pyrophosphates required for each SPX system correlated to given external  $P_i$ -conditions can pin down the whole picture of  $P_i$  homeostasis. Finally, this can lead to therapy approaches for patients with neurodegenerative primary familial brain calcification and engineering of a new kind of crops with a much better phosphate efficiency uptake limiting the use of fertilizers worldwide.

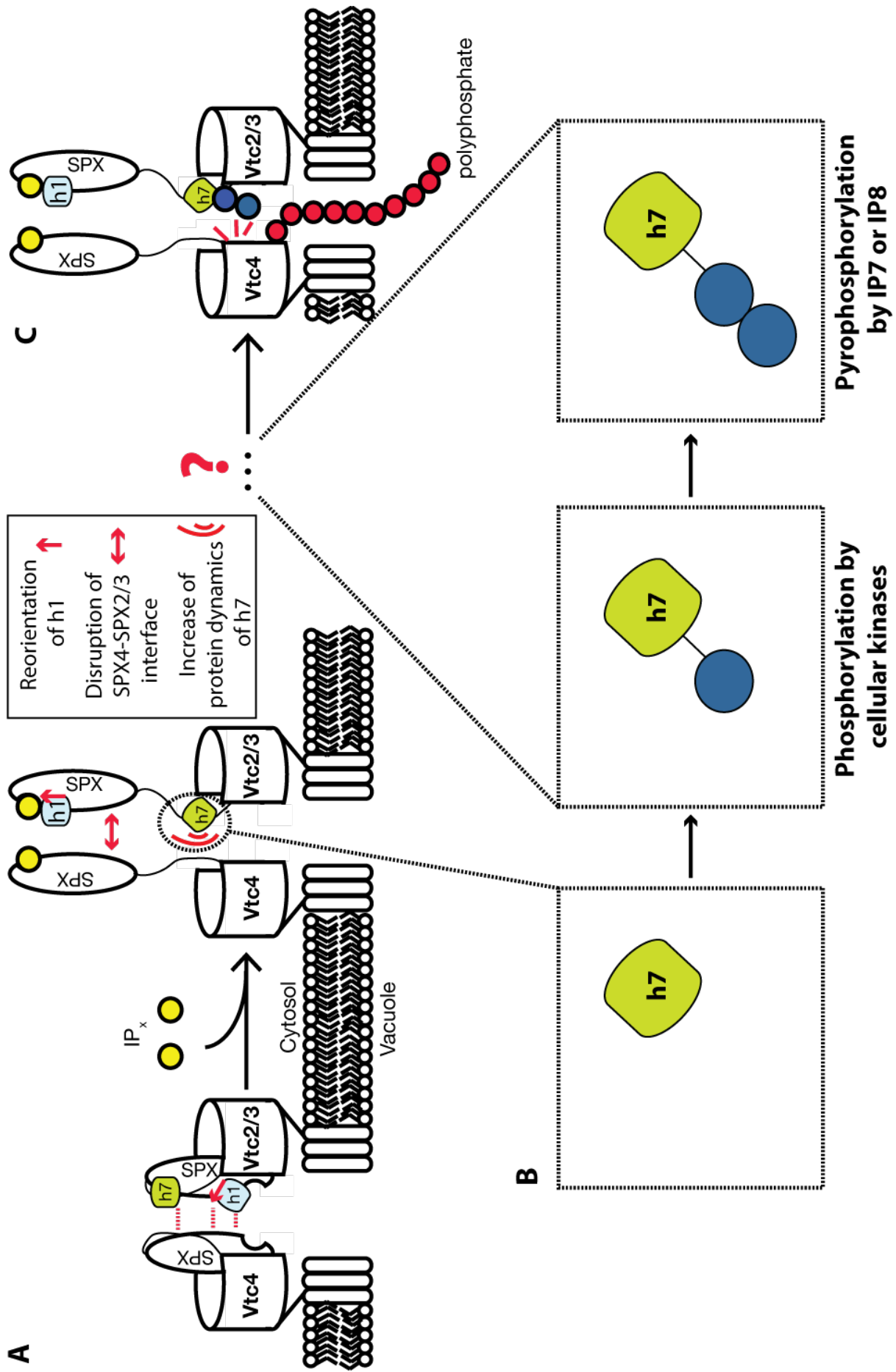


**Fig. 1: Emerging molecular mechanism of SPX.** (A) The structural and functional data obtained suggest  $\alpha$ -helix1 (h1) reorientation and protein dynamics in the previously unreported helix  $\alpha$ 7 region (h7) upon IPx binding, leading to a disruption of SPX-SPX protein interface. (B) A speculation suggesting dynamic h7 to get subsequently phosphorylated by cellular kinases and pyrophosphorylated by IP7 or IP8. (C) Hypothetically pyrophosphorylated h7 activate VTC activity generating polyphosphates.

## References

- [1] R. Wild, R. Gerasimaite, J.-Y. Jung, V. Truffault, I. Pavlovic, A. Schmidt, A. Saiardi, H. J. Jessen, Y. Poirier, M. Hothorn, and A. Mayer, "Control of eukaryotic phosphate homeostasis by inositol polyphosphate sensor domains," *Science*, vol. 352, no. 6288, pp. 986–990, 2016.
- [2] R. Gerasimaite, I. Pavlovic, S. Capolicchio, A. Hofer, A. Schmidt, H. J. Jessen, and A. Mayer, "Inositol Pyrophosphate Specificity of the SPX-Dependent Polyphosphate Polymerase VTC," *ASC Chem. Biol.*, no. 12, p. 648–653, 2017.
- [3] M. K. Ried, R. Wild, J. Zhu, L. Broger, R. K. Harmel, L. A. Hothorn, D. Fiedler, and M. Hothorn, "Inositol pyrophosphates promote the interaction of SPX domains with the coiled-coil motif of PHR transcription factors to regulate plant phosphate homeostasis," *BioRxiv*, vol. 12, 2019.
- [4] C. L. Creasy, S. L. Madden, and L. W. Bergman, "Molecular analysis of the PHO81 cerevisiae of *Saccharomyces*," *Nucleic Acids Res.*, vol. 21, no. 8, pp. 1975–1982, 1993.
- [5] N. Ogawa, K. Noguchi, H. Sawai, and Y. Yamashita, "Functional Domains of Pho81p , an Inhibitor of Pho85p Protein Kinase , in the Transduction Pathway of P i Signals in *Saccharomyces cerevisiae*," *Mol. Cell. Biol.*, vol. 15, no. 2, pp. 997–1004, 1995.
- [6] X. Li, C. Gu, S. Hostachy, S. Sahu, C. Wittwer, H. J. Jessen, D. Fiedler, H. Wang, and S. B. Shears, "Control of XPR1-dependent cellular phosphate efflux by InsP8 is an exemplar for functionally-exclusive inositol pyrophosphate signaling," *PNAS*, vol. 117, no. 7, pp. 3568–3574, 2020.
- [7] M. Hothorn, H. Neumann, E. D. Lenherr, M. Wehner, V. Rybin, P. O. Hassa, A. Uttenweiler, M. Reinhardt, A. Schmidt, J. Seiler, A. G. Ladurner, C. Herrmann, K. Scheffzek, and A. Mayer, "Catalytic Core of a Membrane-Associated Eukaryotic Polyphosphate Polymerase," *Science*, vol. 324, no. 5926, pp. 513–516, 2009.
- [8] H. C. Huerlimann, B. Pinson, M. Stadler-Waibel, S. C. Zeeman, and F. M. Freimoser, "The SPX domain of the yeast low-affinity phosphate transporter Pho90 regulates transport activity," *EMBO*, vol. 10, no. 9, pp. 1003–1008, 2009.
- [9] M. I. Puga, I. Mateos, R. Charukesi, Z. Wang, J. M. Franco-Zorrilla, L. De Lorenzo, M. L. Irigoyen, S. Masiero, R. Bustos, J. Rodríguez, A. Leyva, V. Rubio, H. Sommer, and J. Paz-Ares, "SPX1 is a phosphate-dependent inhibitor of PHOSPHATE STARVATION RESPONSE 1 in *Arabidopsis*," *PNAS*, vol. 111, no. 41, pp. 14947–52, 2014.
- [10] F. Liu, Z. Wang, H. Ren, C. Shen, Y. Li, H. Ling, C. Wu, and X. Lian, "OsSPX1 suppresses the function of OsPHR2 in the regulation of expression of OsPT2 and phosphate homeostasis in shoots of rice," *Plant J.*, vol. 62, no. 3, pp. 508–517, 2010.
- [11] Z. Wang, W. Ruan, J. Shi, L. Zhang, D. Xiang, C. Yang, C. Li, Z. Wu, and Y. Liu, "Rice SPX1 and SPX2 inhibit phosphate starvation responses through interacting with PHR2 in a phosphate-dependent manner," *PNAS*, vol. 111, no. 41, pp. 14953–14958, 2014.
- [12] W. Qi, I. W. Manfield, S. P. Muench, and A. Baker, "AtSPX1 affects the AtPHR1 – DNA-binding equilibrium by binding monomeric AtPHR1 in solution," *Biochem. J.*, vol. 474, no. 21, pp. 3675–3687, 2017.
- [13] Y. Lee, S. Mulugu, J. D. York, and E. K. O. Shea, "Regulation of a Cyclin-CDK-CDK Inhibitor Complex by Inositol Pyrophosphates," *Science*, vol. 316, no. 5821, pp. 109–112, 2007.
- [14] Y. Lee, K. Huang, F. A. Quioco, and E. K. O. Shea, "Molecular basis of cyclin-CDK-CKI regulation by reversible binding of an inositol pyrophosphate," *Nat. Chem. Biol.*, vol. 4, no. 1, pp. 25–32, 2008.
- [15] D. Giovannini, J. Touhami, P. Charnet, M. Sitbon, and J. Battini, "Inorganic Phosphate Export by the Retrovirus Receptor XPR1 in Metazoans," *Cell Rep.*, vol. 3, no. 6, pp. 1866–1873, 2013.

- [16] J. Battini, J. E. J. Rasko, and A. D. Miller, "A human cell-surface receptor for xenotropic and polytropic murine leukemia viruses: Possible role in G protein-coupled signal transduction," *PNAS*, vol. 96, no. February, pp. 1385–1390, 1999.
- [17] E. Potapenko, C. D. Cordeiro, G. Huang, M. Storey, C. Wittwer, A. K. Dutta, H. J. Jessen, V. J. Starai, and R. Docampo, "5-Diphosphoinositol Pentakisphosphate (5-IP7) Regulates Phosphate Release from Acidocalcisomes and Yeast Vacuoles," *J. Biol. Chem.*, vol. 293, no. 49, pp. 19101–19112, 2018.
- [18] D. Desmarini, S. Lev, D. Furkert, B. Crossett, A. Saiardi, K. Kaufman-Francis, C. Li, T. C. Sorrell, L. Wilkinson-White, J. Matthews, D. Fiedler, and J. T. Djordjevic, "IP7-SPX Domain Interaction Controls Fungal Virulence by Stabilizing Phosphate Signaling Machinery," *MBio*, vol. 11, no. 5, pp. e01920–20, Oct. 2020.
- [19] U. López-Sánchez, S. Tury, G. Nicolas, M. S. Wilson, S. Jurici, X. Ayrignac, V. Courgnaud, A. Saiardi, M. Sitbon, and J.-L. Battini, "Interplay between PFBC-associated SLC20A2 and XPR1 phosphate transporters requires inositol polyphosphates for control of cellular phosphate homeostasis," *J. Biol. Chem.*, vol. 295, no. 28, pp. 9366–9378, 2020.
- [20] S. Huang, D. A. Jeffery, M. D. Anthony, and E. K. O. Shea, "Functional Analysis of the Cyclin-Dependent Kinase Inhibitor Pho81 Identifies a Novel Inhibitory Domain," *Mol. Cell. Biol.*, vol. 21, no. 19, pp. 6695–6705, 2001.
- [21] D. Secco, C. Wang, B. A. Arpat, Z. Wang, Y. Poirier, S. D. Tyerman, P. Wu, H. Shou, and J. Whelan, "The emerging importance of the SPX domain-containing proteins in phosphate homeostasis," *New Phytol.*, vol. 193, pp. 842–851, 2012.
- [22] J. Choi, A. Rajagopal, Y. Xu, J. D. Rabinowitz, and E. K. O'Shea, "A systematic genetic screen for genes involved in sensing inorganic phosphate availability in *Saccharomyces cerevisiae*," *PLoS One*, vol. 12, no. 5, p. e0176085, 2017.
- [23] D. D. Wykoff, A. H. Rizvi, J. M. Raser, B. Margolin, and E. K. O'Shea, "Positive feedback regulates switching of phosphate transporters in *S. cerevisiae*," *Mol. Cell*, vol. 27, no. 6, pp. 1005–1013, 2007.
- [24] C. E. Hand and J. F. Honek, "Phosphate transfer from inositol pyrophosphates InsP5PP and InsP4(PP)2: A semi-empirical investigation," *Bioorg. Med. Chem. Lett.*, vol. 17, no. 1, pp. 183–188, 2007.
- [25] R. Bhandari, A. Saiardi, Y. Ahmadibeni, A. M. Snowman, A. C. Resnick, T. Z. Kristiansen, H. Molina, A. Pandey, J. K. Werner, K. R. Juluri, Y. Xu, G. D. Prestwich, K. Parang, and S. H. Snyder, "Protein pyrophosphorylation by inositol pyrophosphates is a posttranslational event," *Proc. Natl. Acad. Sci.*, vol. 104, no. 39, p. 15305 LP – 15310, Sep. 2007.
- [26] A. Legati, D. Giovannini, G. Nicolas, U. López-sánchez, B. Quintáns, J. Oliveira, R. L. Sears, E. M. Ramos, E. Spiteri, M.-J. Sobrido, Á. Carracedo, C. Castro-Fernández, S. Cubizolle, B. L. Fogel, C. Goizet, J. C. Jen, S. Kirdlarp, A. E. Lang, Z. Miedzybrodzka, W. Mitarnun, M. Paucar, H. Paulson, J. Pariente, A.-C. Richard, N. S. Salins, S. A. Simpson, P. Striano, P. Svenningsson, F. Tison, V. K. Unni, O. Vanakker, M. W. Wessels, S. Wetchaphanphesat, M. Yang, F. Boller, D. Champion, D. Hannequin, M. Sitbon, D. H. Geschwind, J.-L. Battini, and G. Coppola, "Mutations in XPR1 cause primary familial brain calcification associated with altered phosphate export," *Nat Genet.*, vol. 47, no. 6, pp. 579–581, 2015.

## Abbreviations

$\alpha, \beta$	Energy levels for spin 1/2
aa	Amino acids
Aah	Adenine deaminase (adenine aminohydrolase)
Adk	Adenylate kinase
Ado1	Adenosine kinase
ADP	Adenosine diphosphate
ATP	Adenosine triphosphate
1-IP7	1-inositol pyrophosphates diphosphoinositol pentakisphosphate
5-IP7	5-inositol pyrophosphates diphosphoinositol pentakisphosphate
1,5-IP8	1,5-bis-diphospho-inositol tetrakisphosphate
$B_0$	External magnetic field
CC	coiled-coil domain
Cln3	G <sub>1</sub> cyclin involved in cell cycle progression
cryo-EM	cryo electron microscopy
CSA	chemical shift anisotropy
CSP	chemical shift perturbation
CV	Column volume
$\delta$	chemical shift
D	Dipolar coupling
DD	Dipol-dipol
Ddp1	di-phosphoinositol polyphosphate hydrolase
DNA	Deoxyribonucleic acid
<i>E. coli</i>	<i>Escherichia coli</i>
EDTA	Ethylenediaminetetraacetic acid
<i>e.g.</i>	<i>Exempli gratia</i>
EM	Electron microscopy
ER	endoplasmic reticulum
FID	free induction decay
$\gamma$	gyromagnetic ratio
Gde1	Glycerophosphocholine phosphodiesterase;

GHz	Gigahertz
Git	Organic P <sub>i</sub> transporter
Gsp1	GTP binding protein
HEPES	4-(2-hydroxyethyl)-1-piperazineethanesulfonic acid
HSQC	heteronuclear single quantum coherence
-I	- inductive effect
+I	+ inductive effect
IL	cytokine
INEPT	insensitive nuclei enhancement by polarization transfer
inositol (pyro-) phosphate	inositol pyrophosphate AND phosphate
IPx	IP6, 5-IP7 and 1,5-IP8
<i>J</i>	Scalar coupling
<i>k<sub>B</sub></i>	Boltzmann constant
Kcs1	inositol hexakisphosphate kinase
<i>K<sub>D</sub></i>	Dissociation constant
kDa	Kilo dalton
<i>k<sub>ex</sub></i>	Chemical exchange
<i>K<sub>m</sub></i>	Michaelis-Menten-constant
KSC	lysine surface cluster
$\mu$	magnetic moment
M	molar
-M	- mesomeric effect
+M	+ mesomeric effect
Mns5	Nuclear receptor
mTOR	nutrient sensitive complex assembly
MWCO	molecular weight cut-off
<i>M<sub>xy</sub></i>	Transverse bulk magnetization
<i>M<sub>z</sub></i>	Longitudinal bulk magnetization
NMR	Nuclear magnetic resonance spectroscopy
OD	optical density
PBC	phosphate binding cluster

PDB	Protein data bank
pf1	filamentous phage used as alignment medium
Phm8	Lysophosphatidic acid phosphatase
Pho2	transcriptor factor of PHO pathway
Pho4	Master switch, transcriptor factor, of PHO pathway
Pho5	Repressible secreted acid phosphatase
Pho11	Cell wall associated repressible acid phosphatases
Pho12	Cell wall associated repressible acid phosphatases
Pho80	Cyclin of the cyclin-dependent Pho85 kinase
Pho81	Cyclin-dependent kinase inhibitor
Pho84	High-affinity phosphate transporter on plasma membrane
Pho85	cyclin-dependent kinase
Pho86	ER residing protein packaging Pho84p into COP vesicles
Pho87	Low-affinity phosphate transporter on plasma membrane
Pho89	High-affinity phosphate transporter on plasma membrane
Pho90	High-affinity phosphate transporter on plasma membrane
Pho91	Low-affinity phosphate transporter on vacuole
PHO pathway	Phosphate-responsive signaling pathway in yeast
P <sub>i</sub>	Inorganic phosphate
PKA	cAMP-dependent protein kinase
PP <sub>i</sub>	Pyrophosphate, diphosphate
PPIP5K2	Vip1 homologue in humans
ppm	parts per million
Ppn1	Endo- and exopolyphosphatase in vacuoles
Ppn2	endopolyphosphatase in vacuoles
Ppx1	Exopolyphosphatase
Pse1	nuclear import receptor
Rim15	Protein kinase
RDC	Residual dipolar coupling
RNA	Ribonucleic acid
<i>S. cerevisiae</i>	<i>Saccharomyces cerevisiae</i>
Siw14	Inositol pyrophosphate hydrolase of 5-InsP7 and InsP8
SP	dipeptide phosphorylation sites

SPX	<u>S</u> yg1/ <u>P</u> ho81/ <u>X</u> pr1
Spl2	Negative regulator of Low-affinity Pi transporter on plasma membrane
SS	Secondary chemical shift
Syg1	Putative export inorganic phosphate transporter
<i>T</i>	temperature
<i>t</i> <sub>1</sub> , <i>t</i> <sub>2</sub>	evolution times
<i>T</i> <sub>1</sub> , <i>T</i> <sub>2</sub>	longitudinal and transversal relaxation
TCEP	Tris(2-carboxyethyl)phosphine hydrochloride
TEV	Tobacco etch virus
Tris	Tris(hydroxymethyl)aminomethane
TROSY	transverse relaxationOptimized spectroscopy
TTM	tunnel-shaped triphosphate tunnel metalloenzyme domain
Vip1	Diphosphoinositol pentakisphosphate kinases
Vtc	Components of VTC complex
VTC complex	Polyphosphate polymerase complex
$\omega_0$	Larmor frequency
Xpr1	Human phosphate exporter

## Attachments

### SPX system in plants

- I Inositol pyrophosphate receptors control phosphate homeostasis by targeting the coiled-coil domain of PHR transcription factors

### Studies on pore-forming proteins

- II Mitomycin-C–induced expression of Colicin Ia bears danger of a Dps contamination
- III GSDMD membrane pore formation constitutes the mechanism of pyroptotic cell death

### Curriculum vitae

# Inositol pyrophosphates promote the interaction of SPX domains with the coiled-coil motif of PHR transcription factors to regulate plant phosphate homeostasis

Martina K. Ried<sup>1,7,9</sup>, Rebekka Wild <sup>1,8,9</sup>, Jinsheng Zhu<sup>1</sup>, Joka Pipercevic<sup>2</sup>, Kristina Sturm<sup>1</sup>, Larissa Broger<sup>1</sup>, Robert K. Harmel<sup>3,4</sup>, Luciano A. Abriata <sup>5</sup>, Ludwig A. Hothorn<sup>6,10</sup>, Dorothea Fiedler<sup>3,4</sup>, Sebastian Hiller <sup>2</sup> & Michael Hothorn <sup>1</sup>✉

Phosphorus is an essential nutrient taken up by organisms in the form of inorganic phosphate (Pi). Eukaryotes have evolved sophisticated Pi sensing and signaling cascades, enabling them to stably maintain cellular Pi concentrations. Pi homeostasis is regulated by inositol pyrophosphate signaling molecules (PP-InsPs), which are sensed by SPX domain-containing proteins. In plants, PP-InsP-bound SPX receptors inactivate Myb coiled-coil (MYB-CC) Pi starvation response transcription factors (PHRs) by an unknown mechanism. Here we report that a InsP<sub>8</sub>-SPX complex targets the plant-unique CC domain of PHRs. Crystal structures of the CC domain reveal an unusual four-stranded anti-parallel arrangement. Interface mutations in the CC domain yield monomeric PHR1, which is no longer able to bind DNA with high affinity. Mutation of conserved basic residues located at the surface of the CC domain disrupt interaction with the SPX receptor in vitro and in planta, resulting in constitutive Pi starvation responses. Together, our findings suggest that InsP<sub>8</sub> regulates plant Pi homeostasis by controlling the oligomeric state and hence the promoter binding capability of PHRs via their SPX receptors.

<sup>1</sup> Structural Plant Biology Laboratory, Department of Botany and Plant Biology, University of Geneva, 1211 Geneva, Switzerland. <sup>2</sup> Biozentrum Basel, 4056 Basel, Switzerland. <sup>3</sup> Leibniz-Forschungsinstitut für Molekulare Pharmakologie, 13125 Berlin, Germany. <sup>4</sup> Department of Chemistry, Humboldt-Universität zu Berlin, 12489 Berlin, Germany. <sup>5</sup> Protein production and structure Core Facility, EPFL, 1015 Lausanne, Switzerland. <sup>6</sup> Institute of Biostatistics, Leibniz University, 30419 Hannover, Germany. <sup>7</sup> Present address: Leibniz Institute of Plant Biochemistry, 06120 Halle, Germany. <sup>8</sup> Present address: Institut de Biologie Structurale (IBS), 38044 Grenoble, France. <sup>9</sup> These authors contributed equally: Martina K. Ried, Rebekka Wild. <sup>10</sup> Ludwig A. Hothorn is retired. ✉email: [michael.hothorn@unige.ch](mailto:michael.hothorn@unige.ch)

Phosphorus is an essential building block for many cellular components such as nucleic acids and membranes. It is essential for energy transfer and storage, and can act as a signaling molecule. Pro- and eukaryotes have evolved intricate systems to acquire phosphorus in the form of inorganic phosphate (Pi), to maintain cytosolic Pi concentrations and to transport and store Pi as needed. In green algae and plants, transcription factors have been previously identified as master regulators of Pi homeostasis and Pi starvation responses (PSR)<sup>1,2</sup>. Phosphorus starvation response 1 (CrPsr1) from *Chlamydomonas* and PHOSPHATE STARVATION RESPONSE 1 (AtPHR1) from *Arabidopsis* were founding members of plant-unique MYB-type coiled-coil (MYB-CC) transcription factors<sup>3</sup>. PHR transcription factors were subsequently characterized as regulators of PSRs in diverse plant species<sup>4–6</sup>. In *Arabidopsis*, there are 15 MYB-CCs with PHR1 and PHL1 controlling the majority of the transcriptional PSRs<sup>7</sup>. Knockout mutations in *Arabidopsis thaliana* PHR1 (AtPHR1) result in impaired responsiveness of Pi starvation induced (PSI) genes and perturbed anthocyanin accumulation, carbohydrate metabolism, and lipid composition<sup>2,8,9</sup>. Overexpression of AtPHR1 causes elevated cellular Pi concentrations and impacts the transcript levels of AtPHO2, which codes for an E2 ubiquitin conjugase involved in PSR, via increased production of its micro RNA miR399d<sup>8,10</sup>. PHR binds to a GNATATNC motif (P1BS), found highly enriched in the promoters of PSI genes and in other *cis*-regulatory motifs, activating gene expression<sup>2,7</sup>. AtPHR1 is not only implicated in Pi homeostasis but also in sulfate, iron, and zinc homeostasis, as well as in the adaptation to high-light stress<sup>11–14</sup>. Moreover, AtPHR1 shapes the plant root microbiome by negatively regulating plant immunity<sup>15</sup>.

AtPHR1 and OsPHR2 have been previously reported to physically interact with stand-alone SPX proteins<sup>16–19</sup>, additional components of PSR in plants<sup>17,20–22</sup>. SPX proteins may regulate PHR function by binding to PHRs under Pi-sufficient condition, keeping the transcription factor from entering the nucleus<sup>23–25</sup>. Alternatively, binding of SPX proteins to PHRs may reduce the ability of the transcription factors to interact with their promoter core sequences<sup>18,19,23,24,26</sup>. Two mechanisms were put forward regarding the regulation of the SPX–PHR interaction in response to changes in nutrient availability: SPX domains were proposed to act as direct Pi sensors, with the SPX–PHR interaction occurring in the presence of millimolar concentrations of Pi<sup>18,19</sup>. Alternatively, the integrity of the SPX–PHR complex could be regulated by protein degradation. Indeed, SPX degradation via the 26S proteasome is increased under Pi starvation<sup>23,24,27</sup>.

Fungal, plant, and human SPX domains<sup>28</sup> have been independently characterized as cellular receptors for inositol pyrophosphates (PP-InsPs), which bind SPX domains with high affinity and selectivity<sup>29,30</sup>. PP-InsPs consist of a fully phosphorylated *myo*-inositol ring, carrying one or two pyrophosphate groups at the C1 and/or C5 position, respectively<sup>31</sup>. In plants, inositol 1,3,4-trisphosphate 5/6-kinase catalyzes the phosphorylation of phytic acid (InsP<sub>6</sub>) to 5PP-InsP<sub>5</sub> (InsP<sub>7</sub> hereafter)<sup>32</sup>. The diphosphoinositol pentakisphosphate kinases VIH1 and VIH2 then generate 1,5(PP)<sub>2</sub>-InsP<sub>4</sub> (InsP<sub>8</sub> hereafter) from InsP<sub>7</sub><sup>29,33–35</sup>. Plant diphosphoinositol pentakisphosphate kinases have been genetically characterized to play a role in jasmonate perception and plant defense responses<sup>34</sup> and, importantly, in nutrient sensing in *Chlamydomonas*<sup>36</sup> and *Arabidopsis*<sup>29,35</sup>. *vih1 vih2* double mutants lack the PP-InsP messenger InsP<sub>8</sub>, overaccumulate Pi, and show constitutive PSI gene expression<sup>29,35</sup>. A *vih1 vih2 phr1 phl1* quadruple mutant rescues the *vih1 vih2* seedling phenotypes and displays wild-type-like Pi levels, suggesting that VIH1, VIH2, PP-InsPs, and PHRs are part of a common signaling pathway<sup>35</sup>. In line with, the AtSPX1–AtPHR1 interaction is reduced in *vih1 vih2* mutant plants when compared

to wild type<sup>29</sup>. Thus, biochemical and genetic evidence implicates InsP<sub>8</sub> in the formation of a SPX–PHR complex<sup>29,35</sup>.

Cellular InsP<sub>8</sub> pools are regulated by nutrient availability at the level of the VIH enzymes themselves. Plant VIH1 and VIH2, and diphosphoinositol pentakisphosphate kinases from other organisms are bifunctional enzymes, with an N-terminal kinase domain that generates InsP<sub>8</sub> from InsP<sub>7</sub> and a C-terminal phosphatase domain that hydrolyzes InsP<sub>8</sub> to InsP<sub>7</sub> and InsP<sub>6</sub><sup>35,37,38</sup>. The relative enzymatic activities of the two domains are regulated in the context of the full-length enzyme: under Pi starvation, cellular ATP levels are reduced, leading to a reduction of the VIH kinase activity and a reduction of InsP<sub>8</sub><sup>29,35</sup>. Pi itself acts as an allosteric regulator of the phosphatase activity<sup>35,37</sup>. Thus, under Pi-sufficient growth conditions, InsP<sub>8</sub> accumulates and triggers the formation of a SPX–InsP<sub>8</sub>–PHR complex. Under Pi starvation, InsP<sub>8</sub> levels drop and the complex dissociates<sup>29</sup>.

How the InsP<sub>8</sub>-bound SPX receptor inactivates PHR function remains to be understood at the mechanistic level. It has been previously reported that AtPHR1 binds P1BS as a dimer<sup>2</sup>. Addition of SPX domains reduces the DNA-binding capacity of PHRs as concluded from electrophoretic mobility shift assays (EMSA)s<sup>18,19,23</sup>. Qi et al.<sup>26</sup> reported that AtPHR1 recombinantly expressed as a maltose-binding protein (MBP) fusion protein forms monomers in solution and binds DNA. This process can be inhibited by preincubating the recombinant transcription factor with AtSPX1 in the presence of high concentrations of InsP<sub>6</sub><sup>26</sup>. A recent crystal structure of the AtPHR1 MYB domain in complex with a promoter core fragment supports a dimeric binding mode of MYB-CC transcription factors<sup>39</sup>. Here we investigate the oligomeric state of PHRs, their DNA-binding kinetics, and the targeting mechanism of the interacting SPX receptors.

## Results

**PP-InsPs trigger AtSPX1–AtPHR1 complex formation in yeast.** The interaction of AtSPX1 with AtPHR1 has been previously characterized in yeast two-hybrid assays<sup>19</sup>. We reproduced the interaction of full-length AtPHR1 and AtSPX1 (Fig. 1a), and verified that all four stand-alone AtSPX proteins (AtSPX1–4) interact with a AtPHR1 fragment (AtPHR1<sup>226–360</sup>) that contains the MYB domain and the CC domain in yeast (Supplementary Fig. 1a). This is in line with previous findings, reporting interaction of SPX domains with larger PHR fragments also containing the MYB and CC domains (AtSPX1–AtPHR1<sup>208–362</sup> and OsSPX1/2–OsPHR2<sup>231–426</sup>)<sup>18,19</sup>.

We next tested whether the SPX–PHR interactions observed in yeast are mediated by endogenous PP-InsPs. The putative PP-InsP-binding surface in AtSPX1 was mapped by homology modeling, using the previously determined *Chaetomium thermophilum* Gde1–InsP<sub>6</sub> complex structure (PDB-ID 5IJJ) as template<sup>30</sup>. We replaced putative PP-InsP-binding residues from the previously identified phosphate binding cluster (PBC: AtSPX1<sup>Y25, K29, K139</sup>) and Lysine (K) surface cluster (KSC: AtSPX1<sup>K136, K140, K143</sup>)<sup>30</sup> with alanines (Supplementary Fig. 1b). The resulting AtSPX1<sup>PBC</sup> and AtSPX1<sup>KSC</sup> mutant proteins failed to interact with AtPHR1<sup>226–360</sup> in yeast two-hybrid assays, whereas mutation of a conserved lysine residue outside the putative PP-InsP-binding site (structural control, AtSPX1<sup>K81</sup>) to alanine had no effect (Supplementary Fig. 1b). We next deleted the known yeast PP-InsP kinase Vip1, which converts InsP<sub>6</sub> to 1PP-InsP<sub>5</sub> and InsP<sub>7</sub> to InsP<sub>8</sub>, or the PP-InsP kinase Kcs1, which converts InsP<sub>6</sub> to InsP<sub>7</sub> and 1PP-InsP<sub>5</sub> to InsP<sub>8</sub><sup>40,41</sup> (Supplementary Fig. 1c, d). We found that deletion of either kinase reduced the interaction between wild-type AtSPX1 and AtPHR1<sup>226–360</sup> (Supplementary Fig. 1c). The interaction between the plant brassinosteroid receptor kinase BRI1 and the inhibitor protein BKI1, known to occur independently of

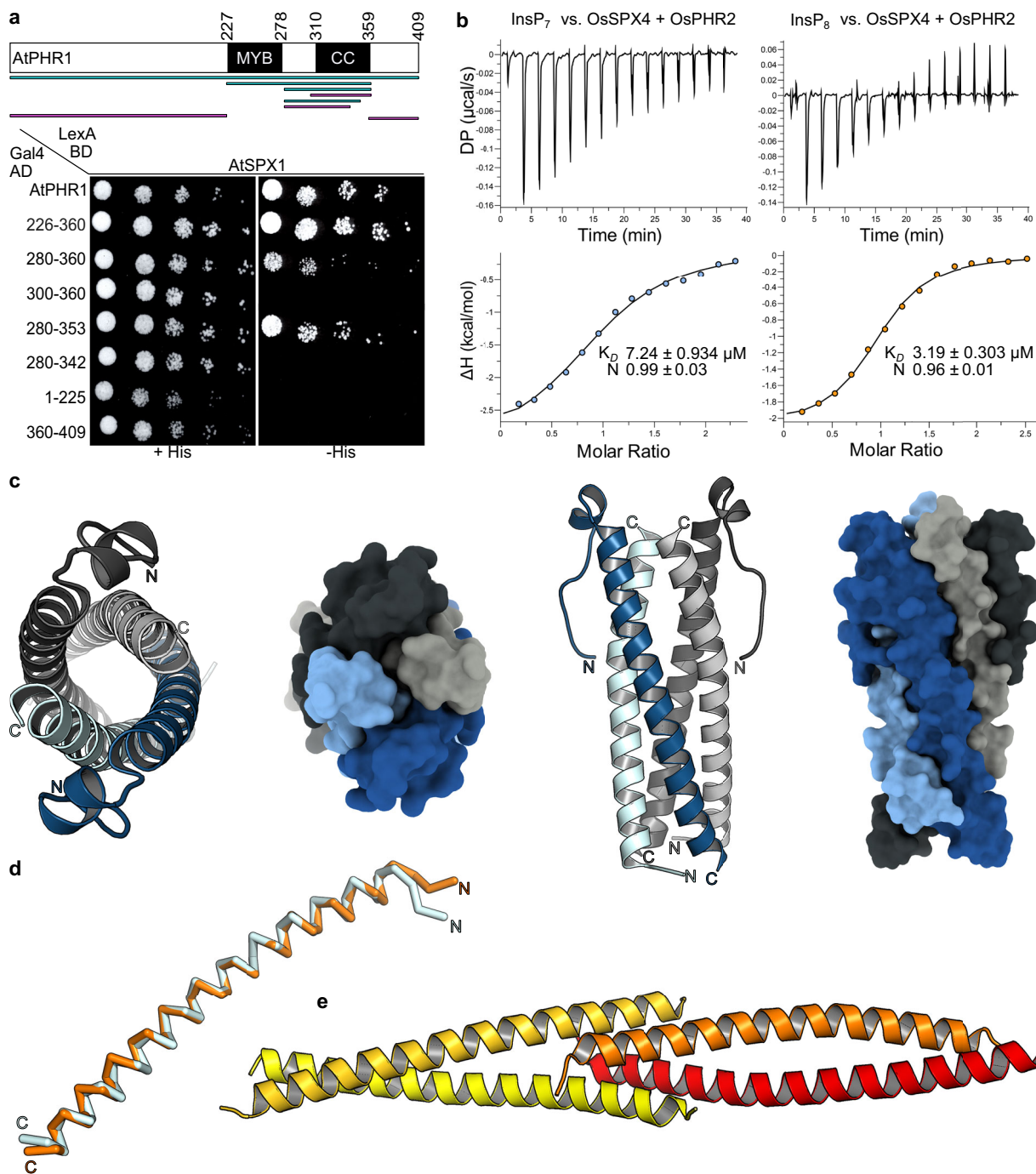


**Fig. 1 AtSPX1 recognizes the AtPHR1 coiled-coil domain that crystallizes as a tetramer.** **a** Yeast co-expressing different AtPHR1 deletion constructs fused to the Gal4-activation domain (AD; prey) and full-length wild-type AtSPX1 fused to the LexA-binding domain (BD; bait) were grown on selective SD medium supplemented with histidine (+His; co-transformation control) or lacking histidine (–His; interaction assay) to map a minimal fragment of AtPHR1 sufficient for interaction with AtSPX1. Shown are serial dilutions from left to right. A schematic overview of the tested interacting (in cyan) and non-interacting (in magenta) AtPHR1 fragments is shown alongside (MYB, MYB-DNA-binding domain; CC, coiled-coil domain). **b** Isothermal titration calorimetry assays of InsP<sub>7</sub> (400 μM 5PP-InsP<sub>5</sub>; left panel) and InsP<sub>8</sub> (500 μM 1,5(PP)<sub>2</sub>-InsP<sub>4</sub>; right panel) binding to OsSPX4–OsPHR2 (30 μM), respectively. Raw heats per injection are shown in the top panel and the bottom panel represents the integrated heats of each injection, fitted to a one-site binding model (solid line). The insets show the dissociation constant ( $K_D$ ) and binding stoichiometry ( $N$ ) ( $\pm$ fitting error). **c** Ribbon and surface diagrams of the AtPHR1 CC four-stranded anti-parallel tetramer. Helices contributing to the dimer interface are shown in light and dark blue, respectively. Corresponding, symmetry-related helices completing the tetramer are shown in light and dark gray. **d** Structural superposition of two AtPHR1 core CC helices ( $C_\alpha$  trace, in light blue) and ScCtp1 (PDB-ID 4 × 01, in orange)<sup>44</sup>. R.m.s.d. is  $\sim 1$  Å comparing 45 corresponding  $C_\alpha$  atoms. **e** Ribbon diagram of the ScCtp1 dimer-of-dimers CC domain, with contributing helices colored from yellow to red.

PP-InsPs<sup>42</sup>, was not affected in either  $\Delta vip1$  or  $\Delta kcs1$  mutants (Supplementary Fig. 1c).

Using quantitative isothermal titration calorimetry (ITC)-binding assays, we have previously determined dissociation constants ( $K_D$ ) for InsP<sub>6</sub> and InsP<sub>7</sub> binding to a OsSPX4–OsPHR2 complex to be  $\sim 50$  and  $\sim 7$   $\mu$ M, respectively<sup>30</sup>. A side-by-side comparison of InsP<sub>7</sub> and InsP<sub>8</sub> binding to OsSPX4–OsPHR2 by ITC revealed dissociation constants of  $\sim 7$  and  $\sim 3$   $\mu$ M, respectively (Fig. 1b). Taken together, the SPX–PHR interaction is mediated by PP-InsPs, with the bona fide Pi signaling molecule InsP<sub>8</sub> being the preferred ligand in vitro.

**AtSPX1 interacts with a unique four-stranded coiled-coil domain in AtPHR1.** We next mapped the SPX–PP-InsP-binding site in AtPHR1 to a fragment (AtPHR1<sup>280–353</sup>), which comprises the CC domain and a 30-amino acid spanning N-terminal extension, in yeast two-hybrid experiments (Fig. 1a). We sought to crystallize an AtSPX1–PP-InsP–AtPHR1 complex either in the pre- or absence of P1BS fragments. We obtained crystals of a putative AtSPX1–InsP<sub>8</sub>–AtPHR1<sup>280–360</sup> complex diffracting to 2.4 Å resolution and solved the structure by molecular replacement, using isolated SPX domain structures as search models<sup>30</sup>. Iterative cycles of model building and crystallographic refinement yielded, to our surprise, a well-refined model of AtPHR1<sup>280–360</sup> only (see “Methods”). Analysis with the program PISA revealed the presence of a crystallographic tetramer in which four long  $\alpha$ -helices fold into an unusual anti-parallel four-stranded coiled-coil (Fig. 1c). AtPHR1<sup>280–360</sup> residues 292–356 and 310–357 are visible in the electron density maps from chain A and B, respectively. Residues 292–311 in chain A fold into a protruding loop region that harbors a small  $\alpha$ -helix, and appear disordered in chain B (Fig. 1c). The anti-parallel  $\alpha$ -helices in AtPHR1 closely align with a root mean square deviation (r.m.s.d.) of  $\sim 0.5$  Å comparing 45 corresponding C $_{\alpha}$  atoms. Structural homology searches with the program DALI<sup>43</sup> returned different coiled-coil structures, with a monomer of the tetrameric coiled-coil domain of the yeast transcription factor Ctp1 representing the closest hit (DALI Z-score 5.9, r.m.s.d. is  $\sim 1$  Å comparing 45 corresponding C $_{\alpha}$  atoms) (Fig. 1d)<sup>44</sup>. However, no anti-parallel four-stranded coiled-coil domain with structural similarity to AtPHR1 was recovered, with, for example, the Ctp1 dimer-of-dimers domain having a very different configuration (Fig. 1e)<sup>44</sup>.

We next assessed the oligomeric state of AtPHR<sup>280–360</sup> using size-exclusion chromatography coupled to right-angle light scattering (SEC-RALS) and determined an apparent molecular weight of  $\sim 37.5$  kDa, thus confirming that the isolated AtPHR1 CC forms tetramers in solution (theoretical molecular weight of the monomer is  $\sim 9.5$  kDa) (Fig. 2a). Two additional crystal structures of AtPHR1<sup>280–360</sup> obtained in different crystal lattices all revealed highly similar tetrameric arrangements (Supplementary Fig. 2 and Supplementary Table 5). Although we found purified full-length AtPHR1 to be too unstable for SEC-RALS analysis, full-length OsPHR2 formed a tetramer in solution (Supplementary Fig. 3). In contrast, untagged AtPHR1<sup>222–358</sup>, which comprises the CC and the MYB domains only, runs as a dimer (Fig. 2a, b black traces), in agreement with earlier reports<sup>2</sup>.

**Mutations in the CC domain abolish AtPHR1 oligomerization and DNA binding in vitro.** The observed oligomeric state differences between full-length OsPHR2, AtPHR1<sup>280–360</sup> (CC), and AtPHR1<sup>222–358</sup> (MYB-CC) prompted us to investigate the putative dimer- and tetramerization interfaces in our AtPHR1 structures with the program PISA<sup>45</sup>. We found the dimerization ( $\sim 1400$  Å<sup>2</sup> buried surface area) and the tetramerization ( $\sim 1900$  Å<sup>2</sup> buried surface area) interfaces to be mainly

formed by hydrophobic interactions (Supplementary Fig. 4a, b). Both interfaces are further stabilized by hydrogen bond interactions and several salt bridges (Supplementary Fig. 4a, b). Importantly, all contributing amino-acids represent sequence fingerprints of the plant-unique MYB-CC transcription factor subfamily and are highly conserved among different plant species (Supplementary Fig. 4c). We identified residues specifically contributing to the formation of a CC dimer (Olig1: AtPHR1<sup>L319</sup>, AtPHR1<sup>L333</sup>, AtPHR1<sup>L337</sup>, shown in cyan in Fig. 2 and Supplementary Fig. 4) or tetramer (Olig2: AtPHR1<sup>L317</sup>, AtPHR1<sup>L327</sup>, AtPHR1<sup>L341</sup>, shown in dark orange in Fig. 2 and Supplementary Fig. 4) in our different CC structures (Supplementary Table 5). We replaced these residues by asparagine to generate two triple mutants in AtPHR1<sup>222–358</sup> and AtPHR1<sup>280–360</sup>, respectively. We found in SEC-RALS assays that both mutant combinations dissolved AtPHR1<sup>280–360</sup> tetramers and AtPHR1<sup>222–358</sup> dimers into monomers, respectively (Fig. 2a, b).

Analysis of the secondary structure content of wild-type AtPHR<sup>280–360</sup> using circular dichroism (CD) spectroscopy revealed a 100%  $\alpha$ -helical protein (Supplementary Fig. 5a), in agreement with our structural model of the AtPHR1 CC domain (Fig. 1c). In contrast, we estimated the secondary structure content of the Olig1 and Olig2 mutant proteins to be  $\sim 50\%$   $\alpha$ -helical and  $\sim 50$  random coil (Supplementary Fig. 5a). The CD melting spectrum for wild-type AtPHR<sup>280–360</sup> indicated the presence of a well-folded protein with a melting temperature ( $T_m$ ) of  $\sim 50$  °C, while we could not reliably determine  $T_m$ 's for the Olig1 and Olig2 mutant proteins (Supplementary Fig. 5b). We conclude that mutation of either AtPHR1<sup>L319</sup>, AtPHR1<sup>L333</sup>, AtPHR1<sup>L337</sup> or AtPHR1<sup>L317</sup>, AtPHR1<sup>L327</sup>, AtPHR1<sup>L341</sup> to asparagine disrupts the tetrameric coiled-coil domain of AtPHR1 and affects the structural integrity of the contributing  $\alpha$ -helix.

It has been recently reported that the AtPHR1 MYB domain associates with its target DNA as a dimer<sup>39</sup>. We thus studied the capacity of AtPHR1<sup>222–358</sup> oligomerization mutants to interact with the P1BS in qualitative EMSA and quantitative grating-coupled interferometry (GCI) assays. AtPHR1<sup>222–358</sup> Olig1 could still interact with the P1BS in EMSAs indistinguishable from wild type (Fig. 2c). However, AtPHR1<sup>222–358</sup> Olig1 and AtPHR1<sup>222–358</sup> Olig2 bound a biotinylated P1BS immobilized on the GCI chip with  $\sim 20$ -fold reduced affinity when compared to the wild-type control (Fig. 2d–f). Together, our experiments suggest that PHR1 may exist as a tetramer or dimer in solution, and that disruption of its plant-unique CC domain interface reduces the capacity of the transcription factor to bind its DNA recognition site.

**CC surface mutations abolish PHR–SPX interactions but do not interfere with DNA binding in vitro.** We next sought to identify the binding site for SPX in the PHR CC domain. In our structures, a conserved set of basic residues maps to the surface of the four CC helices (shown in magenta in Fig. 3a and Supplementary Fig. 4c). A similar set of surface-exposed basic residues has been previously found to form the binding site for PP-InsPs in various SPX receptors<sup>30</sup>. Mutation of AtPHR1<sup>K325</sup>, AtPHR1<sup>H328</sup>, and AtPHR1<sup>R335</sup>, but not of AtPHR1<sup>K308</sup>, AtPHR1<sup>R318</sup>, and AtPHR1<sup>R340</sup> to alanine, disrupted the interaction of AtPHR1 with AtSPX1 in yeast (Fig. 3b). We simultaneously mutated the residues corresponding to AtPHR1<sup>K325</sup>, AtPHR1<sup>H328</sup>, and AtPHR1<sup>R335</sup> to alanine in OsPHR2 (OsPHR2<sup>KHR/A</sup>). The mutant transcription factor showed no detectable binding to OsSPX4-InsP<sub>7</sub> in quantitative ITC assays, but maintained the ability to bind the P1BS (Fig. 3c, d). In line with this, mutation of the KHR motif does not alter the oligomeric state of AtPHR1<sup>280–360</sup> as concluded from SEC-RALS experiments (Fig. 2a magenta traces).

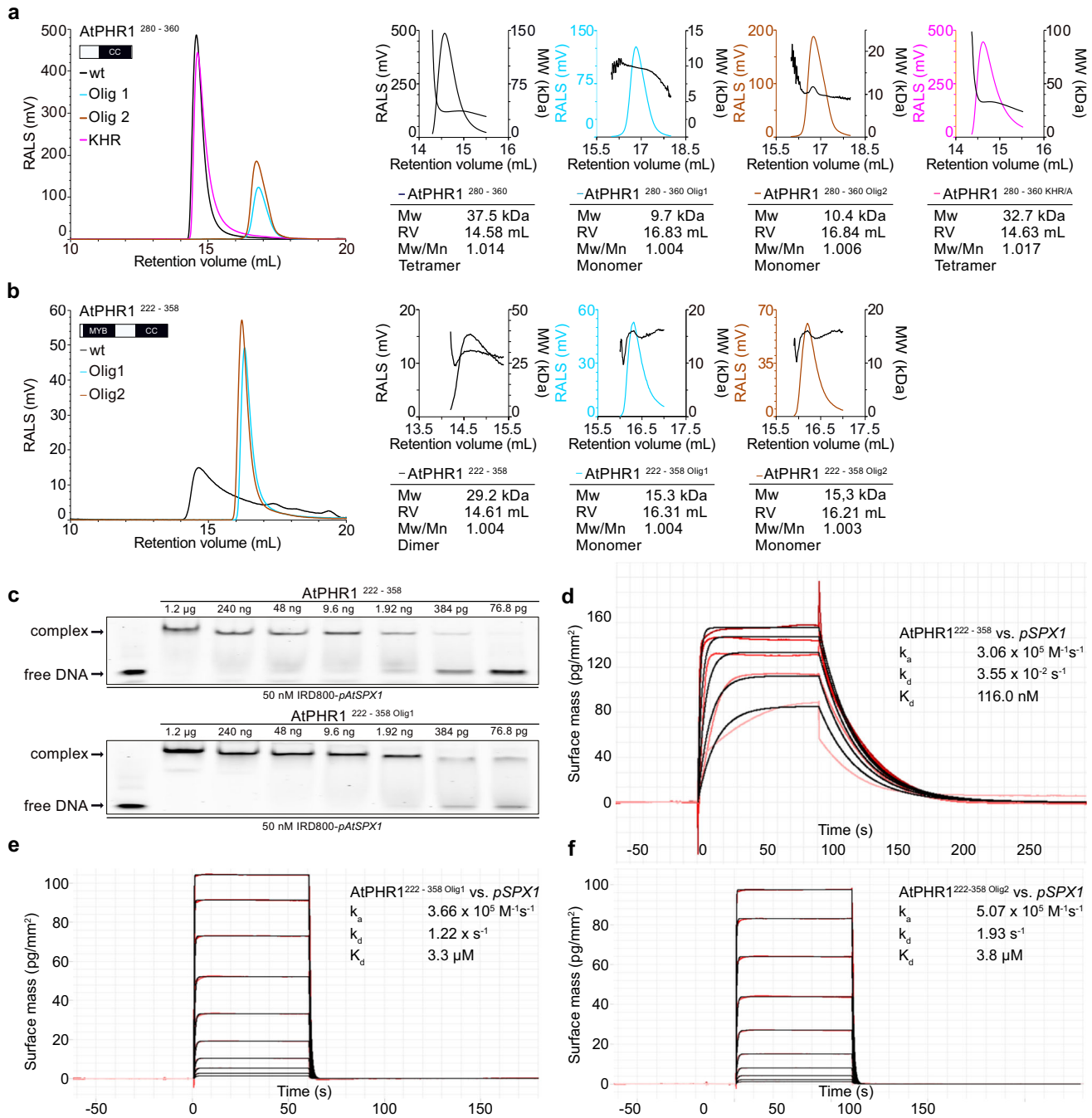


**Fig. 2 Mutations in the AtPHR1 coiled-coil domain impair oligomerisation and DNA binding.** **a** Analytical size-exclusion chromatography traces of wild-type AtPHR1 CC (wt, black line), AtPHR1<sup>280-360</sup> Olig1 (Olig1, cyan), AtPHR1<sup>280-360</sup> Olig2 (Olig2, orange), and of AtPHR1<sup>280-360</sup> KHR/A (KHR, magenta). The corresponding right-angle light scattering (RALS) traces are shown alongside, the molecular masses are depicted by a black line. Table summaries provide the molecular weight (Mw), retention volume (RV), dispersity (Mw/Mn), and the derived oligomeric state of the respective sample. **b** Analysis of AtPHR1 MYB-CC (AtPHR1<sup>222-358</sup>) as described in **a**. **c** Qualitative comparison of the interaction of AtPHR1<sup>222-358</sup> (upper panel) or AtPHR1<sup>222-358</sup> Olig1 (lower panel) binding to IRD800-pAtSPX1 in electrophoretic mobility shift assays. Experiment was performed twice with similar results. **d-f** Quantitative comparison of the interaction of AtPHR1<sup>222-358</sup>, AtPHR1<sup>222-358</sup> Olig1, or AtPHR1<sup>222-358</sup> Olig2 with pSPX1 by grating-coupled interferometry (GCI). Sensorgrams show raw data (red lines) and their respective fits (black lines). Table summaries provide the derived association rate ( $k_a$ ), the dissociation rate ( $k_d$ ), and the dissociation constant ( $K_d$ ).

Using nuclear magnetic resonance (NMR) spectroscopy, we next tested whether the KHR motif in AtPHR1 is directly involved in PP-InsP ligand recognition. We titrated InsP<sub>8</sub> into <sup>15</sup>N, <sup>2</sup>H-labeled AtPHR1<sup>280-360</sup>, and recorded TROSY spectra using potassium phosphate (KPi) as control. Five backbone amide moieties exhibited chemical shift perturbations in the presence of

InsP<sub>8</sub> but not in the presence of the KPi control. We acquired titration spectra using increasing concentrations of InsP<sub>8</sub> and estimated dissociation constants for InsP<sub>8</sub> based on three representative peaks (Supplementary Fig. 6). The derived dissociation constant is in the millimolar range and saturation could not be reached in the available concentration range

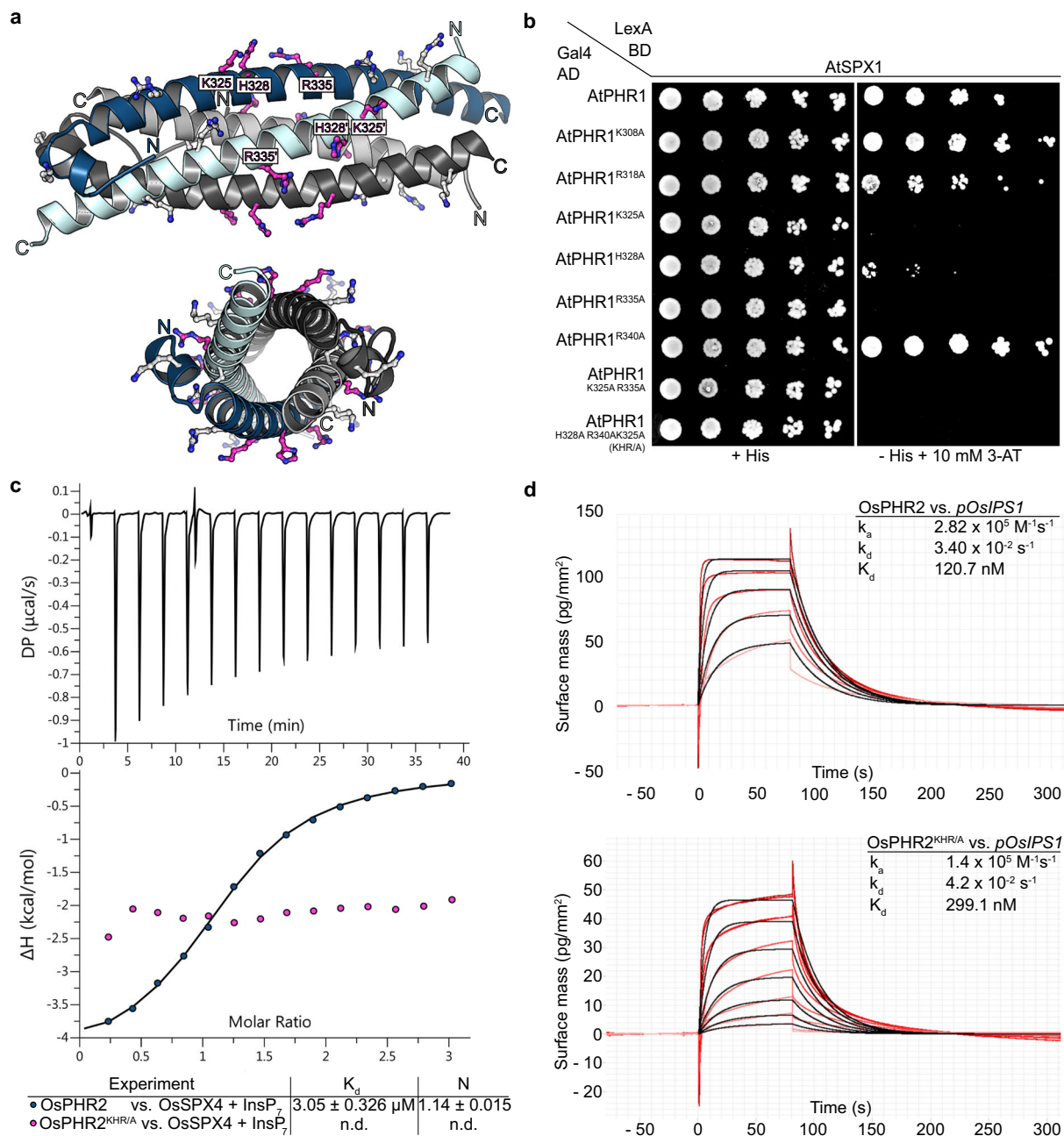


**Fig. 3** The KHR motif at the surface of the PHR coiled-coil domain is required for the interaction with SPX domains. **a** Ribbon diagram of the AtPHR1 CC domain with conserved basic residues located at the surface of the domain shown in bonds representation. The KHR motif (AtPHR1<sup>K325</sup>, AtPHR1<sup>H328</sup>, AtPHR1<sup>R335</sup>) is highlighted in magenta. **b** Mutational analysis of the basic residues in AtPHR1 CC. Yeast co-expressing AtPHR1<sup>K325A</sup>, AtPHR1<sup>H328A</sup>, AtPHR1<sup>R335A</sup> variants in which surface-exposed basic residues have been replaced with alanine fused to the Gal4-AD (prey) and AtSPX1 fused to the LexA-BD (bait) were grown on selective SD medium supplemented with histidine (+His; co-transformation control) or lacking histidine and supplemented with 10 mM 3-amino-1,2,4-triazole (3-AT) (-His + 10 mM 3-AT; interaction assay) to identify residues required for interaction with AtSPX1 in yeast two-hybrid assays. Shown are serial dilutions from left to right. **c** Isothermal titration calorimetry (ITC) assay of wild-type OsPHR2 and OsPHR2<sup>KHR/A</sup> (300  $\mu\text{M}$ ) vs. OsSPX4 (20  $\mu\text{M}$ )-5PP-InsP<sub>5</sub> (100  $\mu\text{M}$ ). Raw heats per injection are shown in the top panel, the bottom panel represents the integrated heats of each injection, fitted to a one-site binding model (solid line). The insets show the dissociation constant ( $K_D$ ) and binding stoichiometry ( $N$ ) ( $\pm$  fitting error, n.d. no detectable binding). **d** Quantitative comparison of the interaction of OsPHR2 (top panel) or OsPHR2<sup>KHR/A</sup> (bottom panel) with *pOsIPS1* by GCI. Sensorgrams show raw data (red lines) and their respective fits (black lines). The insets show summarize association rates ( $k_a$ ), dissociation rates ( $k_d$ ), and the dissociation constant ( $K_d$ ) of the respective sample.

(Supplementary Fig. 6). We next repeated the same set of experiments using the AtPHR1<sup>KHR/A</sup> mutant protein, located the same peaks in the transverse relaxation-optimized spectroscopy (TROSY) spectra and estimated similar dissociation constants (Supplementary Fig. 6).

Taken together, three highly conserved basic residues located at the surface of the PHR coiled-coil domain are critical for the interaction with the PP-InsP-bound SPX receptor (Supplementary Fig. 4c). The NMR titration experiments suggest that AtPHR1 does not contribute to the specific binding of InsP<sub>8</sub> and

that the low affinity interaction between the CC domain and InsP<sub>8</sub> does not involve the KHR motif (Supplementary Fig. 6).

**Mutation of the AtPHR1 KHR motif impairs AtSPX1 binding and Pi homeostasis in planta.** We next tested whether mutation of the SPX-binding site in AtPHR1 can modulate its function in Pi homeostasis in *Arabidopsis*. We expressed wild-type and point-mutant versions of AtPHR1 carrying an N-terminal FLAG tag under the control of its native promoter in a *phr1-3* loss-of-function mutant<sup>8</sup>. At seedling stage, we found that AtPHR1 single, double, and triple point mutations complemented the previously characterized Pi deficiency phenotype of *phr1-3*<sup>2,8</sup> (Fig. 4a and Supplementary Fig. 7a). After transferring the seedlings to soil, variable growth phenotypes became apparent 21 days after germination (DAG) (Supplementary Fig 7b). From three independent lines per genotype, we selected one line each showing similar *AtPHR1* transcript levels for all experiments shown in Fig. 4 (Fig. 4 and Supplementary Fig. 8a). Comparing these lines, we found that AtPHR1<sup>K325A,R335A</sup> double and AtPHR1<sup>K325A,H328A,R335A</sup> triple mutants, but not the single mutants, displayed severe growth phenotypes, with the triple mutant showing the strongest defects (Fig. 4a). We next determined cellular Pi levels in all independent lines and found that (i) Pi levels are positively correlated with AtPHR1 expression levels (Supplementary Fig. 8a), that (ii) all AtPHR1 mutant proteins tested accumulate Pi to significantly higher levels when compared to wild type and *phr1-3*, and that (iii) the AtPHR1<sup>K325A,H328A,R335A</sup> triple mutant displayed the highest Pi levels (Fig. 4b and Supplementary Fig. 8b–d). In line with this, PSI gene expression is misregulated in AtPHR1<sup>K325A,R335A</sup> double and AtPHR1<sup>K325A,H328A,R335A</sup> (AtPHR1<sup>KHR/A</sup>) triple mutants (Fig. 4c). In co-immunoprecipitation assays in *Nicotiana benthamiana* and in *Arabidopsis*, we found the interaction of AtPHR1<sup>K325A,H328A,R335A</sup> with AtSPX1 to be reduced when compared to wild-type AtPHR1 (Fig. 4d and Supplementary Fig. 8).

We next studied the genetic interaction between *PHR1* and *VIH1/2*. As previously reported, the severe phenotypes of *vih1-2 vih2-4* seedlings are partially rescued in the *phr1 phl1 vih1-2 vih2-4* quadruple mutant, suggesting that *VIH1/2*-generated InsP<sub>8</sub> regulates the activity of *PHR1* and *PHL1* by promoting the binding of SPX receptors<sup>29,35</sup>. We performed the orthogonal genetic experiment, by complementing the *phr1 phl1* mutant with AtPHR1<sup>KHR/A</sup> expressed under the control of the AtPHR1 promoter and carrying a N-terminal enhanced green fluorescent protein (eGFP) tag (Fig. 4e, see “Methods”). The complemented lines displayed intermediate growth phenotypes and constitutive PSI gene expression (Fig. 4e, f). Thus, SPX–InsP<sub>8</sub> mediated regulation of *PHR1* and *PHL1* has to be considered one of several PP-InsP regulated processes affected in the *vih1-2 vih2-4* mutant. Together, our *in vivo* experiments reveal that SPX receptors interact with the CC domain of AtPHR1 via the surface-exposed Lys325, His328, and Arg335, and that this interaction negatively regulates *PHR* activity and *PSRs*.

## Discussion

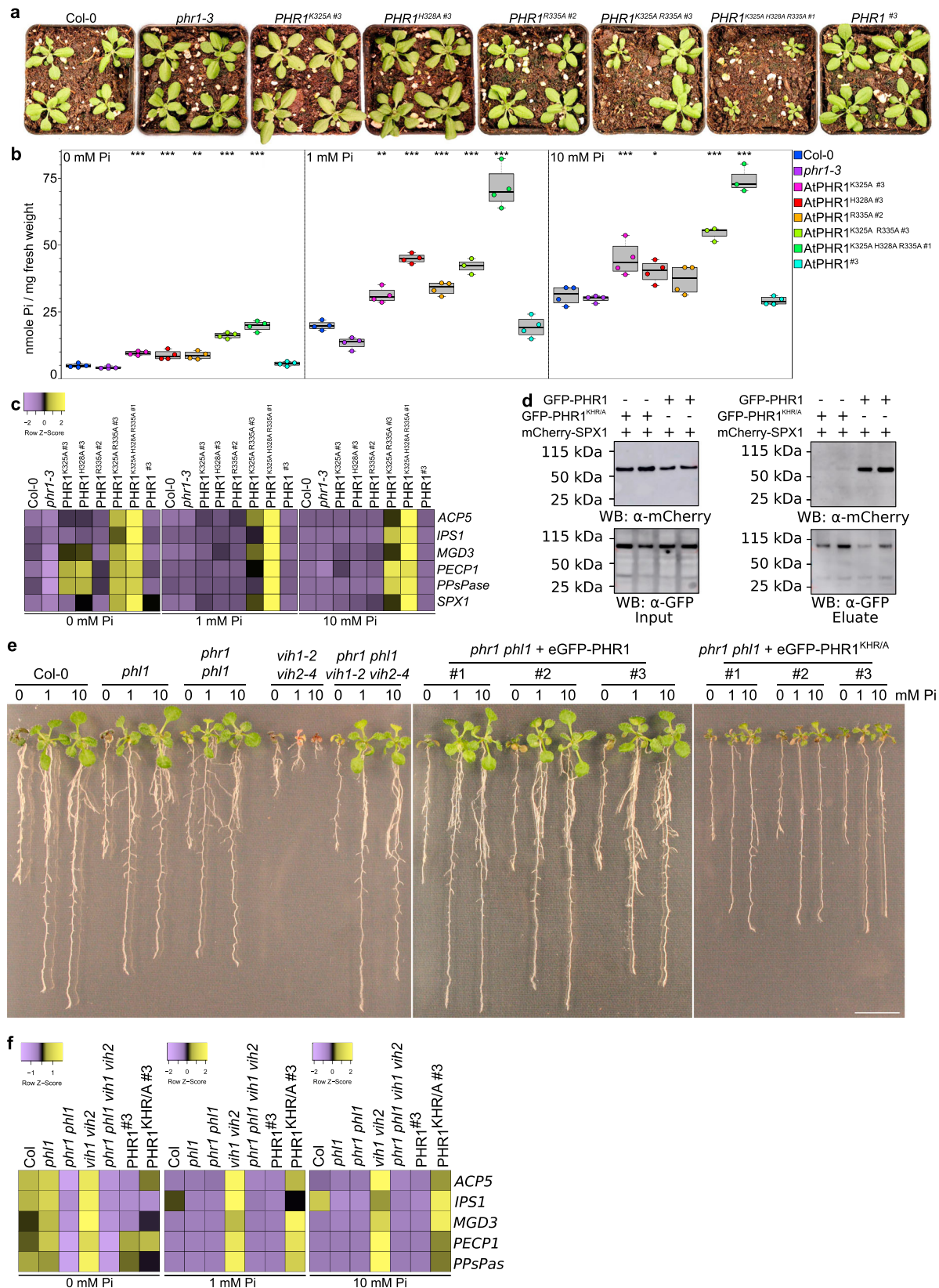
*PHR* transcription factors have been early on recognized as central components of the *PSR* in green algae and in plants, directly regulating the expression of *PSI* genes<sup>1,2,7</sup>. In *Arabidopsis* and in rice *spx* mutants of then unknown function also showed altered *PSI* gene expression<sup>20,22</sup>. This genetic interaction was later substantiated by demonstrating that stand-alone plant SPX proteins can interact with *PHR* orthologs from *Arabidopsis* and rice<sup>18,19,23</sup>. The biochemical characterization of SPX domains as cellular receptors for PP-InsPs and the genetic identification of *VIH* kinases

as master regulators of *PSR* in plants suggested that PP-InsPs, and specifically InsP<sub>8</sub> mediates the interaction of SPX proteins with *PHRs* in response to changing nutrient conditions<sup>29,30,35</sup>.

Our quantitative DNA-binding assays demonstrate that AtPHR1 MYB-CC binds the *P1BS* from the *AtSPX1* promoter with high affinity ( $K_d \sim 0.2 \mu\text{M}$ ), in agreement with previously reported binding constants for different MYB-CC constructs ( $K_d \sim 0.01\text{--}0.1 \mu\text{M}$ )<sup>26,39</sup>. Different oligomeric states have been reported for various *PHR* MYB-CC constructs<sup>2,26</sup>. Our AtPHR1 MYB-CC construct behaves as a dimer in solution, consistent with the recently reported crystal structure of the AtPHR1 MYB–DNA complex and with earlier reports<sup>2,39</sup>. Purified full-length OsPHR2, however, appears to be a homotetramer in solution (Supplementary Fig. 3).

In yeast two-hybrid assays, we found that AtSPX1–4 all are able to interact with AtPHR1 (Fig. 1a and Supplementary Fig. 1a). We mapped their conserved interaction surface to the plant-unique CC motif of *PHRs* (Fig. 1a). Crystal structures of this fragment reveal an unusual, four-stranded anti-parallel coiled-coil domain (Fig. 1c). Given the fact, that AtPHR1 MYB-CC forms dimers in solution (Fig. 2b), we cannot exclude the possibility that the CC tetramers represent crystal packing artifacts. However, we did observe identical CC tetramers in three independent crystal lattices (Supplementary Fig. 2) and in solution (Fig. 2a). The residues contributing to the dimer and to the tetramer interfaces are highly conserved among all plant MYB-CC transcription factors (Supplementary Fig. 4). Mutation of either interface blocks AtPHR1 oligomerization *in vitro* (Fig. 2a, b) and reduces DNA binding (Fig. 2d–f). An attractive hypothesis would thus be that AtPHR1 binds its target promoter as a dimer, but can potentially form homo-tetramers, or hetero-tetramers with other MYB-CC type transcription factors sharing the conserved, plant-unique CC structure and sequence (Supplementary Fig. 4). Notably, *PHR1* *PHL1* heteromers have been previously described<sup>7</sup>.

We found that SPX–*PHR* complex formation is mediated by endogenous PP-InsPs in yeast cells, as deletion of the yeast PP-InsP kinases *Vip1* and *Kcs1* abolished the interaction, and mutation of the PP-InsP-binding surface in AtSPX1 interfered with AtPHR1 binding (Supplementary Fig. 1b, c). In line with this, SPX–*PHR* complexes are found dissociated in *vih1 vih2* mutant plants<sup>29</sup>. It is of note that the observed differences in binding affinity for InsP<sub>7</sub> and InsP<sub>8</sub> to SPX–*PHR* *in vitro* (Fig. 1b)<sup>29</sup> cannot fully rationalize the apparent preference for InsP<sub>8</sub> *in vivo*<sup>29,35</sup>. We identified the binding surface for SPX–InsP<sub>8</sub> by locating a set of highly conserved basic residues exposed at the surface of the CC domain (Fig. 3a and Supplementary Fig. 4). Mutation of this KHR motif did not strongly impact the ability of isolated OsPHR2 to bind *pOsIPS1* *in vitro* (Fig. 3d), but disrupted the interaction of AtPHR1 with AtSPX1 in yeast (Fig. 3b). The corresponding mutations in OsPHR2 had a similar effect on the interaction with OsSPX4 in quantitative ITC assays (Fig. 3c). Expression of AtPHR1<sup>KHR/A</sup> in the *phr1-3* mutant resulted in Pi hyperaccumulation phenotypes and constitutive *PSI* gene expression in *Arabidopsis* (Fig. 4a–c). The intermediate growth phenotypes of *vih1 vih2 phr1 phl1* mutants complemented with AtPHR1<sup>KHR/A</sup> clearly suggests that PP-InsPs do not only regulate the activity of *PHR1* and *PHL1* in plants, but likely the function of other (SPX domain-containing) proteins<sup>30</sup> (Fig. 4e). Notably, binding of AtPHR1<sup>KHR/A</sup> to AtSPX1 was reduced in co-immunoprecipitation assays when compared to wild-type AtSPX1 (Fig. 4d and Supplementary Fig. 9). Thus, our and previous finding suggest that InsP<sub>8</sub> can promote the association of SPX receptors and *PHR* transcription factors. The newly identified basic surface area in *PHR* CC, harboring the conserved KHR motif, likely forms part of the SPX–*PHR* complex interface (Fig. 3a).



It is of note that addition of AtSPX1 to AtPHR1 has been previously demonstrated to reduce AtPHR1's ability to bind to P1BS in the presence of InsP<sub>6</sub><sup>26</sup>. We could not quantify these interactions in ITC or GCI binding assays, as PHR CC formation is much preferred over SPX-InsP<sub>6</sub> binding at the protein concentrations required in these assays. We speculate that InsP<sub>6</sub>

bound SPX proteins can bind to the basic residues we identified in the PHR CC domain to control the oligomeric state and hence the promoter binding capacity of PHRs. As these residues are conserved among all plant MYB-CC proteins this may suggest that transcription factors outside the PHR subfamily may be regulated by SPX domains and PP-InsPs, possibly rationalizing

**Fig. 4 Mutation of the AtPHR1 KHR motif impairs interaction with AtSPX1 and Pi homeostasis in planta.** **a** Growth phenotypes of Col-0 wild type, *phr1-3* of *phr1-3* complementation lines expressing FLAG-AtPHR1, FLAG-AtPHR1<sup>K325A</sup>, FLAG-AtPHR1<sup>H328A</sup>, FLAG-AtPHR1<sup>R335A</sup>, FLAG-AtPHR1<sup>K325A R335A</sup>, and FLAG-AtPHR1<sup>K325A H328A R335A</sup> under the control of the *AtPHR1* promoter at 21 DAG grown in Pi-sufficient conditions. One representative line per complementation construct is shown (specified by a #), additional lines are shown in Supplementary Fig. 4. **b** Plot representing the cellular Pi content of the lines shown in **a**. Bold black line, median; box, interquartile range (IQR); whiskers, lowest/highest data point within 1.5 IQR of the lower/upper quartile. Seedlings were germinated and grown on vertical 1/2MS plates for 8 days, transferred to 1/2MS plates supplemented with either 0, 1, or 10 mM Pi and grown for additional 7 days. For each line, four plants were measured in technical duplicates. Pi contents of all lines can be found in Supplementary Fig. 4 (\**p* < 0.05; \*\**p* < 0.01; \*\*\**p* < 0.001). **c** Heat maps of PSI marker gene (*ACP5*, *IP51*, *MGD3*, *PECP1*, *PPsPase*, *SPX1*) expression analyses of the lines shown in **a**, represented as Z-scores. For each line, three biological replicates were analyzed in technical triplicates by qRT-PCR. **d** Co-immunoprecipitation (Co-IP) experiment assessing the ability for immobilized GFP-AtPHR1 and GFP-AtPHR1<sup>KHR/A</sup> to interact with mCherry-AtSPX1 in *N. benthamiana*. Input western blottings are shown alongside. Experiment was performed twice with similar results. **e** Genetic interactions in the VIH-PHR signaling pathway. Col-0 wild type and the indicated mutant seedlings were grown on 1/2MS plates for 7 DAG, transferred to 1/2MS plates supplemented with either 0, 1, or 10 mM Pi and grown for additional 7 days. For complementation analyses, wild-type AtPHR1 or AtPHR1<sup>KHR/A</sup> was expressed as an N-terminal eGFP fusion protein under the control of the *AtPHR1* promoter. **f** Heat maps of PSI marker gene expression for the lines shown in **e**.

the severe phenotypes of *vih1 vih2* mutant plants (Fig. 4e and Supplementary Fig. 4). The recent findings that VIH kinases and PHRs act together in plant PSR and that SPX–PHR complexes are dissociated in *vih1 vih2* mutants further suggest that InsP<sub>8</sub> is the bona fide signaling molecule promoting the association between SPX domains and MYB-CCs<sup>29,35</sup>. Repressive SPX–PHR complexes consequently form only under Pi-sufficient conditions, where InsP<sub>8</sub> levels are high<sup>29,35</sup>. Under Pi starvation, when InsP<sub>8</sub> levels are reduced, SPX–PHR complexes dissociate, enabling the transcription factors to acquire the oligomeric state required for high affinity promoter binding. The physiological and mechanistic investigation of this central process may, in the long term, contribute to the development of Pi starvation resilient crops. This could in turn sustain the use of the essential and non-renewable resource rock phosphate, which is currently consumed at an alarming scale.

## Methods

**Molecular cloning, constructs, and primers.** For a detailed description of the cloning strategies, constructs and primers used in this study, please refer to Supplementary Tables 2 and 3.

**Generation of stable transgenic *A. thaliana* lines.** All stable transgenic *A. thaliana* lines are listed in Supplementary Table 1. Constructs were introduced into *Agrobacterium tumefaciens* strain pGV2260 and *A. thaliana* plants were transformed via floral dipping<sup>46</sup>. Transformants were identified by mCherry fluorescence with a Zeiss Axio Zoom.V16 stereo microscope (mRFP filter) and a HXP200C illuminator. Homozygous T3 lines have been identified for complementation lines expressing FLAG-AtPHR1, FLAG-AtPHR1<sup>K325A</sup>, FLAG-AtPHR1<sup>H328A</sup>, and FLAG-AtPHR1<sup>R335A</sup> under the control of the native *AtPHR1* promoter. For complementation lines expressing FLAG-AtPHR1<sup>K325A R335A</sup> and FLAG-AtPHR1<sup>K325A H328A R335A</sup> under the control of the native *AtPHR1* promoter, T2 lines were used throughout, and homozygous and heterozygous transformants were selected for all experiments by mCherry fluorescence as described above. T3 homozygous lines expressing eGFP-PHR1 under the control of the *AtPHR1* promoter were identified by their Hygromycin resistance. *PHR1* was amplified from *Arabidopsis* cDNA and introduced into pH7m34GW binary vector. Point mutations were introduced by site-directed mutagenesis (primers are listed in Supplementary Table 3).

**Yeast two-hybrid experiments.** (Screen) AtSPX1<sup>1–252</sup> was used as a bait and screened against an *A. thaliana* seedling cDNA library by Hybrigenics Services. AtSPX1<sup>1–252</sup> was cloned into the pB29 vector providing a C-terminal LexA–DNA-binding domain and transformed into yeast strain L40αGal4 (MATα). Prey genes were cloned into the pP6 vector providing a N-terminal Gal4-activation domain and transformed into yeast strain YHGX13 (MATα). After mating haploid bait and prey strains, positive interactions were detected by growth on histidine deficient medium.

**Yeast strains and media.** For all experiments, either the diploid TATA strain (Hybrigenics Services) or the haploid L40 strain was used (Supplementary Table 2). Cells were routinely maintained on yeast extract-peptone-adenine-dextrose (YPAD) plates (20 g/L glucose, 20 g/L bacto-peptone, 10 g/L yeast extract, 0.04 g/L adenine hemisulfate, and 20 g/L agar). Experiments were performed on synthetic dropout (SD) plates (6.7 g/L yeast nitrogen base with adenine hemisulfate

and without leucine, tryptophan, and histidine, 20 g/L glucose, and 20 g/L agar) supplemented with 0.076 g/L histidine or 10 mM 3-amino-1,2,4-triazole (3-AT).

**Yeast transformation.** One yeast colony was resuspended in 500 μL sterile H<sub>2</sub>O, plated on YPAD plates, and grown for 2 days until the whole plate was covered with yeast. Yeast cells were then resuspended in 50 mL YPAD liquid medium and the OD<sub>600nm</sub> was determined (2 × 10<sup>6</sup> cells/mL were used for one transformation). Cells were centrifuged at 3000 × *g* and 4 °C for 5 min, resuspended in 25 mL Tris-EDTA (TE) buffer, centrifuged again at 3000 × *g* and 4 °C for 5 min, resuspended in 2 mL LiAc/TE buffer, centrifuged at 16,000 × *g* and room temperature (RT) for 15 s, and finally resuspended in 50 μL transformation LiAc/TE buffer. The transformation mix (0.5 μg bait plasmid, 0.5 μg prey plasmid, 10 μL ssDNA (10 mg/mL), 50 μL yeast cells, 345 μL 40% (w/v) PEG3350 in LiAc/TE) was prepared and incubated at 30 °C for 45 min, followed by incubation at 42 °C for 30 min. Finally, yeast cells were centrifuged at 6500 × *g* and RT for 15 s, resuspended in TE buffer, plated on SD plates lacking leucine and tryptophan, and incubated at 30 °C for 3 days.

**Yeast spotting dilution assay.** Positive transformants were selected on SD plates without tryptophan and leucine, and incubated at 30 °C for three days. Cells were counted, washed in sterile water and spotted in 5 times dilution (5000, 1000, 200, 40, and 8 cells) on SD plates without either tryptophan and leucine, or tryptophan, leucine, and histidine supplemented with 10 mM 3-AT. Plates were incubated at 30 °C for 3 days.

**Protein expression and purification.** For in vitro biochemistry, AtPHR1<sup>280–360 wt/KHR/Olig1/Olig2</sup> and AtPHR1<sup>222–358 wt/Olig1/Olig2</sup> were cloned into the pMH-HT protein expression vector, providing a N-terminal 6 × His affinity tag with a tobacco etch virus (TEV) protease recognition site. OsPHR2<sup>1–426 wt/KHR/A</sup> was cloned into the pMH-HSgB1T protein expression vector, providing a N-terminal 8 × His-Strep-GB1 affinity tag with a TEV cleavage site. OsSPX2<sup>1–321</sup> was cloned into the pMH-HSsumo protein expression vector, providing a N-terminal 8xHis-Strep-Sumo affinity tag. All constructs were transformed into *Escherichia coli* BL21 (DE3) (*argU*, *ileY*, *leuW*) RIL cells. For recombinant protein expression, cells were grown at 37 °C in terrific broth (TB) medium to an OD<sub>600nm</sub> of ~0.6. After reducing the temperature to 18 °C, protein expression was induced with 0.3 mM isopropyl β-D-galactoside (IPTG) for 16 h. Cells were centrifuged at 4500 × *g* and 4 °C for 1 h, resuspended in lysis buffer (50 mM Tris-HCl pH 7.8, 500 mM NaCl, 0.1% (v/v) IGEPAL, 1 mM MgCl<sub>2</sub>, 2 mM β-mercaptoethanol), snap-frozen in liquid nitrogen, and stored at –80 °C. For protein preparation, cells were thawed, supplemented with cComplete™ EDTA-free protease inhibitor cocktail (Roch), DNaseI, and lysozyme, and disrupted using a sonicator. Cell lysates were centrifuged at 7000 × *g* and 4 °C for 1 h, sterile filtered, supplemented with 20 mM imidazole, and loaded onto a 5 mL HisTrap HP Ni<sup>2+</sup> affinity column (GE Healthcare). After washing with several column volumes (CVs) of lysis buffer supplemented with 20 mM imidazole, high-salt buffer (50 mM Tris-HCl pH 7.8, 1 M NaCl, 2 mM β-mercaptoethanol), and high-phosphate buffer (200 mM K<sub>2</sub>HPO<sub>4</sub>/KH<sub>2</sub>PO<sub>4</sub> pH 7.8, 2 mM β-mercaptoethanol), proteins were eluted in a gradient from 20 to 500 mM imidazole in lysis buffer. The purified proteins were cleaved by TEV or Sumo protease overnight at 4 °C (1:100 ratio) and dialyzed against lysis buffer for PHR1<sup>222–358 wt/Olig1/Olig2</sup> and PHR1<sup>280–360 wt/KHR/Olig1/Olig2</sup> fragments, against modified lysis buffer (25 mM Tris-HCl pH 7.8, 300 mM NaCl, 0.1% (v/v) IGEPAL, 1 mM MgCl<sub>2</sub>, 2 mM β-mercaptoethanol) for OsPHR2<sup>1–426 wt/KHR/A</sup>, and against modified anion exchange buffer (20 mM Tris-HCl pH 6.5, 500 mM NaCl) for OsSPX4<sup>1–321</sup>. PHR1<sup>280–360 wt/KHR/Olig1/Olig2</sup> and OsPHR2<sup>1–426 wt/KHR/A</sup> were subjected to a second Ni<sup>2+</sup> affinity purification in either lysis buffer or modified lysis buffer, respectively, and the flow-throughs were collected and concentrated. PHR1<sup>222–358 wt/Olig1/Olig2</sup> were subjected to cation exchange (50 mM HEPES pH 7.5, 50–1000 mM NaCl) and OsSPX4<sup>1–321</sup> was subjected to anion exchange (20 mM Tris-HCl, 50–1000 mM NaCl). Fractions corresponding to

the respective proteins were pooled and concentrated. All proteins were loaded onto a HiLoad Superdex 75 pg HR26/60 column (GE Healthcare), pre-equilibrated in gel filtration buffer A (20 mM Tris/HCl pH 7.5, 300 mM NaCl, 0.5 mM tris(2-carboxyethyl)phosphine (TCEP)) for PHR1<sup>222-358 wt/Olig1/Olig2</sup>, or in gel filtration buffer B (20 mM Tris/HCl pH 7, 200 mM NaCl, 0.5 mM TCEP) for the remaining proteins. Fractions containing the respective proteins were pooled and concentrated. Purified and concentrated protein was immediately used for further experiments or snap-frozen in liquid nitrogen and stored at  $-80^{\circ}\text{C}$ .

The AtPHR1<sup>280-360</sup> fragment used for crystallization was cloned into the pMH-HS-Sumo protein expression vector, providing a N-terminal 8  $\times$  His-StrepII tandem affinity tag and a Sumo fusion protein. The construct was transformed into *E. coli* BL21 (DE3) RIL cells. For recombinant protein expression, cells were grown at  $37^{\circ}\text{C}$  in TB medium to an OD<sub>600nm</sub> of  $\sim 0.6$ . After reducing the temperature to  $16^{\circ}\text{C}$ , protein expression was induced with 0.3 mM IPTG for 16 h. Cells were centrifuged for 20 min at  $4000 \times g$  and  $4^{\circ}\text{C}$ , then the cell pellet was washed with PBS, snap-frozen in liquid nitrogen and stored at  $-80^{\circ}\text{C}$ . For the purification of a putative AtSPX1-InsP<sub>8</sub>-AtPHR1<sup>280-360</sup> complex, the AtPHR1 cell pellet was thawed and mixed with twice the amount of cells expressing a His-Strep-MBP-AtSPX1<sup>1-251</sup> fusion protein, which provides a N-terminal, TEV-cleavable MBP. Lysis buffer (200 mM KP<sub>i</sub> pH 7.8, 2 mM  $\beta$ -mercaptoethanol) supplemented with 0.1% (v/v) IGEPAL, 1 mM MgCl<sub>2</sub>, 10 mM imidazole, 500 units TurboNuclease (BioVision), 2 tablets Protease Inhibitor Cocktail (Roche), and 0.1 mM InsP<sub>8</sub> was added and cells were disrupted using an EmulsiFlex-C3 (Avestin). Cell lysates were centrifuged at  $7000 \times g$  and  $4^{\circ}\text{C}$  for 1 h. The cleared supernatant was sterile filtered and loaded onto a 5 mL HisTrap HP Ni<sup>2+</sup> affinity column (GE Healthcare). After washing with several CVs of lysis buffer, the protein was eluted with 250 mM imidazole in lysis buffer. The purified His-Strep-Sumo-AtPHR1/His-Strep-MBP-AtSPX1 fusion proteins were cleaved by TEV and Sumo protease treatment overnight at  $4^{\circ}\text{C}$ , while dialyzing in a buffer containing 200 mM KP<sub>i</sub> pH 7.8, 100 mM NaCl, 2 mM  $\beta$ -mercaptoethanol. Imidazole (10 mM) was added to the cleaved protein sample and a second Ni<sup>2+</sup> affinity step was performed in order to remove the cleaved-off His-Strep-Sumo/MBP fusion tags as well as the 6  $\times$  His-tagged Sumo and TEV proteases. The flow-through was concentrated and loaded onto a HiLoad Superdex 75 pg HR16/60 column (GE Healthcare), pre-equilibrated in gel filtration buffer (20 mM Tris/HCl pH 7.8, 250 mM NaCl, 2.5 mM InsP<sub>6</sub>, 0.5 mM TCEP). Fractions containing the co-eluting AtSPX1<sup>1-251</sup> and AtPHR1<sup>280-360</sup> proteins were pooled and concentrated. A second SEC step was performed using a HiLoad Superdex 200 pg HR26/60 column (GE Healthcare) and the same gel filtration buffer as above. It was later found that AtSPX1<sup>1-251</sup> expressed in *E. coli* is largely unfolded and unable to bind InsP<sub>8</sub> and hence no complex with AtPHR1<sup>280-360</sup> was observed in our crystals. Purified and concentrated protein was immediately used for further experiments or snap-frozen in liquid nitrogen and stored at  $-80^{\circ}\text{C}$ .

For production of [<sup>15</sup>N,<sup>2</sup>H]-labeled AtPHR1<sup>280-360</sup> variants for NMR spectroscopy, AtPHR1<sup>280-360</sup> and AtPHR1<sup>280-360</sup> KHR/A in pMH-HT were transformed and expressed in *E. coli* BL21 (DE3) RIL cells. Luria-Bertani liquid medium (2 mL) was inoculated with freshly transformed cells. After overnight growth at  $37^{\circ}\text{C}$ , cells were transferred to M9<sub>H<sub>2</sub>O</sub> medium and grown overnight at  $37^{\circ}\text{C}$ . From this culture, 150  $\mu\text{L}$  were transferred into 1 mL M9<sub>H<sub>2</sub>O</sub> medium and grown at  $37^{\circ}\text{C}$  overnight. Cells were transferred into 100 mL M9<sub>D<sub>2</sub>O</sub> medium and grown overnight at  $37^{\circ}\text{C}$ . The culture was added to 0.9 L of M9<sub>D<sub>2</sub>O</sub> medium and grown at  $37^{\circ}\text{C}$  to an OD<sub>600nm</sub> of  $\sim 0.4$ , then the temperature was shifted to  $16^{\circ}\text{C}$ . After 1 h, protein expression was induced with 0.3 mM IPTG and cells were grown overnight, reaching a final OD<sub>600nm</sub> of 1.2–1.4. The cell culture was harvested at  $7800 \times g$  and the cell pellet was stored at  $-20^{\circ}\text{C}$ . The cell pellet was resuspended in 50 mM Tris pH 7.8, 500 mM NaCl, 0.1% IGEPAL, 1 mM MgCl<sub>2</sub>, 2 mM  $\beta$ -mercaptoethanol, 20 mM imidazole, and DNaseI (AppliChem). The resuspension was homogenized by magnetic stirring and after 10 min lysozyme was added. The cells were lysed by sonication and subsequently centrifuged at  $42,500 \times g$  for 45 min. The collected supernatant was applied on 5 mL HisTrap HP (GE Healthcare) equilibrated in a buffer A (50 mM Tris pH 7.8, 500 mM NaCl and 2 mM  $\beta$ -mercaptoethanol) and washed with a wash buffer 1 (50 mM Tris pH 7.8, 200 mM KP<sub>i</sub>, and 2 mM  $\beta$ -mercaptoethanol) and with wash buffer 2 (50 mM Tris pH 7.8, 1 M NaCl, 2 mM  $\beta$ -mercaptoethanol), followed by a final wash step with buffer A. His-tagged protein was eluted with a buffer B (50 mM Tris pH 7.8, 500 mM NaCl, 1 M imidazole, and 1 mM  $\beta$ -mercaptoethanol). The fractions containing the eluted protein were incubated with TEV protease overnight at  $4^{\circ}\text{C}$ . The sample was dialyzed against buffer A at  $4^{\circ}\text{C}$  and purified by a second Ni<sup>2+</sup> affinity step. Cleaved AtPHR1<sup>280-360</sup> from the flow-through of the column was concentrated to 3 mL and purified further by SEC on a Superdex 75 16/600 (GE Healthcare) equilibrated in 25 mM HEPES pH 7.0, 200 mM NaCl and 0.5 mM TCEP at a flow rate of 1 mL/min. Fractions containing AtPHR1<sup>280-360</sup> were pooled, concentrated to 0.5 mL, and the protein concentration was determined via Bradford assay (AppliChem). Samples were flash-frozen in liquid nitrogen and subsequently used for NMR spectroscopy experiments.

**Isothermal titration calorimetry.** All ITC experiments were performed at  $25^{\circ}\text{C}$  using a MicroCal PEAQ-ITC system (Malvern Panalytical) equipped with a 200  $\mu\text{L}$  sample cell and a 40  $\mu\text{L}$  injection syringe. InsP<sub>7</sub> and InsP<sub>8</sub> were produced as described<sup>47</sup>. All proteins were dialyzed against ITC buffer (20 mM HEPES pH 7.0,

200 mM NaCl) and PP-InsP ligands were diluted in ITC buffer prior to all measurements. A typical titration consisted of 15 injections, the protein concentrations in the syringe and in the cell are provided in the respective figure legend. Data were analyzed using the MicroCal PEAQ-ITC analysis software (v1.21).

**Crystallization and crystallographic data collection.** Two hexagonal crystal forms containing AtPHR1<sup>280-360</sup> only developed in sitting drops consisting of 0.2  $\mu\text{L}$  protein at a concentration of 12 mg/mL and 0.2  $\mu\text{L}$  reservoir solution (0.1 M phosphate citrate pH 4.2, 0.2 M NaCl, 20% (w/v) PEG 8000). Crystals were cryo-protected by adding reservoir solution containing 10% (v/v) ethylene glycol directly to the drop and subsequently snap-frozen in liquid nitrogen. A third, tetragonal crystal form developed in 0.1 M Bis-Tri pH 6.5, 0.1 M NaCl, 1.5 M (NH<sub>4</sub>)<sub>2</sub>SO<sub>4</sub>. Crystals were cryo-protected by serial transfer into reservoir solution supplemented with 15% (v/v) glycerol and snap-frozen in liquid nitrogen. Crystal forms 1, 2, and 3 diffracted to  $\sim 2.4$ ,  $\sim 2.5$ , and  $\sim 1.9$  Å resolution, respectively. Data were collected at beam-line PXIII of the Swiss Light Source, Villigen, Switzerland. Data processing and scaling were done in XDS<sup>48</sup>.

**Crystallographic structure solution and refinement.** The AtPHR1<sup>280-360</sup> structure was solved by molecular replacement using the previously described SPX<sup>CGdel</sup> (PDB-ID:5IJJ) core helices as search model in calculations with the program PHASER<sup>49</sup>. The structure was completed in iterative cycles of manual model building in COOT<sup>50</sup> and restrained refinement in phenix.refine<sup>51</sup> or Refmac5<sup>52</sup>. Residues 280–294 and 278–280 appear disordered in the final model. Quality of the structural model was assessed by using MolProbity<sup>53</sup>, refinement statistics are shown in Supplementary Table 5. Structure visualization was done with PyMOL (Molecular Graphics System, Version 1.8, Schrödinger, LLC) and ChimeraX<sup>54</sup>. The structure of AtSPX1 was modeled using the program SWISS-MODEL<sup>55</sup> and the SPX<sup>HsXPR1</sup> domain structure of the human phosphate exporter as template (PDB-ID:5IJH, GMQE score  $\sim 0.49$ , QMEAN4 score  $\sim -2.27$ , 29.5% sequence identity<sup>30</sup>). Conserved PP-InsP-binding residues in AtSPX1 were determined by aligning sequences with previously described SPX domains<sup>30</sup> using the program T-coffee<sup>56</sup>.

**Right-angle light scattering.** The oligomeric state of AtPHR1 variants was analyzed by SEC paired with a refractive index detector using an OMNISEC RESOLVE/REVEAL combined system (Malvern). Instrument calibration was performed with a bovine serum albumin (BSA) standard (Thermo Scientific Albumin Standard). Samples of 50  $\mu\text{L}$  containing 2–10 mg/mL AtPHR1 (wild-type AtPHR1<sup>280-360</sup>, AtPHR1<sup>280-360</sup> Olig1, AtPHR1<sup>280-360</sup> Olig2, AtPHR1<sup>280-360</sup> KHR/A, wild-type AtPHR1<sup>222-358</sup>, AtPHR1<sup>222-358</sup> Olig1, and AtPHR1<sup>222-358</sup> Olig2) in OMNISEC buffer (20 mM HEPES pH 7.5, 150 mM NaCl) were separated on a Superdex 200 increase 10/300 GL column (GE Healthcare) at a column temperature of  $25^{\circ}\text{C}$  and a flow rate of 0.7 mL min<sup>-1</sup>. Data were analyzed using the OMNISEC software (v10.41).

**DNA oligonucleotide annealing.** DNA oligonucleotides were dissolved in annealing buffer (10 mM HEPES-NaOH pH 8.0, 50 mM NaCl, 0.1 mM EDTA). Equal volumes of the equimolar DNA oligonucleotides were mixed and incubated in a heat block for 5 min at  $95^{\circ}\text{C}$ . Subsequently, DNA oligonucleotides were cooled down to room temperature for 90 min. Double-stranded DNA oligonucleotides were aliquoted and stored at  $-20^{\circ}\text{C}$ .

**Electrophoretic mobility shift assay.** Mini-PROTEAN TBE precast gels (5%; Bio-Rad) have been pre-electrophoresed in 0.5  $\times$  TBE buffer for 60 min at  $70^{\circ}\text{V}$ . Reactions mixes have been prepared following the Odyssey<sup>®</sup> Infrared EMSA kit manual (LI-COR) without the use of optional components, including 50 nM of IRDye800 end-labeled oligos (refer to Supplementary Table 4a; Metabion), and a 1 : 5 dilution series of wild-type AtPHR1<sup>222-358</sup> or AtPHR1<sup>222-358</sup> Olig1 (1.2  $\mu\text{g}$  to 76.8  $\mu\text{g}$ ). Reaction mixes have been incubated for 30 min at room temperature in the dark and 2  $\mu\text{L}$  of 10 $\times$  Orange Loading Dye (LI-COR) have been added to each sample prior to loading on a 5% TBE gel. Gels have been electrophoresed until orange dye migrated to the bottom of the gel ( $\sim 1$  h) at  $70^{\circ}\text{V}$  in the dark. Gels have been scanned with the 800 nm channel of an Odyssey imaging system (LI-COR).

**Grating-coupled interferometry.** All GCI experiments were performed at  $4^{\circ}\text{C}$  using a Creoptix WAVE system (Creoptix sensors) with 4PCP WAVE chips (Creoptix sensors). Chips were conditioned with borate buffer (100 mM sodium borate pH 9.0, 1 M NaCl) and subsequently neutravidin was immobilized on the chip surface via standard amine-coupling: activation (1 : 1 mix of 400 mM N-(3-dimethylaminopropyl)-N'-ethylcarbodiimide hydrochloride and 100 mM N-hydroxysuccinimide), immobilization (30  $\mu\text{g mL}^{-1}$  of neutravidin in 10 mM sodium acetate, pH 5.0), passivation (5% BSA in 10 mM sodium acetate pH 5.0), and quenching (1 M ethanolamine, pH 8.0). Biotinylated oligos (Supplementary Table 4b; Metabion) were captured on the chip. Analytes were injected in a 1 : 2 dilution series starting from 4  $\mu\text{M}$  (AtPHR1<sup>222-358</sup>), 20  $\mu\text{M}$  (AtPHR1<sup>222-358</sup> Olig1, AtPHR1<sup>222-358</sup> Olig2), or 10  $\mu\text{M}$  (OsPHR2, OsPHR2<sup>KHR/A</sup>) in GCI buffer (for OsPHR2: 20 mM HEPES pH 7.9, 200 mM NaCl; for AtPHR1: 20 mM HEPES pH

7.5, 300 mM NaCl). Blank injections every fourth cycle were used for double referencing and a dimethylsulfoxide (DMSO) calibration curve (0%, 0.5%, 1%, 1.5%, 2%) for bulk correction. Data were corrected and analyzed using the Creoptix WAVE control software (corrections applied: X and Y offset, DMSO calibration, double referencing, refractive index correction), and a one-to-one binding model was used to fit all experiments.

**CD spectroscopy.** Far-UV CD spectra and melting curves were acquired with a Chirascan V100 CD spectrometer holding the protein solutions in quartz cuvettes of 1 mm optical path, scanning from 260 to 190 nm at 1 nm/s with a slit width of 1 nm against an air background obtained with the same settings without any cuvette. Protein concentration was 0.08 mg/mL (8.5  $\mu$ M) in all experiments, the buffer was 10 mM KPi pH 7.5. A reference spectrum of the buffer showed only noise within  $\pm 0.5$  mdeg. All the final spectra reported were obtained with a single scan, as we observed very good signal-to-noise and no saturation of the detector voltage even at low wavelengths. Melting curves were acquired with 2 °C stepwise increments and 30 s intervals from 24 to 98 °C. Data were fitted in the range from 195 nm to 250 nm using the three-component ( $\alpha$ -helix,  $\beta$ -strand, and random coil) fitting (<http://lucianoabriata.altervista.org/jsinscience/cd/cd3.html>) as previously described<sup>57</sup>.

**NMR spectroscopy.** TROSY spectra of [U-<sup>15</sup>N,<sup>2</sup>H]-AtPHR1<sup>280–360</sup> and [U-<sup>15</sup>N,<sup>2</sup>H]-AtPHR1<sup>280–360</sup> KHR/A were acquired on a 600 MHz spectrometer with a cryo-probe at 30 °C. The NMR buffer contained 25 mM HEPES pH 7.0, 200 mM NaCl and 0.5 mM TCEP. NMR data were analyzed by CCPNMR 2.4.2<sup>58</sup>. The dissociation constant  $K_D$  was obtained by calculating chemical shift perturbations of each point by and plotted against InsP<sub>8</sub> concentration. The data points were fitted in MATLAB.

**Plant material, seed sterilization, and plant growth conditions.** All *A. thaliana* plants used in this study were of the Columbia (Col-0) ecotype. Seeds of the T-DNA insertion lines *phr1-3* (SALK\_067629) and *phl1* (SAIL\_731\_B09) were obtained from the European Arabidopsis Stock Center. Homozygous *phr1-3* and *phl1* lines were identified by PCR using T-DNA left and right border primers paired with gene-specific sense and antisense primers (Supplementary Table 3d). The *phr1 phl1* double mutant was kindly provided by Yves Poirier (University of Lausanne, Switzerland); *vih1-2 vih2-4* double and *phr1 phl1 vih1-2 vih2-4* quadruple mutants have been reported previously<sup>35</sup>. Seeds were surface sterilized by incubation in 70% (v/v) CH<sub>3</sub>-CH<sub>2</sub>-OH for 10 min, followed by incubation in 0.5% (v/v) sodium hypochlorite for 10 min, and subsequently washed four times in sterile H<sub>2</sub>O. Seeds were placed on full half-strength Murashige-Skoog plates<sup>59</sup> containing 1 (w/v) % sucrose and 0.8 (w/v) % agar (<sup>1/2</sup>MS plates), and stratified for 2–3 days at 4 °C in the dark prior to transfer into a growth cabinet. Plants were grown on vertical <sup>1/2</sup>MS plates at 22 °C under long day conditions (16 h light–8 h dark) for 8 to 11 days.

**Western blotting.** Proteins were transferred to nitrocellulose membrane (GE Healthcare, Amersham™ Highbond™-ECL) via wet western blotting at 4 °C and 30 V overnight. Membranes were blocked in TBS-Tween (0.1%)–Milk (5%) for 1 h at room temperature. For mCherry detection, membranes were incubated overnight with an anti-mCherry antibody (ab167453, dilution 1 : 2000; Abcam) followed by 1 h incubation with an anti-rabbit-horseradish peroxidase (HRP) antibody (dilution 1 : 10,000, Calbiochem). For GFP detection, membranes were incubated overnight with an anti-GFP-HRP antibody (130-091-833, dilution 1 : 1000, Miltenyi Biotec). For FLAG detection, membranes were incubated overnight with an anti-FLAG-HRP antibody (A8692, dilution 1 : 1000, Sigma). For SPX1 detection, membranes were incubated overnight with an anti-SPX1 antibody (dilution 1 : 1000, kind gift of Professor Mingguang Lei) followed by one hour incubation with an anti-rabbit-HRP antibody (dilution 1 : 10,000, Calbiochem). Antibodies were diluted in TBS-Tween (0.05%)–Milk (2.5%). Membranes were detected with SuperSignal™ West Femto Maximum Sensitivity Substrate (34095, Thermo Scientific™).

**Determination of cellular Pi concentrations.** To determine cellular Pi concentration at seedling stage, plants were transferred from <sup>1/2</sup>MS plates to -Pi <sup>1/2</sup>MS plates containing 1 (w/v)% sucrose and 0.8 (w/v)% agarose supplemented with either 0, 1, or 10 mM Pi (KH<sub>2</sub>PO<sub>4</sub>/K<sub>2</sub>HPO<sub>4</sub> pH 5.7) at 7 DAG, and grown at 22 °C under long day conditions. At 14 DAG, seedlings were weighed and harvested into 1.5 mL tubes containing 500  $\mu$ L nanopure H<sub>2</sub>O. Samples were frozen at –80 °C overnight, thawed at 80 °C for 10 min, refrozen at –80 °C, incubated at 80 °C in a thermomixer shaking at 1400 r.p.m. for 1 h, and briefly centrifuged to sediment plant tissue. Pi content was measured by the colorimetric molybdate assay<sup>60</sup>. In brief, 600  $\mu$ L ammonium molybdate solution (0.44 g of ammonium molybdate tetrahydrate in 97.3 mL nanopure water; add 2.66 mL concentrated (18 M) H<sub>2</sub>SO<sub>4</sub> to a final volume of 100 mL), 100  $\mu$ L 10% ascorbic acid, and 300  $\mu$ L sample (250  $\mu$ L nanopure water + 50  $\mu$ L extracts) or 300  $\mu$ L NaPi standard solution were mixed. Samples were incubated at 37 °C for 1 h and absorbance at 820 nm was measured.

**RNA analyses.** At 14 DAG, 50–150 mg seedlings were harvested in 2 mL Eppendorf tubes containing two metal beads each, shock-frozen in liquid nitrogen and ground in a tissue lyzer (MM400, Retsch). RNA extraction was performed using the ReliaPrep RNA Tissue Miniprep System (Promega) including in column DNaseI treatment to remove genomic DNA. First strand cDNA synthesis was performed from 1 to 2.5  $\mu$ g of total RNA using Superscript II RT (Invitrogen) with oligo(dT) primers. Quantitative reverse transcriptase PCR (qRT-PCR) was performed in 10  $\mu$ L reactions containing 1 $\times$  SYBR-Green fluorescent stain (Applied Biosystems) and measured using a 7900HT Fast Real Time PCR-System (Applied Biosystems). qRT-PCR program: 2'–95 °C; 40 $\times$  (30'–95 °C; 30'–60 °C; 20'–72 °C); melting curve 95 °C–60 °C–95 °C. A primer list can be found in Supplementary Table 3e. Expression levels of target genes were normalized against the housekeeping gene *Actin2*. For every genotype, three biological replicates were analyzed in technical triplicates.

**Transient transformation of *N. benthamiana*.** For each construct, 4 mL of *A. tumefaciens* strain pGV2260 suspension culture were grown overnight at 28 °C. Cells were collected by centrifugation at 700  $\times$  g for 15 min and resuspended in transformation buffer (10 mM MgCl<sub>2</sub>, 10 mM MES pH 5.6, 150  $\mu$ M acetosyringone). Cell density was measured and set to a final OD<sub>600nm</sub> of 0.5 for SPX1 and PHR1, and to 0.1 for the silencing suppressor P19. Suspension cultures were incubated for 2 h in the dark at room temperature and subsequently mixed at a volume ratio of 1 : 1 : 1 (SPX1 : PHR1 : P19). *N. benthamiana* leaves were infiltrated using a 0.5 mL syringe and 3 leaf disks ( $d = 1$  cm) per sample were harvested after 3 days, snap-frozen in liquid nitrogen, and stored at –80 °C.

**Co-immunoprecipitation.** For co-immunoprecipitation experiments with proteins transiently expressed in *N. benthamiana*, samples were ground in liquid nitrogen with plastic mortars and proteins were extracted with 600  $\mu$ L of homogenization buffer (50 mM Tris-HCl pH 7.5, 150 mM NaCl, 0.25% Triton X-100, 5% (v/v) glycerol, 1 mM phenylmethylsulfonyl fluoride, cComplete™ EDTA-free protease inhibitor cocktail (Roche). Samples were incubated at 4 °C for 10 min with gently rotation and subsequently centrifuged at 16,000  $\times$  g and 4 °C for 15 min. Supernatants were transferred to fresh tubes and further centrifuged at 16,000  $\times$  g and 4 °C for 15 min. Supernatants were transferred to fresh tubes, while 50  $\mu$ L of each supernatant were taken and mixed with 10  $\mu$ L 6 $\times$  SDS sample buffer (input), the remaining supernatants were mixed with 50  $\mu$ L magnetic  $\mu$ MACS anti-GFP beads (Miltenyi Biotec) and incubated at 4 °C for 2 h with gently rotation. MACS columns (Miltenyi Biotec) were used with a  $\mu$ MACS Separator (Miltenyi Biotec). MACS columns were washed with 200  $\mu$ L of homogenization buffer and samples were loaded. Columns were washed either four times with 200  $\mu$ L of homogenization buffer and once with wash buffer 2 (Miltenyi Biotec), or three times with 200  $\mu$ L of homogenization buffer, three times with wash buffer 1 (Miltenyi Biotec) and once with wash buffer 2. Columns were incubated with 20  $\mu$ L preheated elution buffer (Miltenyi Biotec) for 5 min at room temperature. Elution buffer (50  $\mu$ L) was added and eluates were recovered. Inputs and eluates were boiled for 5 min at 95 °C prior and separated on 9% SDS-polyacrylamide electrophoresis gels. Co-immunoprecipitation experiments for proteins stably or natively expressed in *A. thaliana* were performed as previously described<sup>29</sup>.

**Statistics.** All statistical analyses and data plots have been performed and generated with R version 3.5.2<sup>61</sup> and the packages “Hmisc<sup>62</sup>,” “agricolae<sup>63</sup>,” “car<sup>64</sup>,” “multcompView<sup>65</sup>,” and “multcomp<sup>66</sup>.” qRT-PCR data were power transformed with the Box–Cox transformation and a significant one-way analysis of variance (ANOVA) followed by a Dunnett's post hoc test was performed for multiple comparisons of several genotypes vs. wild type (Col-0) shown in Supplementary Fig. 8a. Pi content was analyzed with a one-way ANOVA followed by a Dunnett's post hoc test for multiple comparisons of several genotypes vs. wild type (Col-0) shown in Fig. 4b and Supplementary Fig. 8b–d. (\* $p < 0.05$ ; \*\* $p < 0.01$ ; \*\*\* $p < 0.001$ )

**Reporting summary.** Further information on research design is available in the Nature Research Reporting Summary linked to this article.

## Data availability

Data supporting the findings of this manuscript are available from the corresponding authors upon reasonable request. A reporting summary for this article is available as a Supplementary Information file. Coordinates and structure factors have been deposited in the Protein Data Bank (PDB) with accession codes 6TO5 (form1), 6TO9 (form2), and 6TOC (form3). The associated X-ray diffraction images and data processing files have been deposited at <http://zenodo.org> with DOIs <https://doi.org/10.5281/zenodo.3570698> (form1), <https://doi.org/10.5281/zenodo.3570977> (form2), and <https://doi.org/10.5281/zenodo.3571040> (form3). Source data are provided with this paper.

Received: 13 December 2019; Accepted: 9 December 2020;

Published online: 15 January 2021

## References

- Wykoff, D. D., Grossman, A. R., Weeks, D. P., Usuda, H. & Shimogawara, K. Psl1, a nuclear localized protein that regulates phosphorus metabolism in *Chlamydomonas*. *Proc. Natl Acad. Sci. USA* **96**, 15336–15341 (1999).
- Rubio, V. et al. A conserved MYB transcription factor involved in phosphate starvation signaling both in vascular plants and in unicellular algae. *Genes Dev.* **15**, 2122–2133 (2001).
- Riechmann, J. L. et al. *Arabidopsis* transcription factors: genome-wide comparative analysis among eukaryotes. *Science* **290**, 2105–2110 (2000).
- Zhou, J. et al. OsPHR2 is involved in phosphate-starvation signaling and excessive phosphate accumulation in shoots of plants. *Plant Physiol.* **146**, 1673–1686 (2008).
- Ren, F. et al. *Brassica napus* PHR1 gene encoding a MYB-like protein functions in response to phosphate starvation. *PLoS ONE* **7**, e44005 (2012).
- Wang, J. et al. A phosphate starvation response regulator Ta-PHR1 is involved in phosphate signalling and increases grain yield in wheat. *Ann. Bot.* **111**, 1139–1153 (2013).
- Bustos, R. et al. A central regulatory system largely controls transcriptional activation and repression responses to phosphate starvation in *Arabidopsis*. *PLoS Genet.* **6**, e1001102 (2010).
- Nilsson, L., Müller, R. & Nielsen, T. H. Increased expression of the MYB-related transcription factor, PHR1, leads to enhanced phosphate uptake in *Arabidopsis thaliana*. *Plant Cell Environ.* **30**, 1499–1512 (2007).
- Pant, B. D. et al. The transcription factor PHR1 regulates lipid remodeling and triacylglycerol accumulation in *Arabidopsis thaliana* during phosphorus starvation. *J. Exp. Bot.* **66**, 1907–1918 (2015).
- Bari, R., Datt Pant, B., Stitt, M. & Scheible, W.-R. PHO2, microRNA399, and PHR1 define a phosphate-signaling pathway in plants. *Plant Physiol.* **141**, 988–999 (2006).
- Rouached, H., Secco, D., Arpat, B. & Poirier, Y. The transcription factor PHR1 plays a key role in the regulation of sulfate shoot-to-root flux upon phosphate starvation in *Arabidopsis*. *BMC Plant Biol.* <https://doi.org/10.1186/1471-2229-11-19> (2011).
- Khan, G. A. et al. Coordination between zinc and phosphate homeostasis involves the transcription factor PHR1, the phosphate exporter PHO1, and its homologue PHO1;H3 in *Arabidopsis*. *J. Exp. Bot.* **65**, 871–884 (2014).
- Nilsson, L., Lundmark, M., Jensen, P. E. & Nielsen, T. H. The *Arabidopsis* transcription factor PHR1 is essential for adaptation to high light and retaining functional photosynthesis during phosphate starvation. *Physiol. Plant* **144**, 35–47 (2012).
- Bournier, M. et al. *Arabidopsis* ferritin 1 (AtFer1) gene regulation by the phosphate starvation response 1 (AtPHR1) transcription factor reveals a direct molecular link between iron and phosphate homeostasis. *J. Biol. Chem.* **288**, 22670–22680 (2013).
- Castrillo, G. et al. Root microbiota drive direct integration of phosphate stress and immunity. *Nature* **543**, 513–518 (2017).
- Liu, F. et al. OsSPX1 suppresses the function of OsPHR2 in the regulation of expression of OsPT2 and phosphate homeostasis in shoots of rice. *Plant J.* **62**, 508–517 (2010).
- Shi, J. et al. The paralogous SPX3 and SPX5 genes redundantly modulate Pi homeostasis in rice. *J. Exp. Bot.* **65**, 859–870 (2014).
- Wang, Z. et al. Rice SPX1 and SPX2 inhibit phosphate starvation responses through interacting with PHR2 in a phosphate-dependent manner. *Proc. Natl Acad. Sci. USA* **111**, 14953–14958 (2014).
- Puga, M. I. et al. SPX1 is a phosphate-dependent inhibitor of phosphate starvation response 1 in *Arabidopsis*. *Proc. Natl Acad. Sci. USA* **111**, 14947–14952 (2014).
- Duan, K. et al. Characterization of a sub-family of *Arabidopsis* genes with the SPX domain reveals their diverse functions in plant tolerance to phosphorus starvation. *Plant J.* **54**, 965–975 (2008).
- Wang, C. et al. Involvement of OsSPX1 in phosphate homeostasis in rice. *Plant J.* **57**, 895–904 (2009).
- Wang, Z. et al. Regulation of OsSPX1 and OsSPX3 on expression of OsSPX domain genes and Pi-starvation signaling in rice. *J. Integr. Plant Biol.* **51**, 663–674 (2009).
- Lv, Q. et al. SPX4 negatively regulates phosphate signaling and homeostasis through its interaction with PHR2 in rice. *Plant Cell* **26**, 1586–1597 (2014).
- Zhong, Y. et al. Rice SPX6 negatively regulates the phosphate starvation response through suppression of the transcription factor PHR2. *N. Phytol.* **219**, 135–148 (2018).
- Osorio, M. B. et al. SPX4 acts on PHR1-dependent and -independent regulation of shoot phosphorus status in *Arabidopsis*. *Plant Physiol.* **181**, 332–352 (2019).
- Qi, W., Manfield, I. W., Muench, S. P. & Baker, A. AtSPX1 affects the AtPHR1–DNA-binding equilibrium by binding monomeric AtPHR1 in solution. *Biochem. J.* **474**, 3675–3687 (2017).
- Ruan, W. et al. Two RING-finger ubiquitin E3 ligases regulate the degradation of SPX4, an internal phosphate sensor, for phosphate homeostasis and signaling in rice. *Mol. Plant* **12**, 1060–1074 (2019).
- Jung, J.-Y., Ried, M. K., Hothorn, M. & Poirier, Y. Control of plant phosphate homeostasis by inositol pyrophosphates and the SPX domain. *Curr. Opin. Biotechnol.* **49**, 156–162 (2018).
- Dong, J. et al. Inositol pyrophosphate InsP8 acts as an intracellular phosphate signal in *Arabidopsis*. *Mol. Plant* **12**, 1463–1473 (2019).
- Wild, R. et al. Control of eukaryotic phosphate homeostasis by inositol polyphosphate sensor domains. *Science* **352**, 986–990 (2016).
- Shears, S. B. Intimate connections: Inositol pyrophosphates at the interface of metabolic regulation and cell signaling. *J. Cell. Physiol.* **233**, 1897–1912 (2018).
- Laha, D. et al. *Arabidopsis* ITPK1 and ITPK2 have an evolutionarily conserved phytic acid kinase activity. *ACS Chem. Biol.* **14**, 2127–2133 (2019).
- Desai, M. et al. Two inositol hexakisphosphate kinases drive inositol pyrophosphate synthesis in plants. *Plant J.* **80**, 642–653 (2014).
- Laha, D. et al. VIH2 regulates the synthesis of inositol pyrophosphate InsP8 and jasmonate-dependent defenses in *Arabidopsis*. *Plant Cell* **27**, 1082–1097 (2015).
- Zhu, J. et al. Two bifunctional inositol pyrophosphate kinases/phosphatases control plant phosphate homeostasis. *eLife* **8**, e43582 (2019).
- Couso, I. et al. Synergism between inositol polyphosphates and TOR kinase signaling in nutrient sensing, growth control, and lipid metabolism in *Chlamydomonas*. *Plant Cell* **28**, 2026–2042 (2016).
- Gu, C. et al. The significance of the bifunctional kinase/phosphatase activities of diphosphoinositol pentakisphosphate kinases (PPIP5Ks) for coupling inositol pyrophosphate cell signaling to cellular phosphate homeostasis. *J. Biol. Chem.* **292**, 4544–4555 (2017).
- Pascual-Ortiz, M. et al. Asp1 bifunctional activity modulates spindle function via controlling cellular inositol pyrophosphate levels in *Schizosaccharomyces pombe*. *Mol. Cell. Biol.* **38** (2018).
- Jiang, M. et al. Structural basis for the Target DNA recognition and binding by the MYB domain of phosphate starvation response 1. *FEBS J.* **286**, 2809–2821 (2019).
- Dražkovič, P. et al. Inositol hexakisphosphate kinase products contain diphosphate and triphosphate groups. *Chem. Biol.* **15**, 274–286 (2008).
- Mulugu, S. et al. A conserved family of enzymes that phosphorylate inositol hexakisphosphate. *Science* **316**, 106–109 (2007).
- Jaillass, Y. et al. Tyrosine phosphorylation controls brassinosteroid receptor activation by triggering membrane release of its kinase inhibitor. *Genes Dev.* **25**, 232–237 (2011).
- Holm, L. & Sander, C. Protein structure comparison by alignment of distance matrices. *J. Mol. Biol.* **233**, 123–138 (1993).
- Andres, S. N. et al. Tetrameric Ctp1 coordinates DNA binding and DNA bridging in DNA double-strand-break repair. *Nat. Struct. Mol. Biol.* **22**, 158–166 (2015).
- Krissinel, E. & Henrick, K. Inference of macromolecular assemblies from crystalline state. *J. Mol. Biol.* **372**, 774–797 (2007).
- Clough, S. J. & Bent, A. F. Floral dip: a simplified method for *Agrobacterium*-mediated transformation of *Arabidopsis thaliana*. *Plant J.* **16**, 735–743 (1998).
- Puschmann, R., Harmel, R. K. & Fiedler, D. Scalable chemoenzymatic synthesis of inositol pyrophosphates. *Biochemistry* **58**, 3927–3932 (2019).
- Kabsch, W. Automatic processing of rotation diffraction data from crystals of initially unknown symmetry and cell constants. *J. Appl. Crystallogr.* **26**, 795–800 (1993).
- McCoy, A. J. et al. Phaser crystallographic software. *J. Appl. Crystallogr.* **40**, 658–674 (2007).
- Emsley, P. & Cowtan, K. Coot: model-building tools for molecular graphics. *Acta Crystallogr. D. Biol. Crystallogr.* **60**, 2126–2132 (2004).
- Adams, P. D. et al. PHENIX: a comprehensive Python-based system for macromolecular structure solution. *Acta Crystallogr. D. Biol. Crystallogr.* **66**, 213–221 (2010).
- Murshudov, G. N., Vagin, A. A. & Dodson, E. J. Refinement of macromolecular structures by the maximum-likelihood method. *Acta Crystallogr. D. Biol. Crystallogr.* **53**, 240–255 (1997).
- Davis, I. W. et al. MolProbity: all-atom contacts and structure validation for proteins and nucleic acids. *Nucleic Acids Res.* **35**, W375–W383 (2007).
- Goddard, T. D. et al. UCSF ChimeraX: meeting modern challenges in visualization and analysis. *Protein Sci.* **27**, 14–25 (2018).
- Bordoli, L. et al. Protein structure homology modeling using SWISS-MODEL workspace. *Nat. Protoc.* **4**, 1–13 (2009).
- Notredame, C., Higgins, D. G. & Heringa, J. T-coffee: a novel method for fast and accurate multiple sequence alignment. *J. Mol. Biol.* **302**, 205–217 (2000).
- Abriata, L. A. A simple spreadsheet program to simulate and analyze the far-UV circular dichroism spectra of proteins. *J. Chem. Educ.* **88**, 1268–1273 (2011).
- Vranken, W. F. et al. The CCPN data model for NMR spectroscopy: development of a software pipeline. *Proteins* **59**, 687–696 (2005).

59. Murashige, T. & Skoog, F. A revised medium for rapid growth and bio assays with tobacco tissue cultures. *Physiol. Plant.* **15**, 473–497 (1962).
60. Ames, B. Assay of inorganic phosphate, total phosphate and phosphatases. *Methods Enzymol.* **8**, 115–118 (1966).
61. R Core Team. *R: A Language and Environment for Statistical Computing*. <https://www.R-project.org/> (R Foundation for Statistical Computing, Vienna, Austria, 2017).
62. Harrell Jr, F. E. *Hmisc: Harrell Miscellaneous*. <https://CRAN.R-project.org/package=Hmisc> (2020).
63. Mendiburu, F. *agricolae: Statistical Procedures for Agricultural Research. R package version 1.3-3*. <https://CRAN.R-project.org/package=agricolae> (2020)
64. Fox, J. & Weisberg, S. *An {R} Companion to Applied Regression*. 3rd edn. <https://socialsciences.mcmaster.ca/jfox/Books/Companion/> (Sage, Thousand Oaks, CA, 2019).
65. Graves, S. et al. *multcompView: Visualizations of Paired Comparisons. R package version 0.1-8*. <https://CRAN.R-project.org/package=multcompView> (2019).
66. Hothorn, T., Bretz, F. & Westfall, P. Simultaneous inference in general parametric models. *Biom. J.* **50**, 346–363 (2008).

## Acknowledgements

This work was supported by European Research Council Consolidator Grant 818696/INSPIRE (to M.H.), by Swiss National Foundation Sinergia Grant CRSII5\_170925 (to M.H., S.H., and D.F.), and by an HHMI International Research Scholar Award (to M.H.). M.K.R. was supported by an EMBO long-term fellowship (ALTF-129-2017). We thank Irene Sabater for providing LI SPX1 and members of the Hothorn lab for critically reading the manuscript.

## Author contributions

M.K.R.: Conceptualization, data curation, formal analysis, validation, investigation, visualization, methodology, and writing (original draft, review, and editing). R.W.: Conceptualization, data curation, formal analysis, validation, investigation, methodology, and writing (review and editing). J.Z.: Investigation, methodology, and writing (review and editing). J.P.: Conceptualization, data curation, formal analysis, validation, investigation, methodology, and writing (review and editing). K.S.: investigation, formal analysis, and methodology. L.B.: Investigation and methodology. R.K.H.: Methodology. L.A.A.: formal analysis and methodology. L.A.H.: Software, formal analysis, and methodology. D.F.: Resources, methodology, and writing (review and editing). S.H.: Resources,

methodology, supervision, and writing (review and editing). M.H.: Conceptualization, resources, data curation, formal analysis, supervision, funding acquisition, validation, investigation, visualization, methodology, project administration, and writing (original draft, review, and editing).

## Competing interests

The authors declare no competing interests.

## Additional information

**Supplementary information** is available for this paper at <https://doi.org/10.1038/s41467-020-20681-4>.

**Correspondence** and requests for materials should be addressed to M.H.

**Peer review information** *Nature Communications* thanks Aiwu Dong and the other, anonymous, reviewer(s) for their contribution to the peer review of this work. Peer review reports are available.

**Reprints and permission information** is available at <http://www.nature.com/reprints>

**Publisher's note** Springer Nature remains neutral with regard to jurisdictional claims in published maps and institutional affiliations.



**Open Access** This article is licensed under a Creative Commons Attribution 4.0 International License, which permits use, sharing, adaptation, distribution and reproduction in any medium or format, as long as you give appropriate credit to the original author(s) and the source, provide a link to the Creative Commons license, and indicate if changes were made. The images or other third party material in this article are included in the article's Creative Commons license, unless indicated otherwise in a credit line to the material. If material is not included in the article's Creative Commons license and your intended use is not permitted by statutory regulation or exceeds the permitted use, you will need to obtain permission directly from the copyright holder. To view a copy of this license, visit <http://creativecommons.org/licenses/by/4.0/>.

© The Author(s) 2021

**Supplementary Information for “Inositol pyrophosphates promote the interaction of SPX domains with the coiled-coil motif of PHR transcription factors to regulate plant phosphate homeostasis.”**

Martina K. Ried<sup>1,\*,%</sup>, Rebekka Wild<sup>1,\*,#</sup>, Jinsheng Zhu<sup>1</sup>, Joka Pipercevic<sup>2</sup>, Kristina Sturm<sup>1</sup>, Larissa Broger<sup>1</sup>, Robert K. Harmel<sup>3</sup>, Luciano A. Abriata<sup>4</sup>, Ludwig A. Hothorn<sup>5,&</sup>, Dorothea Fiedler<sup>3</sup>, Sebastian Hiller<sup>2</sup>, Michael Hothorn<sup>1,§</sup>

ORCID IDs: MKR: 0000-0003-1582-5016, RW: 0000-0003-2025-7228. JZ: 0000-0002-8131-1876, JP: 0000-0002-3316-0268, KS: 0000-0003-1653-5168, LB: 0000-0002-1303-9778, RKH: 0000-0003-4413-7730, LAA: 0000-0003-3087-8677, LAH: 0000-0002-5162-1486, DF: 0000-0002-0798-946X, SH: 0000-0002-6709-4684, MH 0000-0002-3597-5698

<sup>1</sup>Structural Plant Biology Laboratory, Department of Botany and Plant Biology, University of Geneva, 1211 Geneva, Switzerland.

<sup>2</sup>Biozentrum Basel, 4056 Basel, Switzerland

<sup>3</sup>Leibniz-Forschungsinstitut für Molekulare Pharmakologie, 13125 Berlin, Germany & Department of Chemistry, Humboldt-Universität zu Berlin, 12489 Berlin, Germany.

<sup>4</sup>Protein production and structure Core Facility, EPFL, 1015 Lausanne, Switzerland

<sup>5</sup>Institute of Biostatistics, Leibniz University, 30419 Hannover, Germany.

\*contributed equally

%Present address: Leibniz Institute of Plant Biochemistry, 06120 Halle, Germany.

#Present address: Institut de Biologie Structurale (IBS), 38044 Grenoble, France.

&retired

§To whom correspondence should be addressed. Email: [michael.hothorn@unige.ch](mailto:michael.hothorn@unige.ch)

### Supplementary Table 1 – Stable transgenic *A. thaliana* lines.

Promoter	N-terminal tag	Gene	Genetic background	Selection
<i>pPHR1</i>	FLAG	<i>PHR1</i>	<i>phr1-3</i>	<i>p35S:mCherry</i>
<i>pPHR1</i>	FLAG	<i>PHR1</i> <sup>K325A</sup>	<i>phr1-3</i>	<i>p35S:mCherry</i>
<i>pPHR1</i>	FLAG	<i>PHR1</i> <sup>H328A</sup>	<i>phr1-3</i>	<i>p35S:mCherry</i>
<i>pPHR1</i>	FLAG	<i>PHR1</i> <sup>R335A</sup>	<i>phr1-3</i>	<i>p35S:mCherry</i>
<i>pPHR1</i>	FLAG	<i>PHR1</i> <sup>K325A, R335A</sup>	<i>phr1-3</i>	<i>p35S:mCherry</i>
<i>pPHR1</i>	FLAG	<i>PHR1</i> <sup>K325A H328A R335A</sup>	<i>phr1-3</i>	<i>p35S:mCherry</i>
<i>pPHR1</i>	eGFP	<i>PHR1</i>	<i>phr1 phl1</i>	hygromycin
<i>pPHR1</i>	eGFP	<i>PHR1</i> <sup>K325A H328A R335A</sup>	<i>phr1 phl1</i>	hygromycin

### Supplementary Table 2 – Yeast strains.

Plasmids for yeast transformation have been generated via Gibson cloning<sup>67</sup>. Mutations targeting AtPHR1 K325, H328 and R335 were introduced by site-directed mutagenesis PCR<sup>68</sup>.

Strain	Plasmids	Genotype
TATA	untransformed	gal4::loxP-kanMX-loxP/Gal4D, ade2 trp1-901/ade2-101::loxP-kanMX-loxP, leu2-3,112/ leu2-3,-112, his3D200/ his3D200, LYS2/lys2::(lexAop)4-HIS3, ura3-52::URA3(lexAop)8-lacZ/ ura3-52 URA3::UASGAL1-LacZ
TATA	<i>pB29:AtSPX1</i> <sup>1-252</sup> <i>pP6:AtPHR1</i> <sup>1-409</sup>	gal4::loxP-kanMX-loxP/Gal4D, ade2 trp1-901/ade2-101::loxP-kanMX-loxP, leu2-3,112/ leu2-3,-112, his3D200/ his3D200, LYS2/lys2::(lexAop)4-HIS3, ura3-52::URA3(lexAop)8-lacZ/ ura3-52 URA3::UASGAL1-LacZ, pB29-pADH1-AtSPX1-LexA-tADH1-TRP1-TetR, pP6-pADH1-Gal4_AD-AtPHR_1-1227-tADH1-LEU2-ampR
TATA	<i>pB29:AtSPX1</i> <sup>1-252</sup> <i>pP6:AtPHR1</i> <sup>226-360</sup>	gal4::loxP-kanMX-loxP/Gal4D, ade2 trp1-901/ade2-101::loxP-kanMX-loxP, leu2-3,112/ leu2-3,-112, his3D200/ his3D200, LYS2/lys2::(lexAop)4-HIS3, ura3-52::URA3(lexAop)8-lacZ/ ura3-52 URA3::UASGAL1-LacZ, pB29-pADH1-AtSPX1-LexA-tADH1-TRP1-TetR, pP6-pADH1-Gal4_AD-AtPHR_678-1080-tADH1-LEU2-ampR
TATA	<i>pB29:AtSPX1</i> <sup>1-252</sup> <i>pP6:AtPHR1</i> <sup>280-360</sup>	gal4::loxP-kanMX-loxP/Gal4D, ade2 trp1-901/ade2-101::loxP-kanMX-loxP, leu2-3,112/ leu2-3,-112, his3D200/ his3D200, LYS2/lys2::(lexAop)4-HIS3, ura3-52::URA3(lexAop)8-lacZ/ ura3-52 URA3::UASGAL1-LacZ, pB29-pADH1-AtSPX1-LexA-tADH1-TRP1-TetR, pP6-pADH1-Gal4_AD-PHR_840-1080-tADH1-LEU2-ampR
TATA	<i>pB29:AtSPX1</i> <sup>1-252</sup> <i>pP6:AtPHR1</i> <sup>300-360</sup>	gal4::loxP-kanMX-loxP/Gal4D, ade2 trp1-901/ade2-101::loxP-kanMX-loxP, leu2-3,112/ leu2-3,-112, his3D200/ his3D200, LYS2/lys2::(lexAop)4-HIS3, ura3-52::URA3(lexAop)8-lacZ/ ura3-52 URA3::UASGAL1-LacZ, pB29-pADH1-AtSPX1-LexA-tADH1-TRP1-TetR, pP6-pADH1-Gal4_AD-PHR_900-1080-tADH1-LEU2-ampR
TATA	<i>pB29:AtSPX1</i> <sup>1-252</sup> <i>pP6:AtPHR1</i> <sup>280-353</sup>	gal4::loxP-kanMX-loxP/Gal4D, ade2 trp1-901/ade2-101::loxP-kanMX-loxP, leu2-3,112/ leu2-3,-112, his3D200/ his3D200, LYS2/lys2::(lexAop)4-HIS3, ura3-52::URA3(lexAop)8-lacZ/ ura3-52 URA3::UASGAL1-LacZ, pB29-pADH1-AtSPX1-LexA-tADH1-TRP1-TetR, pP6-pADH1-Gal4_AD-PHR_840-1059-tADH1-LEU2-ampR
TATA	<i>pB29:AtSPX1</i> <sup>1-252</sup> <i>pP6:AtPHR1</i> <sup>280-342</sup>	gal4::loxP-kanMX-loxP/Gal4D, ade2 trp1-901/ade2-101::loxP-kanMX-loxP, leu2-3,112/ leu2-3,-112, his3D200/ his3D200,

		LYS2/lys2::(lexAop)4-HIS3, ura3-52::URA3(lexAop)8-lacZ/ ura3-52 URA3::UASGAL1-LacZ, pB29-pADH1-AtSPX1-LexA-tADH1-TRP1-TetR, pP6-pADH1-Gal4_AD-PHR_840-1026-tADH1-LEU2-ampR
TATA	<i>pB29:AtSPX1<sup>1-252</sup></i> <i>pP6:AtPHR1<sup>1-225</sup></i>	gal4::loxP-kanMX-loxP/Gal4D, ade2 trp1-901/ade2-101::loxP-kanMX-loxP, leu2-3,112/ leu2-3,-112, his3D200/ his3D200, LYS2/lys2::(lexAop)4-HIS3, ura3-52::URA3(lexAop)8-lacZ/ ura3-52 URA3::UASGAL1-LacZ, pB29-pADH1-AtSPX1-LexA-tADH1-TRP1-TetR, pP6-pADH1-Gal4_AD-PHR_1-675-tADH1-LEU2-ampR
TATA	<i>pB29:AtSPX1<sup>1-252</sup></i> <i>pP6:AtPHR1<sup>360-409</sup></i>	gal4::loxP-kanMX-loxP/Gal4D, ade2 trp1-901/ade2-101::loxP-kanMX-loxP, leu2-3,112/ leu2-3,-112, his3D200/ his3D200, LYS2/lys2::(lexAop)4-HIS3, ura3-52::URA3(lexAop)8-lacZ/ ura3-52 URA3::UASGAL1-LacZ, pB29-pADH1-AtSPX1-LexA-tADH1-TRP1-TetR, pP6-pADH1-Gal4_AD-PHR_1080-1227-tADH1-LEU2-ampR
TATA	<i>pB29 AtSPX2<sup>1-287</sup></i> <i>pP6:AtPHR1<sup>226-360</sup></i>	gal4::loxP-kanMX-loxP/Gal4D, ade2 trp1-901/ade2-101::loxP-kanMX-loxP, leu2-3,112/ leu2-3,-112, his3D200/ his3D200, LYS2/lys2::(lexAop)4-HIS3, ura3-52::URA3(lexAop)8-lacZ/ ura3-52 URA3::UASGAL1-LacZ, pB29-pADH1-AtSPX2_1-861-LexA-tADH1-TRP1-TetR, pP6-pADH1-Gal4_AD-AtPHR_678-1080-tADH1-LEU2-ampR
TATA	<i>pB29:AtSPX3<sup>1-245</sup></i> <i>pP6:AtPHR1<sup>226-360</sup></i>	gal4::loxP-kanMX-loxP/Gal4D, ade2 trp1-901/ade2-101::loxP-kanMX-loxP, leu2-3,112/ leu2-3,-112, his3D200/ his3D200, LYS2/lys2::(lexAop)4-HIS3, ura3-52::URA3(lexAop)8-lacZ/ ura3-52 URA3::UASGAL1-LacZ, pB29-pADH1-AtSPX3_1-735-LexA-tADH1-TRP1-TetR, pP6-pADH1-Gal4_AD-AtPHR_678-1080-tADH1-LEU2-ampR
TATA	<i>pB29:AtSPX4<sup>1-318</sup></i> <i>pP6:AtPHR1<sup>226-360</sup></i>	gal4::loxP-kanMX-loxP/Gal4D, ade2 trp1-901/ade2-101::loxP-kanMX-loxP, leu2-3,112/ leu2-3,-112, his3D200/ his3D200, LYS2/lys2::(lexAop)4-HIS3, ura3-52::URA3(lexAop)8-lacZ/ ura3-52 URA3::UASGAL1-LacZ, pB29-pADH1-AtSPX4_1-954-LexA-tADH1-TRP1-TetR, pP6-pADH1-Gal4_AD-AtPHR_678-1080-tADH1-LEU2-ampR
TATA	<i>pB29:AtSPX1<sup>1-252</sup> PBC</i> <i>pP6:AtPHR1<sup>226-360</sup></i>	gal4::loxP-kanMX-loxP/Gal4D, ade2 trp1-901/ade2-101::loxP-kanMX-loxP, leu2-3,112/ leu2-3,-112, his3D200/ his3D200, LYS2/lys2::(lexAop)4-HIS3, ura3-52::URA3(lexAop)8-lacZ/ ura3-52 URA3::UASGAL1-LacZ, pB29-pADH1-AtSPX1_Y25F_K29A_K140A-LexA-tADH1-TRP1-TetR, pP6-pADH1-Gal4_AD-PHR_678-1080-tADH1-LEU2-ampR
TATA	<i>pB29:AtSPX1<sup>1-252</sup> KSC</i> <i>pP6:AtPHR1<sup>226-360</sup></i>	gal4::loxP-kanMX-loxP/Gal4D, ade2 trp1-901/ade2-101::loxP-kanMX-loxP, leu2-3,112/ leu2-3,-112, his3D200/ his3D200, LYS2/lys2::(lexAop)4-HIS3, ura3-52::URA3(lexAop)8-lacZ/ ura3-52 URA3::UASGAL1-LacZ, pB29-pADH1-AtSPX1_K136A_K139A_K143A-LexA-tADH1-TRP1-TetR, pP6-pADH1-Gal4_AD-PHR_678-1080-tADH1-LEU2-ampR
TATA	<i>pB29:AtSPX1<sup>1-252</sup> K81A</i> <i>pP6:AtPHR1<sup>226-360</sup></i>	gal4::loxP-kanMX-loxP/Gal4D, ade2 trp1-901/ade2-101::loxP-kanMX-loxP, leu2-3,112/ leu2-3,-112, his3D200/ his3D200, LYS2/lys2::(lexAop)4-HIS3, ura3-52::URA3(lexAop)8-lacZ/ ura3-52 URA3::UASGAL1-LacZ, pB29-pADH1-AtSPX1_K81A-LexA-tADH1-TRP1-TetR, pP6-pADH1-Gal4_AD-PHR_678-1080-tADH1-LEU2-ampR
TATA	<i>pB29:AtSPX1<sup>1-252</sup></i> <i>pP6:AtPHR1<sup>226-360</sup> K308A</i>	gal4::loxP-kanMX-loxP/Gal4D, ade2 trp1-901/ade2-101::loxP-kanMX-loxP, leu2-3,112/ leu2-3,-112, his3D200/ his3D200, LYS2/lys2::(lexAop)4-HIS3, ura3-52::URA3(lexAop)8-lacZ/ ura3-52 URA3::UASGAL1-LacZ, pB29-pADH1-AtSPX1-LexA-tADH1-TRP1-TetR, pP6-pADH1-Gal4_AD-PHR_678-1080_K308A-tADH1-LEU2-ampR
TATA	<i>pB29:AtSPX1<sup>1-252</sup></i> <i>pP6:AtPHR1<sup>226-360</sup> R318A</i>	gal4::loxP-kanMX-loxP/Gal4D, ade2 trp1-901/ade2-101::loxP-kanMX-loxP, leu2-3,112/ leu2-3,-112, his3D200/ his3D200, LYS2/lys2::(lexAop)4-HIS3, ura3-52::URA3(lexAop)8-lacZ/ ura3-52 URA3::UASGAL1-LacZ, pB29-pADH1-AtSPX1-LexA-tADH1-TRP1-TetR, pP6-pADH1-Gal4_AD-PHR_678-1080_R318A-tADH1-

		LEU2-ampR
TATA	<i>pB29:AtSPX1<sup>1-252</sup></i> <i>pP6:AtPHR1<sup>226-360 K325A</sup></i>	gal4::loxP-kanMX-loxP/Gal4D, ade2 trp1-901/ade2-101::loxP-kanMX-loxP, leu2-3,112/ leu2-3,-112, his3D200/ his3D200, LYS2/lys2::(lexAop)4-HIS3, ura3-52::URA3(lexAop)8-lacZ/ ura3-52 URA3::UASGAL1-LacZ, pB29-pADH1-AtSPX1-LexA-tADH1-TRP1-TetR, pP6-pADH1-Gal4_AD-PHR_678-1080_K325A-tADH1-LEU2-ampR
TATA	<i>pB29:AtSPX1<sup>1-252</sup></i> <i>pP6:AtPHR1<sup>226-360 H328A</sup></i>	gal4::loxP-kanMX-loxP/Gal4D, ade2 trp1-901/ade2-101::loxP-kanMX-loxP, leu2-3,112/ leu2-3,-112, his3D200/ his3D200, LYS2/lys2::(lexAop)4-HIS3, ura3-52::URA3(lexAop)8-lacZ/ ura3-52 URA3::UASGAL1-LacZ, pB29-pADH1-AtSPX1-LexA-tADH1-TRP1-TetR, pP6-pADH1-Gal4_AD-PHR_678-1080_H328A-tADH1-LEU2-ampR
TATA	<i>pB29:AtSPX1<sup>1-252</sup></i> <i>pP6:AtPHR1<sup>226-360 R335A</sup></i>	gal4::loxP-kanMX-loxP/Gal4D, ade2 trp1-901/ade2-101::loxP-kanMX-loxP, leu2-3,112/ leu2-3,-112, his3D200/ his3D200, LYS2/lys2::(lexAop)4-HIS3, ura3-52::URA3(lexAop)8-lacZ/ ura3-52 URA3::UASGAL1-LacZ, pB29-pADH1-AtSPX1-LexA-tADH1-TRP1-TetR, pP6-pADH1-Gal4_AD-PHR_678-1080_R335A-tADH1-LEU2-ampR
TATA	<i>pB29:AtSPX1<sup>1-252</sup></i> <i>pP6:AtPHR1<sup>226-360 K325A R335A</sup></i>	gal4::loxP-kanMX-loxP/Gal4D, ade2 trp1-901/ade2-101::loxP-kanMX-loxP, leu2-3,112/ leu2-3,-112, his3D200/ his3D200, LYS2/lys2::(lexAop)4-HIS3, ura3-52::URA3(lexAop)8-lacZ/ ura3-52 URA3::UASGAL1-LacZ, pB29-pADH1-AtSPX1-LexA-tADH1-TRP1-TetR, pP6-pADH1-Gal4_AD-PHR_678-1080_K325AR335A -tADH1-LEU2-ampR
TATA	<i>pB29:AtSPX1<sup>1-252</sup></i> <i>pP6:AtPHR1<sup>226-360 K325A H328A R335A</sup></i>	gal4::loxP-kanMX-loxP/Gal4D, ade2 trp1-901/ade2-101::loxP-kanMX-loxP, leu2-3,112/ leu2-3,-112, his3D200/ his3D200, LYS2/lys2::(lexAop)4-HIS3, ura3-52::URA3(lexAop)8-lacZ/ ura3-52 URA3::UASGAL1-LacZ, pB29-pADH1-AtSPX1-LexA-tADH1-TRP1-TetR, pP6-pADH1-Gal4_AD-PHR_678-1080_K325AH328AR335A-tADH1-LEU2-ampR
TATA	<i>pB29:AtSPX1<sup>1-252</sup></i> <i>pP6:AtPHR1<sup>226-360 R340A</sup></i>	gal4::loxP-kanMX-loxP/Gal4D, ade2 trp1-901/ade2-101::loxP-kanMX-loxP, leu2-3,112/ leu2-3,-112, his3D200/ his3D200, LYS2/lys2::(lexAop)4-HIS3, ura3-52::URA3(lexAop)8-lacZ/ ura3-52 URA3::UASGAL1-LacZ, pB29-pADH1-AtSPX1-LexA-tADH1-TRP1-TetR, pP6-pADH1-Gal4_AD-PHR_678-1080_R340A-tADH1-LEU2-ampR
L40	untransformed	MATa ade2 trp1-901 leu2-3,112 lys2-801am his3D200 lys2::(lexAop)4-HIS3, ura3-52::URA3 (lexAop)8-lacZa
L40 ΔVIP1	untransformed	MATa ade2 trp1-901 leu2-3,112 lys2-801am his3D200 lys2::(lexAop)4-HIS3 ura3-52::URA3 (lexAop)8-lacZa vip1::natNT2
L40 ΔKCS1	untransformed	MATa ade2 trp1-901 leu2-3,112 lys2-801am his3D200 lys2::(lexAop)4-HIS3, ura3-52::URA3 (lexAop)8-lacZa kcs1::natNT2
L40	<i>pB29:AtSPX1<sup>1-252</sup></i> <i>pP6:AtPHR1<sup>226-360</sup></i>	MATa ade2 trp1-901 leu2-3,112 lys2-801am his3D200 lys2::(lexAop)4-HIS3, ura3-52::URA3 (lexAop)8-lacZa pB29-pADH1-AtSPX1-LexA-tADH1-TRP1-TetR, pP6-pADH1-Gal4_AD-AtPHR_678-1080-tADH1-LEU2-ampR
L40 ΔVIP1	<i>pB29:AtSPX1<sup>1-252</sup></i> <i>pP6:AtPHR1<sup>226-360</sup></i>	MATa ade2 trp1-901 leu2-3,112 lys2-801am his3D200 lys2::(lexAop)4-HIS3, ura3-52::URA3 (lexAop)8-lacZa vip1::natNT2 pP6-pADH1-Gal4_ADAtPHR_678-1080-tADH1-LEU2-ampR pB29-pADH1-AtSPX1-LexA-tADH1-TRP1-TetR
L40 ΔKCS1	<i>pB29:AtSPX1<sup>1-252</sup></i> <i>pP6:AtPHR1<sup>226-360</sup></i>	MATa ade2 trp1-901 leu2-3,112 lys2-801am his3D200 lys2::(lexAop)4-HIS3, ura3-52::URA3 (lexAop)8-lacZa kcs1::natNT2 pP6-pADH1-Gal4_ADAtPHR_678-1080-tADH1-LEU2-ampR pB29-pADH1-AtSPX1-LexA-tADH1-TRP1-TetR
L40	<i>pB29:AtBRI1<sup>828-1196</sup></i> <i>pP6:AtBKII1<sup>1-337</sup></i>	MATa ade2 trp1-901 leu2-3,112 lys2-801am his3D200 lys2::(lexAop)4-HIS3, ura3-52::URA3 (lexAop)8-lacZa pP6-pADH1-Gal4_AD_pP6_AtBKII1_1-1011-tADH1-LEU2-ampR pB29-pADH1-

		AtBRI1_2484-3588-LexA-tADH1-TRP1-TetR
L40 ΔVIP1	<i>pB29:AtBRI1<sup>828-1196</sup></i> <i>pP6:AtBKII<sup>1-337</sup></i>	MATa ade2 trp1-901 leu2-3,112 lys2-801am his3D200 lys2:: (lexAop)4-HIS3, ura3-52::URA3 (lexAop)8-lacZa vip1::natNT2 pP6- pADH1-Gal4_AD_pP6_AtBKII_1-1011-tADH1-LEU2-ampR pB29- pADH1-AtBRI1_2484-3588-LexA-tADH1-TRP1-TetR
L40 ΔKCS1	<i>pB29:AtBRI1<sup>828-1196</sup></i> <i>pP6:AtBKII<sup>1-337</sup></i>	MATa ade2 trp1-901 leu2-3,112 lys2-801am his3D200 lys2:: (lexAop)4-HIS3 ura3-52::URA3 (lexAop)8-lacZa kcs1::natNT2 pP6- pADH1-Gal4_AD_pP6_AtBKII_1-1011-tADH1-LEU2-ampR pB29- pADH1-AtBRI1_2484-3588-LexA-tADH1-TRP1-TetR

### Supplementary Table 3 – Constructs and primers.

**a, Golden Gate Level 0 constructs and primers.** The *PHR1* promoter and gene were amplified from *A. thaliana* gDNA, and *SPX1* was amplified from *A. thaliana* cDNA. Level 0 constructs were generated via *StuI* or *SmaI* cut-ligation into pUC Amp<sup>69</sup>.

Name	Primer	Sequences
pPHR1.1	OutFwdProm InRevProm	ACGAAGACGTTACGGGTCTCTGCGGATTTTGTAAACTATGAATC AGGAAGACGGAAAACGAATCGAATCGGAGAAAATG
pPHR1.2	InFwdProm OutRevProm	ATGAAGACCGTTTTCTTGGTCTGGATTGC ATGAAGACACCAGAGGTCTCTCAGATGTTGCTCTGCAAGAGAGAATC
PHR1.1	OutFwdGene InRevGene1	AAGAAGACTCTACGGGTCTCCACCATGGAGGCTCGTCCAGTTCATAGATCA GGTTCGAGGGACC GCGAAGACTTTTGGTCTCTAAAAAAGTGTGTCCAG
PHR1.2	InFwdGene1 InRevGene2	TTGAAGACGACCAAAAAGACACTGCAAATTCGCAACC TAGAAGACGAAGCCAATTATATGCATTAGCAGG
PHR1.3	InFwdGene2 InRevGene3	GCGAAGACTTGGCTTCTAATATTAGATTGTG TTGAAGACTCCTCTTGTTCAGATTTGGCTGCGGA
PHR1.4	InFwdGene3 OutRevGene	AAGAAGACCAAGAGGACAAGAAAAGTGTGATTTCG ATGAAGACAACAGAGGTCTCTCCTTATTATCGATTTTGGGACGC
<i>PHR1</i> <sup>K325A</sup> a <i>PHR1</i> <sup>K325A R335A</sup> a <i>PHR1</i> <sup>K325A H328A R335A</sup> a	InFwdGene2 InRevKA	GCGAAGACTTGGCTTCTAATATTAGATTGTG CAGAAGACTGCGCTGTACTTCCATCTGAAGTCG
<i>PHR1</i> <sup>K325A</sup> b	InFwdKA InRevGene3	GTGAAGACACGGCGCAACTCCATGAGCAGCTCGAG TTGAAGACTCCTCTTGTTCAGATTTGGCTGCGGA
<i>PHR1</i> <sup>H328A</sup> a	InFwdGene2 InRevHA	GCGAAGACTTGGCTTCTAATATTAGATTGTG CGGAAGACTCAGCGAGTTGCTTCTGTACTTCC
<i>PHR1</i> <sup>H328A</sup> b	InFwdHA InRevGene3	AGGAAGACCTCGCTGAGCAGCTCGAGGTATGTTT TTGAAGACTCCTCTTGTTCAGATTTGGCTGCGGA
<i>PHR1</i> <sup>R335A</sup> a	InFwdGene2 InRevRA	GCGAAGACTTGGCTTCTAATATTAGATTGTG GTGAAGACTTTGCTTGAATCTGCAGGCAAAGG
<i>PHR1</i> <sup>R335A</sup> b <i>PHR1</i> <sup>K325A R335A</sup> c <i>PHR1</i> <sup>K325A H328A R335A</sup> c	InFwdRA InRevGene3	TAGAAGACCAAGCAAACCTGCAACTCCGAATAGAAG TTGAAGACTCCTCTTGTTCAGATTTGGCTGCGGA
<i>PHR1</i> <sup>K325A R335A</sup> b	InFwdKA InRevRA	GTGAAGACACGGCGCAACTCCATGAGCAGCTCGAG GTGAAGACTTTGCTTGAATCTGCAGGCAAAGG
<i>PHR1</i> <sup>K325A H328A R335A</sup> b	InFwdKAHA InRevRA	GTGAAGACACGGCGCAACTCGCTGAGCAGCTCGAG GTGAAGACTTTGCTTGAATCTGCAGGCAAAGG
SPX1.1	OutFwdGene InRevGene1	AAGAAGACCATACGGGTCTCGCACCATGAAGTTTGGTAAGAGTC TCGAAGACGTCTCTAACAATTGGATGAAATTG
SPX1.2	InFwdGene1 InRevGene2	CCGAAGACTAGAGGACGAGTTGGAGAAATTCAAC TCGAAGACTGGAGACTCTCCATGAACTTATGC
SPX1.3	InFwdGene2 OutRevGene	TCGAAGACAGTCTCCATATGAAGAGACAATCGC AGGAAGACTGCAGAGGTCTCACCTTTTGGCTTCTTGTCTCCAAC

**b, Level I, II & III constructs.** Level 1 and level 3 constructs were generated via *BpiI* cut-ligation, and level 2 constructs via *BsaI* cut-ligation<sup>69</sup>.

Name	Assembly	Purpose
LI <i>BpiI</i> pPHR1	pPHR1.1 + pPHR1.2	Cloning

LI BpiI PHR1	PHR1.1 + PHR1.2 + PHR1.3 + PHR1.4	Cloning
LI BpiI PHR1 <sup>K</sup>	PHR1.1 + PHR1.2 + PHR1 <sup>K325A</sup> a + PHR1 <sup>K325A</sup> b + PHR1.4	Cloning
LI BpiI PHR1 <sup>H</sup>	PHR1.1 + PHR1.2 + PHR1 <sup>H328A</sup> a + PHR1 <sup>H328A</sup> b + PHR1.4	Cloning
LI BpiI PHR1 <sup>R</sup>	PHR1.1 + PHR1.2 + PHR1 <sup>R335A</sup> a + PHR1 <sup>R335A</sup> b + PHR1.4	Cloning
LI BpiI PHR1 <sup>KR</sup>	PHR1.1 + PHR1.2 + PHR1 <sup>K325A R335A</sup> a + PHR1 <sup>K325A R335A</sup> b + PHR1 <sup>K325A R335A</sup> c + PHR1.4	Cloning
LI BpiI PHR1 <sup>KHR/A</sup>	PHR1.1 + PHR1.2 + PHR1 <sup>K325A H328A R335A</sup> a + PHR1 <sup>K325A H328A R335A</sup> b + PHR1 <sup>K325A H328A R335A</sup> c + PHR1.4	Cloning
LI SPX1	SPX1.1 + SPX1.2 + SPX1.3	Cloning
LII R5-6 pPHR1:FLAG-PHR1	LI A-B pPHR1 + LI FLAG B-C + LI C-D PHR1 + LI dy D-E + LI E-F nos-T + LI dy F-G	Cloning
LII R5-6 pPHR1:FLAG-PHR1 <sup>K</sup>	LI A-B pPHR1 + LI FLAG B-C + LI C-D PHR1 <sup>K</sup> + LI dy D-E + LI E-F nos-T + LI dy F-G	Cloning
LII R5-6 pPHR1:FLAG-PHR1 <sup>H</sup>	LI A-B pPHR1 + LI FLAG B-C + LI C-D PHR1 <sup>H</sup> + LI dy D-E + LI E-F nos-T + LI dy F-G	Cloning
LII R5-6 pPHR1:FLAG-PHR1 <sup>R</sup>	LI A-B pPHR1 + LI FLAG B-C + LI C-D PHR1 <sup>R</sup> + LI dy D-E + LI E-F nos-T + LI dy F-G	Cloning
LII R5-6 pPHR1:FLAG-PHR1 <sup>KR</sup>	LI A-B pPHR1 + LI FLAG B-C + LI C-D PHR1 <sup>KR</sup> + LI dy D-E + LI E-F nos-T + LI dy F-G	Cloning
LII R5-6 pPHR1:FLAG-PHR1 <sup>KHR/A</sup>	LI A-B pPHR1 + LI FLAG B-C + LI C-D PHR1 <sup>KHR</sup> + LI dy D-E + LI E-F nos-T + LI dy F-G	Cloning
LII F1-2 p35S:mCherry	LI A-B p35S + LI dy B-C + LI C-D mCherry + LI dy D-E + LI E-F 35S-T + LI dy F-G	Cloning / <i>N. benthamiana</i> transformation
LII F1-2 p35S:mCherry-SPX1	LI A-B p35S + LI mCherry B-C + LI C-D SPX1 + LI dy D-E + LI E-F nos-T + LI dy F-G	<i>N. benthamiana</i> transformation
LII F1-2 p35S:GFP-PHR1	LI A-B p35S + LI GFP B-C + LI C-D PHR1 + LI dy D-E + LI E-F nos-T + LI dy F-G	<i>N. benthamiana</i> transformation
LII F1-2 p35S:GFP-PHR1 <sup>KHR/A</sup>	LI A-B p35S + LI GFP B-C + LI C-D PHR1 <sup>KHR</sup> + LI dy D-E + LI E-F nos-T + LI dy F-G	<i>N. benthamiana</i> transformation
LIIIβ fin p35S:mCherry pPHR1:FLAG-PHR1	LII p35S:mCherry 1-2 + LII ins 2-3 + LII dy 3-4 + LII ins 4-5 + LII F LII pPHR1:FLAG-PHR1 5-6	<i>A. thaliana</i> transformation
LIIIβ fin p35S:mCherry pPHR1:FLAG-PHR1 <sup>K</sup>	LII p35S:mCherry 1-2 + LII ins 2-3 + LII dy 3-4 + LII ins 4-5 + LII F LII pPHR1:FLAG-PHR1 <sup>K</sup> 5-6	<i>A. thaliana</i> transformation
LIIIβ fin p35S:mCherry pPHR1:FLAG-PHR1 <sup>H</sup>	LII p35S:mCherry 1-2 + LII ins 2-3 + LII dy 3-4 + LII ins 4-5 + LII F LII pPHR1:FLAG-PHR1 <sup>H</sup> 5-6	<i>A. thaliana</i> transformation
LIIIβ fin p35S:mCherry pPHR1:FLAG-PHR1 <sup>R</sup>	LII p35S:mCherry 1-2 + LII ins 2-3 + LII dy 3-4 + LII ins 4-5 + LII F LII pPHR1:FLAG-PHR1 <sup>R</sup> 5-6	<i>A. thaliana</i> transformation
LIIIβ fin p35S:mCherry pPHR1:FLAG-PHR1 <sup>KR</sup>	LII p35S:mCherry 1-2 + LII ins 2-3 + LII dy 3-4 + LII ins 4-5 + LII F LII pPHR1:FLAG-PHR1 <sup>KR</sup> 5-6	<i>A. thaliana</i> transformation
LIIIβ fin p35S:mCherry pPHR1:FLAG-PHR1 <sup>KHR/A</sup>	LII p35S:mCherry 1-2 + LII ins 2-3 + LII dy 3-4 + LII ins 4-5 + LII F LII pPHR1:FLAG-PHR1 <sup>KHR</sup> 5-6	<i>A. thaliana</i> transformation

### c, Plasmids for recombinant protein expression in *E. coli*.

Plasmids for recombinant protein expression in *E. coli* have been generated via Gibson cloning<sup>67</sup>. Mutations targeting AtPHR1 K325, H328 and R335 were introduced by site-directed mutagenesis PCR<sup>68</sup>.

Vector	Construct	Purpose
pMH_HT	<i>AtPHR1</i> <sup>222-358</sup>	OmniSEC, GCI, EMSA

pMH_HT	<i>AtPHR1</i> <sup>222-358 Olig1</sup>	OmniSEC, GCI, EMSA
pMH_HT	<i>AtPHR1</i> <sup>222-358 Olig2</sup>	OmniSEC, GCI, EMSA
pMH_HT	<i>AtPHR1</i> <sup>280 – 360</sup>	OmniSEC
pMH_HT	<i>AtPHR1</i> <sup>280 – 360 Olig1</sup>	OmniSEC
pMH_HT	<i>AtPHR1</i> <sup>280 – 360 Olig2</sup>	OmniSEC
pMH_HT	<i>AtPHR1</i> <sup>280-360 K325A, H328A, R335A</sup>	OmniSEC
pMH_HSgb1T	<i>OsPHR2</i> <sup>1 – 426</sup>	OmniSEC, GCI, ITC
pMH_HSgb1T	<i>OsPHR2</i> <sup>1 – 426 KHR/A</sup>	OmniSEC, GCI, ITC
pMH_Hssumo	<i>OsSPX4</i> <sup>1-321</sup>	ITC
pMH_Hssumo	<i>AtPHR1</i> <sup>280 – 360</sup>	Crystallisation

#### d, Characterisation of T-DNA mutants.

Name	5'-3' Sequence
LBb1.3	ATTTTGCCGATTCGGAAC
LP_PHR1	GAGAGACCTCACACGCACTTC
RP_PHR1	CTTTCTGGCGAACCTGTAGTG
ph11-LP	GTGGAGACGTTTCTGCACTTC
ph11-RP	TCCCACAATCCAAATTCAGAG

#### e, Gene expression analysis.

Gene identifier	Name	Sequence
At3g18780	Actin2_F	AGTGGTTCGTACAACCGGTATTGT
	Actin2_R	GATGGCATGGAGGAAGAGAGAAAC
At4g28610	PHR1_F	G TTCAGCAGCAACCTTCTCC
	PHR1_R	GCTCTTCACTACCGCCAAG
At1g23010	LPR1_F	CCGGGCTATGTCTACCATTGTAC
	LPR1_R	GCACCATCAAACTTCGCAGAGATCG
At3g52820	ACP5_F	CAGTTTCTAACTAGTGGTGCTGGA
	ACP5_R	GCTTGGGATTGATGGTCACT
At3g09922	IPS1_F	TGAAGACTGCAGAAGGCTGA
	IPS1_R	CGAAGCTTGCCAAAGGATAG
At2g11810	MGD3_F	AGAGGCCGGTTTAATGGAGT
	MGD3_R	CATCAGAGGATGCACGCTAA
At1g52940	PAP5_F	TCGAACCCGAAAGGCCAAGCGGTGC
	PAP5_R	GCGCTTGGTTCCACAAACCGGCCGTA
At2g38940	PHT1;4_F	CCTCGTTCGATTTATTACCACG
	PHT1;4_R	CCATCACAGCTTTTGGCTCATG
At5g20150	SPX1_F	CGGGTTTTGAAGGAGATCAG
	SPX1_R	GCGGCAATGAAAACACACTA

#### f, Primers used for cloning PHR1 into the pH7m34GW vector.

Name	5'-3' Sequence
PHR1_B2F	GGGGACAGCTTTCTGTACAAAGTGGATGAGGCTCGTCCAGTTCATAG

PHR1_B3R	GGGGACAACCTTTGTATAATAAAGTTGATCAATTATCGATTTTGGGACG
eGFP_B1F	GGGGACAAGTTTGTACAAAAAAGCAGGCTTAATGGTGAGCAAGGGCGAGGAGCTG
eGFP_B2R	GGGGACCACTTTGTACAAGAAAGCTGGGTACTTGTACAGCTCGTCCATGCC
PHR1_H328A_F	CAACTCGCTGAGCAGCTCGAAATTC AAGCAAACCTGCAACTCCG
PHR1_H328A_R	AGCTGCTCAGCGAGTTGCGCCTGTACTTCCATCTGAAGTCGTAGA
PHR1_R335A_F	ATCAAGCAAACCTGCAACTCCGAATAGAAGAACAAGG
PHR1_R335A_R	CAGGTTTGCTTGAATTCGAGCTGCTCATGGAG
PHR1_K325A_F	GTACAGGCGCAACTCCATGAGCAGCTCAGAAATT
PHR1_K325A_R	GAGTTGCGCCTGTACTTCCATCTGAAGTCGTAGAGC

### Supplementary Tabel 4 – Modified DNA oligos.

The P1BS (GNATATNC) is shown in bold.

#### a, IRdye end-labelled oligos for EMSA.

Name	Sequence
AtSPX1_800_F	5'-IRD800-CAG AGA AAA AAG <b>GAT ATT CTA</b> ATT AGA AAC CTT AAG <b>AAT ATT CTT</b> TTT AAT CCC-3'
AtSPX1_800_R	5'-IRD800-GGG ATT AAA AAG <b>AAT ATT CTT</b> AAG GTT TCT AAT TAG <b>AAT ATC CTT</b> TTT TCT CTG-3'

#### b, Biotinylated oligos for GCI.

Name	Sequence
AtSPX1_Biotin_F	5'-Biotin-CAG AGA AAA AAG <b>GAT ATT CTA</b> ATT AGA AAC CTT AAG <b>AAT ATT CTT</b> TTT AAT CCC-3'
AtSPX1_R	5'-GGG ATT AAA AAG <b>AAT ATT CTT</b> AAG GTT TCT AAT TAG <b>AAT ATC CTT</b> TTT TCT CTG-3'
OsIPS1_Biotin_F	5'-Biotin-TAA TGC TCG CCG <b>CAT ATC CTT</b> TGG TAG ATA-3'
OsIPS1_R	5'-TAT CTA CCA AAG <b>GAT ATG</b> CGG CGA GCA TTA-3'

**Supplementary Table 5 – Crystallographic data collection and refinement statistics.**

<b>PDB-ID</b>	<b>AtPHR1<sup>280-360</sup> form1 6TO5</b>	<b>AtPHR1<sup>280-360</sup> form2 6TO9</b>	<b>AtPHR1<sup>280-360</sup> form3 6TOC</b>
<b>Data collection</b>			
Space group	P 6 <sub>1</sub> 2 2	P 3 <sub>2</sub> 2 1	P 4 <sub>2</sub>
Cell dimensions			
<i>a</i> , <i>b</i> , <i>c</i> (Å)	70.4, 70.4, 148.88	70.05, 70.05, 80.17	31.52, 31.52, 81.60
α, β, γ (°)	90, 90, 120	90, 90, 120	90, 90, 90
Resolution (Å)	47.18 – 2.38 (2.52 – 2.38)	48.37 – 2.45 (2.59 – 2.44)	31.52 – 1.85 (1.97 – 1.85)
<i>R</i> <sub>meas</sub> <sup>#</sup>	0.189 (2.21)	0.164 (2.77)	0.073 (2.76)
CC(1/2) <sup>#</sup>	0.99 (0.69)	0.99 (0.51)	1.0 (0.40)
<i>I</i> /σ <i>I</i> <sup>#</sup>	14.85 (1.48)	15.86 (1.07)	21.41 (0.98)
Completeness (%) <sup>#</sup>	99.8 (98.9)	99.3 (96.0)	99.9 (99.3)
Redundancy <sup>#</sup>	20.8 (20.2)	19.0 (18.4)	13.5 (13.4)
Wilson B-factor <sup>#</sup>	56.7	67.8	47.1
<b>Refinement</b>			
Resolution (Å)	41.18 – 2.38	48.37 – 2.45	31.52 – 1.85
No. reflections	16,560	8,702	6,433
<i>R</i> <sub>work</sub> / <i>R</i> <sub>free</sub> <sup>§</sup>	0.22 (0.23)	0.23 (0.26)	0.21 (0.26)
No. atoms			
protein	940	952	753
solvent	18	4	27
Res. B-factors <sup>§</sup>			
protein	64.6	79.1	41.3
solvent	57.4	59.3	40.7
R.m.s deviations <sup>§</sup>			
bond lengths (Å)	0.0047	0.0049	0.012
bond angles (°)	0.89	0.98	1.61
Ramachandran plot <sup>§</sup> :			
most favored regions (%)	99.08	99.07	98.8
outliers (%)	0	0	0
MolProbity score <sup>§</sup>	1.31	1.19	1.24

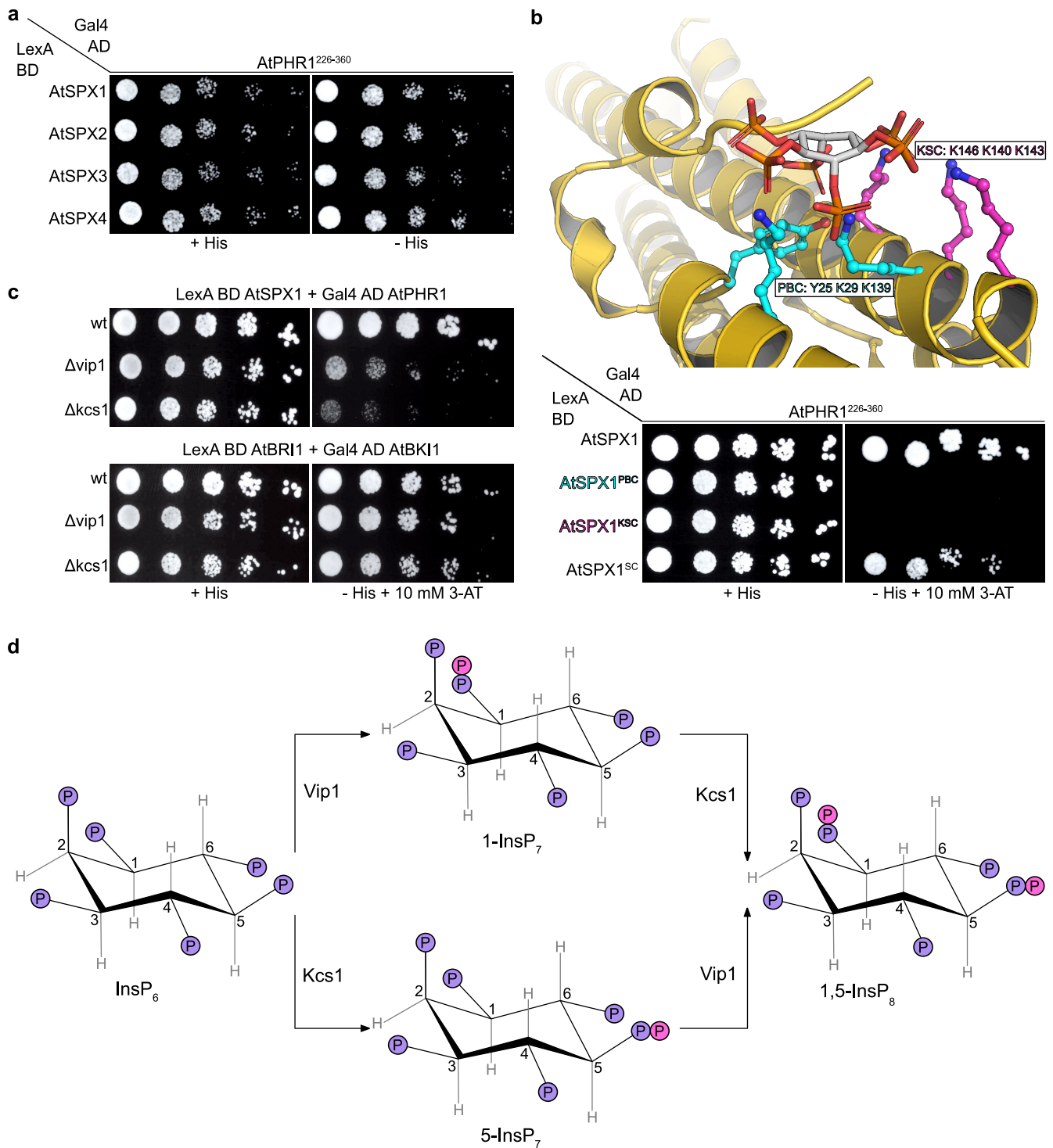
<sup>#</sup>as defined in XDS<sup>48</sup>

<sup>§</sup>as defined phenix.refine<sup>51</sup> (form 1, form2) or Refmac<sup>52</sup> (form 3, using twin laws h,k,l and -k, -h, -l with twin fractions of 0.5, apparent point group was P 4 2 2)

<sup>§</sup>as defined in Molprobity<sup>53</sup>

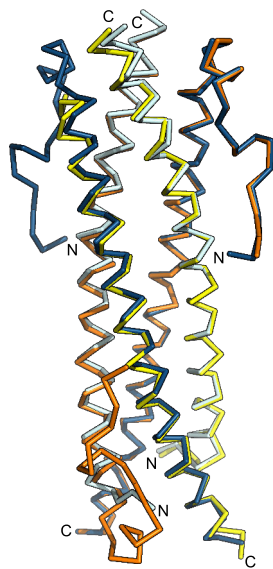
## Supplementary References

67. Gibson, D. G. et al. Enzymatic assembly of DNA molecules up to several hundred kilobases. *Nat. Methods* **6**, 343–345 (2009).
68. Liu, H. & Naismith, J. H. An efficient one-step site-directed deletion, insertion, single and multiple-site plasmid mutagenesis protocol. *BMC Biotechnol.* **8**, 91 (2008).
69. Binder, A. et al. A modular plasmid assembly kit for multigene expression, gene silencing and silencing rescue in plants. *PloS One* **9**, e88218 (2014).
70. Kabsch, W. & Sander, C. Dictionary of protein secondary structure: pattern recognition of hydrogen-bonded and geometrical features. *Biopolymers* **22**, 2577–2637 (1983).

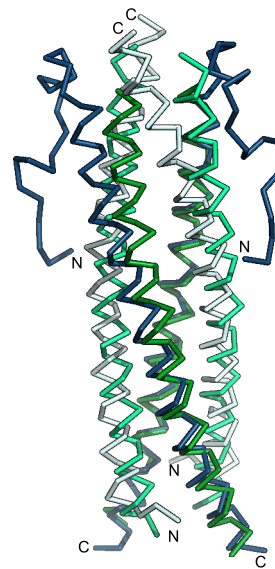


**Supplementary Fig. 1** The AtPHR1 – AtSPX1 interaction in yeast is mediated by PP-InsPs.

**a** Yeast-two-hybrid assay. Yeast co-expressing AtPHR1<sup>226-360</sup> fused to the Gal4-AD (prey) and different AtSPX proteins fused to the LexA-BD (bait) were grown on selective SD medium supplemented with histidine (+ His; co-transformation control) or lacking histidine (- His; interaction assay). Shown are serial dilutions from left to right. **b** (Top panel) Homology model of an AtSPX1<sup>1-182</sup>-InsP<sub>6</sub> complex. AtSPX1<sup>1-182</sup> is shown as blue ribbon diagram and side chains involved in InsP<sub>6</sub> binding are highlighted in green (PBC, phosphate binding cluster) and purple (KSC, lysine surface cluster) and depicted in bonds representation. The InsP<sub>6</sub> ligand is shown in grey (in bonds representation). (Bottom panel) Yeast co-expressing AtPHR1<sup>226-360</sup> fused to the Gal4-AD (prey) and different AtSPX1 versions mutated in residues involved in InsP<sub>6</sub> binding, or a structural control mutant (SC<sup>30</sup>) fused to the LexA-BD (bait) were grown on selective SD medium supplemented with histidine (+ His; co-transformation control) or lacking histidine and supplemented with 10 mM 3-AT (- His + 3-AT; interaction assay) to investigate the importance of the PP-InsP binding surface in AtSPX1 for the AtSPX1 – AtPHR1 interaction in yeast. **c** Yeast knock-out strains for the PP-InsP biosynthesis enzymes Vip1 or Kcs1 co-expressing either AtPHR1<sup>226-360</sup> fused to the Gal4-AD (prey) and AtSPX1 fused to the LexA-BD (bait) (upper panel), or AtBKI1 fused to the Gal4-AD (prey) and AtBRI1 fused to the LexA-BD (bait) (lower panel) were grown on selective SD medium supplemented with histidine (+ His; co-transformation control) or lacking histidine and supplemented with 10 mM 3-AT (- His + 3-AT; interaction assay) to investigate the importance of the availability of specific PP-InsPs for the AtSPX1-AtPHR1 interaction in yeast. **d** Schematic representation of the PP-InsP biosynthesis pathway in yeast.

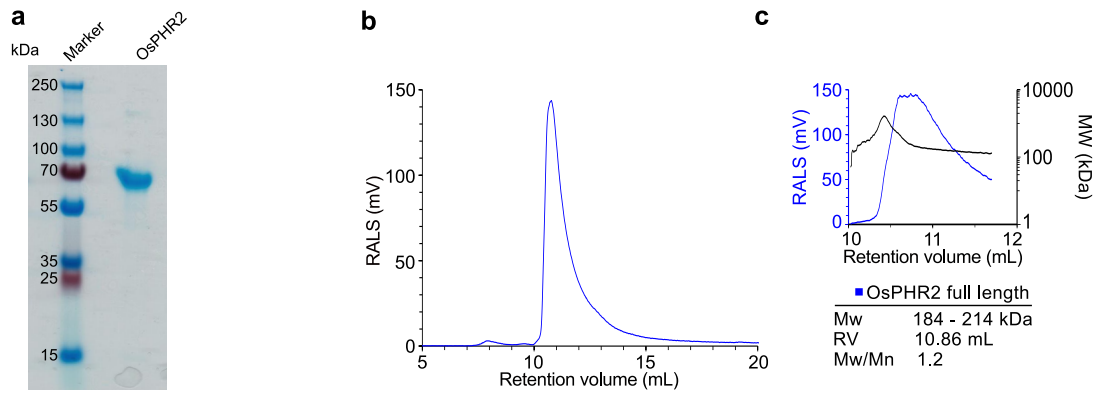


form 1 A+C  
 form 1 B+D  
 form 2 A+C  
 form 2 B+D



form 1 A+C  
 form 1 B+D  
 form 3 A+C  
 form 3 B+D

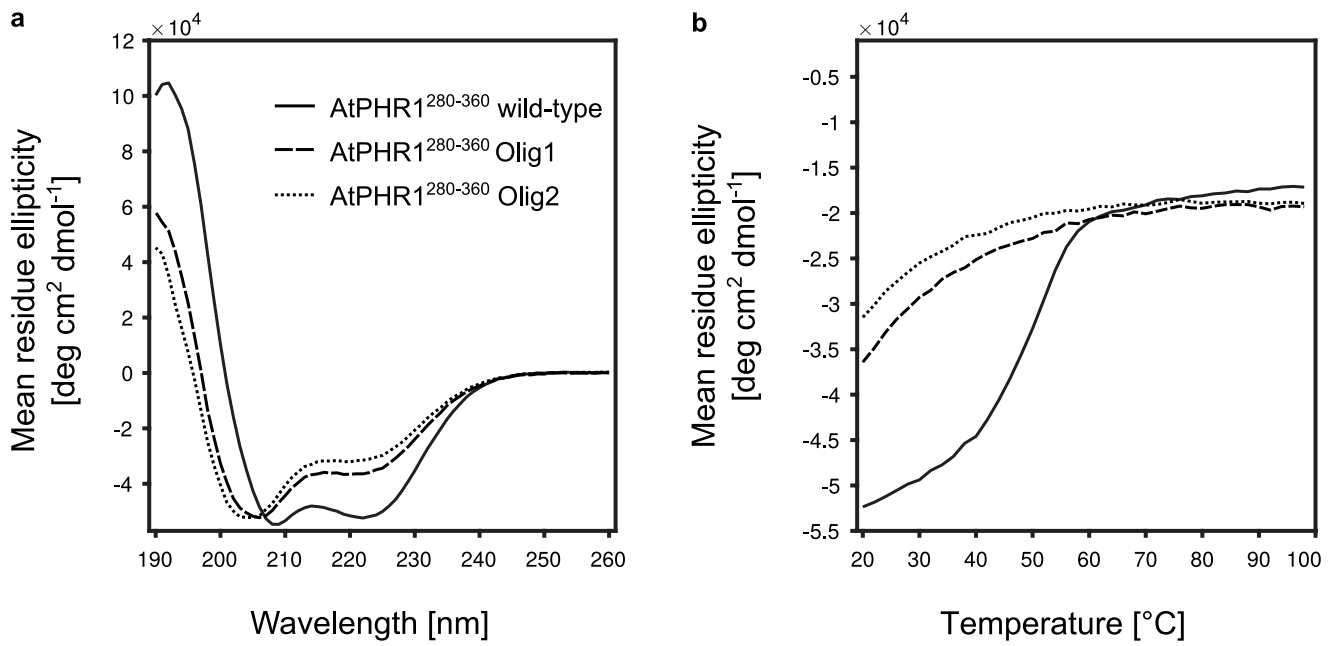
**Supplementary Fig. 2** Three different AtPHR1 coiled-coil domain crystal structures all share the same tetrameric arrangement. Structural superposition (shown as  $C_{\alpha}$  traces) of the four-stranded anti-parallel CC domain of AtPHR1 from crystal forms 1-3.



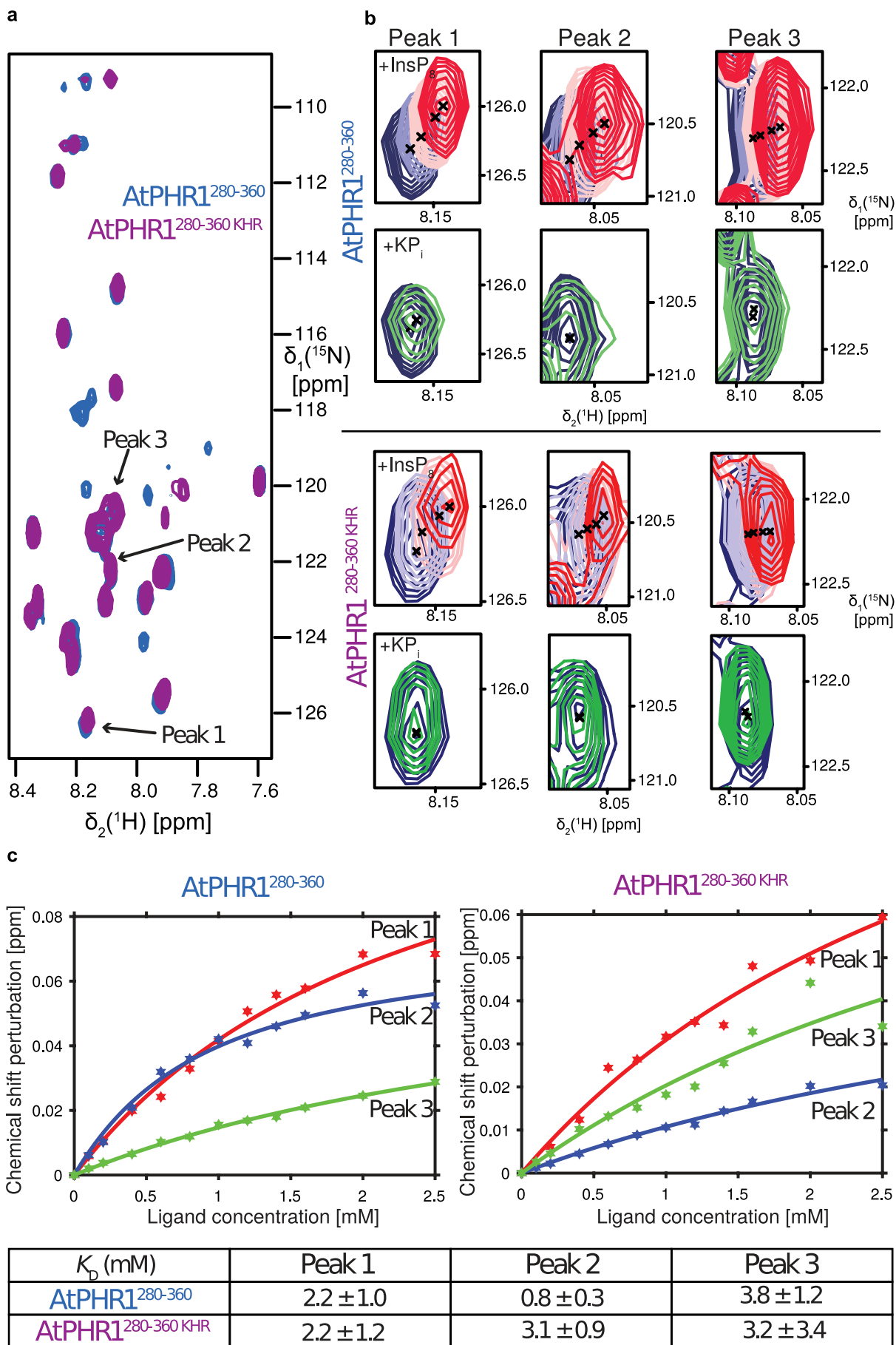
**Supplementary Fig. 3** Bacterial expressed full-length OsPHR2 behaves as a tetramer in solution.

**a** SDS-PAGE of OsPHR2 purified from *E. coli*. **b** Analytical size exclusion chromatography traces of wild type OsPHR2. The corresponding right-angle light scattering (RALS) traces are shown in **c**, the molecular masses are depicted by a black line. Table summaries provide the molecular weight (Mw), retention volume (RV) and dispersity (Mw/Mn).

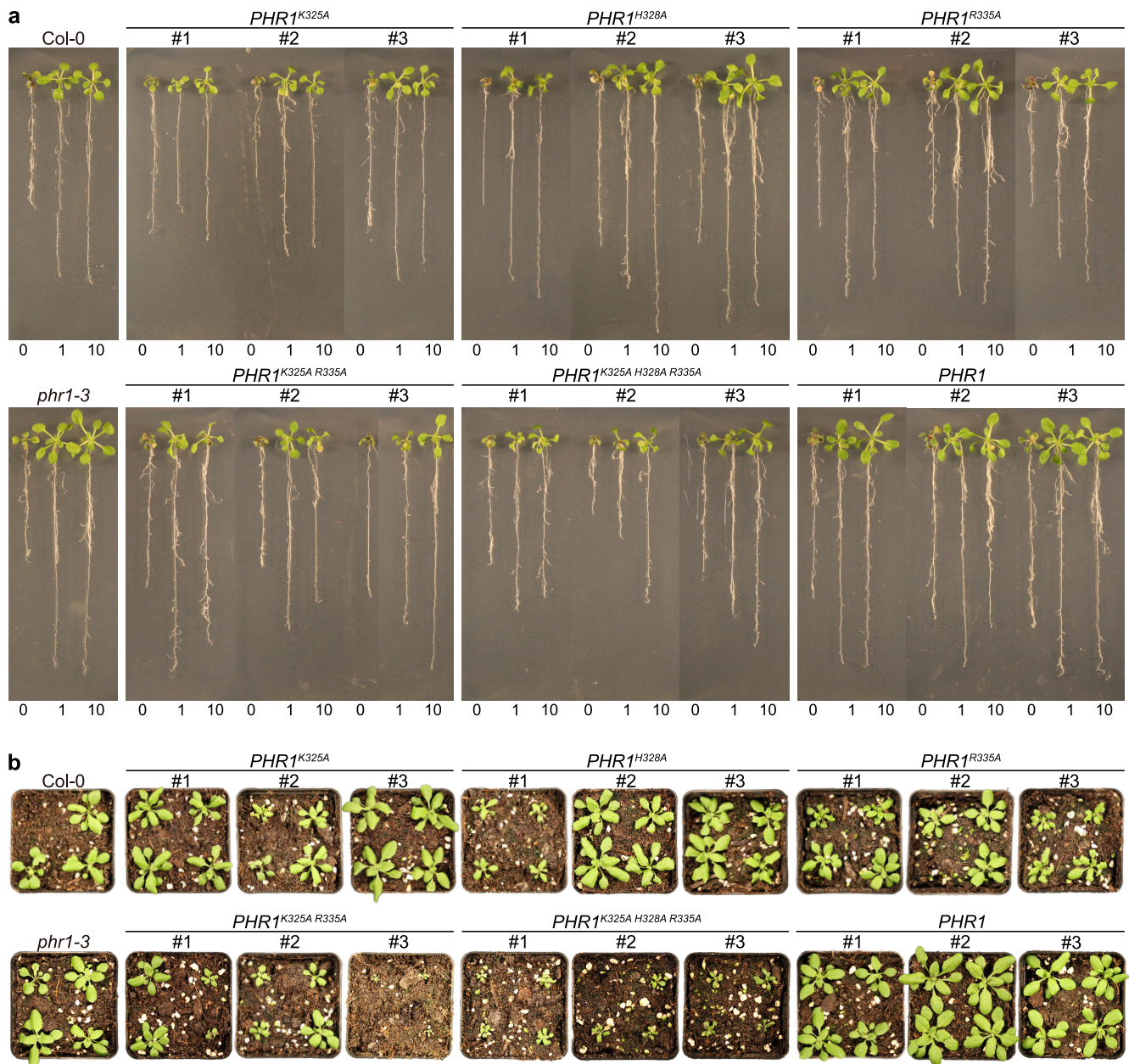




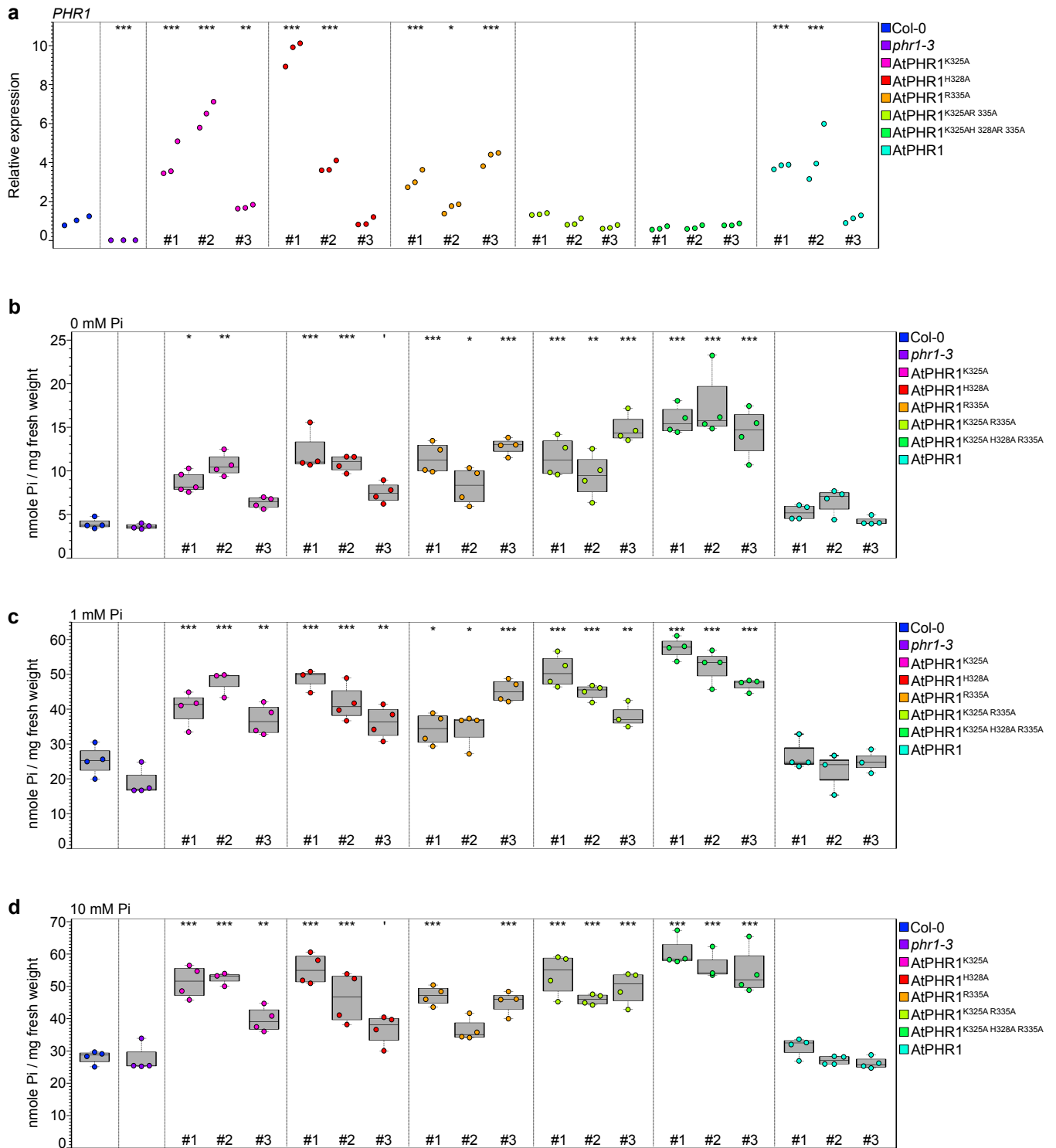
**Supplementary Fig. 5** Circular Dichroism (CD) spectroscopy of wild-type and mutant AtPHR1 coiled-coil domains. **a** CD spectra of AtPHR1 CC fragments from 260 nm to 190 nm, measured at 24 °C. **b** Thermal denaturation of AtPHR1 CC domain fragments. Melting curves were acquired at 222 nm with 2 °C stepwise increments in 30 intervals from 24 to 98 °C.



**Supplementary Fig. 6** Wild-type and mutant AtPHR1 weakly bind  $\text{InsP}_8$  with a dissociation constant in the low millimolar range. **a** Comparison of 2D  $^{15}\text{N}, ^1\text{H}$ -TROSY spectra of AtPHR1<sup>280-360</sup> (blue) and AtPHR1<sup>280-360 KHR/A</sup> (purple). Black arrows indicate backbone resonance peaks 1-3 that were used to estimate an approximate dissociation constant for  $\text{InsP}_8$ . Both TROSY spectra were recorded with 4 scans and with 128 points in the indirect dimension. **b** Chemical shift perturbations of backbone resonance peaks 1-3 of AtPHR1<sup>280-360</sup> or **c** AtPHR1<sup>280-360 KHR/A</sup>, respectively, while titrating  $\text{InsP}_8$  (top) or  $\text{KP}_i$  as a negative control (bottom). The TROSY titration spectra of the protein to  $\text{InsP}_8$  and  $\text{KP}_i$  and  $\text{InsP}_8$  were recorded with 128 points in the indirect dimension and four scans. Dark blue - 200  $\mu\text{M}$  of  $[\text{U-}^{15}\text{N}, ^2\text{H}]$ - AtPHR1<sup>280-360</sup> or  $[\text{U-}^{15}\text{N}, ^2\text{H}]$ - AtPHR1<sup>280-360 KHR/A</sup>, light blue - 2 equivalent of  $\text{InsP}_8$ , purple - 6 equivalent of  $\text{InsP}_8$ , red - 10 equivalent  $\text{InsP}_8$  and green - 80 equivalent of  $\text{KP}_i$ . **d** Estimated dissociation constant ( $K_D$ ) of AtPHR1<sup>280-360</sup> (right) and AtPHR1<sup>280-360 KHR/A</sup> (left) by chemical shift perturbations (top) and an overview of the  $K_D$ 's extracted from backbone resonance peaks 1-3 (below).

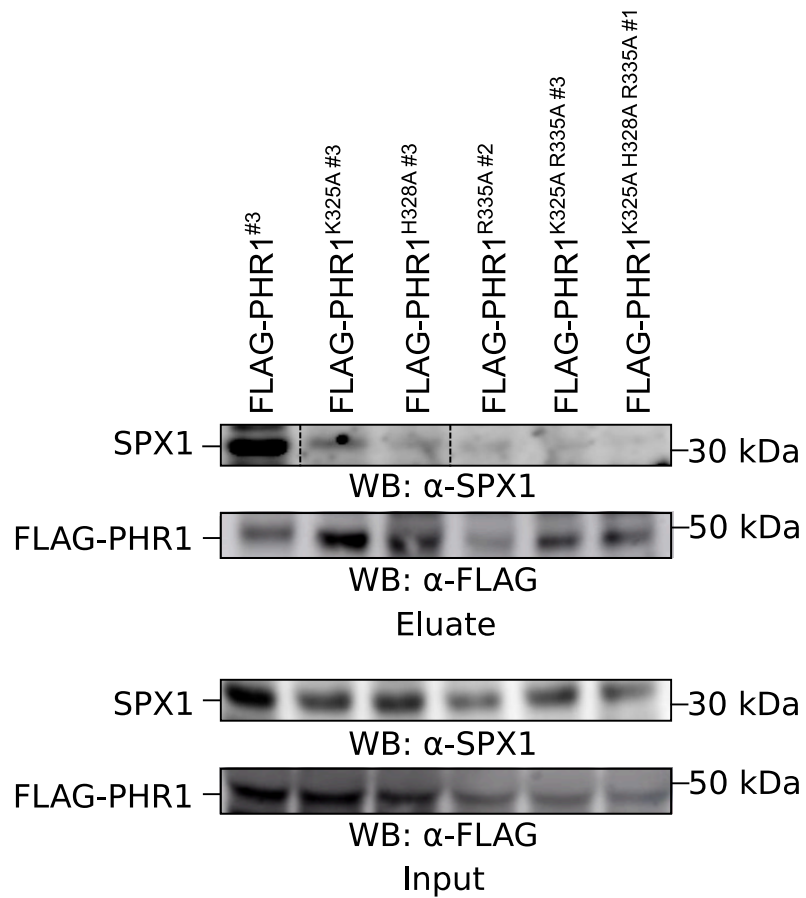


**Supplementary Fig. 7** Growth phenotypes of AtPHR1 CC domain mutants that abolish interaction with AtSPX1 and impact Pi homeostasis. **a** Growth phenotype of Col-0 wild type, *phr1-3*, and seedlings of *phr1-3* complementation lines expressing FLAG-AtPHR1, FLAG-AtPHR1<sup>K325A</sup>, FLAG-AtPHR1<sup>H328A</sup>, FLAG-AtPHR1<sup>R335A</sup>, FLAG-AtPHR1<sup>K325A R335A</sup>, and FLAG-AtPHR1<sup>K325A H328A R335A</sup> under the control of the *AtPHR1* promoter at 14 d after germination (DAG). Seedlings were germinated and grown on vertical <sup>1/2</sup>MS plates for 8 d, transferred to <sup>1/2</sup>MS plates supplemented with either 0 mM, 1 mM or 10 mM Pi and grown for additional 7 d. **b** Growth phenotypes of the lines in **a**, at 21 DAG. Seedlings were germinated and grown on vertical <sup>1/2</sup>MS plates for eight days, transferred to soil and grown for additional 14 d.



**Supplementary Fig. 8** Mutations in the AtPHR1 KHR motif result in Pi hyper-accumulation.

**a** Expression of *PHR1* in Col-0, *phr1-3*, and seedlings of *phr1-3* complementation lines expressing FLAG-AtPHR1, FLAG-AtPHR1<sup>K325A</sup>, FLAG-AtPHR1<sup>H328A</sup>, FLAG-AtPHR1<sup>R335A</sup>, FLAG-AtPHR1<sup>K325A R335A</sup>, and FLAG-AtPHR1<sup>K325A H328A R335A</sup> under the control of the *AtPHR1* promoter relative to the housekeeping gene *Actin2* at 14 DAG. Seedlings were germinated and grown on vertical <sup>1/2</sup>MS plates for 8 d, transferred to <sup>1/2</sup>MS plates supplemented with 1 mM Pi and grown for additional 7 d. For each line, three biological replicates were analysed in technical triplicates by qRT-PCR. Stars indicate significant differences to Col-0 (\*,  $p < 0.05$ ; \*\*,  $p < 0.01$ ; \*\*\*,  $p < 0.001$ ). **b-d** Plot represents Pi content of Col-0 wild type, *phr1-3* seedlings and seedlings of *phr1-3* complementation lines described in **a**. Bold black line, median; box, Interquartile range (IQR); whiskers, lowest/highest data point within 1.5 IQR of the lower/upper quartile. Seedlings were germinated and grown on vertical <sup>1/2</sup>MS plates for 8 d, transferred to <sup>1/2</sup>MS plates supplemented with either 0 mM (**b**), 1 mM (**c**) or 10 mM (**d**) Pi and grown for additional 7 d. For each line, 4 plants were measured in technical duplicates. (\*,  $p < 0.05$ ; \*\*,  $p < 0.01$ ; \*\*\*,  $p < 0.001$ ).



**Supplementary Fig. 9** Mutation in the KHR motif reduces AtPHR1 binding to AtSPX1 in Arabidopsis.

Co-immunoprecipitation experiments using FLAG-tagged wild type and mutant AtPHR1 variants stably expressed in Arabidopsis under the control of the *AtPHR1* promoter. Total protein was extracted from *phr1-3* complementation lines at 10 DAG. Seedlings were germinated and grown on vertical  $^{1/2}$ MS plates supplemented with 1 mM Pi. FLAG-tag fusions were affinity bound with magnetic FLAG-tag trap, and immunoprecipitation of FLAG-AtPHR1 was monitored by immunoblot with an anti-FLAG antibody. Co-enrichment of endogenous AtSPX1 was monitored by immunoblot with an anti-SPX1 antibody.



33 **Abstract**

34 Colicins are bacterial toxins targeting Gram-negative bacteria, including *E. coli* and related  
35 *Enterobacteriaceae* strains. Some colicins form ion-gated pores in the inner membrane of  
36 attacked bacteria that are lethal to their target. Colicin Ia was the first pore-forming *E. coli*  
37 toxin, for which a high-resolution structure of the monomeric full-length protein was  
38 determined. It is so far also the only colicin, for which a low-resolution structure of its  
39 membrane-inserted pore was reported by negative-stain electron microscopy. Resolving this  
40 structure at the atomic level would allow an understanding of the mechanism of toxin pore  
41 formation. Here, we report an observation that we made during an attempt to determine  
42 the Colicin Ia pore structure at atomic resolution. Colicin Ia was natively expressed by  
43 mitomycin-C induction under a native SOS promoter and purified following published  
44 protocols. The visual appearance in the electron microscope of negatively stained  
45 preparations and the lattice parameters of 2D crystals obtained from the material were  
46 highly similar to those reported earlier resulting from the same purification protocol.  
47 However, a higher-resolution structural analysis revealed that the protein is Dps (DNA-  
48 binding protein from starved cells), a dodecameric *E. coli* protein. This finding suggests that  
49 the previously reported low-resolution structure of a “Colicin Ia oligomeric pore” actually  
50 shows Dps.

## 51 Introduction

52 Colicin Ia is a membrane pore-forming toxin in *E. coli*. It exerts its toxicity as a membrane-  
53 inserted form, which conducts ions to destroy a target membrane potential (1). In the non-  
54 inserted form, colicin Ia is an  $\alpha$ -helical protein of elongated Y-like shape (2). The central R-  
55 domain is recognizing and binding to the outer membrane protein Cir (3, 4) and is separated  
56 by a 160 Å coiled-coiled region from the lethal C-terminal channel-forming domain and the  
57 N-terminal T-domain (2). The latter contains a TonB box (5), typical for TonB/Exb-dependent  
58 translocation along the outer membrane into the periplasmic space (6). Its C-terminal  
59 channel-forming domain is made of ten  $\alpha$ -helices (2) and is structurally similar to pore-  
60 forming domain of colicins E1, N and A (7–10), as well as to the T domain of diphtheria  
61 toxin (11) and Bcl-X<sub>L</sub> (12). The two central hydrophobic  $\alpha$ -helices form a helical hairpin and  
62 are surrounded by amphipathic helices (13). For Colicin Ia, it was shown that this helical  
63 hairpin can integrate into a lipid-bilayer in a voltage-independent manner (14). The region  
64 containing amphipathic helices II–V (residues 474–541) are translocated through the lipid  
65 bilayer by an applied voltage (15, 16). From these single-channel conductance studies, it has  
66 been proposed that the helical hairpin together with a part of helix I and a region ranging  
67 from helices VI to VII are forming a four-transmembrane ion channel (16). Two other studies  
68 based on the same method suggested that this channel has an hourglass shape (17, 18) with  
69 a pore diameter of 1.8 nm at the cis-side, a diameter of 1 nm at the trans-side, and a  
70 restriction to around 7 Å in between the two entrances (17). In stark contrast to these  
71 dimensions, Greig *et al.* presented a structure of the membrane-inserted Colicin Ia oligomer  
72 at a resolution of  $\sim 17$  Å reconstituted in 2D crystals (19). The structure featured a crown  
73 shape, with an outer diameter of 8.1 nm, an inner diameter of 3.4 nm and an averaged  
74 height of 4.3 nm.

75 Virtually all studies on colicin Ia reported so far, as well as studies on other colicins including  
76 Colicin K (20), Colicin E1 (21, 22), Colicin E3 (23), used mitomycin-C (MMC) to stimulate the  
77 colicin overexpression. MMC is a natural antibiotic of *Streptomyces* and is a genotoxicant  
78 causing DNA damage (24). DNA damage is repaired by SOS-response proteins (25) that are  
79 known to participate in different types of DNA repair mechanisms as well as in the eventual  
80 cell division arrest (26–29). These proteins have characteristic LexA sites in their regulon that  
81 are also found in the regulon region of colicins (30). Normally, a LexA dimer (31) represses  
82 the DNA transcription of SOS-response proteins. However, under conditions like DNA

83 damage, an activator RecA enables their transcription while mediating (32) autocatalytical  
84 cleaving of repressor LexA (33). MMC was found to cause DNA damage by DNA alkylation  
85 that can lead to a formation of DNA crosslinks (24). Especially DNA inter-crosslinks led to a  
86 strong SOS response in *E. coli*. Here, a single unrepaired DNA inter-crosslink can lead to a  
87 death of bacterium (24). The alkylation of DNA occurred when MMC was in its reduced  
88 highly DNA-electrophilic mitosene form (34). MMC alkylates the DNA preferably at 5'-CpG-3'  
89 and 5'-GpG-3' (35, 36) positions; specifically on a 2-amino position of deoxyguanines located  
90 in a minor groove (37). This enables introduction of an inter-strand (24) crosslink of 5'-CpG-  
91 3' that reacts with the complementary deoxyguanine in 3'-GpC-5' (37). As well, an intra-  
92 strand crosslink (38) by a covalent bond between neighboring deoxyguanines in 5'-GpG-3'  
93 are possible.

94 MMC was also shown to act as an oxidizing reagent. MMC gets reduced in presence of an  
95 oxygen and generates hydrogen peroxide (39). Upon MMC treatment of *E.coli* cells in their  
96 exponential phase, expectedly, proteins that protect the cell from the oxidative stress like  
97 two catalases KatE and KatG (40) as well as DNA-binding protein from starved cells (Dps) (41,  
98 42) were found up-regulated on the transcriptional level(43). Dps plays a protective role in  
99 starvation (41), extreme pH changes as well as upon exposure to heat, UV radiation and  
100 heavy metals (44). Normally, Dps would only be present in minimal amounts during the  
101 bacterial exponential growth phase. This is different in the transition to stationary phase and  
102 especially during the stationary phase itself. In later phase, Dps is prominently expressed in a  
103 RhoS regulon-dependent way, reaching up to 20'000 molecules (41).

104 Structurally, electron-microscopy-based 2D projections of Dps revealed a ring-like shape  
105 with a diameter between 8 and 9 nm (41, 45, 46). Dps is known to form hexagonal 2D  
106 crystals either in presence or absence of a non-specific DNA (41, 46), respectively, assigning  
107 Dps a DNA protective role by biocrystalization (46). Published X-ray structures reveal a  
108 hollow spherical dodecamer with a tetrahedral symmetry. The sphere has an inner diameter  
109 of 4.5 nm (47). Its monomer has a four-helix bundle fold similar to structurally related  
110 bacterial ferritin (47). The shell inside is highly negatively charged (47) and can harbor up to  
111 ~500 of iron(III) molecules (48).

112 Here, we report the result of a structural study aimed at elucidating the structure of the  
113 colicin Ia pore at atomic resolution. Colicin Ia was expressed by MMC treatment and  
114 purified. Structural studies that include negative-stain and cryo-electron microscopy of 2D

115 crystals and X-ray crystallography suggest that the spherical particles observed previously  
116 arise from the contaminant Dps.

## 117 **Materials and Methods**

118

### 119 **Protein expression and purification**

120 *E. coli* TG1 cells (Lucigen) were transformed with bacterial plasmid pKSJ340 obtained from  
121 Addgene (#27125), containing genes for Colicin Ia and the Colicin Ia immunity protein (49).  
122 Cells were grown in LB medium at 37 °C to an OD<sub>600nm</sub> of 0.7, whereupon Colicin Ia was  
123 induced by 0.5 µg/mL mitomycin-C (Roche). After 4 h, the culture was harvested at 6'000  
124 rpm and the cell pellet was resuspended in 50 mM boric acid/NaOH at pH 8.9 and 2 mM  
125 EDTA with additional protease inhibitors (Roche) and lysozyme, 5 mM MgCl<sub>2</sub> and DNase I  
126 (Applichem). The cells were disrupted by sonication and centrifuged at 12'000 rpm at 4 °C  
127 for 40 minutes. The cell lysate was applied on a 15 mL column, containing sulpho-propyl  
128 (SP) FF sepharose (GE Healthcare) of an Äkta purifier (GE Healthcare) system. The column  
129 was equilibrated with 50 mM boric acid/NaOH at pH 8.9 and 2 mM EDTA. The run was  
130 conducted by a flow rate of 0.5 mL/min. The column was washed with the respective buffer  
131 for 3 column volumes (CV) and subsequently the protein was elted by a 0-80% 1M NaCl  
132 linear gradient. The fractions resulting from the cation ion exchange (CIEX) chromatography  
133 step and containing Colicin Ia were concentrated to 4.5 mL and applied on a Superdex 200  
134 16/600 GL size-exclusion chromatography (SEC) column (GE Healthcare), which had been  
135 equilibrated with 20 mM sodium citrate at pH 5.2 and 50 mM NaCl. The volume of this  
136 column comprised 121 mL with a void volume around 48 mL. The flow rate used was  
137 0.5 mL/min. A second size-exclusion chromatography step was included. The protein-  
138 containing fractions B5-B13 from first SEC step were pooled, concentrated to 0.4 mL and  
139 applied on a second Superdex 200 10/300 GL SEC column (GE Healthcare) with a column  
140 volume of 24 mL and a void volume around 8 mL. The running buffer was composed of 20  
141 mM sodium citrate at pH 5.2 and 50 mM NaCl. The elution fraction was immediately flash  
142 frozen, stored at -80 °C and used for further experiments.

143 For 3D crystallization, Colicin Ia was labelled by selenomethionine. Hereby, the protein was  
144 expressed in one litre M9 culture with 4 g glucose as described in the section above with a  
145 slight difference. At an OD<sub>600nm</sub> of 0.2–0.3 an amino acid mixture containing 100 mg lysine,  
146 100 mg phenylalanine, 100 mg threonine, 50 mg isoleucine, 50 mg leucine, 50 mg valine  
147 and 100 mg DL-selenomethionine was added.

148

149

150 **Reconstitution of Colicin Ia into lipids and 2D crystallization trials**

151 1,2-dimyristoyl-sn-glycero-3-phosphoglycerol (DMPG) and 1,2-Dimyristoyl-sn-glycero-3-  
152 phosphorylcholine (DPMC) were mixed in a ratio of 3:7 (w/w) and a supplement of 2% octyl-  
153  $\beta$  glucoside in a buffer containing 20 mM sodium citrate at pH 5.2 and 50 mM NaCl. For a  
154 lipid-to-protein ratio (LPR, w/w) of 0.55 in a total volume of 2.2 mL, 0.9 mg/mL colicin Ia was  
155 added and incubated for two hours at 37 °C. The sample was transferred to a 10 kDa MWCO  
156 dialysis cassette and dialysed against a buffer without detergent containing 50 mM sodium  
157 acetate at pH 4.5 and 150 mM NaCl for few days at 37 °C. After the dialysis, the sample was  
158 centrifuged at 15'000 rpm for 10 minutes. The soluble fraction and the pellet were both  
159 used for further studies. The soluble fraction was concentrated by small *Vivaspin* centricon  
160 with 30 kDa MWCO. It was subsequently dialysed against 20 mM HEPES, pH 8.0 and  
161 150 mM NaCl by exchanging buffer for several times by a small *Vivaspin* centricon with  
162 30 kDa MWCO.

163

164 **Negative-stain electron microscopy**

165 For the preparation of negative-stain electron microscopy grids, 3.5  $\mu$ L of protein sample  
166 was applied onto glow-discharged carbon grids and incubated for one minute. The grids  
167 were blotted with filter paper and washed three times with MiliQ-water with blotting steps  
168 in-between. Staining was performed twice with 5  $\mu$ L of 2% uranyl-acetate drops applied onto  
169 the grids with an incubation time of 0 and 30 seconds. Finally, the grids were blotted and air-  
170 dried for five minutes. Micrographs were taken with a CM10 (Philips) transmission electron  
171 microscope (TEM), operated at 80 kV under 92'000x or 130'000x nominal magnification  
172 (pixel sizes 5.44Å resp. 3.85Å) and recorded with a Veleta CCD camera (EMSIS GmbH,  
173 Münster, Germany), or with a T12 (FEI) TEM, operated at 120 kV and recorded with a TVIPS  
174 F416 CMOS camera at a nominal magnification of 34'000x (pixel size 1.98Å). The distances in  
175 recorded images were measured with the ImageJ 1.x software (50). The particles resulting  
176 from the soluble fraction obtained after reconstitution of Colicin Ia into lipids were  
177 evaluated with the EMAN2 software (51). For 2D classification, approximately 350 single  
178 particle images were picked manually, CTF corrected and classified in 6 iterations into 24  
179 classes with EMAN2.

180

181 **Cryo-electron microscopy**

182 3.5  $\mu\text{L}$  of the soluble fraction after 2D crystallization trial and centrifugation was applied to  
183 300-mesh lacey EM grid that had been covered with a 5 nm-thin carbon film and glow-  
184 discharged for 15 seconds. The protein sample was incubated on the grid for one minute and  
185 blotted for 2 seconds on filter paper. Another 3.5  $\mu\text{L}$  of the soluble fraction was applied on  
186 the blotted filter paper as well as incubated and blotted in the same way twice. The grid was  
187 plunge frozen in liquid ethane using a FEI Vitrobot MK4 (Vitrobot, Maastrich Instruments)  
188 with 100% humidity in the chamber. Micrographs were acquired with a T12 (FEI) operated at  
189 120 kV and a TVIPS F416 camera at a nominal magnification of 54'000x and evaluated by  
190 2dx (52) routines within the FOCUS (53) software.

191

192 **3D crystallization, data collection and structure determination of Dps**

193 10.6 mg/mL Colicin Ia sample stored in 15mM sodium acetate pH 4.5 and 150 mM NaCl was  
194 incubated with 0.5 % octyl- $\beta$  glucoside at 37 °C for 45 minutes. 3D crystals were obtained by  
195 a sitting-drop vapor diffusion experiments in a 2:1 ratio of protein and precipitant at room  
196 temperature. They grew to their final size within one week. Crystals were cryo-preserved by  
197 addition of ethylene glycol to a final concentration of 20% (v/v) and flash cooled in liquid  
198 nitrogen. Six data sets of a single crystal were collected at the SLS beamLine X06DA (Swiss  
199 Light Source, Paul Scherrer Institute, Switzerland) at 100 K and were integrated, indexed and  
200 scaled using XDS software (54, 55). The crystal structure was determined by SeMet-SAD  
201 phasing and refined at 2.80 Å. Selenium sites were identified in the Se-Met dataset by  
202 Phenix-HySS (56). Initial automated model building was carried out with Phenix (57) and  
203 Buccaneer (58) and suggested a dodecameric structure with homology to ferritin. Following  
204 molecular replacement using PDB ID: 1DPS (47) revealed unambiguously, that the crystal  
205 consists of Dps dodecamers only. Based on this replacement solution, manual model  
206 building and structure refinement were performed with Coot (59) and PHENIX (60). Model  
207 quality was validated with Molprobit (61). Data collection and refinement statistics are  
208 summarized in Table S1. The atomic coordinates and structure factors have been deposited  
209 in the Protein Data Bank under PDB ID: 7AQS.

210

211 **Liposome pull-down assay**

212 Liposomes were prepared from one of the following lipids: *E. coli* polar extract (*Avanti*),  
213 Soybean polar extract (*Avanti*), DMPC : DMPG (*Avanti*) in a 3:7 (w/w) ratio. The respective  
214 lipids were dried with argon gas and left in an exicator overnight at room temperature. The  
215 lipid biofilm was dissolved in 20 mM Tris pH 7.5 and 100 mM NaCl to a lipid concentration of  
216 10 mg/mL and were incubated for 3 hours at a room temperature. Several cycles of freezing  
217 in liquid nitrogen and thawing at 42 °C were performed. Lipid samples were applied 10 times  
218 on a pressure-based extruder through a polycarbonate membrane of 100 nm. Dynamic light  
219 scattering on a Zetasizer Nano ZS (*Malvern Panalytical*) was used to verify the homogeneity  
220 of liposomes. Lipids were incubated with 0.9 mg/mL protein at different pH by using one of  
221 the following buffers and in 150 mM NaCl; 75 mM Sodium acetate pH 4.5, 50 mM MES pH  
222 6.5 or 50 mM Tris pH 8.0. An analytical ultracentrifugation was conducted on an Optima  
223 MAX XP (*Beckman*) with a TLA 120.1 rotor at 100'000 rpm for one hour.

## 224 Results

225

### 226 *Ring-like shaped particles observed during purification of Colicin Ia*

227 Colicin Ia was expressed and purified following a published protocol (19). In brief, colicin Ia  
228 was induced by MMC at an OD<sub>600nm</sub> of 0.7, and expression continued for four hours (Fig. 1A)  
229 (19). DNA was removed by DNase I and Colicin Ia was purified by cation ion-exchange  
230 chromatography and subsequent size-exclusion chromatography (Fig. 1A). Already the first  
231 purification step by cation-exchange chromatography yielded highly pure Colicin Ia (Fig. 1B).  
232 In the second purification step by size exclusion chromatography, three elution peaks were  
233 observed (Fig. 1C). The fractions collected from peaks at 60 mL and 75 mL indicated the  
234 presence of a protein with a size between 50 and 75 kDa, as revealed by SDS-PAGE. This is in  
235 accordance with the size of monomeric Colicin Ia of 69 kDa. The identity of the protein was  
236 further confirmed by mass spectrometry. As Colicin Ia was observed to degrade over time,  
237 the Colicin Ia fractions were subjected to a second round of size-exclusion chromatography,  
238 yielding pure Colicin Ia with no significant impurities visible in SDS-PAGE (fraction C1 in  
239 Fig. 1D). Negative-stain electron microscopy after the first SEC revealed soluble particles of  
240 spherical shape with approx. 8.5 nm diameter (Fig. 2A). TEM images after the second SEC  
241 showed smaller particles below 6 nm diameter, and less frequently some elongated shapes  
242 of up to 15.7 nm length (Fig. 2B). The smaller spherical particles might correspond to  
243 monomeric aggregated Colicin Ia, while the elongated shape corresponded well to the  
244 published X-ray structure of soluble monomeric Colicin Ia (2), with a coiled-coiled region of  
245 around 160 Å separating the receptor binding R-domain from the membrane channel-  
246 forming C-domain and the N-terminal T-domain.

247 As mentioned above, the first size-exclusion chromatography displayed peaks at 60 mL,  
248 75 mL and 115 mL. The first elution peak of 61 mL corresponded to an effective protein size  
249 between 158–440 kDa. Negative-stain electron micrographs of this sample displayed ring-  
250 shaped soluble particles of a diameter between 8 nm and 9 nm (Fig. 2A). These particles are  
251 visually highly similar to previously reported Colicin Ia oligomers that were obtained upon  
252 incubating Colicin Ia with detergents and lipids and subsequent dialysis (19). At the same  
253 time, these 2D projections also resemble the Dps oligomer (41, 45, 46), an endogenous  
254 *E. coli* protein of around 19 kDa that can form a dodecamer of around 220 kDa in size (47).  
255 The presence of Dps monomers was further evident as faint protein bands in the fractions

256 obtained by cation ion-exchange chromatography (asterik in the Fig. 1B) and size-exclusion  
257 chromatography (asterik in the Fig. 1C).

258

### 259 *Reconstitution into lipids yields 2D crystals of ring-like shaped particles*

260 A reconstitution of soluble Colicin Ia in a lipid bilayer was performed following published  
261 protocols (19). Shortly, lipids DMPC and DMPG were mixed in a ratio of 3:7 (w/w) and  
262 supplemented by 2 % of octyl- $\beta$  glucoside (Fig. 1A). Colicin Ia and lipids were incubated in a  
263 lipid-to-protein ratio of 0.55. This sample was dialyzed extensively against a buffer with a pH  
264 of 4.5 and no detergent (Fig. 1A). After the dialysis, the soluble fraction and the pellet  
265 containing lipid-bound protein were obtained by a centrifugation step (Fig. 1A). They were  
266 further analysed by negative-stain electron microscopy.

267 The soluble fraction of the dialyzed sample contained ring-like shaped particles. They were  
268 visually similar to the particles obtained during size-exclusion chromatography (Fig. 3A). The  
269 2D classification of particles from the soluble fraction showed for all classes ring-shaped  
270 particles with an approximate diameter of 8 nm (Fig. 3B). This suggests that the protein  
271 either had a preferential orientation on the electron microscopy grids or that the protein is  
272 formed as a hollow sphere, so that all projections resemble a ring. A further treatment of the  
273 soluble fraction by changing the pH from 4.5 to a pH of 8 led to the formation of 2D crystals  
274 (Fig. 4). These were found to have a hexagonal packing and cell unit parameters  $a = 90 \text{ \AA}$ ,  
275  $b = 92 \text{ \AA}$  and  $\gamma = 120^\circ$  (Table 1). These values are very similar to reported 2D crystal  
276 parameters of a proposed Colicin Ia oligomer (Table 1) (19).

277 A preliminary analysis by negative stain electron microscopy was also performed on the re-  
278 suspended pellet obtained after reconstitution of Colicin Ia in lipids. This revealed the  
279 presence of membrane patches of irregular texture, compatible with the presence of  
280 reconstituted but not crystalline membrane proteins in the lipid bilayers (Fig. 3B).  
281 Furthermore, a lipid-pull down assay confirmed that Colicin Ia at pH 4.5 is exclusively  
282 associated with the lipid fraction in the pellet (Fig. S1). However, in our hands we did not  
283 notice the formation of well-ordered 2D crystals at pH 4.5 as reported earlier (19).

284

### 285 *Formation of 3D crystals from the Colicin Ia sample*

286 The Colicin Ia sample was utilized in two different ways for X-ray crystallization experiments.  
287 Firstly, the soluble fraction obtained after reconstitution of Colicin Ia in lipids was used for

288 setting-up the crystallization plates (Fig. 1A). It contained ring-like shaped particles (Fig. 3A)  
289 similar to those published earlier (19) that were suggested to represent an oligomeric pore  
290 of Colicin Ia. Secondly, the protein sample was incubated with a detergent - octyl- $\beta$   
291 glucoside or n-dodecyl  $\beta$ -D-maltoside (DDM), respectively. The rationale behind this was  
292 that electrophysiological studies of Colicin Ia had reported that detergents can lead to an  
293 increased amount of Colicin Ia channels formed in a lipidic bilayer if compared to non-  
294 treated Colicin Ia (14). This was suggesting that some detergents can shift the  
295 conformational equilibrium between soluble and oligomeric Colicin Ia, which could possibly  
296 lead to crystals of oligomeric Colicin Ia. Protein 3D crystals were obtained from both sample  
297 preparations. The structure of the crystals was determined by selenomethionine-labeling.  
298 The structure obtained is a dodecameric sphere with a tetrahedral symmetry, identical to  
299 the known structure of Dps (PDB ID: 1DPS) (47) (Fig. 5, Table 1 and Table S1).

## 300 Discussion

301  
302 When aiming at a high-resolution structure of the membrane-inserted Colicin Ia oligomer,  
303 we purified and reconstituted protein particles that were resembling and reported  
304 oligomeric Colicin Ia (19) in size and visual appearance, but at the same time also the protein  
305 Dps (41, 45, 46) (Table 1). 2D crystallization attempts resulted in a pellet fraction that upon  
306 preliminary TEM inspection showed membrane patches of irregular structure but did not  
307 show well-ordered 2D crystals. In view of the recent improvements of single particle cryo-  
308 EM, 2D crystallization attempts were not pursued further. However, well-ordered 2D crystals  
309 were obtained from particles from the soluble fraction that showed in projection images a  
310 ring-like appearance. Such particles were observed as a minor population after the first  
311 purification step, and such particles were also observed in the soluble fraction after  
312 membrane reconstitution attempts. A pH change from 4.5 to 8 for the soluble fraction then  
313 produced well-ordered 2D crystals that had very similar lattice parameters as those reported  
314 from an alleged reconstruction of the oligomeric Colicin pore (19). However, also Dps is  
315 known to form 2D crystals with similar hexagonal packing (41, 46) (see Table 2).

316 It appears highly unlikely that the particles obtained in the soluble fraction after  
317 reconstitution of Colicin Ia into lipids were membrane-bound Colicin Ia. In lipid-pull down  
318 experiments under the same conditions, soluble Colicin Ia shifted completely to the lipid-  
319 bound state, indicating that is not soluble at these conditions. Hence, the particles obtained  
320 in the soluble fraction were most likely a contaminating other protein. In our 3D  
321 crystallization experiments, the protein Dps was successfully crystalized from the Colicin Ia  
322 sample, (Table 1) indicating that Dps was present as a co-purified product. The high amounts  
323 of Dps were most likely due to the induction of Colicin Ia expression by MMC, which is  
324 known to also significantly increase the amount of Dps in *E. coli* (43). Additionally, the  
325 purification protocol employed contained a cation ion-exchange step that favors Dps binding  
326 as well. Dps is known to get extracted natively without tags, while bound to hydroxyl-group  
327 rich agarose-based sepharose 6B and eluting with 200 mM NaCl (41). In this study, the ion-  
328 exchange material used was agarose-based sulpho-propyl (SP) sepharose that has similar  
329 properties.

330 Taken together, our results thus suggest that the previously reported low-resolution  
331 structure of oligomeric Colicin (19) was a misinterpretation and actually represented the  
332 contaminant Dps. Our protein expression and purification protocol of Colicin Ia followed the

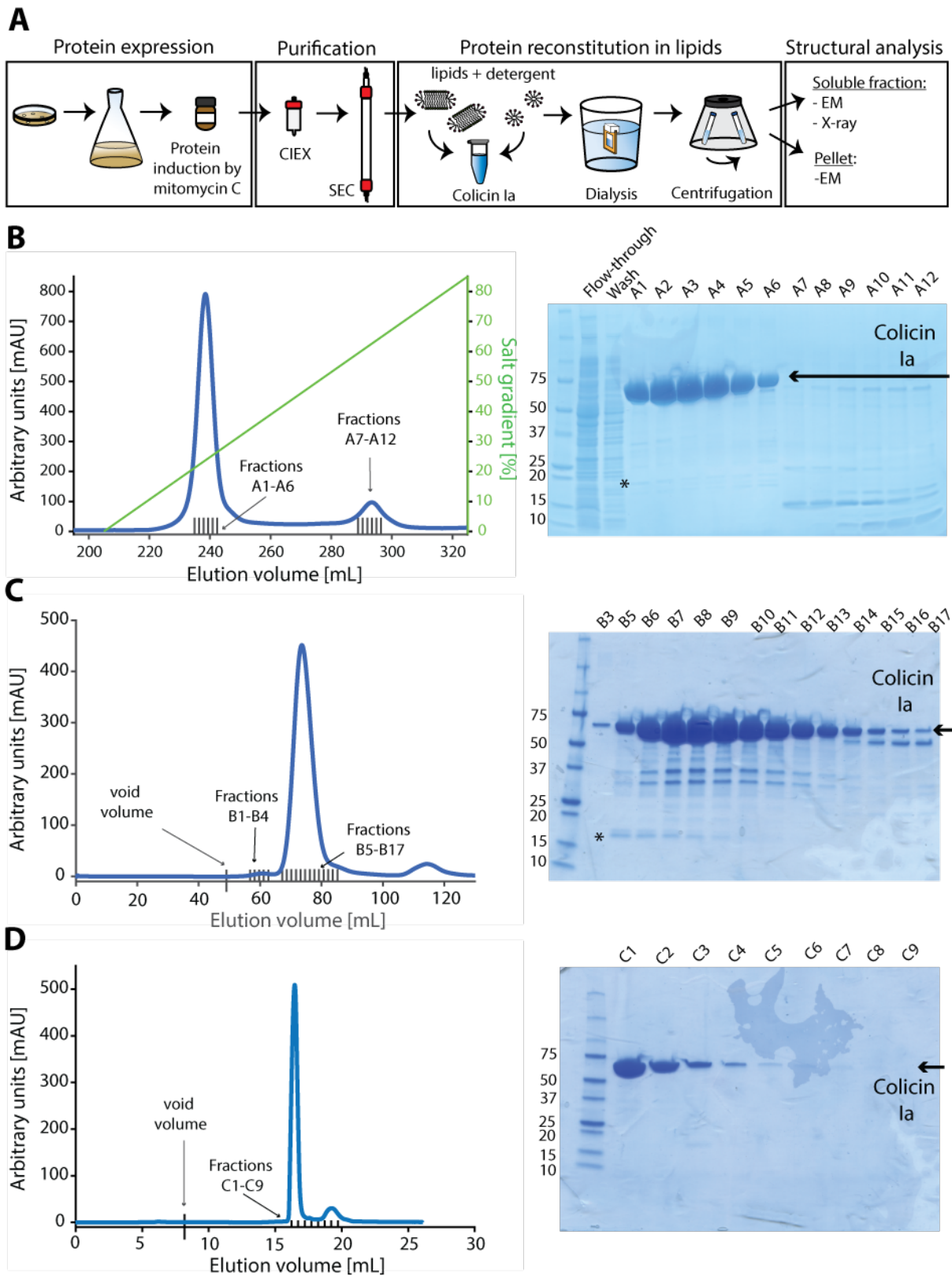
333 earlier report (19), making it likely that the earlier study also co-purified Dps. Because the  
334 publication of Greig et al. (19) is as of today the only report describing colicin as forming a  
335 large pore in its membrane-inserted form, we suggest that the membrane-inserted form of  
336 Colicin Ia is likely smaller (16, 17).

337

### 338 **Acknowledgments**

339 We thank Mohamed Chami for help with 2D crystallization.

340 Fig.s  
341



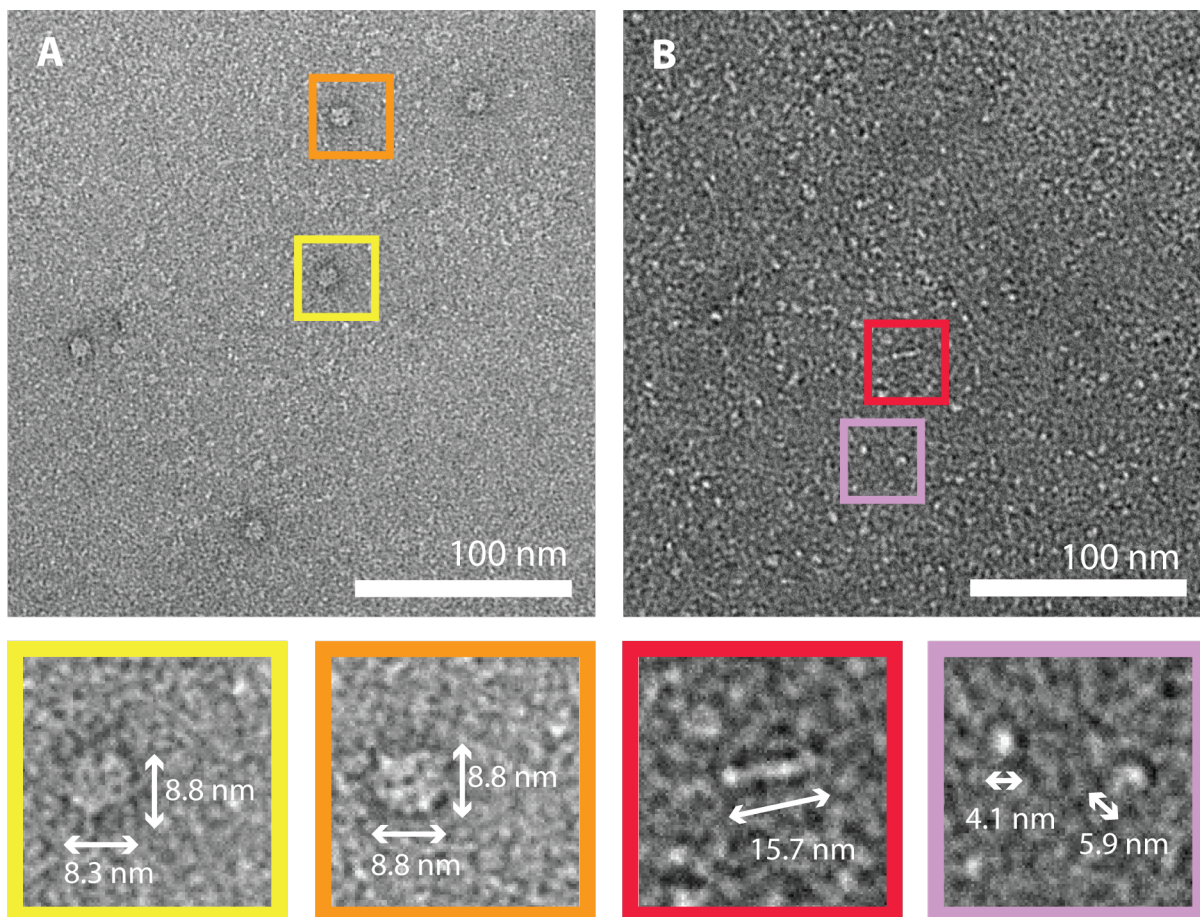
342

343

344 **Figure 1. Expression and purification of Colicin Ia.** A, A schematic overview of the Colicin Ia

345 purification steps, its reconstitution into lipids and further structural studies. B, Elution

346 profile from cation exchange (CIEX) chromatography and its analysis by SDS-PAGE. Left lane -  
347 standard protein ladder, lane 2 – flow-through fraction, lane 3 – wash fraction, lanes 4 – 15  
348 fractions of cation ion exchange run. *C*, First size-exclusion chromatogram (SEC, with a  
349 Superdex 200 16/600 GL) and SDS-PAGE of collected fractions. Left lane - standard protein  
350 ladder, lane 2 – 15 are the fractions of respective size-exclusion chromatography. *D*, Second  
351 size-exclusion chromatogram (SEC, with a Superdex 200 10/300 GL) and SDS-PAGE of size-  
352 exclusion chromatography fractions that are depicted on the left side. Lane 1 – standard  
353 protein ladder, lanes 2 – 15 are fractions of the size exclusion chromatography indicated in  
354 the left chromatogramm besides. Blue line – protein absorbance at 280 nm and green  
355 trendline depicted in (A) – 0-100% NaCl gradient. Black arrows indicate collected fractions,  
356 void volume and proteins collected.



357

358

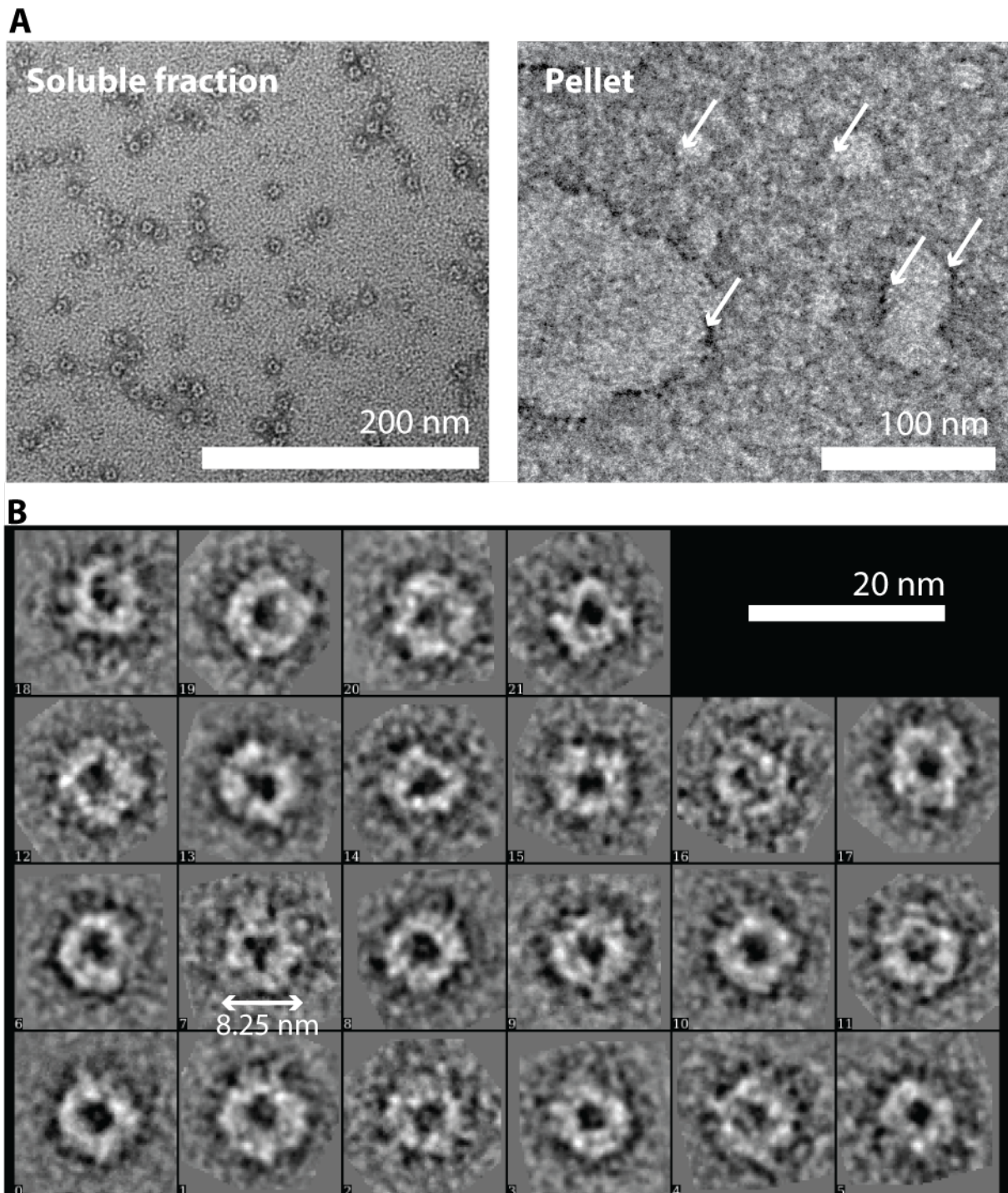
359 **Figure 2. Negative-stain electron microscopy of selected size-exclusion chromatography**

360 **fractions.** A, Analysis of the concentrated fractions B1-B4 from first size-exclusion

361 chromatography (see Fig. 1B). B, Analysis of the fraction C1 from second size-exclusion

362 chromatography (see Fig. 1C). Some of the particles indicated by a colored square in A and B

363 were further magnified and are shown below in square of a corresponding color.

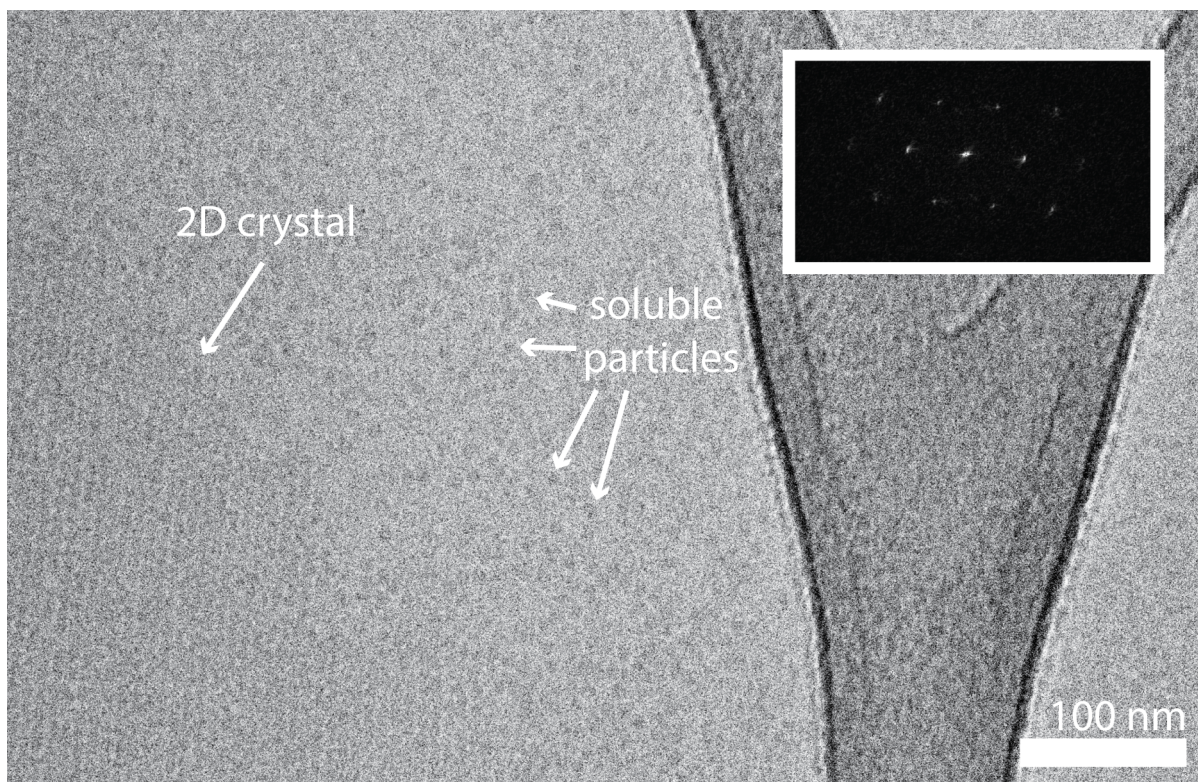


364  
365

366 **Figure 3. Analysis of soluble fraction and pellet after Colicin Ia is reconstituted into lipids.**

367 A, Protein sample containing Colicin Ia was incubated with detergent and lipids and  
368 subsequently dialysed in a buffer at pH 4.5 without detergent. After the centrifugation step,  
369 both, the soluble fraction, left side, and the pellet, right side, obtained were analysed by  
370 negative-stain electron microscopy. Arrows indicate protein within the lipidic membranes.

371 B, 2D classification of particles from the soluble fraction.



372

373

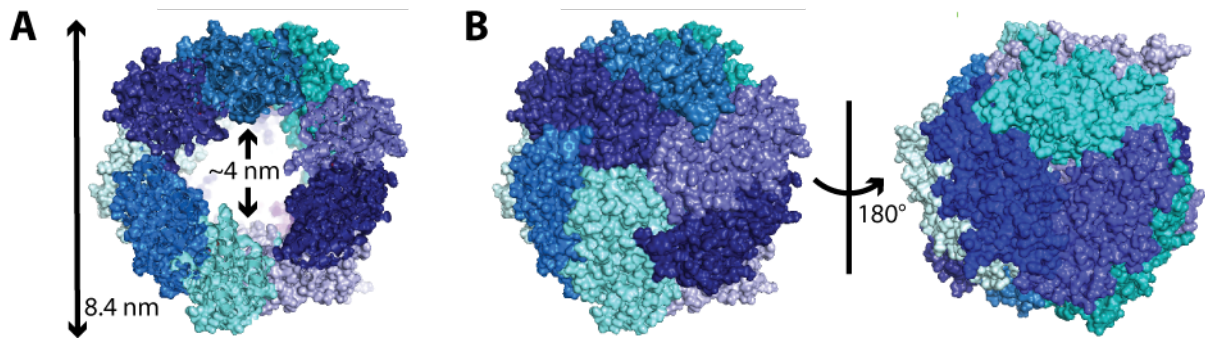
374 **Figure 4. Soluble fraction obtained after Colicin Ia is reconstituted into lipids can form 2D**

375 **crystals.** Cryo-electron microscopy of the soluble fraction obtained after reconstitution of

376 Colicin Ia in lipids. 2D crystals were formed upon a pH shift from pH 4.5 to pH 8. White

377 arrows indicate 2D crystal and soluble particles. Upper right corner displays Fourier

378 transformation of masked 2D crystal.



379

380

381 **Figure 5. Atomic resolution structure of Dps.** *A*, Cross-section through the Dps dodecamer.

382 Different colors represent single Dps monomers. The arrows indicate the size of the outer

383 and the inner diameter of the Dps oligomer. *B*, Side view on the complete Dps dodecamer.

384 The protein forms a hollow sphere.

385 **Table 1.** Comparison of ring-shaped particles obtained in different studies  
 386

	<b>Colicin Ia</b>	<b>Dps</b>	<b>This study</b>
<b>Soluble particles</b>	Ring-like	Ring-like	Ring-like
<b>in EM</b>	~ 8 nm (19)	~ 9 nm (41, 45, 46)	8-9 nm
<b>Unit cell lattice of 2D crystal</b>	Hexagonal packing: a=b=94 Å, $\gamma = 120^\circ$ (19)	Hexagonal packing: a=b=78 Å, $\gamma = 120^\circ$ (46)	Hexagonal packing: a=90 Å, b=92 Å, $\gamma = 120^\circ$

387

388 **References**

- 389 1. Schein, S. J., Kagan, B. L., and Finkelstein, A. (1978) Colicin K acts by forming voltage-  
390 dependent channels in phospholipid bilayer membranes. *Nature*. **276**, 159–163
- 391 2. Wiener, M., Freymann, D., Ghosh, P., and Stroud, R. (1997) Crystal structure of colicin  
392 Ia. *Nature*. **385**, 461–464
- 393 3. Cowell, B. S., and Konisky, J. (1972) Interaction of Colicin Ia with Bacterial Cells. Direct  
394 Measurement of Ia-receptor Interaction. *J. Biol. Chem.* **247**, 6524–6529
- 395 4. Buchanan, S. K., Lukacik, P., Grizot, S., Ghirlando, R., Ali, M. M. U., Barnard, T. J., Jakes,  
396 K. S., Kienker, P. K., and Esser, L. (2007) Structure of colicin I receptor bound to the R-  
397 domain of colicin Ia: implications for protein import. *EMBO J.* **26**, 2594–604
- 398 5. Schramm, E., Mende, J., Braun, V., and Kamp, R. M. (1987) Nucleotide sequence of the  
399 colicin B activity gene *cba*: consensus pentapeptide among TonB-dependent colicins  
400 and receptors. *J. Bacteriol.* **169**, 3350–3357
- 401 6. Braun, V. (1995) Energy-coupled transport and signal transduction through the Gram-  
402 negative outer membrane via TonB-ExbB-ExbD-dependent receptor proteins. *FEMS*  
403 *Microbiol. Rev.* **16**, 295–307
- 404 7. Parker, M. W., Pattus, F., Tucker, A. D., and Tsernoglou, D. (1989) Structure of the  
405 membrane-pore-forming fragment of colicin A. *Nature*. **337**, 93–96
- 406 8. Elkins, P., Bunker, A., Cramer, W. A., and Stauffacher, C. V (1997) A mechanism for  
407 toxin insertion into membranes is suggested by the crystal structure of the channel-  
408 forming domain of colicin E1. *Structure*. **5**, 443–458
- 409 9. Vetter, I. R., Parker, M. W., Tucker, A. D., Lakey, J. H., Pattus, F., and Tsernoglou, D.  
410 (1998) Crystal structure of a colicin N fragment suggests a model for toxicity.  
411 *Structure*. **6**, 863–874
- 412 10. Zakharov, S. D., Kotova, E. a, Antonenko, Y. N., and Cramer, W. a (2004) On the role of  
413 lipid in colicin pore formation. *Biochim. Biophys. Acta.* **1666**, 239–49
- 414 11. Bennett, M. J., and Eisenberg, D. (1994) Refined structure of monomeric diphtheria  
415 toxin at 2.3 Å resolution. *Protein Sci.* **3**, 1464–1475
- 416 12. Muchmore, S. W., Sattler, M., Liang, H., Meadows, R. P., Harlan, J. E., Yoon, H. S.,  
417 Nettlesheim, D., Chang, B. S., Thompson, C. B., Wong, S. L., Ng, S. L., and Fesik, S. W.  
418 (1996) X-ray and NMR structure of human Bcl-xL, an inhibitor of programmed cell  
419 death. *Nature*. **381**, 335–41
- 420 13. Zakharov, S. D., and Cramer, W. A. (2002) Colicin crystal structures: pathways and  
421 mechanisms for colicin insertion into membranes. *Biochim. Biophys. Acta.* **1565**, 333–  
422 346

- 423 14. Kienker, P. K., Qiu, X.-Q., Slatin, S. L., Finkelstein, A., and Jakes, K. S. (1997)  
424 Transmembrane Insertion of the Colicin Ia Hydrophobic Hairpin. *J. Membr. Biol.* **157**,  
425 27–37
- 426 15. Slatin, S. L., Qiu, X., Jakes, K. S., and Finkelstein, A. (1994) Identification of a  
427 translocated protein segment in a voltage-dependent channel. *Nature.* **371**, 158–161
- 428 16. Qiu, X., Jakes, K. S., Kienker, P. K., and Finkelstein, A. (1996) Major Transmembrane  
429 Movement Associated with Colicin Ia Channel Gating. *J. Gen. Physiol.* **107**, 313–328
- 430 17. Krasilnikov, O. V, Cruz, J. B. Da, Yuldasheva, L. N., Varanda, W. A., and Nogueira, R. A.  
431 (1998) Membrane Biology A Novel Approach to Study the Geometry of the Water  
432 Lumen of Ion Channels : Colicin Ia Channels in Planar Lipid Bilayers. *J. Membr. Biol.* **92**,  
433 83–92
- 434 18. Kienker, P. K., Jakes, K. S., and Finkelstein, A. (2008) Identification of channel-lining  
435 amino acid residues in the hydrophobic segment of colicin Ia. *J. Gen. Physiol.* **132**,  
436 693–707
- 437 19. Greig, S. L., Radjainia, M., and Mitra, A. K. (2009) Oligomeric structure of colicin ia  
438 channel in lipid bilayer membranes. *J. Biol. Chem.* **284**, 16126–34
- 439 20. Tsao, S.-S., and Goebel, W. F. (1969) Colicin K. 8. The immunological properties of  
440 mitomycin-induced colicin K. *J Exp Med.* **130**, 1313–35
- 441 21. Jakes, K. S., Abrams, C. K., Finkelstein, A., and Slatin, S. L. (1990) Alteration of the pa-  
442 dependent Ion Selectivity Channel by Site-directed Mutagenesis of the Colicin. *J. Biol.*  
443 *Chem.* **265**, 6984–6991
- 444 22. Jakes, K. S. (2017) The Colicin E1 TolC Box: Identification of a Domain Required for  
445 Colicin E1 Cytotoxicity and TolC Binding. *J. Bacteriol.* **199**, e00412–16
- 446 23. Jakes, K. S., and Zinder, N. D. (1974) Highly Purified Colicin E3 Contains Immunity  
447 Protein. *PNAS.* **71**, 3380–3384
- 448 24. Szybalski, W., and Iyer, W. N. (1964) Crosslinking of DNA by enzymatically or  
449 chemically activated mitomycins and porfiromycins, bifunctionally “alkylating”  
450 antibiotics. *Fed. Proc.* **23**, 946—957
- 451 25. Kelley, W. L. (2006) Lex marks the spot: the virulent side of SOS and a closer look at  
452 the LexA regulon. *Mol. Microbiol.* **62**, 1228–1238
- 453 26. Radman, M. (1975) SOS repair hypothesis: phenomenology of an inducible DNA repair  
454 which is accompanied by mutagenesis. in *Molecular Mechanisms for Repair of DNA*,  
455 Basic Life (Hanawalt, P. C., and Setlow, R. B. eds), p. 355—367, Springer, Boston, MA,  
456 **5A**, 355—367
- 457 27. Little, J. W., and Mount, D. W. (1982) The SOS Regulatory Escherichia coli System. *Cell.*  
458 **29**, 11–22

- 459 28. Walker, G. C. (1987) The SOS Response of *Escherichia coli*. in *Escherichia coli and*  
460 *Salmonella typhimurium*, Cellular a (Neidhardt, F., Ingraham, J., Low, K., Magasanik,  
461 B., Schaechter, M., and Umberger, H. eds), pp. 1346–1357, American Society for  
462 Microbiology, Washington, DC, US
- 463 29. Friedberg, E. C., Walker, G. C., Siede, W., Wood, R. D., Schultz, R., and Ellenburger, T.  
464 (2006) *DNA Repair and Mutagenesis*, 2nd Ed., American Society for Microbiology  
465 Press, Washington, DC
- 466 30. Gillor, O., Vriezen, J. A. C., and Riley, M. A. (2009) The role of SOS boxes in enteric  
467 bacteriocin regulation. *Microbiology*. **154**, 1783–1792
- 468 31. Giese, K. C., Michalowski, C. B., and Little, J. W. (2009) RecA-Dependent Cleavage of  
469 LexA Dimers. *J. Mol. Biol.* **377**, 148–161
- 470 32. Lin, L.-L., and Little, J. W. (1989) Autodigestion and RecA-dependent Cleavage of Ind-  
471 Mutant LexA Proteins. *J. Mol. Biol.* **210**, 439–452
- 472 33. Little, J. W. (1984) Autodigestion of *lexA* and phage lambda repressors. *PNAS*. **81**,  
473 1375–1379
- 474 34. Kumar, G. S., Lipman, R., Cummings, J., and Tomasz, M. (1997) Mitomycin C - DNA  
475 Adducts Generated by DT-Diaphorase. Revised Mechanism of the Enzymatic  
476 Reductive Activation of Mitomycin C. *Biochemistry*. **36**, 14128–14136
- 477 35. Li, V.-S., and Kohn, H. (1991) Studies on the bonding specificity for mitomycin C-DNA  
478 monoalkylation processes. *JACS*. **113**, 275–283
- 479 36. Kumar, S., Lipman, R., and Tomasz, M. (1992) Recognition of Specific DNA Sequences  
480 by Mitomycin C for Alkylation. *Biochemistry*. **31**, 1399–1407
- 481 37. Tomasz, M., Lipman, Roselyn, Chowdary, D., Pawlak, J., Verdine, G. L., and Nakanishi,  
482 K. (1987) Isolation and structure of a covalent cross-link adduct between mitomycin C  
483 and DNA. *Science*. **235**, 1204–1208
- 484 38. Bizanek, R., McGuinness, B. F., Nakanishi, K., and Tomasz, M. (1992) Isolation and  
485 structure of an intrastrand cross-link adduct of mitomycin C and DNA. *Biochemistry*.  
486 **31**, 3084–3091
- 487 39. Tomasz, M. (1976) H<sub>2</sub>O<sub>2</sub> generation during the redox cycle of mitomycin C and dna-  
488 bound mitomycin C. *Chem. Biol. Interact.* **13**, 89–97
- 489 40. Loewen, P. C., Switala, J., and Triggs-Raine, B. L. (1985) Catalases HPI and HPII in  
490 *Escherichia coli* are induced independently. *Arch. Biochem. Biophys.* **243**, 144–149
- 491 41. Almiron, M., Link, A. J., Furlong, D., and Kolter, R. (1992) A novel DNA-binding protein  
492 with regulatory and protective roles in starved *Escherichia coli*. *Genes Dev.* **6**, 2646–  
493 2654

- 494 42. Martinez, A., and Kolter, R. (1997) Protection of DNA during Oxidative Stress by the  
495 Nonspecific DNA-Binding Protein Dps. *J. Bacteriol.* **179**, 5188–5194
- 496 43. Khil, P. P., and Camerini-otero, R. D. (2002) Over 1000 genes are involved in the DNA  
497 damage response of Escherichia coli. *Mol. Biol.* **44**, 89–105
- 498 44. Nair, S., and Finkel, S. E. (2004) Dps Protects Cells against Multiple Stresses during  
499 Stationary Phase. *J. Bacteriol.* **186**, 4192–4198
- 500 45. Zhang, Y., Fu, J., Chee, S. Y., Ang, E. X. W., and Orner, B. P. (2011) Rational disruption  
501 of the oligomerization of the mini-ferritin E. coli DPS through protein-protein  
502 interface mutation. *Protein Sci.* **20**, 1907–1917
- 503 46. Wolf, S. G., Frenkiel, D., Arad, T., Finkel, S. E., Kolter, R., and Minsky, A. (1999) DNA  
504 protection by stress-induced biocrystallization. *Nature.* **400**, 83–85
- 505 47. Grant, R. A., Filman, D. J., Finkel, S. E., Kolter, R., and Hogle, J. M. (1998) The crystal  
506 structure of Dps, a ferritin homolog that binds and protects DNA. *Nature.* **5**, 294–303
- 507 48. Zhao, G., Ceci, P., Ilari, A., Giangiacomo, L., Laue, T. M., Chiancone, E., Chasteen, N. D.,  
508 Hampshire, N., Moloculare, C. S. B., Biochimiche, S., and Sapienza, L. (2002) Iron and  
509 Hydrogen Peroxide Detoxification Properties of DNA-binding Protein from Starved  
510 Cells. A Ferritin-Like DNA-binding Protein of Escherichia Coli. *J. Biol. Chem.* **277**,  
511 27689–27696
- 512 49. Jakes, K. S., and Finkelstein, A. (2010) The colicin Ia receptor, Cir, is also the  
513 translocator for colicin Ia. *Mol. Microbiol.* **75**, 567–78
- 514 50. Schneider, C. A., Rasband, W. S., and Eliceiri, W. K. (2012) NIH Image to ImageJ: 25  
515 years of image analysis. *Nat. Methods.* **9**, 671–675
- 516 51. Tang, G., Peng, L., Baldwin, P.R., Mann, D.S., Jiang, W., Rees, I. & Ludtke, S. J. (2007)  
517 EMAN2: an extensible image processing suite for electron microscopy. *J. Struct. Biol.*  
518 **157**, 38–46
- 519 52. Gipson, B., Zeng, X., Zhang, Z. Y., and Stahlberg, H. (2007) 2dx — User-friendly image  
520 processing for 2D crystals. *J. Struct. Biol.* **157**, 64–72
- 521 53. Biyani, N., Righetto, R. D., Mcleod, R., Caujolle-bert, D., Castano-diez, D., Goldie, K. N.,  
522 and Stahlberg, H. (2017) Focus: The interface between data collection and data  
523 processing in. *J. Struct. Biol.* **198**, 124–133
- 524 54. Kabsch, W. (2010) Integration, scaling, space-group assignment and post-refinement.  
525 *Biol. Crystallogr.* **66**, 133–144
- 526 55. Kabsch, W. (2010) XDS. *Biol. Crystallogr.* **66**, 125–132
- 527 56. Zwart, P. H., Afonine, P. V., Grosse-Kunstleve, R. W., Hung, L. W., Ioerger, T. R.,  
528 McCoy, A. J., McKee, E., Moriarty, N. W., Read, R. J., Sacchettini, J. C., Sauter, N. K.,

- 529 Storoni, L. C., Terwilliger, T. C., and Adams, P. D. (2008) Automated structure solution  
530 with the PHENIX suite. *Methods Mol. Biol.* **426**, 419–435
- 531 57. Terwilliger, T. C., Grosse-Kunstleve, Ralf W., Afonine, P. V., Moriarty, N. W., Zwart, P.  
532 H., Hung, L.-W., Read, R. J., and Adams, P. D. (2008) Iterative model building, structure  
533 refinement and density modification with the PHENIX AutoBuild wizard. *Biol.*  
534 *Crystallogr.* **64**, 61–69
- 535 58. Cowtan, K. (2006) The Buccaneer software for automated model building. 1. Tracing  
536 protein chains. *Biol. Crystallogr.* **62**, 1002–1011
- 537 59. Emsley, P., and Cowtan, K. (2004) Coot: model-building tools for molecular graphics.  
538 *Biol. Crystallogr.* **60**, 2126–2132
- 539 60. Adams, P. D., Ralf, W., Read, R. J., Sacchettini, J. C., and Sauter, N. K. (2002) PHENIX:  
540 building new software for automated crystallographic structure determination. *Biol.*  
541 *Crystallogr.* **58**, 1948–1954
- 542 61. Chen, V. B., Arendall, B. W., Headd, J. J., Keedy, D. A., Immormino, R. M., Kapral, G. J.,  
543 Murray, L. W., Richardson, J. S., and Richardson, D. C. (2010) MolProbity: all-atom  
544 structure validation for macromolecular crystallography. *Biol. Crystallogr.* **66**, 12–21
- 545

## Supplementary information

### **Mitomycin-C–induced expression of Colicin Ia bears danger of a Dps contamination**

Joka Pipercevic, Roman P. Jakob, Ricardo Righetto, Kenneth Goldie, Henning Stahlberg, Timm Maier, Sebastian Hiller\*

\* corresponding author. [sebastian.hiller@unibas.ch](mailto:sebastian.hiller@unibas.ch)

This file contains:

- Supplementary Figure S1
- Supplementary Table S1

## Supplementary Figure

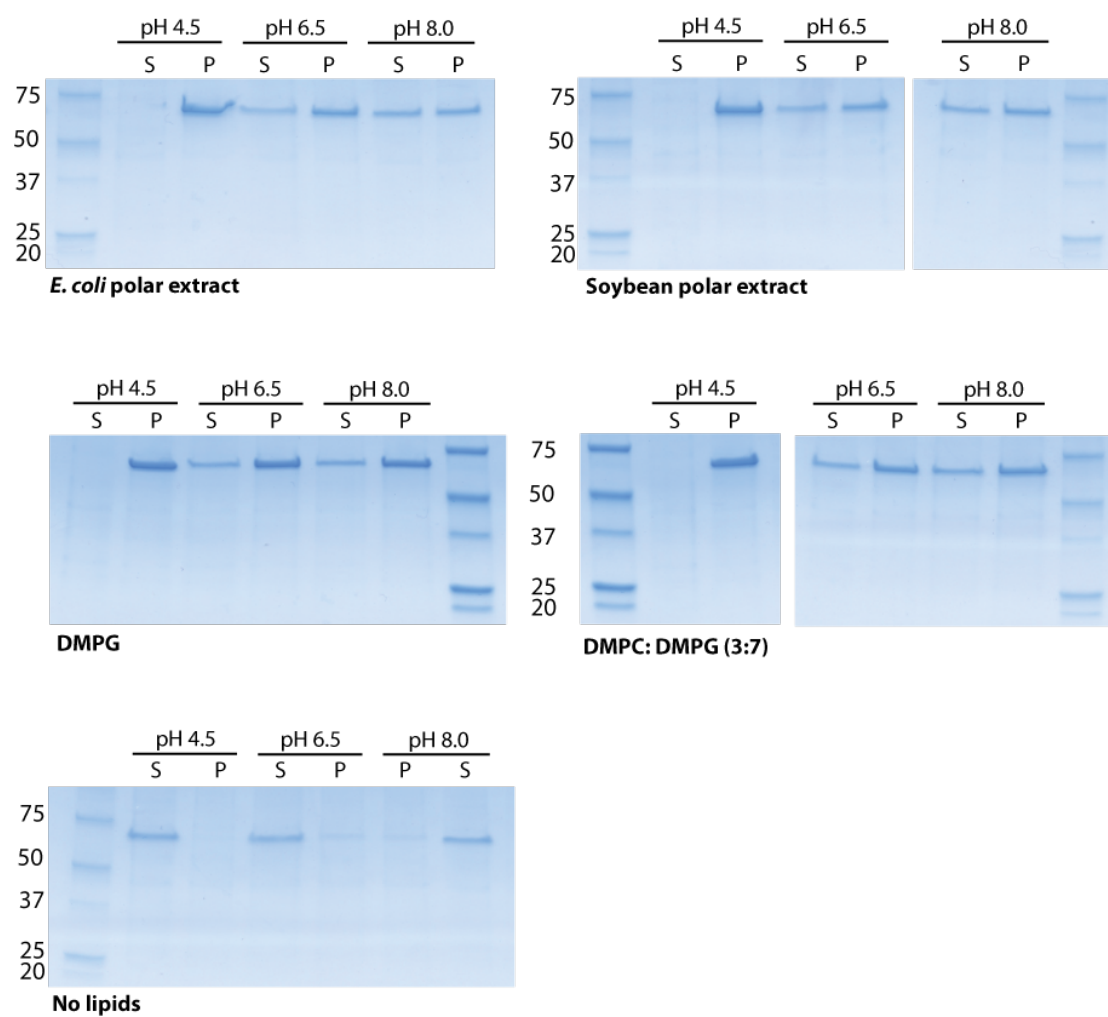


**Figure S1. Affinity of Colicin Ia for different lipids.** Colicin Ia was subjected to a liposome pull-down assay with different lipids and at different pH values, as indicated, and subjected to SDS-PAGE. Colicin Ia migrates at an effective molecular weight of around 70 kDa. The soluble and the pellet fraction is indicated by “S” and “P”, respectively.

## Supplementary Table

**Table S1:** Statistics on diffraction data and refinement of Dps.

	Dps
PDB ID	7AQS
Wavelength (Å)	0.979399
Resolution range (Å)	45.9 – 2.80 (2.87 – 2.80)*
Space group	P1
Unit cell (Å)	91.5, 91.8, 172.6
$\alpha, \beta, \gamma$ (°)	91.2 100.5, 119.9
Unique reflections	116604 (11605)
Multiplicity	10.7 (10.6)
Completeness (%)	99.69 (99.18)
Mean I/sigma(I)	6.4 (1.4)
Wilson B-factor	33.00
R-means	0.397 (1.676)
CC <sub>1/2</sub>	0.988 (0.744)
R-work	0.200 (0.289)
R-free	0.242 (0.338)
Number of non-hydrogen atoms	30370
Number of Macromolecules	29733
Number of Ligands	24
Number of Water molecules	613
Protein residues	3755
RMS(bonds)	0.007
RMS(angles)	1.09
Ramachandran favored (%)	98.41
Ramachandran outliers (%)	0.0
Rotamer outliers (%)	0.43
Clashscore	4.0
B-factor (All)	37.5
<b>Molprobity Score</b>	1.02

\*Values in parenthesis are for the highest resolution shell.

# GSDMD membrane pore formation constitutes the mechanism of pyroptotic cell death

Lorenzo Sborgi<sup>1,†</sup>, Sebastian Rühl<sup>1,†</sup>, Estefania Mulvihill<sup>2</sup>, Joka Pipercevic<sup>1</sup>, Rosalie Heilig<sup>1</sup>, Henning Stahlberg<sup>1</sup>, Christopher J Farady<sup>3</sup>, Daniel J Müller<sup>2</sup>, Petr Broz<sup>1,\*</sup> & Sebastian Hiller<sup>1,\*\*</sup>

## Abstract

Pyroptosis is a lytic type of cell death that is initiated by inflammatory caspases. These caspases are activated within multi-protein inflammasome complexes that assemble in response to pathogens and endogenous danger signals. Pyroptotic cell death has been proposed to proceed via the formation of a plasma membrane pore, but the underlying molecular mechanism has remained unclear. Recently, gasdermin D (GSDMD), a member of the ill-characterized gasdermin protein family, was identified as a caspase substrate and an essential mediator of pyroptosis. GSDMD is thus a candidate for pyroptotic pore formation. Here, we characterize GSDMD function in live cells and *in vitro*. We show that the N-terminal fragment of caspase-1-cleaved GSDMD rapidly targets the membrane fraction of macrophages and that it induces the formation of a plasma membrane pore. *In vitro*, the N-terminal fragment of caspase-1-cleaved recombinant GSDMD tightly binds liposomes and forms large permeability pores. Visualization of liposome-inserted GSDMD at nanometer resolution by cryo-electron and atomic force microscopy shows circular pores with variable ring diameters around 20 nm. Overall, these data demonstrate that GSDMD is the direct and final executor of pyroptotic cell death.

**Keywords** atomic force microscopy; cell death; gasdermin; inflammasomes; inflammation; pyroptosis

**Subject Categories** Autophagy & Cell Death; Immunology

**DOI** 10.15252/embj.201694696 | Received 3 May 2016 | Revised 19 June 2016 | Accepted 28 June 2016 | Published online 14 July 2016

**The EMBO Journal (2016) 35: 1766–1778**

## Introduction

Inflammatory caspases (caspase-1, human caspase-4, human caspase-5, and murine caspase-11) are a group of cysteine-dependent aspartate-directed proteases that is essential for host innate immune defense. Caspase-1 is activated within large multi-protein complexes termed inflammasomes, which are assembled by

the protein pyrin or members of the NOD-like receptor (NLR) and PYHIN protein families (Latz *et al.*, 2013; von Moltke *et al.*, 2013). These proteins act as cytosolic pattern-recognition receptors (PRRs) and detect a variety of pathogen-associated molecular patterns (PAMPs) or endogenous danger signals (DAMPs). In contrast, the bacterial cell wall component lipopolysaccharide (LPS), one of the strongest immune-system activators, leads to the assembly of “non-canonical” inflammasomes through activation of caspase-4, caspase-5 or caspase-11 (Kayagaki *et al.*, 2011, 2013; Hagar *et al.*, 2013; Shi *et al.*, 2014).

The downstream signaling pathways that follow the activation of inflammatory caspases and how the active caspases initiate these events are still poorly understood (Lamkanfi, 2011). Initial work has identified the pro-inflammatory cytokine interleukin (IL)-1 $\beta$  as a key substrate of caspase-1 (Thornberry *et al.*, 1992). Subsequently, it was found that caspase-1, as well as caspase-11 and its human orthologs caspase-4 and caspase-5, induces a novel programmed cell death pathway that is characterized by cell swelling, lysis, and the release of cytoplasmic content (Fink & Cookson, 2007; Kayagaki *et al.*, 2011; Shi *et al.*, 2014), presumably as a result of the formation of membrane pores (Fink *et al.*, 2008). Since this type of cell death is morphologically distinct from apoptosis and intrinsically pro-inflammatory, it was named pyroptosis, from the Greek *pyro* (fire or fever) and *ptosis* (to fall) (Bergsbaken *et al.*, 2009). The physiological function of pyroptosis is thought to be the prevention of intracellular pathogen replication and to re-expose pathogens to extracellular killing mechanisms (Miao *et al.*, 2010).

Several landmark studies have recently identified GSDMD (gasdermin D), a member of the gasdermin protein family, as an essential mediator of pyroptosis in human and murine cells (He *et al.*, 2015; Kayagaki *et al.*, 2015; Shi *et al.*, 2015). GSDMD is required for pyroptosis induction after canonical and non-canonical inflammasome activation and is processed by caspase-1, caspase-11, caspase-4, and caspase-5, but not by apoptotic caspases. The N-terminal fragment of GSDMD (GSDMD<sup>Nterm</sup>) was found sufficient to induce cell death with the morphological features of pyroptosis (Kayagaki *et al.*, 2015; Shi *et al.*, 2015), and overexpression of the C-terminal domain GSDMD<sup>Cterm</sup> was found to block GSDMD<sup>Nterm</sup>-dependent cell death

<sup>1</sup> Biozentrum, University of Basel, Basel, Switzerland

<sup>2</sup> Department of Biosystems Science and Engineering, Eidgenössische Technische Hochschule (ETH) Zurich, Basel, Switzerland

<sup>3</sup> Novartis Institutes for BioMedical Research, Forum 1, Basel, Switzerland

\*Corresponding author. Tel: +41 6126 72342; E-mail: petr.broz@unibas.ch

\*\*Corresponding author. Tel: +41 6126 72082; E-mail: sebastian.hiller@unibas.ch

<sup>†</sup>These authors contributed equally to this work

(Shi *et al*, 2015). These results gave rise to the hypothesis that caspase-dependent cleavage releases the N-terminal domain from an inhibitory interaction with the C-terminus, allowing GSDMD<sup>Nterm</sup> to induce cell death by a yet undefined mechanism. Since pyroptosis had long been speculated to involve the formation of a plasma membrane pore, immediate destruction of the electrochemical gradient, and subsequent osmotic lysis of the host cell (Lamkanfi, 2011), it is likely that GSDMD<sup>Nterm</sup> either promotes the formation of this pore or itself has pore-forming activity (Broz, 2015). Here, we investigate the functional role of GSDMD<sup>Nterm</sup> in live cells and *in vitro*. We demonstrate that after cleavage by caspase-1, GSDMD<sup>Nterm</sup> targets cellular membranes and that it induces the formation of a large permeability pore in the plasma membrane. *In vitro* experiments with purified recombinant GSDMD show that GSDMD<sup>Nterm</sup> forms large pores in liposomes. We visualize these with cryo-electron and atomic force microscopy. Overall, these results close the gaps in the pyroptotic signaling pathway by providing the proof that GSDMD is the final and direct executor of pyroptotic cell death.

## Results

### The N-terminal GSDMD fragment induces the formation of a large plasma membrane pore

Pyroptotic cell death involves the formation of a plasma membrane pore, cell swelling, and rupture of the plasma membrane. To investigate whether GSDMD, a recently identified mediator of pyroptosis, mediates pore formation directly, we developed a doxycycline-inducible system to express the N-terminal fragment (GSDMD<sup>Nterm</sup>) of mouse GSDMD in HEK293T cells. Doxycycline treatment caused cell death in HEK293T cells harboring the GSDMD<sup>Nterm</sup>-expressing plasmid, but not in cells harboring a vector control, in a concentration-dependent manner (Fig 1A). To characterize whether GSDMD<sup>Nterm</sup> expression induced a lytic type of cell death, characteristic for pyroptosis, we next measured the amount of LDH (lactate dehydrogenase) release after doxycycline-induced expression of the GSDMD<sup>Nterm</sup> (Fig 1B). Increasing levels of GSDMD<sup>Nterm</sup> expression resulted in increased levels of LDH release, indicating that ectopic expression of the GSDMD<sup>Nterm</sup> induced death through cell lysis. Microscopy analysis showed that GSDMD<sup>Nterm</sup>-induced death had the morphological features of pyroptosis, *that is*, cell swelling and nuclear condensation. To estimate the size of the GSDMD<sup>Nterm</sup>-induced plasma membrane pore, we next employed an osmoprotection assay based on the addition of polyethylene glycols (PEGs) of increasing molecular weight. Addition of these high-molecular polymers can prevent water influx through pores and the resulting swelling and osmotic lysis, if the molecular diameter of the agent is larger than the diameter of the pore (Appendix Fig S1A). We induced GSDMD<sup>Nterm</sup> expression by doxycycline addition in HEK293T cells in the presence of PEGs and measured LDH release as a readout for osmotic lysis and propidium iodide (PI) staining as a measure of plasma membrane pore formation (Fig 1C and D). Only the largest sized agent, PEG3000, was able to reduce LDH release partially, while smaller PEGs did not reduce cell lysis. Importantly, PEG3000 did not prevent PI influx, indicating that it does not block the pore directly, but functions as an osmoprotectant. PEGs in the range of 600–3,000 Da did not induce significant levels of cell death when

added to cells (Appendix Fig S1B), but larger PEGs could not be used, since they proved to be cytotoxic.

Infection of primary murine bone marrow-derived macrophages (BMDMs) with *Salmonella enterica* serovar Typhimurium (*S. typhimurium*) activates the NLRC4 inflammasome (Mariathasan *et al*, 2004) and results in caspase-1- and GSDMD-dependent pyroptosis and cytokine release (Appendix Fig S1C and D). To estimate the size of the GSDMD-dependent plasma membrane pore in BMDMs, we measured cell lysis as a function of time in the presence of PEGs of increasing size (Fig 1E and F). Consistent with the osmoprotection experiment done in HEK293T cells, we observed that only PEG3000 had a small protective effect, while all smaller PEGs did not prevent pyroptosis. PI influx was not affected by any of the osmoprotectants. IL-1 $\beta$  release was also partially affected by PEG treatment (Appendix Fig S1E); consistent with the observation that pyroptosis is required for efficient release of the mature cytokine in BMDMs (Shi *et al*, 2015). Overall, these experiments suggest that GSDMD-dependent pyroptosis involves the formation of a plasma membrane pore with an inner diameter of over 3.5 nm, the estimated molecular size of PEG3000 (Scherrer & Gerhardt, 1971).

### The N-terminal GSDMD fragment targets cellular membranes

GSDMD<sup>Nterm</sup> might itself form a pore in the plasma membrane or alternatively initiate other events that result in pore formation (Broz, 2015). To define the fate of GSDMD<sup>Nterm</sup> after caspase-1-dependent cleavage of GSDMD, we followed caspase-1 activation, GSDMD processing, and cell death over time in immortalized wild-type macrophages infected with *S. typhimurium* (Fig 2A, Appendix Fig S2A). The processed caspase-1 p20 fragment, an indicator of caspase-1 activation, appeared within 20 min after infection in the supernatant of macrophages. GSDMD processing correlated with caspase-1 activation and was detectable in the cell lysate as well as in the cell supernatant. LDH release was also detectable at the same time points (Fig 1F and Appendix Fig S1C). Based on these data, we decided to determine the subcellular localization of full-length GSDMD and GSDMD<sup>Nterm</sup> in either uninfected cells or in cells infected with *S. typhimurium* for 10 and 20 min. Cells were harvested at each of these time points and subjected to subcellular fractionation as outlined (Fig 2B). GSDMD full length was exclusively found in the cytosolic fraction (S150) in uninfected cells (Fig 2C and Appendix Fig S2B), in line with the notion that it is a soluble, cytosolic protein. After infection, full-length GSDMD, but very little GSDMD<sup>Nterm</sup> was detected in the S150 fraction. Instead, the majority of GSDMD<sup>Nterm</sup> was found in the P150 fraction and in the P10 fraction, correlating with the presence of the plasma membrane marker Na<sup>+</sup>K<sup>+</sup> ATPase. The Na<sup>+</sup>K<sup>+</sup> ATPase was also strongly present in the P10, presumably since it is secreted *via* the ER/Golgi pathway. The mitochondrial marker VDAC, a porin of the outer mitochondrial membrane, did not correlate with the GSDMD<sup>Nterm</sup> and was mainly found in the P0.7 and P10 fractions, but not in the P150 fraction. Overall, these results suggest that the GSDMD<sup>Nterm</sup> targets membranes after caspase-1-mediated cleavage. To characterize the interaction, we isolated plasma membrane fractions of BMDMs after *S. typhimurium* infection and subjected them to different treatments (Fig 2D). Conditions known to release membrane-associated proteins or destabilize protein–protein

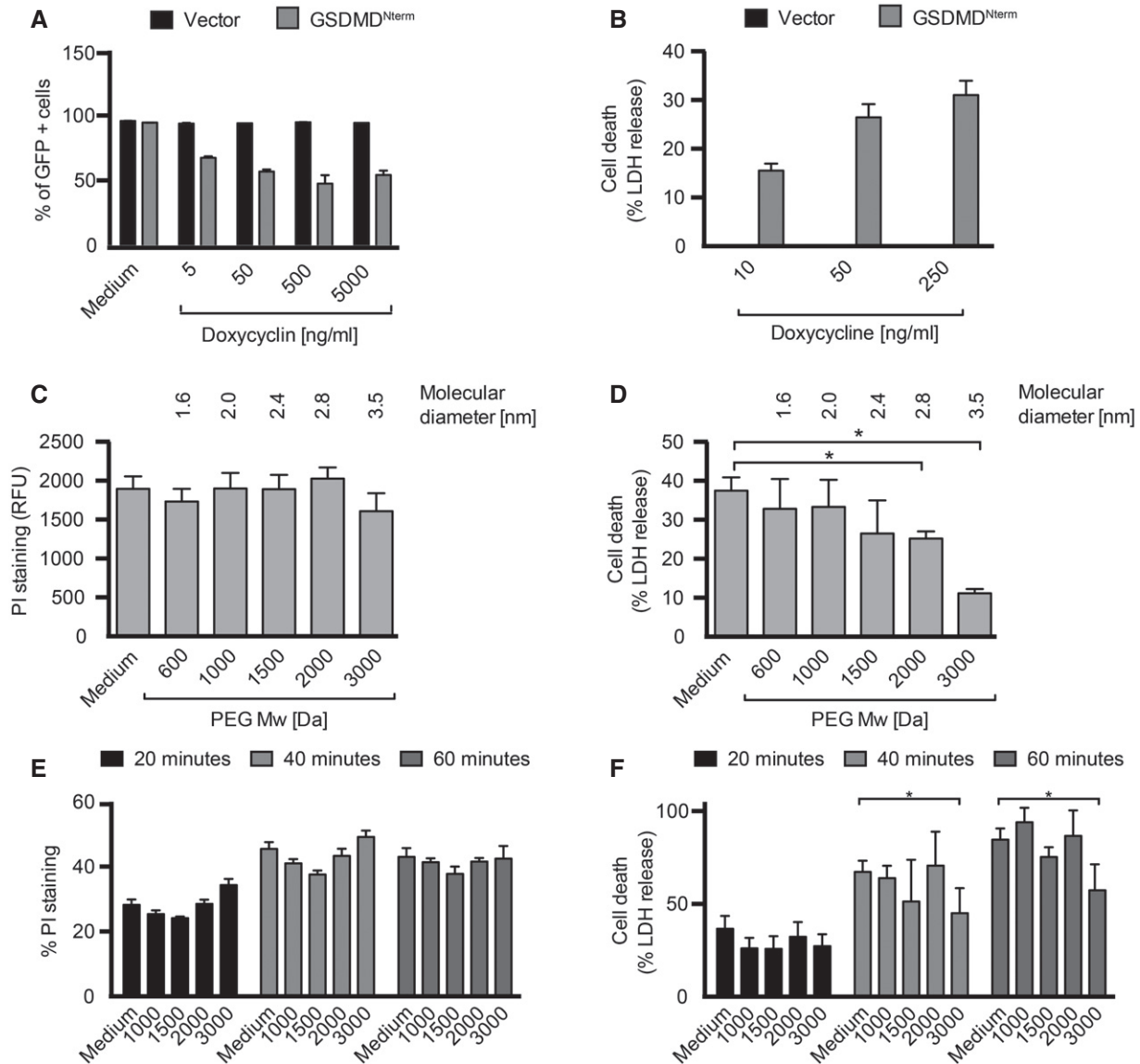


**Figure 1. GSDMD<sup>Nterm</sup> induces the formation of a large plasma membrane pore.**

**A** Cell viability as assessed by GFP expression in HEK293T cells transfected with the pRetroX TetOne3G-eGFP plasmid only (vector) or pRetroX TetOne3G-eGFP harboring the N-terminal fragment of GSDMD. Cells were treated with the indicated concentrations of doxycycline 24 h post-transfection, and the percentage of GFP-positive cells was determined 16 h later by flow cytometry.

**B** LDH release from HEK293T cells transfected with the pRetroX TetOne3G-eGFP plasmid only (vector) or pRetroX TetOne3G-eGFP harboring the N-terminal fragment of GSDMD. At 24 h post-transfection, cells were treated with the indicated concentrations of doxycycline for 8 h and the percentage of LDH release was determined. Graphs show mean and s.d. of quadruplicate wells.

**C, D** PI staining of and LDH release from HEK293T cells transfected with pRetroX TetOne3G-eGFP harboring the N-terminal fragment of GSDMD in the presence of osmoprotectants. At 24 h post-transfection, PEGs of the indicated molecular weights were added to a final concentration of 30 mM, cells were treated with 250 ng ml<sup>-1</sup> doxycycline for 8 h, and the level of PI staining (C) or LDH release (D) was determined.

**E, F** PI staining of and LDH release from LPS-primed primary BMDMs infected with log-phase *S. typhimurium* for the indicated time points in the presence of PEGs of the indicated molecular weight (numbers on the x-axis, 30 mM final concentration).

Data information: Graphs show mean and s.d. of quadruplicate wells (B–F) or the mean and s.d. of duplicate wells (A). \**P* < 0.05 as determined by Student's *t*-test. Data are representative of at least three independent experiments.

interactions (Gatfield & Pieters, 2000), such as high salt (1 M NaCl) and sodium carbonate (pH 11) did not solubilize GSDMD<sup>Nterm</sup>. Extraction of the plasma membrane with 0.02% digitonin, a cholesterol-sequestering detergent, did not solubilize GSDMD<sup>Nterm</sup>

either. Only the disruption of the membrane with low concentrations of the detergent SDS (0.1%) was able to fully solubilize GSDMD<sup>Nterm</sup>. Consistently, extraction of BMDMs membranes with 1% Triton was also able to partly solubilize GSDMD<sup>Nterm</sup>

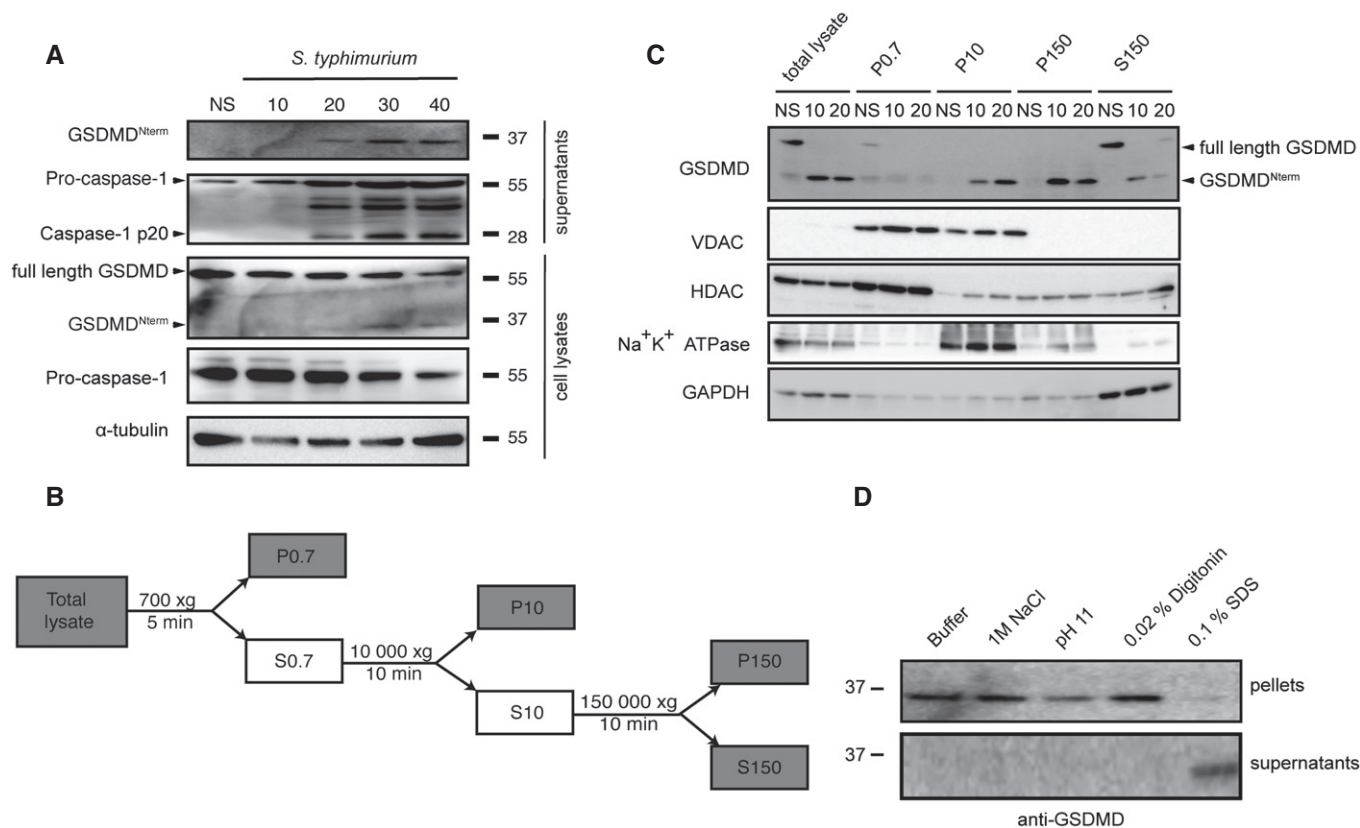


**Figure 2. GSDMD<sup>Nterm</sup> localizes to cellular membranes after inflammasome activation.**

- A Immunoblot analysis of cleaved GSDMD in culture supernatants and full-length GSDMD, cleaved GSDMD and  $\alpha$ -tubulin in the cell lysates of immortalized LPS-primed WT macrophages left uninfected (NS) or infected for 10–40 min with log-phase *S. typhimurium* (MOI = 50).
- B Schematic representation of the subcellular fractionation shown in (C).
- C Fractionation and immunoblot analysis for GSDMD, Na<sup>+</sup>K<sup>+</sup> ATPase, VDAC (voltage-dependent anion channel), HDAC1 (histone deacetylase 1), and GAPDH (glyceraldehyd-3-phosphate dehydrogenase) of WT macrophages infected for 10 and 20 min with log-phase *S. typhimurium* (MOI = 50). Fractionation was carried out as described in the Materials and Methods section, and equivalent amount of protein was loaded per lane.
- D Extraction of cleaved GSDMD from isolated membranes of WT macrophages infected for 10 min with log-phase *S. typhimurium* (MOI = 50). Extraction was carried in variable conditions as described in the Materials and Methods section.

Source data are available online for this figure.

(Appendix Fig S2C). Thus, GSDMD<sup>Nterm</sup> integrates into cellular membranes in a cholesterol-independent manner, and this integration is associated with formation of a pore and cell lysis.

### The N-terminal fragment of GSDMD associates to liposomes *in vitro*

These findings encouraged us to attempt the reconstitution of a possible pore-forming function of GSDMD<sup>Nterm</sup> *in vitro*. We established recombinant expression for full-length human GSDMD in *E. coli* BL21(DE3) expression cells. The protein expressed well with yields of 1.5 mg l<sup>-1</sup> cell culture. Notably, following the same protocol, GSDMD<sup>Nterm</sup> did not express in *E. coli* BL21(DE3) cells to detectable levels by SDS-PAGE, in agreement with the hypothesis that the protein might have a toxic effect on the host cells. Full-length GSDMD was isolated and purified to homogeneity (Appendix Fig S3A). It elutes as a monodisperse, homogeneous elution peak from size exclusion chromatography, at the position of the expected monomeric species. Thermal denaturation showed a

melting point of 43°C, indicating that the protein is folded and can be thermally denatured. Upon incubation with different human caspases, we confirmed that recombinant GSDMD is cleaved by caspase-1, but not by the apoptotic caspase-3 or caspase-8 (Shi *et al*, 2015). Recombinant GSDMD is thus a functional substrate of its native enzyme. Then, we characterized the time dependence of GSDMD cleavage (Fig 3A). About 5 nM of caspase-1 cleaves more than 50% of 2  $\mu$ M of GSDMD in 40 min. GSDMD cleavage by caspase-1 results in a 30-kDa N-terminal (GSDMD<sup>Nterm</sup>) and a 22-kDa C-terminal (GSDMD<sup>Cterm</sup>) fragment. In aqueous solution in the absence of a lipidic phase, GSDMD<sup>Nterm</sup> is not soluble and forms aggregates, as demonstrated in a cross-linking experiment (Fig 3B). After cleavage, the N-terminus is highly cross-linked by DSS (disuccinimidyl suberate), while the 22-kDa GSDMD<sup>Cterm</sup> remains soluble. To determine whether the poorly soluble GSDMD<sup>Nterm</sup> associates with lipids, GSDMD was incubated in the presence or absence of active caspase-1 with unilamellar liposomes made of either 1,2-dimyristoyl-sn-glycero-3-phosphocholine (DMPC) or from *E. coli* polar lipid extract. Ultracentrifugation allowed for separation of the

liposomes from the soluble fraction. Whereas full-length GSDMD did not associate with either the DMPC or the *E. coli* polar extract liposomes, the GSDMD<sup>Nterm</sup> fully associated with either of the two membrane mimetics. GSDMD<sup>Cterm</sup> did not associate with the liposomes (Fig 3C). Therefore, the soluble GSDMD<sup>Cterm</sup> domain is acting in full-length GSDMD not only as an inhibitor of GSDMD<sup>Nterm</sup> but also as a solubility tag for the intrinsically insoluble and lipophilic GSDMD<sup>Nterm</sup>, preventing it from aggregation and membrane association. Once cleaved, GSDMD<sup>Nterm</sup> associates strongly to available membranes. DMPC liposomes are made from a chemically pure compound, showing that membrane association by GSDMD<sup>Nterm</sup> does not require any specific receptors in the membrane.

### The N-terminal fragment of GSDMD forms pores in liposomes

Next, we asked whether liposome-associated GSDMD<sup>Nterm</sup> forms transmembrane pores. Liposomes filled with a self-quenching concentration of the fluorophore 6-carboxyfluorescein were incubated with recombinant full-length GSDMD in the presence or absence of active caspase-1 (Fig 4). Release of the fluorophore from the liposome interior results in a strong reduction in the concentration-dependent self-quenching effect and consequently in an increase of the overall fluorescence signal, as demonstrated by chemical rupture of the liposomes with the detergent Triton X in a control experiment (Appendix Fig S5). Neither caspase-1 nor full-length GSDMD alone was able to release dye from the liposomes, but in the presence of both GSDMD and caspase-1, dye release was observed, indicating the formation of permeability pores with open

diameters of at least the molecular size of 6-carboxyfluorescein ( $\approx 1$  nm). The dye release reaction from liposomes includes at least three kinetic steps: the first step is the proteolytic cleavage of GSDMD by caspase-1, the second step is the membrane association, and the third step is pore formation of GSDMD<sup>Nterm</sup>. Whereas the first step follows classical Michaelis–Menten kinetics, the reaction mechanisms of the second and third steps may include additional oligomerization steps with non-trivial concentration dependence. In an attempt to visualize the concentration dependence of the overall reaction, we measured the kinetics of dye release as a function of GSDMD concentration at a constant caspase-1 concentration of 5 nM (Fig 4A). At a GSDMD concentration of 520 nM, the dye release is very efficient so that in 20 min, already more than 90% of the total fluorescence signal is observed. With decreasing GSDMD concentration, the overall reaction rate decreases, but the overall dye release nonetheless reaches 100%, showing that sufficient GSDMD is available to permeate all liposomes. This conclusion breaks down at a GSDMD concentration of 65 nM, where only about 50% of the liposomes are permeated at late time points.

We then measured the kinetics of dye release as a function of the caspase-1 concentration in the range 1.2–15 nM, while keeping the GSDMD concentration constant at 130 nM (Fig 4B). In this experiment, by decreasing the concentration of caspase-1, we expect a reduction of the availability of cleaved GSDMD<sup>Nterm</sup> by the initial protease cleavage step, and consequently, we observe a deceleration of the dye release reaction. The total amount of GSDMD is always sufficient to permeate all liposomes in the setup, and consequently, we observe 100% dye release levels in all measurements.

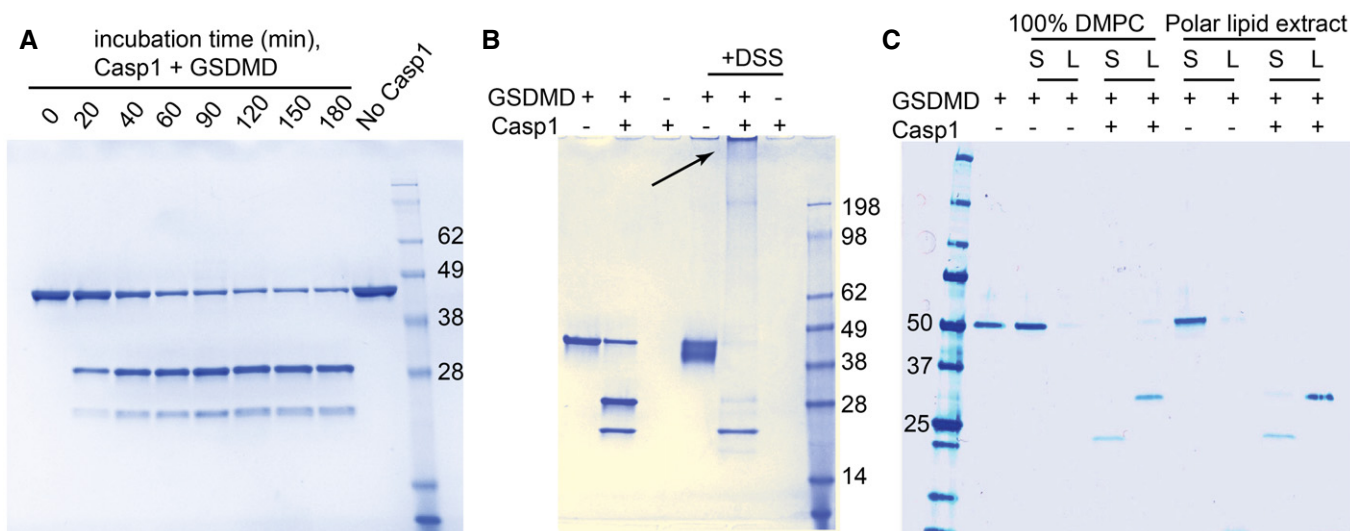


**Figure 3. GSDMD<sup>Nterm</sup> targets liposomes after caspase-1 cleavage.**

- A Human GSDMD at a concentration of 2  $\mu$ M was incubated at room temperature with 5 nM caspase-1. The protein was cleaved in a time-dependent manner into two bands of 31 kDa (GSDMD<sup>Nterm</sup>) and 22 kDa (GSDMD<sup>Cterm</sup>).
- B Cross-linking experiment of full-length and cleaved GSDMD. GSDMD at a concentration of 2  $\mu$ M was incubated at room temperature with 5 nM caspase-1. After enzymatic cleavage, GSDMD<sup>Nterm</sup> is highly cross-linked by DSS, resulting in the gel-impenetrating species highlighted by the arrow. GSDMD<sup>Cterm</sup> is not cross-linked.
- C GSDMD at a concentration of 1  $\mu$ M was incubated at room temperature with 5 nM caspase-1 and liposomes composed of 4 mM DMPC or polar lipid extract derived from *E. coli*. After 2 h, the lipid fraction (L) was separated from the supernatant (S) by ultracentrifugation at 4°C for 1 h at 120,000 g.

Source data are available online for this figure.

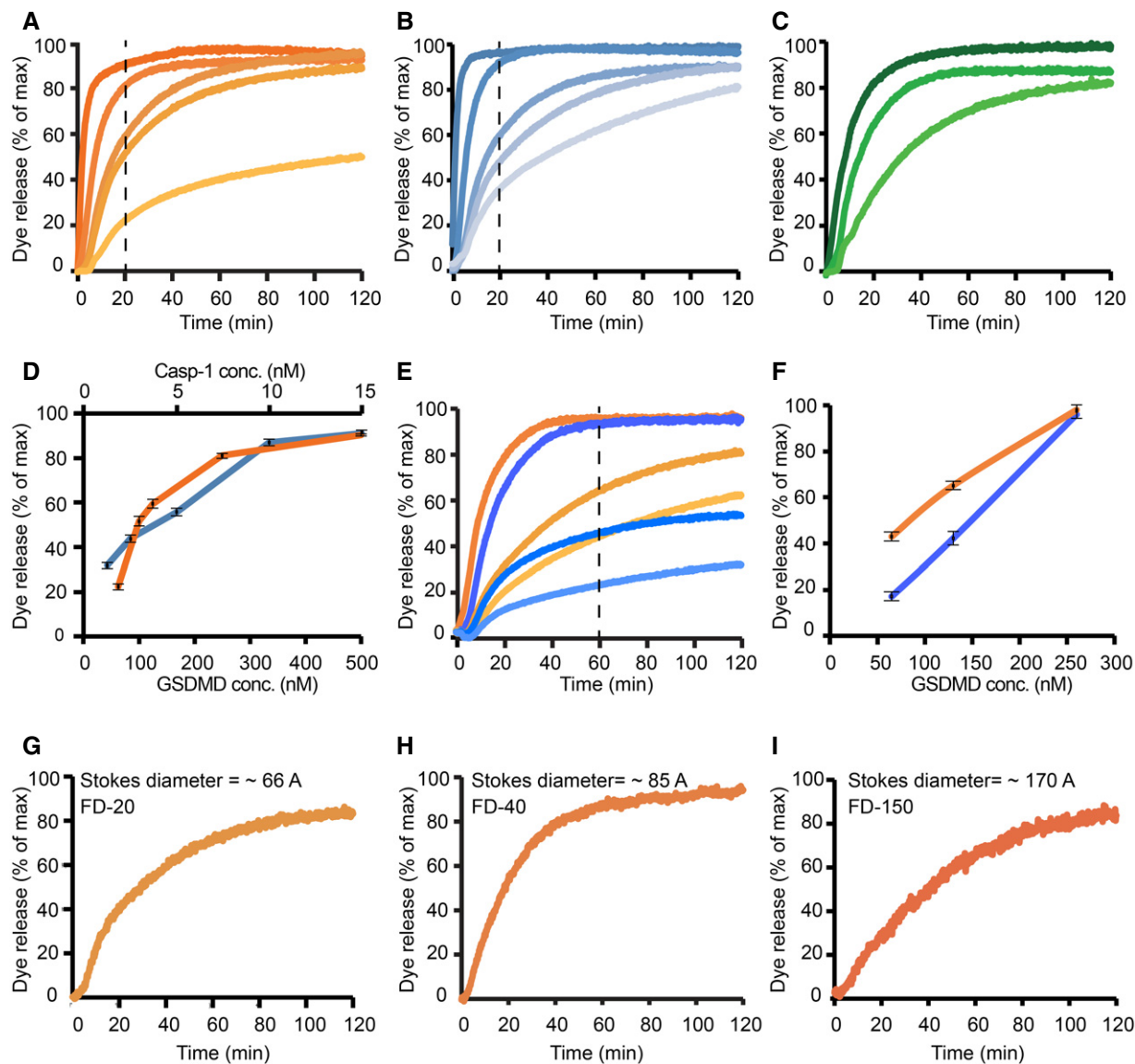


**Figure 4. GSDMD<sup>N-term</sup> causes liposome permeability by pore formation.**

A–I Dye release time courses from liposomes as a percentage of maximal release. (A) Five different reactions, where 5 nM caspase-1 and 400  $\mu$ M 6-carboxyfluorescein-loaded liposomes prepared with *E. coli* polar lipids were incubated with GSDMD concentrations of (nM): 520, 260, 130, 100, 65 (colored dark to light orange). The time point of 20 min is highlighted by a vertical dashed line. (B) Five different reactions, where 130 nM of GSDMD and 400  $\mu$ M 6-carboxyfluorescein-loaded liposomes prepared with *E. coli* extract polar lipid, were incubated with caspase-1 concentration of (nM): 15, 8, 5, 2.5, 1.2 (colored dark to light blue). The time point of 20 min is highlighted by a vertical dashed line. (C) Three different reactions, where 5 nM caspase-1 and 400  $\mu$ M 6-carboxyfluorescein-loaded liposomes prepared with porcine brain total lipid extract, were incubated with GSDMD concentrations of (nM): 520, 260, 100 (colored dark to light green). (D) Dye release at 20-min reaction as a function of GSDMD (dark orange) and caspase-1 (dark blue) concentrations. Error bars for three independent experiments are shown. (E) Two different sets of reactions, where wild-type GSDMD (dark to light orange) and the mutant GSDMD<sup>I104N</sup> (dark to light blue) were independently incubated at the concentrations of 260, 130, and 65 nM with 5 nM caspase-1 and 400  $\mu$ M 6-carboxyfluorescein-loaded liposomes. The time point of 60 min is highlighted by a vertical dashed line. (F) Dye release at 60 min of reaction as a function of GSDMD wild-type (dark orange) and GSDMD<sup>I104N</sup> (dark blue) concentration. Error bars for three independent experiments are shown. (G–I) Dye release from 400  $\mu$ M liposomes loaded with the 6-carboxyfluorescein derivatives FD-20, FD-40, and FD-150, with variable Stokes diameters, as indicated. 130 nM of GSDMD and 5 nM caspase-1 were incubated with the liposomes. For each experiment, a representative from three independent experiments is shown. The corresponding raw data are shown in Appendix Figure S5.

Importantly, GSDMD did not only permeate liposomes made of bacterial lipid extract (Fig 4A and B), but similarly also liposomes from a eukaryotic source (Fig 4C). In a next experiment, we examined the functionality of the I105N mutant of GSDMD. This mutant had played a key role in the discovery of GSDMD, since it

had previously been identified as a loss-of-function mutant in mouse models (Kayagaki *et al.*, 2015). We generated the analogous mutation I104N in GSDMD and expressed and purified the mutant protein with the same biochemical protocols as the wild-type protein. GSDMD<sup>I104N</sup> is cleaved by caspase-1 with kinetics

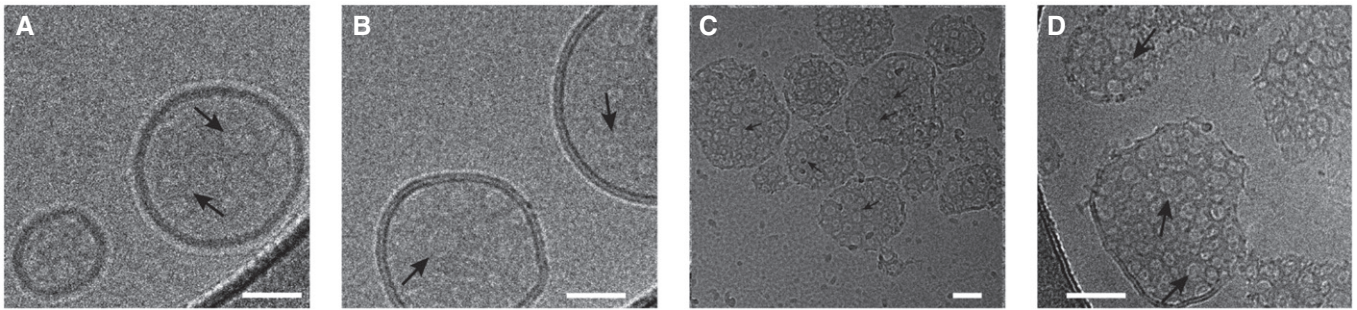


**Figure 5. Visualization of GSDMD<sup>Nterm</sup> pores in liposomes by cryo-electron microscopy.**

A–C Cryo-electron micrographs of GSDMD<sup>Nterm</sup> pores in *E. coli* polar lipid liposomes. The micrographs were acquired at protein/lipid molar ratios of 1/1,000, 1/500, and 1/100, respectively. Black arrows indicate ring-shaped structures corresponding to oligomeric GSDMD<sup>Nterm</sup> pore forms. Scale bars = 80 nm.  
 D Proteoliposome with protein/lipid molar ratio of 1/100 at higher magnification. Black arrows indicate ring-shaped structures corresponding to oligomeric GSDMD<sup>Nterm</sup> pore forms. Scale bar = 80 nm.

indistinguishable from wild-type GSDMD (Appendix Fig S4A and B). In the dye release assay, at high protein concentrations, GSDMD<sup>I104N</sup> is able to form functional pores with only minor differences to the wild-type protein. At reduced protein concentrations, however, it showed reduced activity compared to the wild-type protein (Fig 4E and F). Consistent with these data and previously published work (Kayagaki *et al*, 2015), we found that GSDMD<sup>I104N</sup> could also induce cell death of HEK293T cells when expressed by a doxycycline-inducible promoter, although significantly less than the WT protein (Appendix Fig S4D). Similarly, expression of the I104N mutant of human GSDMD in immortalized *Gsdmd*-deficient mouse macrophages partially restored pyroptosis after *Salmonella* infection when compared to wild-type human GSDMD (Appendix Fig S4C). The quantitative differences observed here may well translate into an effective loss-of-function effect in whole animals, and our experiments thus confirm the functional deficiency of the mouse I105N mutant. As an additional control experiment, we verified that uncleaved GSDMD full length does not form pores in liposomes (Appendix Fig S5E and F). Next, we addressed the size of the GSDMD pore in liposomes by using carbohydrate-conjugated fluorophores as markers. These fluorophores have differently long carbohydrate chains attached, resulting in different overall Stokes radii. We selected three different fluorophores with Stokes radii of 33, 45, and 85 Å, but all of them were still released by the GSDMD pore (Fig 4G–I). This suggests that the pyroptosis pore formed by GSDMD<sup>Nterm</sup> can reach diameters of at least 15 nm, in full agreement with the cellular experiments.

### Visualization of GSDMD pores

We employed two methods to resolve pores of GSDMD<sup>Nterm</sup> in liposomes at nanometer resolution. Cryo-electron micrographs of untreated liposomes show intact spherical shapes (Appendix Fig S6A). Also the incubation with full-length GSDMD in the absence of caspase-1 did not result in visual distortions of the liposomes (Appendix Fig S6B). However, upon addition of caspase-1 and subsequent incubation, large ruptures of the liposome structure were observed. In these preparations, the liposome surface features numerous large rings of dense material with inner diameters of  $\approx 20$  nm (Fig 5A–D and Appendix Fig S6C–E). These rings are

formed by GSDMD<sup>Nterm</sup> and although the liposomes appear completely covered by the assemblies, from the available contrast of the micrographs, it remains inconclusive, whether these rings are lipid-filled protrusions or actual transmembrane pores. The lack of contrast also did not allow for a clear identification of the different shapes of GSDMD oligomers. To characterize the assembly of the transmembrane pores convincingly, we thus imaged GSDMD oligomers and pore formation on liposomes by atomic force microscopy (AFM). In an initial control experiment, we adsorbed either GSDMD alone, or caspase-1 alone, or GSDMD and caspase-1 together to freshly cleaved mica, which we used as sample support in our AFM studies (Appendix Fig S7A–D). GSDMD and caspase-1 readily adsorbed to the negatively charged hydrophilic mica surface as monomers or small oligomers, but did not assemble into arcs or rings. After this, we incubated liposomes composed of *E. coli* polar lipids with GSDMD and caspase-1 for 90 min at 37°C and adsorbed the sample onto freshly cleaved mica. The AFM topographs recorded in buffer solution showed that upon adsorption to mica, the liposomes opened as single-layered membrane patches (Appendix Fig S7E). At higher resolution, the topographs showed GSDMD bound to the lipid membranes and forming arc-, slit- and ring-shaped oligomers (Fig 6A–E and Appendix Fig S7F). The height profile around the arc-, slit- and ring-like oligomers indicates that they protruded  $4.3 \pm 0.3$  nm (average  $\pm$  s.d.;  $n = 218$ ) from the lipid surface and that each of them could form pores through the lipid membrane (Fig 6F and G). Occasionally, arcs and slits combined into ring-shaped structures, which were not yet perfectly circular and only partially associated with the formation of membrane pores. Several pore-forming toxins (PFTs) have shown the ability to bind to lipid membranes as oligomers forming arcs or slits that can dynamically rearrange on the membrane surface to form larger pores (Leung *et al*, 2014; Sonnen *et al*, 2014; Mulvihill *et al*, 2015; Podobnik *et al*, 2015). In agreement with this observation, GSDMD arcs and slits were found that presumably fused into perfect ring-shaped GSDMD<sup>Nterm</sup> oligomers of variable diameters, with an average value of 21 nm (Fig 6F–H). These AFM topographs thus clearly show a structural variability of the GSDMD<sup>Nterm</sup> assembly, which is, however, determined to eventually lead to the assembly of ring-like structures. These ring-like structures correspond to the pyroptotic membrane pores.

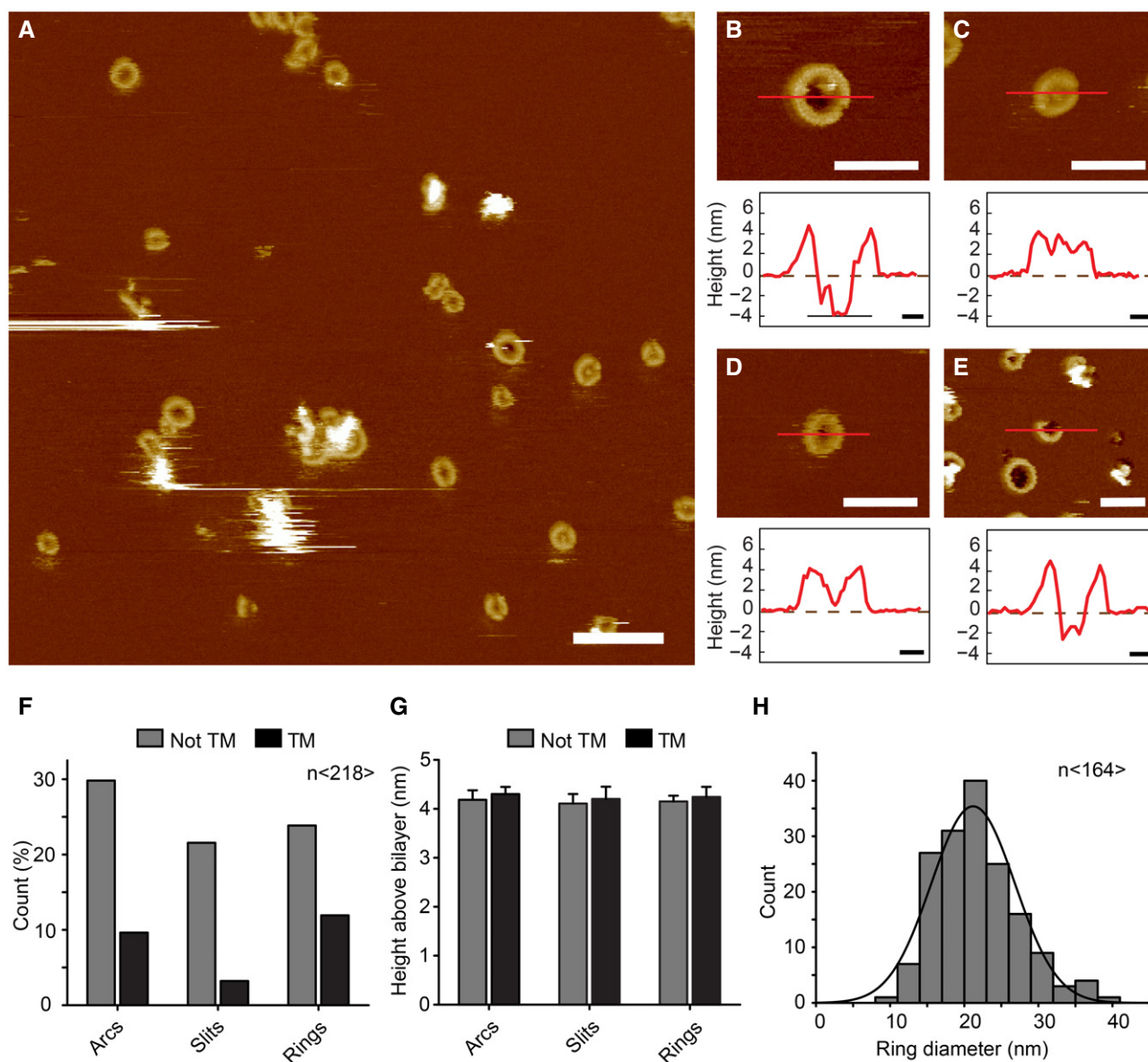


**Figure 6. Characterization of GSDMD<sup>Nterm</sup> pores by atomic force microscopy.**

**A** AFM topograph of GSDMD<sup>Nterm</sup> bound to lipid membranes of *E. coli* polar lipids. Overview topograph showing arc-, slit-, and ring-like GSDMD oligomers. Scale bar corresponds to 100 nm.

**B–E** High-resolution AFM topographs and height profiles of GSDMD<sup>Nterm</sup> oligomers (red curves). Height profiles were measured along the red lines in the topographs. Dashed zero lines (0 nm) indicate the surface of the lipid membrane; heights of < -4 nm indicate that the oligomers formed transmembrane pores. Topographs were taken in buffer solution (150 NaCl, 20 mM HEPES, pH 7.8) at room temperature. The experiment was reproduced at least three times using independent liposome and GSDMD preparations. Scale bars of topographs correspond to 50 nm and of height profiles 10 nm. The full color range of the AFM topographs corresponds to a vertical scale (height) of 20 nm.

**F–H** Analysis of GSDMD<sup>Nterm</sup> oligomers bound to lipid membranes of *E. coli* polar lipids. (F) GSDMD<sup>Nterm</sup> oligomers assembled into arcs, slits, and rings leading to transmembrane (TM) pores or not transmembrane aggregate ( $n = 218$ ). (G) Height of GSDMD<sup>Nterm</sup> oligomers protruding from the lipid membrane. Bars represent mean, and error bars represent s.e.m. ( $n = 218$ ). (H) Distribution of the diameters of rings formed by GSDMD<sup>Nterm</sup> oligomers. The average distribution was  $21.2 \pm 5.6$  nm ( $n = 164$ ; average  $\pm$  s.d.), and the bin size was 3 nm.

## Discussion

Pyroptotic death is a defining feature of canonical and non-canonical inflammasome engagement and the final step associated with the activation of human and mouse caspase-1, but also mouse caspase-11 and human caspase-4/-5. Although the morphological

features of pyroptotic cell death indicated the formation of a plasma membrane pore and subsequent lysis of the cell (Lamkanfi, 2011), the molecules involved in pyroptosis induction had remained elusive. The recent identification of GSDMD as an essential mediator of pyroptosis significantly expanded our understanding of pyroptotic cell death (He *et al.*, 2015; Kayagaki *et al.*, 2015; Shi *et al.*, 2015), but

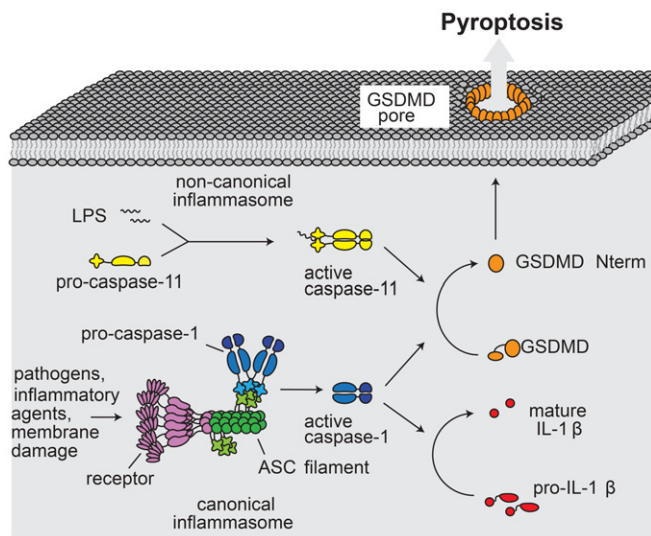


**Figure 7. Model for GSDMD-mediated pyroptotic cell death.**

Canonical inflammasomes act as sensors for a variety of pathogens and cellular insults. Assembly of these types of inflammasomes involves multimerization of the receptor (purple), which initiates filament formation of the adaptor protein ASC (green). ASC filaments act as activation platforms for caspase-1 (blue). In the noncanonical pathway, LPS is directly bound by caspase-11 (yellow), resulting in its activation. Caspase-1 processes interleukin IL-1 $\beta$  (red). Both caspase-1 and caspase-11 process GSDMD (orange), which results in release of the GSDMD<sup>Nterm</sup> fragment. GSDMD<sup>Nterm</sup> forms a large pore in the plasma membrane. Pore formation results in rapid loss of membrane integrity, the dissipation of the electrochemical gradient, and ultimately in cell death.

whether after cleavage by caspases GSDMD executes pyroptosis directly, or by initiating other signaling events remained unclear. In this work, we have shown that the N-terminal fragment of GSDMD, GSDMD<sup>Nterm</sup>, can form pores with average diameters of 21 nm in artificial liposomes, as well as large pores in the plasma membrane of cells (Figs 5 and 6). GSDMD oligomers were found to form pre-pore states consisting of arcs, slits, and rings. Each of these oligomeric states had a certain probability to also show a pore state, among which the GSDMD rings with their variable diameter formed the largest transmembrane pores. The variable pore size suggests that GSDMD possesses an intrinsic high structural variability and that GSDMD arcs and slits represent intermediates that presumably may fuse toward the ring-shaped structures, similar to observations for several other pore-forming toxins (PFTs) that dynamically rearrange on the membrane surface (Leung *et al*, 2014; Sonnen *et al*, 2014; Mulvihill *et al*, 2015; Podobnik *et al*, 2015). Importantly, our *in vitro* assays show that the formation of the GSDMD pore does not require other proteins as co-factors or membrane receptors, demonstrating that GSDMD<sup>Nterm</sup> is the sole and final executor of pyroptotic cell death (Fig 7). While this manuscript was in revision, other reports have been published that confirm our findings that the N-terminal fragment of GSDMD causes pyroptosis through the formation of a plasma membrane pore and that demonstrate that the N-terminal domains of other gasdermin family members share this pore-forming activity (Aglietti *et al*, 2016; Ding *et al*, 2016).

The placement and function of GSDMD in the canonical and non-canonical inflammasome pathway strongly resembles the

placement and function of Bax (Bcl-2-associated X protein) in the apoptotic cell death pathways (Youle & Strasser, 2008). Bax is the final executor of apoptosis and forms a large pore in the mitochondrial outer membrane. Interestingly, whereas both proteins form large permeability pores in their respective target membranes, their mechanism of activation is entirely different. Whereas GSDMD is activated by proteolytic cleavage, Bax is activated by interactions within the Bcl-2 family of proteins (Gavathiotis *et al*, 2008; Czabotar *et al*, 2013). A strong difference can also be expected for the atomic structure of the two proteins. Bax features a bundle of nine  $\alpha$ -helices (Suzuki *et al*, 2000), thereby burying the two presumed pore-forming helices in its central core. The prediction of secondary structure elements shows that GSDMD<sup>Nterm</sup> consists mainly of  $\beta$ -strand secondary structure, whereas the soluble GSDMD<sup>Cterm</sup> consists of  $\alpha$ -helical secondary structure (Appendix Fig S8). Thus, while Bax resembles the bacterial pore-forming colicins, structural studies of the membrane-inserted form of GSDMD will be of highest interest.

Another functionally related pathway is necroptotic cell death, which is for instance initiated by TNF (tumor necrosis factor)- $\alpha$  or the engagement of Toll-like receptor (TLRs) in absence of caspase-8 activity (Pasparakis & Vandenabeele, 2015). Necroptosis involves the formation of the necrosome, a complex consisting of RIP (receptor serine-threonine-protein kinase)1, RIP3 and MLKL (mixed lineage kinase domain-like) and similarly to pyroptosis it is characterized by cell lysis (Pasparakis & Vandenabeele, 2015). Recent work has demonstrated that recruitment of MLKL to RIP3 and MLKL phosphorylation results in the conformational change that leads to the exposure of its four-helix bundle domain (FHBD) and oligomerization of MLKL (Murphy *et al*, 2013). Binding of the FHBD to negatively charged phosphatidylinositol phosphates has been proposed to recruit MLKL to the plasma membrane allowing it to directly permeabilize the membrane by forming a pore (Dondelinger *et al*, 2014; Su *et al*, 2014; Wang *et al*, 2014). Alternatively, it has been also proposed that plasma membrane-bound MLKL recruits Ca<sup>2+</sup> or Na<sup>+</sup> ion channels to permeabilize the membrane (Cai *et al*, 2014; Chen *et al*, 2014). Thus, although the steps leading up to necroptosis are markedly different from pyroptosis, the execution of both types of lytic cell death involves the formation of plasma membrane pores.

The fact that GSDMD targets membranes after cleavage by caspases and forms permeability pores also sheds some light on the function of the regulatory C-terminal domain. Cleavage of GSDMD by inflammatory caspases results in the release of the GSDMD C-terminal fragment (Kayagaki *et al*, 2015; Shi *et al*, 2015), but overexpression of GSDMD<sup>Cterm</sup>, which was found to bind GSDMD<sup>Nterm</sup>, results in the inhibition of cell death (Shi *et al*, 2015). This gave rise to a model in which cleavage releases an intramolecular autoinhibition exerted by GSDMD<sup>Cterm</sup> on the GSDMD<sup>Nterm</sup>, thus preventing GSDMD<sup>Nterm</sup> to unleash its cytotoxic activity. Interestingly, we have observed that GSDMD<sup>Cterm</sup> is a soluble protein, while GSDMD<sup>Nterm</sup> is insoluble and aggregates, when GSDMD is cleaved in the absence of a target membrane (Fig 3). This result supports a slightly different model in which GSDMD<sup>Cterm</sup> does not only act as an inhibitory domain, but simultaneously also as a solubility tag for the N-terminal domain, maybe by shielding certain hydrophobic or amphipathic segments required for membrane insertion. Based on these functions, the alternative names pore-forming domain (PFD) and solubilizing inhibitory domain (SID) appear well suited for the GSDMD<sup>Nterm</sup> and GSDMD<sup>Cterm</sup>, respectively.

The identification of GSDMD as an essential mediator of pyroptosis has shed light on the possible functions of other gasdermin family members in programmed cell death. All gasdermins (GSDMA, GSDMB, GSDMC, and GSDMD in humans; GSDMA1-3, GSDMC1-4, and GSDMD in mice) are composed of a distinct N-terminal and C-terminal domain (Tanaka *et al*, 2013), a feature shared by the extended gasdermin family members DFNA5 and DFNB59 (deafness, autosomal-dominant 5/autosomal-recessive 59). Several lines of evidence suggest that the N-terminal domain of other gasdermin family members is intrinsically cytotoxic (Saeki *et al*, 2007; Op de Beeck *et al*, 2011; Shi *et al*, 2015). Given the functional and sequence similarity between gasdermin N-terminal domains, it is not surprising that all gasdermins induce membrane permeability pores and subsequent cell death (Ding *et al*, 2016). Structural studies of GSDMD and other gasdermin family members in their full-length and membrane inserted forms as well as the stoichiometry of these pores will thus remain of high interest. Furthermore, it remains to be shown whether several gasdermins might cooperate in pore formation, given that caspase-1-dependent cell death does not solely rely on GSDMD (Kayagaki *et al*, 2015). Finally, to fully understand this emerging group of cell death effectors, it will be necessary to define how other gasdermin family members are activated and to identify the physiological context in which they induce cell death.

## Materials and Methods

### Cell culture and reagents

HEK293T were maintained in DMEM (Sigma), 10% FCS (Amimed), 1% penicillin/streptomycin (Amimed) and split, when they reached 90% confluency. Immortalized macrophages were obtained from R. Vance (UC Berkeley) and cultured in DMEM, 10% FCS, 1% PenStrep, 10 mM HEPES (Amimed), 1% non-essential amino acids (NEAA, Amimed). Polyethylenimine was from Polysciences Inc, LDH detection kit from Takara, IL-1 $\beta$  ELISA from eBiosciences, near IR live/dead marker from Thermo Scientific, propidium iodide from Santa Cruz Biotechnology, PEGs of different sizes from Merck. pRetroX TetONE3G-Puro was obtained from Clontech. The puromycin resistance cassette was replaced by an EGFP by standard cloning procedures yielding pRetroX TetONE-eGFP. GSDMD<sup>Nterm</sup> was amplified from murine cDNA and cloned into pRetroX TetONE-eGFP by standard cloning procedures. Anti-GSDMD and anti-GAPDH antibodies were from SCBT (both used at 1:250), anti-caspase-1 p20 from Adipogen (used at 1:4,000), anti-alpha tubulin from Abcam (used at 1:2,500), anti-VDAC, anti-HDAC1, and anti-Na<sup>+</sup>/K<sup>+</sup> ATPase antibodies were from Cell Signaling Technologies (all at 1:1,000). HEK293T cells were seeded in 96-well plates (30,000 cells per well) 1 day prior to transfection. Cells were subsequently transfected with 300 ng of plasmid DNA and 3 $\times$  (wt/vol) linear PEI (polyethylenimine). Twenty-four post-transfection cells were treated as indicated in the respective figures.

### Generation of stable cell lines

For complementation of *Gsdmd*<sup>KO</sup> cell lines (Dick *et al*, 2016), human *Gsdmd* was amplified from HeLa cell cDNA (Clontech) and

cloned into pLJM1 (addgene #19319) where the puromycin resistance cassette was replaced with a hygromycin resistance cassette. The I104N mutant was generated using the Q5 site-directed mutagenesis kit (NEB). To produce lentiviral particles, 1  $\times$  10<sup>6</sup> HEK293T cells were transfected with the 2  $\mu$ g lentiviral plasmid, 2  $\mu$ g psPax2, and 0.4  $\mu$ g VSV-G for 6 hrs. Medium was exchanged, and lentiviral particles were collected 24 h later. *Gsdmd*-deficient immortalized macrophages were spin-infected with these particles, and transduced cells were selected with Hygromycin (500  $\mu$ g/ml, invivogen) for 7 days. Selected cells were used for experiments.

### Macrophage infection

Immortalized macrophages were seeded the day before the experiment (30,000 cells per well of a 96-well plate, 1.5  $\times$  10<sup>6</sup> cells per well of a 6-well plate). *S. typhimurium* (SL1344) was grown overnight in Luria broth (LB) medium. On the day of experiment, bacteria were subcultured 1:40 in LB and grown for 4 h to logarithmic phase to induce SPI-1 expression. Cells were washed once with PBS and infected at an MOI of 50 with *S. typhimurium* diluted in OptiMEM. LDH and IL-1 $\beta$  release was determined as described in the respective manufacturer's instructions. Cell lysates and supernatants were prepared for Western blot and analyzed by SDS-PAGE as described previously (Broz *et al*, 2012).

### Subcellular fractionation and membrane extraction

About 1.5  $\times$  10<sup>7</sup> million immortalized macrophages were seeded in 10-cm tissue culture-treated dishes the day before the experiment. The next day, cells were left either uninfected or infected with log-phase *S. Typhimurium* at a MOI of 50 for 10 and 20 min at 37°C. Cells were washed three times with homogenization buffer (10 mM Tris, 10 mM acetic acid, 1 mM EDTA, 7.5 mM MgCl<sub>2</sub>, 250 mM sucrose), scraped, and homogenized using a syringe equipped with a 25G needle (30 strokes) (Total lysate). Samples were centrifuged for 700 g for 5 min; supernatants were transferred to a new tube and centrifuged the same way again. Combined pellets yielded the P0.7 fraction, while the remaining supernatant yielded the S0.7 fraction. Pellets were washed twice with homogenization buffer and lysed in RIPA buffer. Supernatants (S0.7) were centrifuged 10,000 g for 15 min; supernatant was transferred to new tube and centrifuged the same way again. Pellets (P10) were combined, washed twice with homogenization buffer, and resuspended in SOL buffer (50 mM Tris-HCl pH 6.8, 1 mM EDTA, 1% Triton X-100). Supernatants (S10) were centrifuged at 150,000 g for 30 min; supernatant was transferred to a new tube and centrifuged the same way again. Pellets were combined, washed again twice, and resuspended in SOL buffer (P150). The supernatants were analyzed as S150. Protein concentration of every sample was determined by BCA, and equal amounts were analyzed by SDS-PAGE. For extraction of membrane fractions, cells were infected for 15 min with log-phase *S. typhimurium*, homogenized as described above, and membrane preparation and extraction were performed as described in Gatfield and Pieters (2000).

### Cloning, expression, and purification of GSDMD and caspases

cDNA coding for the full-length human *GSDMD* was cloned with an N-terminal His<sub>6</sub>-SUMO-tag into a pET28a vector under control of a

T7 promoter. Single amino acid point mutation I104N was generated by QuickChange site-directed mutagenesis kit (Stratagene). All plasmids were verified by DNA sequencing. The protein construct was transformed in BL21 (DE3) *E. coli* strains, and the protein was expressed by growing the cultures at 37°C to an OD<sub>600</sub> of 0.7 and by inducing with 0.5 mM IPTG overnight at 18°C. The cells were harvested by centrifugation and the pellet was resuspended in 20 mM Tris buffer pH 7.5, 50 mM NaCl, 5 mM imidazole, 20 mM MgCl<sub>2</sub>, 10 mM KCl, 0.5 mM TCEP, 0.1 mM protease inhibitor, and DNase I. The resuspended cells were disrupted by high-pressure microfluidization and centrifuged at 30,000 g at 4°C for 45 min. The supernatant was incubated for 2 h at room temperature with pre-equilibrated Ni-NTA affinity resin (Thermo Scientific) and then passed through a column for gravity flow purification. The column was washed with 20 column volumes of resuspension buffer containing 15 mM imidazole, and the fusion protein was eluted with 3 column volumes of the same buffer with 250 mM imidazole. SUMO-tag cleavage was achieved by addition of ULP1 protease to the solution and subsequent dialysis overnight at 4°C against 20 mM Tris buffer pH 7.5, 50 mM NaCl, 0.5 mM TCEP. GSDMD was eluted from a second round of purification through pre-equilibrated Ni-NTA affinity resin. The protein was further purified by Hi-trapQ ion-exchange and a Superdex 75 gel filtration column (GE Healthcare) pre-equilibrated with 20 mM Tris buffer pH 7.5, 50 mM NaCl, 0.5 mM TCEP. Purified GSDMD was frozen in small aliquots in liquid N<sub>2</sub>. Human caspase-1, caspase-3, and caspase-8 were cloned into pET22 expression vectors, expressed as inclusion bodies in *E. coli*, and refolded as previously described (Ramage *et al.*, 1995). Briefly, inclusion bodies were solubilized in 8M urea, and protein was refolded by rapid dilution; during which the enzymes auto-activated. A gel filtration column was run to purify the final product, and the concentration of active enzyme determined by active site titration.

### Liposome preparation

The polar lipid extract derived from *E. coli*, total lipid extract derived from porcine brain, and DMPC were purchased from Avanti Polar Lipids, Inc. (Alabaster AL, USA). Chloroform lipid solutions at a concentration of 25 mg ml<sup>-1</sup> were gently dried in a glass tube into a thin film under nitrogen flow and placed under vacuum overnight to further evaporate any residual solvent. The lipid layers were that rehydrated in 1 ml of 50 mM HEPES buffer, 150 mM NaCl, pH 7.5 under continuous shaking at 50°C for 2 h. The lipid dispersions were subjected to 10 freeze-thaw cycles, and the resultant liposomes were extruded 20 times through 100-nm polycarbonate membranes to form large unilamellar vesicles (LUV). The mean size diameter of the liposomes was verified by dynamic light scattering (DLS). To prepare dye-filled LUVs, the dry lipid film was hydrated with 0.5 ml of 50 mM HEPES buffer, 50 mM NaCl, 70 mM 6-carboxyfluorescein, 5 mM TCEP, pH 7.5) or by adding 100 mg ml<sup>-1</sup> of fluorescein isothiocyanate dextran FD-20, FD-40, and FD-150. For the 6-carboxyfluorescein containing liposome, the removal of extra-vesicular dye was achieved by a purification step through a PD-10 column (GE Healthcare) pre-equilibrated with 50 mM HEPES buffer, 150 mM NaCl, 5 mM TCEP pH 7.5. The FD-20, FD-40, and FD-150 dye-filled liposomes were washed twice by ultracentrifugation at 4°C for 20 min at 100,000 g and then

resuspended in 0.5 ml of the same isotonic solution. All liposomes were stored at 4°C and used within 24 h.

### Liposome leakage assay

Membrane leakage experiments were performed using 6-carboxy-fluorescein, FD-20, FD-40, and FD-150-filled liposomes composed of polar lipid extract derived from *E. coli* and total lipid extract derived from porcine brain. The samples were initially prepared by diluting 40 mM total lipid concentration in 100 µl solution of 50 mM HEPES buffer, 150 mM NaCl, 5 mM TCEP, pH 7.5 supplemented with different aliquots of a 2.6 µM GSDMD stock solution. The NaCl concentration in the reaction buffer outside the LUV was optimized to preserve caspase-1 activity and to minimize the dye release due to the osmotic pressure exerted by the dye on the membrane bilayer. To initiate the cleavage of GSDMD and the consequent pore formation reaction, different amounts of caspase-1 from a 12 µM stock solution were added to 100 µl of premixed LUV-GSDMD solution. The membrane leakage was detected by measuring the time-course increase in fluorescence resulting from the dye dilution and subsequent dequenching upon membrane pore formation. The experiments were carried out in a Corning 384-well non-binding surface plate, and the fluorescence was continuously recorded for 2 h at 10-s intervals using a Biotek Synergy 2 plate reader with excitation and emission wavelengths at 492 and 520 nm, respectively. At each time point, the percentage of dye release was calculated as:

$$\text{Dye release} = (I - I_0) / (I_{\text{max}} - I_0)$$

where  $I$  is the emission intensity of the sample,  $I_0$  is the emission intensity from an experiment with the liposome solution only (negative control), and  $I_{\text{max}}$  is the emission intensity from an experiment with added Triton X-100 to the liposome solution (positive control).

### Gel-shift assays

Recombinant GSDMD was incubated with different caspases for the indicated time period in a reaction vessel in caspase activity buffer of 100 mM Hepes, pH 7.4, 0.5 mM EDTA, 50 mM NaCl, 0.1% CHAPS, 0.005% Novexin, and 5 mM TCEP. Final concentrations were 5 nM enzyme, 2 µM GSDMD. Reactions were quenched with 6xSDS loading buffer and analyzed by SDS-PAGE. For cross-linking experiments, 2 mM DSS (ThermoFisher) were added to the reaction, and protein was cross-linked for 30 min before quenching the reaction.

### Thermofluor assay

To monitor GSDMD thermal stability, the protein was incubated with the fluorescent dye Sypro orange and the thermal shift assay was conducted in the CFX96 Real Time Detection System (Bio-Rad, Hercules, CA). Solutions of 2 µl of 2 µM GSDMD, 8 µl of 5x Sypro orange, 10 µl solution of screened condition were loaded to a 96-well plate. The plate was heated from 10 to 90°C with a heating rate of 0.5°C min<sup>-1</sup>. The fluorescence intensity was measured with excitation and emission wave lengths of 490 and 530 nm, respectively.

### Cryo-electron microscopy (cryo-EM)

Cryo-EM was used to visualize GSDMD-mediated pore on liposome surfaces. The samples were prepared by 2-h incubation of freshly prepared liposome (2 mM lipids) with 2.6  $\mu\text{M}$  of GSDMD in the presence and the absence of catalytic amounts of caspase-1. All samples were adsorbed for 10 s on glow-discharged thin carbon film-coated 300-mesh lacey EM grids, blotted for 2 s, and plunge frozen in liquid ethane using a FEI Vitrobot MK4 (Vitrobot, Maastricht Instruments). Cryo-EM micrographs were acquired with a Philips CM200FEG transmission electron microscope operated at 200 kV and a nominal magnification of 66,000 $\times$ . Images were recorded with a TVIPS F416 CMOS camera.

### Liposome Preparation for atomic force microscopy (AFM)

Unilamellar liposomes were prepared at room temperature ( $\approx 23^\circ\text{C}$ ) by hydration of lipid films and extrusion through polycarbonate filters with 0.1- $\mu\text{m}$  pore diameter (Nucleopore Polycarbonate, Whatman) according to the method described by Avanti Polar Lipids ([www.avantilipids.com](http://www.avantilipids.com)). The *E. coli* polar lipids and the extruding equipment used for liposome preparation were purchased from Avanti Polar Lipids. The liposomes were stored at  $-80^\circ\text{C}$  in buffer solution (150 mM NaCl, 20 mM Hepes, pH 7.25). After incubation with 1  $\mu\text{M}$  mM GSDMD and 0.2  $\mu\text{M}$  caspase-1 for 90 min at  $37^\circ\text{C}$  in buffer solution (50 mM NaCl, 100 mM Hepes, 5 mM TCEP, pH 7.4), the liposomes were adsorbed onto freshly cleaved mica in buffer solution (50 mM NaCl, 20 mM Hepes, pH 7.4) (Muller *et al.*, 1997). After an adsorption time of 30 min, the sample was washed several times with the AFM imaging buffer (150 mM NaCl, 20 mM Hepes, pH 7.8) to remove weakly adsorbed protein. Buffer solutions were freshly made using nanopure water ( $18.2 \text{ M}\Omega \text{ cm}^{-1}$ ) and pro-analysis (> 98.5%) purity grade reagents from Sigma-Aldrich and Merck. Each experimental condition characterized by AFM was reproduced at least three times. Liposomes made from *E. coli* polar lipids incubated in buffer solution but in the absence of GSDMD showed no arc-, slit- or ring-like structures when imaged by AFM (Mulvihill *et al.*, 2015).

### AFM

Force-distance curve-based AFM (FD-based AFM) (Dufrene *et al.*, 2013) was performed using a Nanoscope Multimode 8 (Bruker, Santa Barbara, USA) operated in the PeakForce Tapping mode. The AFM was equipped with a 120- $\mu\text{m}$  piezoelectric scanner and fluid cell. AFM cantilevers used (BioLever mini BL-AC40, Olympus Corporation, Tokyo, Japan) had a nominal spring constant of  $0.1 \text{ N m}^{-1}$ , a resonance frequency of  $\approx 110 \text{ kHz}$  in liquid and sharpened silicon tip with a nominal radius of 8–10 nm. The FD-based AFM topographs were recorded in AFM imaging buffer (150 mM NaCl, 20 mM Hepes, pH 7.8) and at room temperature as described (Pfreundschuh *et al.*, 2014). The maximum force applied to image the samples was 70 pN, and the oscillation frequency and oscillation amplitude of the cantilever were set to 2 kHz and 40 nm, respectively. The AFM was placed inside a home-built temperature controlled acoustic isolation box. For data analysis, we took unprocessed AFM topographs. Diameters of ring-like GSDMD oligomers were measured from the highest protruding rim. Heights of GSDMD

arcs, slits, and rings were measured from their highest protruding feature relative to the surface of the lipid membrane. GSDMD oligomers were classified to having formed transmembrane pores if the inside of the pore was at least 3.5 nm deeper compared to the surface of the surrounding lipid membrane.

**Expanded View** for this article is available online.

### Acknowledgements

We thank Paul Erbel for help with the protein preparation. This work was supported by the European Research Council (FP7 contract MOMP 281764 to S.H.), the Swiss National Science Foundation (PPOOP3\_139120/1 to P.B.), and by the European Union Marie Curie Actions program through the ACRITAS Initial Training Network (FP7-PEOPLE-2012-ITN, Project 317348 to D.J.M.).

### Author contributions

LS, SR, PB, SH designed the study. LS, SR, EM, JP, RH, CJF carried out research experiments. All authors (including HS) analyzed data. LS, SR, DJM, PB, SH wrote the paper.

### Conflict of interest

The authors declare that they have no conflict of interest.

### References

- Aglietti RA, Estevez A, Gupta A, Ramirez MG, Liu PS, Kayagaki N, Ciferri C, Dixit VM, Dueber EC (2016) GsdmD p30 elicited by caspase-11 during pyroptosis forms pores in membranes. *Proc Natl Acad Sci USA* 113: 7858–7963
- Bergsbaken T, Fink SL, Cookson BT (2009) Pyroptosis: host cell death and inflammation. *Nat Rev Microbiol* 7: 99–109
- Broz P, Ruby T, Belhocine K, Bouley DM, Kayagaki N, Dixit VM, Monack DM (2012) Caspase-11 increases susceptibility to Salmonella infection in the absence of caspase-1. *Nature* 490: 288–291
- Broz P (2015) Immunology: caspase target drives pyroptosis. *Nature* 526: 642–643
- Cai Z, Jitkaew S, Zhao J, Chiang HC, Choksi S, Liu J, Ward Y, Wu LG, Liu ZG (2014) Plasma membrane translocation of trimerized MLKL protein is required for TNF-induced necroptosis. *Nat Cell Biol* 16: 55–65
- Chen X, Li W, Ren J, Huang D, He WT, Song Y, Yang C, Li W, Zheng X, Chen P, Han J (2014) Translocation of mixed lineage kinase domain-like protein to plasma membrane leads to necrotic cell death. *Cell Res* 24: 105–121
- Czabotar PE, Westphal D, Dewson G, Ma S, Hockings C, Fairlie WD, Lee EF, Yao S, Robin AY, Smith BJ, Huang DC, Kluck RM, Adams JM, Colman PM (2013) Bax crystal structures reveal how BH3 domains activate Bax and nucleate its oligomerization to induce apoptosis. *Cell* 152: 519–531
- Dick MS, Sborgi L, Ruhl S, Hiller S, Broz P (2016) ASC filament formation serves as a signal amplification mechanism for inflammasomes. *Nat Commun* 7: 11929
- Ding J, Wang K, Liu W, She Y, Sun Q, Shi J, Sun H, Wang DC, Shao F (2016) Pore-forming activity and structural autoinhibition of the gasdermin family. *Nature* 535: 111–116
- Dondelinger Y, Declercq W, Montessuit S, Roelandt R, Goncalves A, Bruggeman I, Hulpiau P, Weber K, Sehon CA, Marquis RW, Bertin J, Gough PJ, Savvides S, Martinou JC, Bertrand MJ, Vandenabeele P (2014) MLKL compromises plasma membrane integrity by binding to phosphatidylinositol phosphates. *Cell Rep* 7: 971–981

- Dufrene YF, Martinez-Martin D, Medalsy I, Alsteens D, Muller DJ (2013) Multiparametric imaging of biological systems by force-distance curve-based AFM. *Nat Methods* 10: 847–854
- Fink SL, Cookson BT (2007) Pyroptosis and host cell death responses during Salmonella infection. *Cell Microbiol* 9: 2562–2570
- Fink SL, Bergsbaken T, Cookson BT (2008) Anthrax lethal toxin and Salmonella elicit the common cell death pathway of caspase-1-dependent pyroptosis via distinct mechanisms. *Proc Natl Acad Sci USA* 105: 4312–4317
- Gatfield J, Pieters J (2000) Essential role for cholesterol in entry of mycobacteria into macrophages. *Science* 288: 1647–1650
- Gavathiotis E, Suzuki M, Davis ML, Pitter K, Bird GH, Katz SG, Tu HC, Kim H, Cheng EH, Tjandra N, Walensky LD (2008) BAX activation is initiated at a novel interaction site. *Nature* 455: 1076–1081
- Hagar JA, Powell DA, Aachoui Y, Ernst RK, Miao EA (2013) Cytoplasmic LPS activates caspase-11: implications in TLR4-independent endotoxic shock. *Science* 341: 1250–1253
- He WT, Wan H, Hu L, Chen P, Wang X, Huang Z, Yang ZH, Zhong CQ, Han J (2015) Gasdermin D is an executor of pyroptosis and required for interleukin-1 $\beta$  secretion. *Cell Res* 25: 1285–1298
- Kayagaki N, Warming S, Lamkanfi M, Vande Walle L, Louie S, Dong J, Newton K, Qu Y, Liu J, Heldens S, Zhang J, Lee WP, Roose-Girma M, Dixit VM (2011) Non-canonical inflammasome activation targets caspase-11. *Nature* 479: 117–121
- Kayagaki N, Wong MT, Stowe IB, Ramani SR, Gonzalez LC, Akashi-Takamura S, Miyake K, Zhang J, Lee WP, Muszynski A, Forsberg LS, Carlson RW, Dixit VM (2013) Noncanonical inflammasome activation by intracellular LPS independent of TLR4. *Science* 341: 1246–1249
- Kayagaki N, Stowe IB, Lee BL, O'Rourke K, Anderson K, Warming S, Cuellar T, Haley B, Roose-Girma M, Phung QT, Liu PS, Lill JR, Li H, Wu J, Kummerfeld S, Zhang J, Lee WP, Snipas SJ, Salvesen GS, Morris LX et al (2015) Caspase-11 cleaves gasdermin D for non-canonical inflammasome signalling. *Nature* 526: 666–671
- Lamkanfi M (2011) Emerging inflammasome effector mechanisms. *Nat Rev Immunol* 11: 213–220
- Latz E, Xiao TS, Stutz A (2013) Activation and regulation of the inflammasomes. *Nat Rev Immunol* 13: 397–411
- Leung C, Dudkina NV, Lukoyanova N, Hodel AW, Farabella I, Pandurangan AP, Jahan N, Pires Damaso M, Osmanovic D, Reboul CF, Dunstone MA, Andrew PW, Lonnen R, Topf M, Saibil HR, Hoogenboom BW (2014) Stepwise visualization of membrane pore formation by sulfolysin, a bacterial cholesterol-dependent cytolysin. *elife* 3: e04247
- Mariathasan S, Newton K, Monack DM, Vucic D, French DM, Lee WP, Roose-Girma M, Erickson S, Dixit VM (2004) Differential activation of the inflammasome by caspase-1 adaptors ASC and Ipaf. *Nature* 430: 213–218
- Miao EA, Leaf IA, Treuting PM, Mao DP, Dors M, Sarkar A, Warren SE, Wewers MD, Aderem A (2010) Caspase-1-induced pyroptosis is an innate immune effector mechanism against intracellular bacteria. *Nat Immunol* 11: 1136–1142
- von Moltke J, Ayres JS, Kofoed EM, Chavarria-Smith J, Vance RE (2013) Recognition of bacteria by inflammasomes. *Annu Rev Immunol* 31: 73–106
- Muller DJ, Amrein M, Engel A (1997) Adsorption of biological molecules to a solid support for scanning probe microscopy. *J Struct Biol* 119: 172–188
- Mulvihill E, van Pee K, Mari SA, Muller DJ, Yildiz O (2015) Directly Observing the Lipid-Dependent Self-Assembly and Pore-Forming Mechanism of the Cytolytic Toxin Listeriolysin O. *Nano Lett* 15: 6965–6973
- Murphy JM, Czabotar PE, Hildebrand JM, Lucet IS, Zhang JG, Alvarez-Diaz S, Lewis R, Lalaoui N, Metcalf D, Webb AI, Young SN, Varghese LN, Tannahill GM, Hatchell EC, Majewski IJ, Okamoto T, Dobson RC, Hilton DJ, Babon JJ, Nicola NA et al (2013) The pseudokinase MLKL mediates necroptosis via a molecular switch mechanism. *Immunity* 39: 443–453
- Op de Beek K, Van Camp G, Thys S, Cools N, Callebaut I, Vrijens K, Van Nassauw L, Van Tendeloo VF, Timmermans JP, Van Laer L (2011) The DFNA5 gene, responsible for hearing loss and involved in cancer, encodes a novel apoptosis-inducing protein. *Eur J Hum Genet* 19: 965–973
- Pasparakis M, Vandenabeele P (2015) Necroptosis and its role in inflammation. *Nature* 517: 311–320
- Pfreundschuh M, Martinez-Martin D, Mulvihill E, Wegmann S, Muller DJ (2014) Multiparametric high-resolution imaging of native proteins by force-distance curve-based AFM. *Nat Protoc* 9: 1113–1130
- Podobnik M, Marchiorretto M, Zanetti M, Bavdek A, Kisovec M, Cajnko MM, Lunelli L, Dalla Serra M, Anderlueh G (2015) Plasticity of listeriolysin O pores and its regulation by pH and unique histidine. *Sci Rep* 5: 9623
- Ramage P, Cheneval D, Chvei M, Graff P, Hemmig R, Heng R, Kocher HP, Mackenzie A, Memmert K, Revesz L, Wishart W (1995) Expression, refolding, and autocatalytic proteolytic processing of the interleukin-1 $\beta$  converting enzyme precursor. *J Biol Chem* 270: 9378–9383
- Saeki N, Kim DH, Usui T, Aoyagi K, Tatsuta T, Aoki K, Yanagihara K, Tamura M, Mizushima H, Sakamoto H, Ogawa K, Ohki M, Shiroishi T, Yoshida T, Sasaki H (2007) GASDERMIN, suppressed frequently in gastric cancer, is a target of LMO1 in TGF- $\beta$ -dependent apoptotic signalling. *Oncogene* 26: 6488–6498
- Scherrer R, Gerhardt P (1971) Molecular sieving by the Bacillus megaterium cell wall and protoplast. *J Bacteriol* 107: 718–735
- Shi J, Zhao Y, Wang Y, Gao W, Ding J, Li P, Hu L, Shao F (2014) Inflammatory caspases are innate immune receptors for intracellular LPS. *Nature* 514: 187–192
- Shi J, Zhao Y, Wang K, Shi X, Wang Y, Huang H, Zhuang Y, Cai T, Wang F, Shao F (2015) Cleavage of GSDMD by inflammatory caspases determines pyroptotic cell death. *Nature* 526: 660–665
- Sonnen AF, Plitzko JM, Gilbert RJ (2014) Incomplete pneumolysin oligomers form membrane pores. *Open Biol* 4: 140044
- Su L, Quade B, Wang H, Sun L, Wang X, Rizo J (2014) A plug release mechanism for membrane permeation by MLKL. *Structure* 22: 1489–1500
- Suzuki M, Youle RJ, Tjandra N (2000) Structure of Bax: coregulation of dimer formation and intracellular localization. *Cell* 103: 645–654
- Tanaka S, Mizushima Y, Kato Y, Tamura M, Shiroishi T (2013) Functional conservation of Gsdma cluster genes specifically duplicated in the mouse genome. *G3 (Bethesda)* 3: 1843–1850
- Thornberry NA, Bull HG, Calaycay JR, Chapman KT, Howard AD, Kostura MJ, Miller DK, Molineaux SM, Weidner JR, Aunins J, Elliston KO, Ayala JM, Casano FJ, Chin J, Ding GJF, Egger LA, Gaffney EP, Limjuco G, Palyha OC, Raju SM et al (1992) A novel heterodimeric cysteine protease is required for interleukin-1 $\beta$  processing in monocytes. *Nature* 356: 768–774
- Wang H, Sun L, Su L, Rizo J, Liu L, Wang LF, Wang FS, Wang X (2014) Mixed lineage kinase domain-like protein MLKL causes necrotic membrane disruption upon phosphorylation by RIP3. *Mol Cell* 54: 133–146
- Youle RJ, Strasser A (2008) The BCL-2 protein family: opposing activities that mediate cell death. *Nat Rev Mol Cell Biol* 9: 47–59



**License:** This is an open access article under the terms of the Creative Commons Attribution-NonCommercial-NoDerivs 4.0 License, which permits use and distribution in any medium, provided the original work is properly cited, the use is non-commercial and no modifications or adaptations are made.

## Appendix

### **GSDMD membrane pore formation constitutes the mechanism of pyroptotic cell death**

Lorenzo Sborgi<sup>1,\*</sup>, Sebastian Rühl<sup>1,\*</sup>, Estefania Mulvihill<sup>2</sup>, Joka Pipercevic<sup>1</sup>, Rosalie Heilig<sup>1</sup>, Henning Stahlberg<sup>1</sup>, Christopher J. Farady<sup>3</sup>, Daniel J. Müller<sup>2</sup>, Petr Broz<sup>1</sup> and Sebastian Hiller<sup>1</sup>

\* these authors contributed equally

#### Affiliations

- <sup>1</sup> Biozentrum, University of Basel, Klingelbergstr. 70, 4056 Basel, Switzerland
- <sup>2</sup> Eidgenössische Technische Hochschule (ETH) Zurich, Department of Biosystems Science and Engineering, Mattenstr. 26, 4058 Basel, Switzerland
- <sup>3</sup> Novartis Institutes for BioMedical Research, Forum 1, Novartis Campus, 4002 Basel, Switzerland

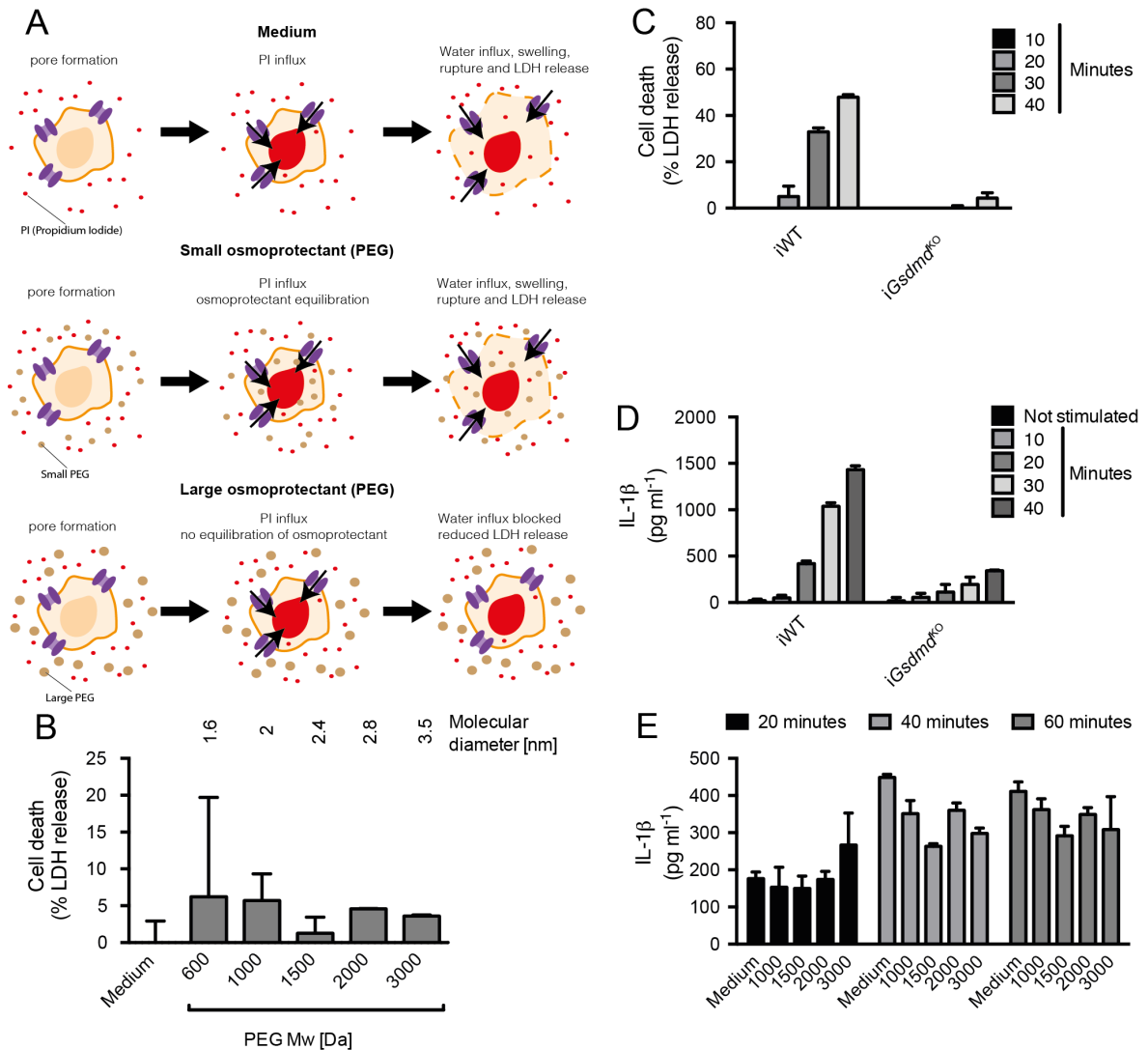
Correspondence to:

Petr Broz ([petr.broz@unibas.ch](mailto:petr.broz@unibas.ch))

Sebastian Hiller ([sebastian.hiller@unibas.ch](mailto:sebastian.hiller@unibas.ch))

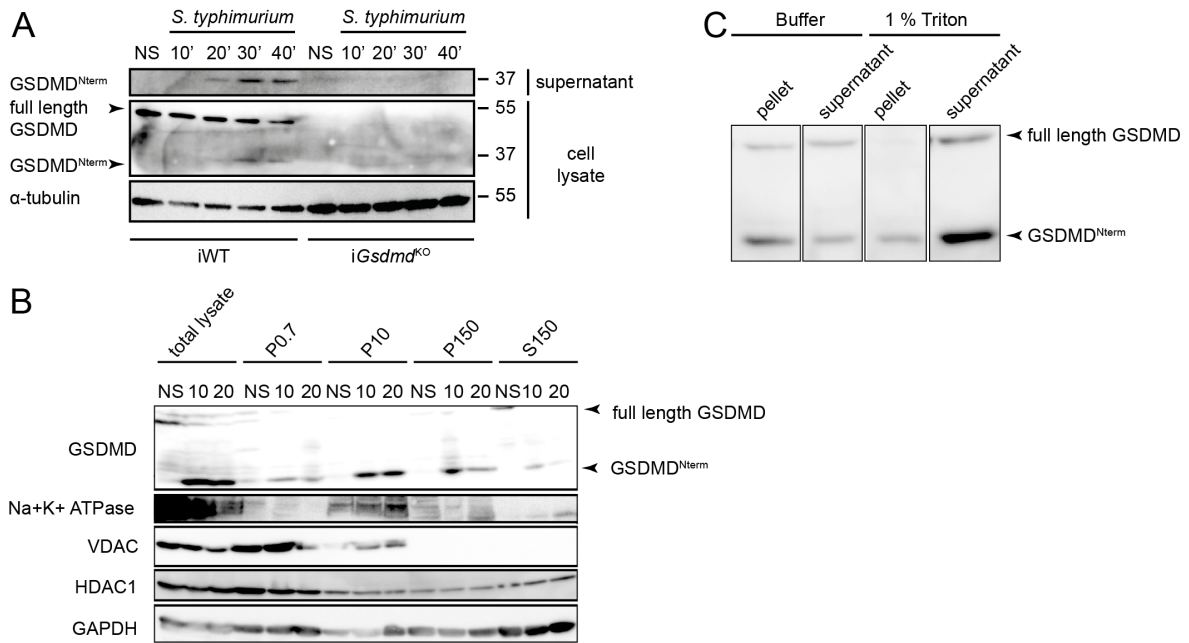
### **Appendix Table Of Contents**

Appendix Figures S1-S8



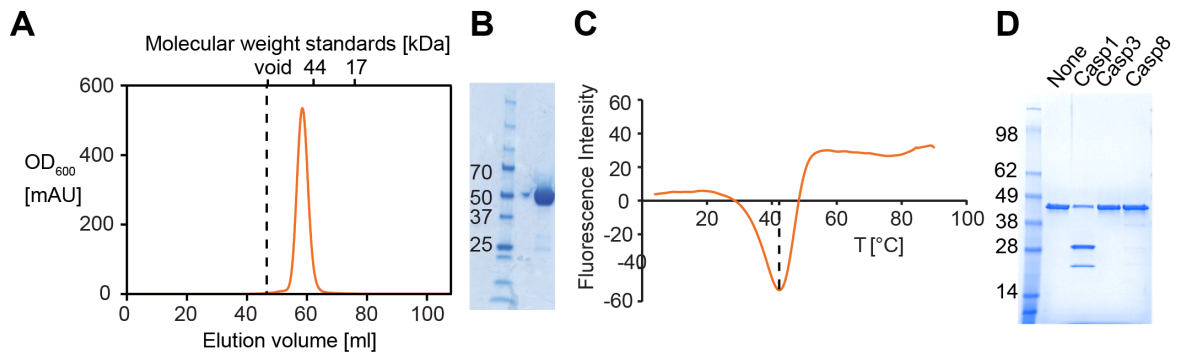
**Appendix Figure S1. GSDMD is essential for caspase-1-mediated cell death and cytokine release.**

**A.** Schematic representation of the principle of an osmoprotection assay. **B.** Cell death as measured by LDH release from HEK 293T treated for 8 h with PEGs of increasing molecular weight. **C-D.** LDH and IL-1 $\beta$  release from LPS-primed immortalized wild-type and *Gsdmd*-deficient macrophages infected for 10–40 minutes with log phase *S. typhimurium* (MOI=50). **E.** IL-1 $\beta$  release from LPS-primed primary BMDMs shown in **Fig. 1E–F**. Graphs show mean and s.d. of quadruplicate wells and data are representative of at least three independent experiments.



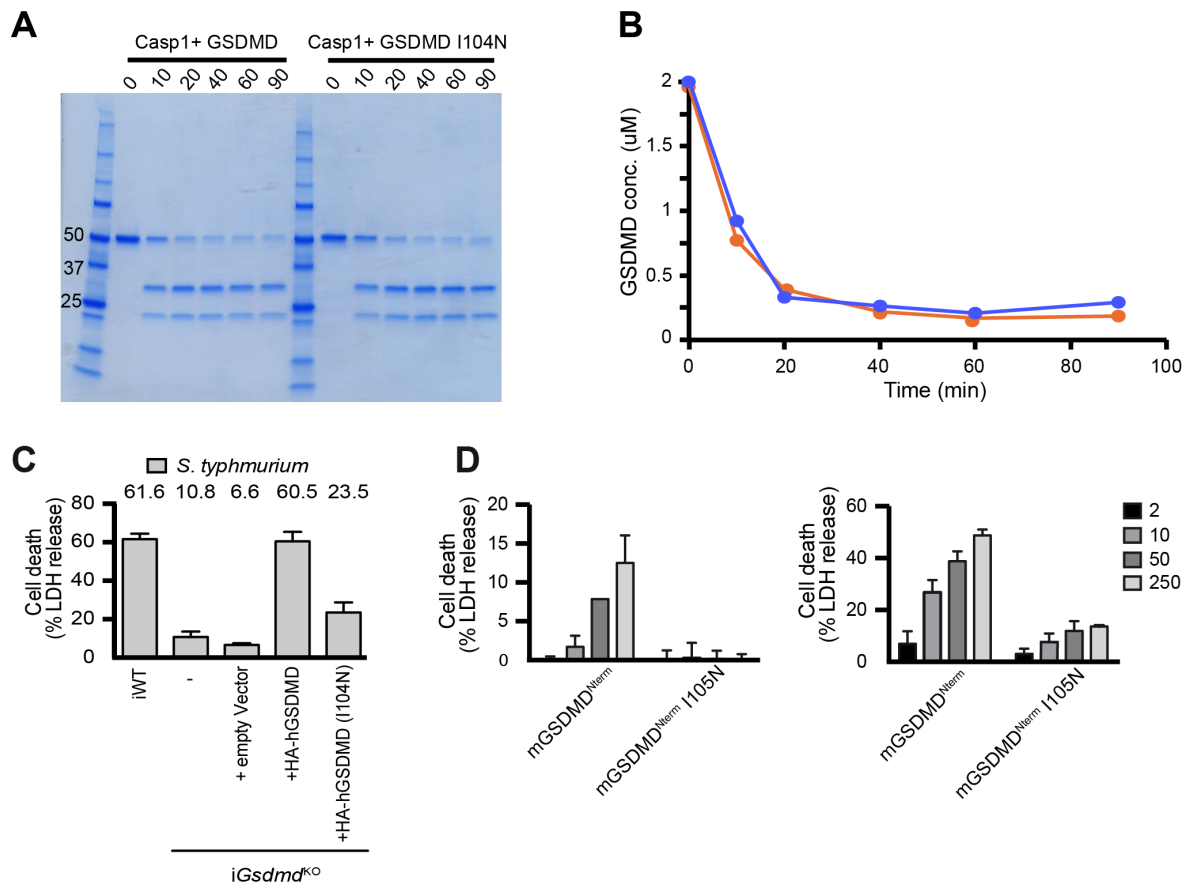
**Appendix Figure S2. Membrane targeting of endogenous GSDMD**

**A.** Immunoblot analysis of cleaved Gasdermin-D (GSDMD) in culture supernatants and full length GSDMD, cleaved GSDMD and  $\alpha$ -tubulin in the cell lysates of immortalized LPS-primed WT and *Gsdmd*-deficient macrophages left uninfected (NS) or infected for 10–40 minutes with log phase *S. typhimurium* (MOI=50). **B.** Fractionation and immunoblot analysis for Gasdermin-D, Na+K+ ATPase, VDAC (Voltage-dependent anion channel), HDAC1 (Histone deacetylase 1) and GAPDH (Glycerinaldehyd-3-phosphat-Dehydrogenase) of WT macrophages infected for 10 minutes with log phase *S. typhimurium* (MOI=50). Fractionation was carried out as described in the Material and Methods section, but in contrast to Figure 2 the total fraction from equivalent numbers of cells ( $2.8 \times 10^6$  cells/lane) instead of equivalent amount of protein was loaded. **C.** Extraction of full-length GSDMD and GSDMD<sup>Nterm</sup> from isolated membranes of WT macrophages infected for 10 minutes with log phase *S. typhimurium* (MOI=50). Data are representative of 2 (A), 1 (B) and 1 (C) independent experiments.



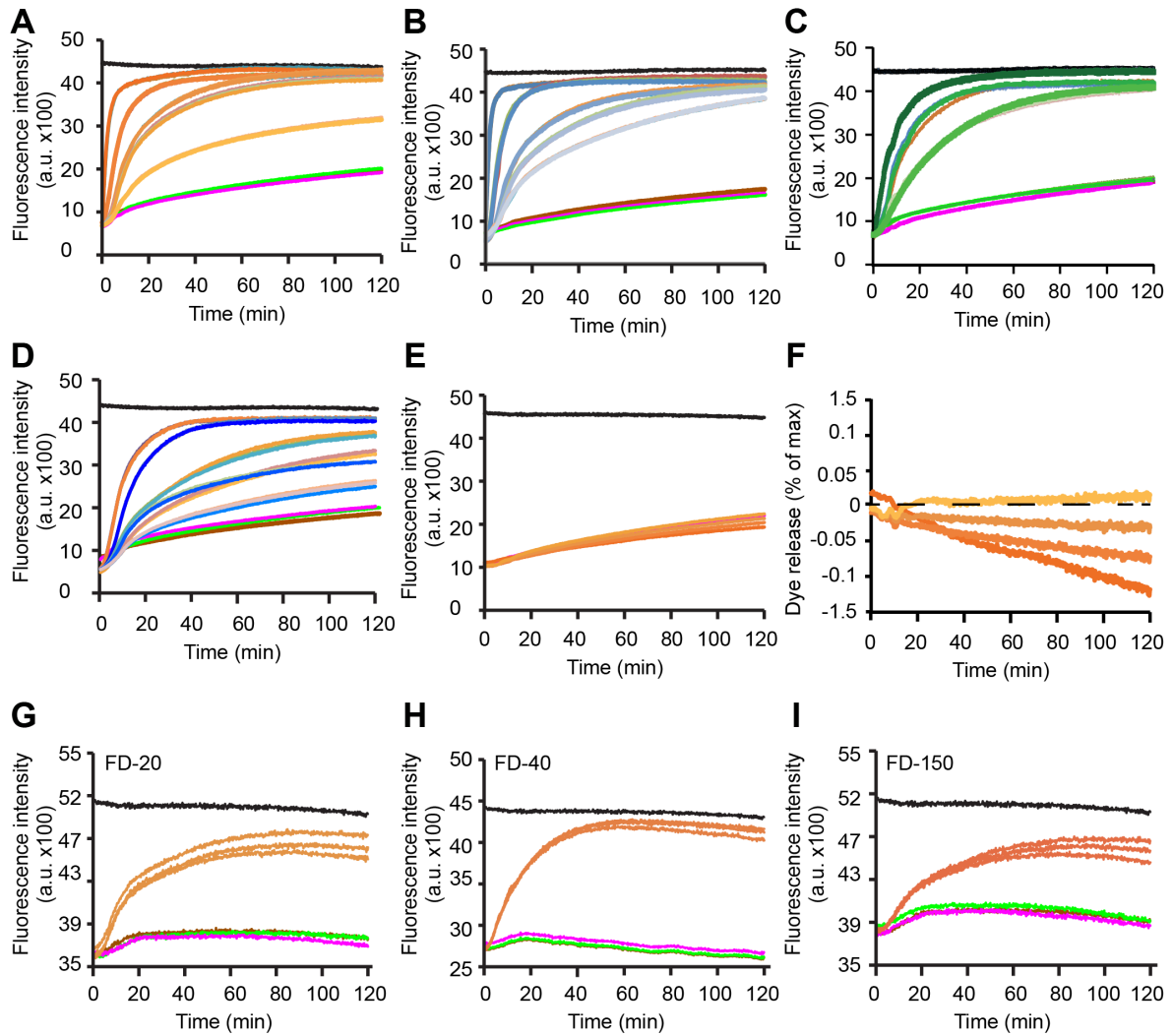
**Appendix Figure S3. Purified full-length GSDMD is stable and monomeric in solution**

**A.** Gel filtration profile of purified full-length GSDMD. The chromatogram was recorded using 20 mM Tris buffer, pH 7.5, 50 mM NaCl, 0.5 mM TCEP on a Superdex S75 size exclusion column. The void volume and the molecular weights of a standard calibration curve are indicated. **B.** SDS-PAGE analysis of GSDMD after size exclusion purification. **C.** Thermofluor-assay to assess the stability of GSDMD at the conditions used for the *in vitro* experiments. **D.** SDS-PAGE of 2  $\mu$ M GSDMD incubated at room temperature with 5 nM of either caspase-1, caspase-3 or caspase-8. Only upon addition of caspase-1, GSDMD was cleaved in into two bands of roughly 30 and 22 kDa.



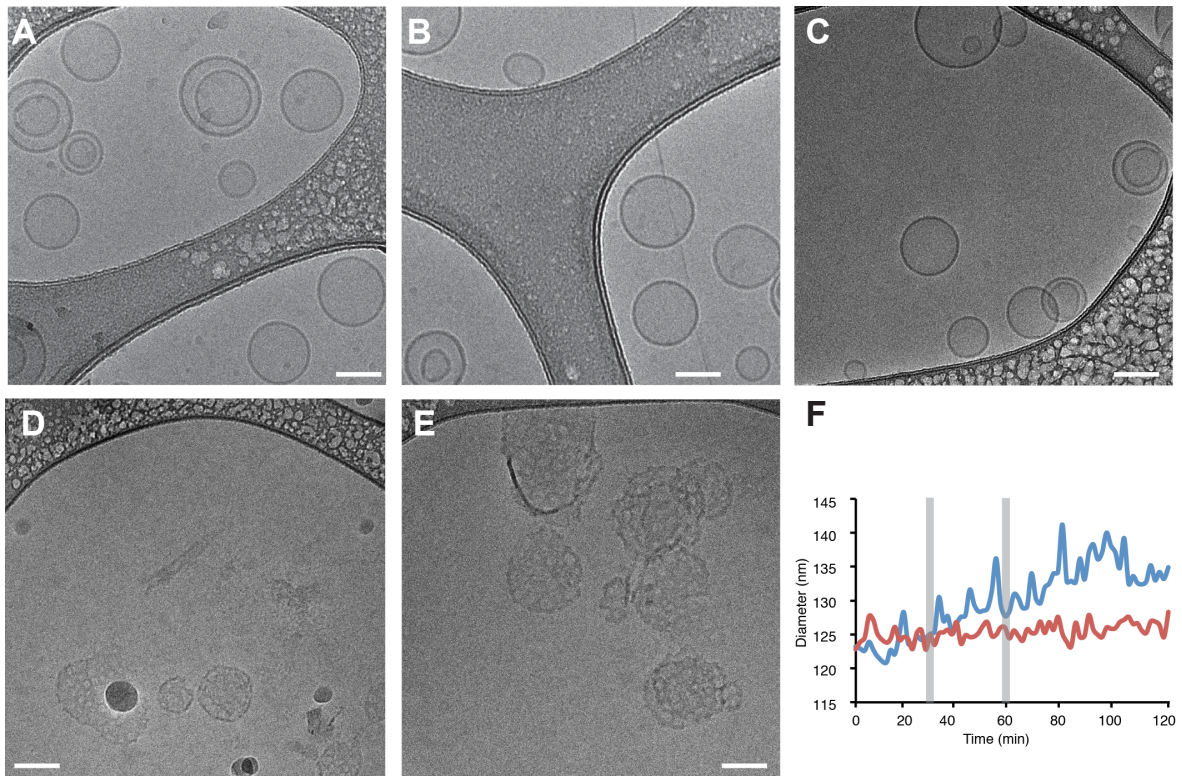
#### Appendix Figure S4. Cleavage and cell death activity of GSDMD<sup>I104N</sup>

**A.** Cleavage of 2  $\mu$ M human wild-type GSDMD (left) or GSDMD<sup>I104N</sup> (right) incubated with 5 nM caspase-1 at room temperature. **B.** Cleavage kinetics of GSDMD wild type (orange) and GSDMD<sup>I104N</sup> (blue), as obtained from quantification of the SDS-PAGE band intensities in panel A with the software ImageJ. **C.** LDH release from immortalized wildtype macrophages or *Gsdmd*<sup>KO</sup> macrophages, either untransduced or transduced with the indicated constructs in pLJM1-Hygro 7 days post transduction. Transduced cells were selected by Hygromycin treatment. Cells were infected with *S. typhimurium* for 40 minutes. **D.** HEK 293T cells were seeded as described in Figure 1 and transfected with pRetroX tetONE 3G containing the murine GSDMD<sup>Nterm</sup> or the GSDMD<sup>I104N</sup> of the protein under a doxycycline inducible promotor. Cells were treated for 8 h (right panel) or 16 h (left panel) with the indicated concentrations of doxycycline. Cell death was analyzed by LDH release. Bars indicate average  $\pm$  s.d. of quadruplicate wells. Results are representative of 4 (C) and 2 (D) independent experiments.



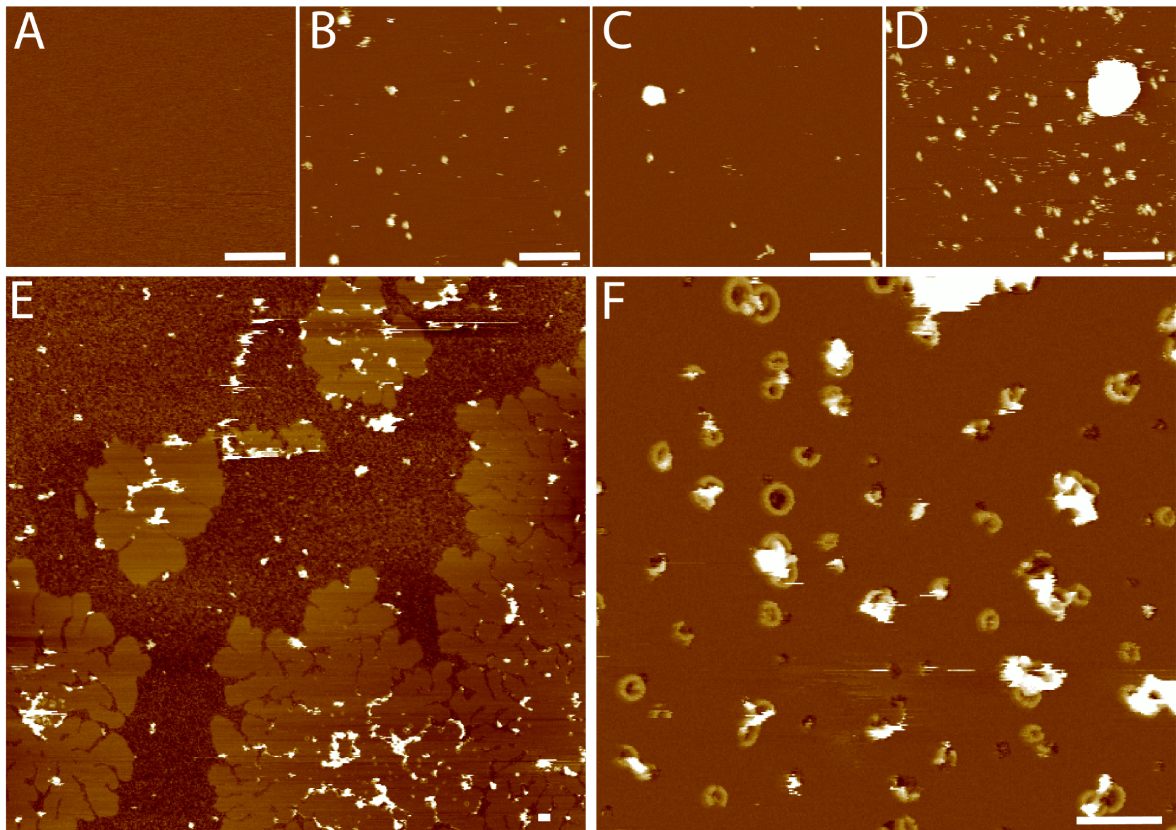
**Appendix Figure S5. Experimental raw data of liposome dye release experiments**

**A–I.** Fluorescence intensity time course of dye-loaded liposomes. **A–E.** Triplicate measurements of the experiments described in Figure 4 A–E. The experimental conditions and color code are identical to panels Figure 4 A–E. **F.** Four different reactions where 400  $\mu$ M 6-carboxyfluorescein-loaded liposomes were incubated with GSDMD concentrations of (nM): 2000, 1000, 512, 216 (dark to light orange). **G–I.** Triplicate measurements of the experiments described in Figure 4 G–I. For A–D and G–I, each panel shows the emission intensity for the following control experiments: liposomes (magenta), for liposomes + GSDMD (green) and for liposomes + caspase-1 (brown), as well as the maximum emission intensity for each assay, recorded by adding Triton X-100 to the liposome solution (black).



**Appendix Figure S6. Time course visualization of GSDMD<sup>Nterm</sup> pores by cryo-EM.**

**A.** Cryo-EM micrograph of liposomes from *E. coli* polar extract lipids. Scale bar, 80 nm. **B.** Cryo-EM micrograph of 260  $\mu$ M liposome solution incubated with 2.6  $\mu$ M of GSDMD in the absence of caspase-1. Scale bar, 80 nm. **C–E.** Cryo-EM micrographs acquired at time points 0 min (C), 30 min (D) and 60 min (E), after incubation of 260  $\mu$ M liposome solution + 2.6  $\mu$ M of GSDMD with 48 nM of caspase-1. Scale bars, 80 nm. **F.** Average liposome diameter as determined by time-resolved dynamic light scattering (DLS) measurements at the sample conditions of the cryo-EM experiments (blue) and of the liposome leakage assay (red). Grey bars highlight the 30 and 60 min time points.



**Appendix Figure S7. Control experiments showing that full-length GSDMD adsorbed to mica does not assemble into defined oligomeric structures**

**A.** AFM topograph of freshly cleaved mica after incubation of 0.3  $\mu\text{M}$  GSDMD, 0.2  $\mu\text{M}$  caspase-1, or 1  $\mu\text{M}$  GSDMD and 0.2  $\mu\text{M}$  caspase-1 for 90 minutes at 37  $^{\circ}\text{C}$  in buffer solution (50 mM NaCl, 100 mM Hepes, 5 mM TCEP, pH 7.4) the samples were adsorbed onto freshly cleaved mica for 30 minutes and then the mica was rinsed with imaging buffer (150 mM NaCl, 20 mM Hepes, pH 7.8) solution to remove weakly attached molecules. **B.** AFM topograph showing GSDMD adsorbed onto the mica surface as presumably monomers or small oligomers. **C.** AFM topograph showing caspase-1 adsorbed onto the mica surface as presumably monomers or small oligomers. **D.** AFM topograph showing GSDMD and caspase-1 adsorbed onto the mica surface as presumably monomers or small oligomers. **E.** Overview AFM topograph of liposome made from *E. coli* polar lipids extract after being incubated with GSDMD and caspase-1 for 90 min at 37 $^{\circ}\text{C}$ . The liposome upon adsorption to the mica support opened showing single membrane patches. **F.** At higher resolution of these membrane patches the AFM topographs show the arc-, slit- and ring-shaped GSDMD oligomers at detail. AFM topographs were taken in buffer solution at room temperature. The full-range color scales of the AFM topographs correspond to a height of 10 nm (A–D) and 22 nm (E–F). Scale bars, 100 nm.



**Joka Piperčević**

**Citizenships** Slovenian, German

**Education**

- 09/2015 – 01/2021 Doctor of Philosophy (PhD) in Structural Biology in the laboratory of Prof. Sebastian Hiller at University of Basel, Switzerland
- 09/2011 – 09/2013 Master of Science in Biochemistry at Technical University of Munich, Germany
- 09/2008 – 08/2011 Bachelor of Science in Biochemistry at Technical University of Munich, Germany

**Research positions**

- 08/2014 – 06/2015 Research associate in the laboratory of Prof. Franz Hagn at Technical University of Munich, Germany
- 11/2013 – 07/2014 Research associate in the laboratory of Prof. Gerhard Wagner at Harvard Medical School, USA
- 03/2008 – 08/2013 Master's Thesis in the laboratory of Prof. Michael Sattler at Technical University of Munich, Germany

**Experience in Organization and Teaching**

- 12/2016 – 12/2018 Head of PhD community at Biozentrum, University of Basel, Switzerland
- 09/2017 – 09/2018 Head of organisation for annual PhD retreat at Biozentrum, University of Basel, Switzerland
- 06/2017 – 07/2017 Teaching about Toxicology at German Summer Academy for high school students organized by Bildung&Begabung, Germany
- 09/2011 – 06/2013 Tutoring about Organic Chemistry Synthesis at Technical University of Munich, Germany

**Awards**

- 2015 - 2018 *Fellowship for Excellence* at Biozentrum, University of Basel, Switzerland
- 2008 - 2010 Fellowship of *Studienstiftung des deutschen Volkes*, Germany